

A multi-sensor approach for land cover classification and monitoring of tidal flats in the German Wadden Sea

Richard Jung

Institute for Geoinformatics and Remote Sensing

University of Osnabrueck

A thesis submitted to the
Faculty Mathematics-Informatics
of the
University of Osnabrueck
in fulfilment of the requirements for the degree of

Dr. rer. nat.

December 2015

Supervisor: Prof. Dr.-Ing. Manfred Ehlers
University of Osnabrueck
Institute for Geoinformatics and Remote Sensing
Osnabrueck, Germany

Abstract

Sand and mud traversed by tidal inlets and channels, which split in subtle branches, salt marshes at the coast, the tide, harsh weather conditions and a high diversity of fauna and flora characterize the ecosystem Wadden Sea. No other landscape on the Earth changes in such a dynamic manner. Therefore, land cover classification and monitoring of vulnerable ecosystems is one of the most important approaches in remote sensing and has drawn much attention in recent years. The Wadden Sea in the southeastern part of the North Sea is one such vulnerable ecosystem, which is highly dynamic and diverse. The tidal flats of the Wadden Sea are the zone of interaction between marine and terrestrial environments and are at risk due to climate change, pollution and anthropogenic pressure. Due to that, the European Union has implemented various directives, which formulate objectives such as achieving or maintaining a good environmental status respectively a favourable conservation status within a given time. In this context, a permanent observation for the estimation of the ecological condition is needed. Moreover, changes can be tracked or even foreseen and an appropriate response is possible. Therefore, it is important to distinguish between short-term changes, which are related to the dynamic manner of the ecosystem, and long-term changes, which are the result of extraneous influences. The accessibility both from sea and land is very poor, which makes monitoring and mapping of tidal flat environments from in situ measurements very difficult and cost-intensive. For the monitoring of big areas, time-saving applications are needed. In this context, remote sensing offers great possibilities, due to its provision of a large spatial coverage and non-intrusive measurements of the Earth's surface. Previous studies in remote sensing have focused on the use of electro-optical and radar sensors for remote sensing of tidal flats, whereas microwave systems using synthetic aperture radar (SAR) can be a complementary tool for tidal flat observation, especially due to their high spatial resolution and all-weather imaging capability. Nevertheless, the repetitive tidal event and dynamic sedimentary processes make an integrated observation of tidal flats from multi-sourced datasets essential for mapping and monitoring.

The main challenge for remote sensing of tidal flats is to isolate the sediment, vegetation or shellfish bed features in the spectral signature or backscatter intensity from interference by water, the atmosphere, fauna and flora. In addition, optically active materials, such as plankton, suspended matter and dissolved organics, affect the scattering and absorption of radiation. Tidal flats are spatially complex and temporally quite variable and thus mapping

tidal land cover requires satellites or aircraft imagers with high spatial and temporal resolution and, in some cases, hyperspectral data.

In this research, a hierarchical knowledge-based decision tree applied to multi-sensor remote sensing data is introduced and the results have been visually and numerically evaluated and subsequently analysed. The multi-sensor approach comprises electro-optical data from RapidEye, SAR data from TerraSAR-X and airborne LiDAR data in a decision tree. Moreover, spectrometric and ground truth data are implemented into the analysis. The aim is to develop an automatic or semi-automatic procedure for estimating the distribution of vegetation, shellfish beds and sediments south of the barrier island Norderney. The multi-sensor approach starts with a semi-automatic pre-processing procedure for the electro-optical data of RapidEye, LiDAR data, spectrometric data and ground truth data. The decision tree classification is based on a set of hierarchically structured algorithms that use object and texture features. In each decision, one satellite dataset is applied to estimate a specific class. This helps to overcome the drawbacks that arise from a combined usage of all remote sensing datasets for one class. This could be shown by the comparison of the decision tree results with a popular state-of-the-art supervised classification approach (random forest).

Subsequent to the classification, a discrimination analysis of various sediment spectra, measured with a hyperspectral sensor, has been carried out. In this context, the spectral features of the tidal sediments were analysed and a feature selection method has been developed to estimate suitable wavelengths for discrimination with very high accuracy. The developed feature selection method 'JMDFS' (Jeffries-Matusita distance feature selection) is a filter-based supervised band elimination technique and is based on the local Euclidean distance and the Jeffries-Matusita distance. An iterative process is used to subsequently eliminate wavelengths and calculate a separability measure at the end of each iteration. If distinctive thresholds are achieved, the process stops and the remaining wavelengths are applied in the further analysis. The results have been compared with a standard feature selection method (ReliefF). The JMDFS method obtains similar results and runs 216 times faster.

Both approaches are quantitatively and qualitatively evaluated using reference data and standard methodologies for comparison. The results show that the proposed approaches are able to estimate the land cover of the tidal flats and to discriminate the tidal sediments with moderate to very high accuracy. The accuracies of each land cover class vary according to the dataset used. Furthermore, it is shown that specific reflection features can be identified that

help in discriminating tidal sediments and which should be used in further applications in tidal flats.

Table of Contents

ABSTRACT.....	II
LIST OF FIGURES.....	VIII
LIST OF TABLES.....	XV
LIST OF ABBREVIATIONS.....	XVII
1 Introduction.....	1
1.1 Motivation and problem statement.....	1
1.2 Goals and scientific contribution.....	3
1.3 Organisation of the dissertation.....	4
2 Review of classification applications in tidal flats and feature selection methods ..	6
2.1 Introduction.....	6
2.2 Sediments.....	6
2.3 Tidal vegetation.....	9
2.4 Shellfish beds, blue mussel and oyster beds.....	10
2.5 Alternative methods and applications in intertidal flat areas.....	11
2.6 Feature selection.....	12
2.7 Summary.....	13
3 Study area and datasets.....	15
3.1 Study area ‘Norderney’.....	15
3.2 RapidEye.....	16
3.3 Terra SAR-X.....	19
3.4 LiDAR.....	23
3.5 Spectrometry data.....	26
3.6 Other ground truth data.....	28
3.7 Summary.....	30
4 Methodology.....	32
4.1 Introduction.....	32
4.2 Class definition and ecological value.....	32

4.2.1	Sediments.....	33
4.2.2	Tidal vegetation	34
4.2.3	Blue mussel/oyster beds	37
4.3	Data pre-processing.....	38
4.3.1	RapidEye.....	38
4.3.2	TerraSAR-X.....	43
4.3.3	LiDAR	43
4.3.4	Spectrometry data	44
4.4	Classification.....	49
4.4.1	Hierarchical knowledge-based classification	49
4.4.1.1	Classification of shellfish beds based on TerraSAR-X.....	53
4.4.1.2	Classification of tidal vegetation based on RapidEye.....	54
4.4.1.3	Classification of sediments based on RapidEye.....	55
4.4.1.4	Improvement of sediment classification with LiDAR	56
4.4.1.4.1	Object-based water classification.....	59
4.4.1.4.2	Extraction of the tidal channel network and geometric features.....	64
4.4.2	Random Forest.....	72
4.5	Analysis of the spectral discrimination of sediments with spectrometric data	74
4.5.1	Jeffries-Matusita distance feature selection.....	76
4.5.2	ReliefF	80
4.5.3	Selection of the most important wavelengths.....	81
4.6	Summary	85
5	Results	86
5.1	Data pre-processing.....	86
5.1.1	RapidEye.....	86
5.1.2	LiDAR	87
5.2	Classifications	89
5.2.1	Evaluation methods	89

5.2.2	Hierarchical decision tree	92
5.2.2.1	Blue mussel/oyster beds	92
5.2.2.2	Vegetation (salt marsh, algae and seagrass).....	97
5.2.2.3	Sediments with RapidEye	101
5.2.2.4	Improvement of sediment classification with LiDAR	107
5.2.2.4.1	Object-based water classification.....	107
5.2.2.4.2	Extraction of the tidal stream network and geometric features.....	111
5.2.3	Intertidal classification with Random Forest.....	120
5.3	Spectrometry data.....	127
5.4	Summary	139
6	Conclusion.....	144
7	Outlook.....	148
	ACKNOWLEDGEMENTS	151
	REFERENCES	152
	APPENDIX.....	169

List of figures

Figure 3-1: Location of the study area in the German bight (a) and an example of a RapidEye image (b) and TerraSAR-X image (c). The green polygons represent areas of sandy sediments, the red polygon represents an area of muddy sediments, the purple polygon represents an area of mixed sediments and the blue polygon represents an extended shellfish bed consisting of blue mussels and Pacific oysters.	15
Figure 3-2: The electromagnetic spectrum with the microwave portion of radar systems (changed after Lusch 1999).	20
Figure 3-3: Concept of the SAR (Knuth 2008).	21
Figure 3-4: Boundaries of the LiDAR data from 2010, 2012 and 2013 with a RE image and OSM data in the background.	23
Figure 3-5: Cloud coverage during the spectrometric measurements in 03 June 2013, 04 June 2013 and 06 June 2013.	26
Figure 3-6: Distribution of the stations from 03 – 06 June 2013 and 11 June 2015 of the spectrometric measurements.	28
Figure 3-7: A map of ground truth data representing sediments with an underlying pre-processed image of RE from 25 April 2010. The different markers represent different years of ground truth measuring. The ground truth measurements of 2008/09 were acquired by the project DeMarine.	29
Figure 4-1: Example for a dense seagrass patch in the study area.	36
Figure 4-2: The magnitude image of April 2010 (left) and the binary filter (right) of the FFT process. The green polygons on the right side represent the applied filter.	39
Figure 4-3: Advanced parameters for FLAASH.	42
Figure 4-4: Calculation of zenith and azimuth angle for FLAASH.	43
Figure 4-5: Detailed description of the overlap removal.	44
Figure 4-6: Flow chart for the pre-processing of the spectrometer data.	46
Figure 4-7: SNR values in dB of specific wavelength ranges from 2013 (plot a)) and 2015 (plot b)). Plot c) represents distinctive spectra that create a very low SNR in the data of 2015.	47
Figure 4-8: Examples for the analysis of the changing illumination conditions. Plot a) represents the lowest RMSE of 2013, plot b) the highest RMSE of 2013, plot c) the lowest RMSE of 2015 and plot d) the highest RMSE of 2015.	49

Figure 4-9: Workflow of the hierarchical classification procedure (see text for explanations).....	52
Figure 4-10: Subset of a RE image (left, RGB of 27 June 2011) and a TSX image (right, 16 July 2011) of an old and well developed shellfish bed and a small shellfish bed. The bright pixels in the TSX image represent the shellfish beds which can be seen partly as dark brownish pixels in the RE image.....	54
Figure 4-11: Scheme of the hierarchical decision tree classification of the sediments.....	56
Figure 4-12: Two subsets of the LiDAR DEM from 2010 showing the differences of the channel geometry in relation to the underlying sediment type. On the left hand side is an example for a sandy area and on the right hand side an example for a muddy area.	58
Figure 4-13: Integration of LiDAR data into the existing sediment classification scheme of RE.	59
Figure 4-14: The multiresolution segmentation algorithm in a nutshell (Definiens 2010)....	60
Figure 4-15: Relationship between the parameters of the multiresolution segmentation algorithm (after Definiens 2010).	60
Figure 4-16: Original spatial extent of the DEM of 2010 compared to the subset (red polygon) used for the development of the rule set.	62
Figure 4-17: Plot a) represents a subset of the DEM and plot b) to d) illustrates the growing strategy.	63
Figure 4-18: Rule set of the object-based water classification.....	63
Figure 4-19: Subset of the object-based tidal channel classification result from the LiDAR data of 2010.	64
Figure 4-20: Plot a) represents the eight possible flow directions from a grid cell, plot b) is an example for heights of an DEM with the possible downhill directions, plot c) shows the resulting runoff of the D8 method and plot d) shows the resulting runoff of the MFD method (after Holmgren 1994).	65
Figure 4-21: Subset of the channel network extraction (blue lines) from the LiDAR data of 2010.	67
Figure 4-22: Sub-channel stream networks that are detected after the network extraction with 'GRASS GIS'.	68
Figure 4-23: Schematic examples of the search for confluences using a 3x3 array. The red square represents a confluence.	68
Figure 4-24: Schematic example for the elimination of redundant confluence results.....	69

Figure 4-25: Schematic example for the definition of flow direction for every adjacent channel network pixel.....	69
Figure 4-26: Examples of flow direction changes.	70
Figure 4-27: Identified sub-channel stream networks for sand flats (plot a)) and mudflats (plot b)). One of each sub-channel stream networks for sand flats and mudflats are not shown, because they are out of the chosen subset boundary.....	71
Figure 4-28: Flow chart of the RF algorithm.	74
Figure 4-29: Stepwise execution of the ‘Jeffries-Matusita distance feature selection’ algorithm with the stopping criteria Jeffries-Matusita distance (JMD) and the number of bands left (BNR).....	78
Figure 4-30: A result of the ‘Jeffries-Matusita Distance feature selection’ of 2015 (plot a)) and an artificial result (plot b)) in comparison. The horizontal black and bold dashed line is the actual spectrum that is compared with all the others. The black dots/lines represent the remaining wavelengths, the vertical blue dashed lines represent the wavelength of RE and the red dots/lines of plot b) are the resulting common wavelengths.	79
Figure 4-31: Extended flow chart for the methodology of the spectrometric data. The first part (pre-processing), which was already discussed in Figure 4-6, is greyed out.	82
Figure 4-32: Schematic example for the two wavelength selection approaches ‘peaks’ and ‘ranges’.....	84
Figure 4-33: Two examples for obtaining the most important wavelengths from both feature selection methods (JMDFS and ReliefF). Plot a) represents the method ‘peaks’ and plot b) represents the method ‘ranges’. The obtained wavelengths are displayed next to the plots.	85
Figure 5-1: The original RE image with noise and artefacts (left), the result of the Fourier transform based filter (centre) and the result after the MNF transform (right).	86
Figure 5-2: Comparison of the height values derived from the LiDAR data of 2012 with the RTK measurements of 2012. Plot) shows the height values for both measurements, plot b) represents the difference in height and plot c) shows the accordance using a linear regression.....	88
Figure 5-3: Subset of the combined shellfish bed and water classification from 16 July 2011 (TSX data) and 11 July 2011 (RE data) in the western part (left) and the eastern part (right) of the study area superimposed with the vector layer of 2011. The arrow	

shows a young mussel bed which cannot be detected with electro-optical satellite data alone.....	92
Figure 5-4: Change of the shellfish bed distribution derived with the decision tree approach. Plot b) represents only a small area of change, due to the TSX image of 28 October 2011 that covers only the eastern part of the study area.....	96
Figure 5-5: Subset of the seagrass/algae and salt marsh classification from 11 July 2011 (above) and the corresponding CIR aerial photos of September 2011 (below).	98
Figure 5-6: Two examples for the sparse seagrass meadows in the study area. One is taken from topview and one from oblique view.	98
Figure 5-7: Bar chart of the salt marsh changes in km ² from 25 April 2010 to 27 June 2011, from 27 June 2011 to 11 July 2011 and from 11 July 2011 to 22 October 2011. These are results of the hierarchical knowledge-based decision tree classifications.....	101
Figure 5-8: The plots a) to f) show comparison of the statistical parameters (mean, maximum, minimum, stdev and RMSE) of spectra from wet-sand polygon, dry-sand polygon, mud polygon and mixed-sediment polygon. All the polygons comprise 100 samples. The different lines represent the minimum (bottom dotted line), stdev (dashed lines), mean (solid line) and maximum (top dotted line). Discrete spectral band values (symbolized by squares, triangles, circles and crosses) were linked for better comparison.....	105
Figure 5-9: Examples of the balanced sampling design of the accuracy assessment. The red dots represent reference pixel for the class ‘water’	108
Figure 5-10: A subset of the object-based water classification (blue area) from 2010 showing a shellfish bed in the centre and the influence on the classification result.	109
Figure 5-11: Comparison of the visibility of small intertidal streams on a) sand flats and b) mudflats with the corresponding schematic profile.....	109
Figure 5-12: Plot a) shows an example for errors that occur during the stream network extraction. Plot b) shows the same process as an advantage. The errors and advantages are highlighted by the red polygons.	112
Figure 5-13: Classification of the derived and reference channel network into true positives (TP), false positives (FP) and false negatives (FN).....	113
Figure 5-14: Representative channel network areas to validate the search for confluences approach.....	114
Figure 5-15: Example for the extraction of the flow direction from a channel network	115
Figure 5-16: Three examples for the extraction of the flow direction change on a mudflat.	115

Figure 5-17: A subset of classified mudflats using geometric information derived from LiDAR data.....	119
Figure 5-18: Bar chart of the salt marsh changes in km ² from 25 April 2010 to 27 June 2011, from 27 June 2011 to 11 July 2011 and from 11 July 2011 to 22 October 2011. The results are obtained using the random forest classification.....	125
Figure 5-19: Normalized mean reflectance of the classes from 2015 coloured by their specific influences. The red spectra are influenced by microalgae, the blue by water, the purple by seagrass and the black by nothing specific. The black dashed lines are the wavelengths of the RE bands.....	130
Figure 5-20: Two examples of 2013 for the analysis of the JMDFS for common wavelengths between all combinations of one spectrum to all the others. The black dots/lines representing the remaining wavelengths after achieving a JMD greater than 1.9, the red dots/ lines represent a 100% accordance between all combinations, the blue dots/ lines on plot a) represent an accordance greater than 80%, the blue dashed line are the wavelengths of RE and the black dashed line represents the actual spectrum that is compared with all the others. Plot a) represents the common wavelengths between spectrum 1 and all the others and plot b) represents the same for spectrum 2.	131
Figure 5-21: The result of the JMDFS feature selection method. The red line represents the relative frequency (i.e., importance) of the wavelengths, the grey lines are the mean spectra of the selected classes (e.g., 14 classes) and the blue dashed lines are the wavelengths of the RE bands.....	133
Figure 5-22: The result of the ReliefF feature selection method. The red line represents the weights (i.e., importance) for the wavelengths, the grey lines are every measured spectra (50 samples in 2013 and 45 samples in 2015) and the blue dashed lines are the wavelengths of the RE bands.....	134
Figure 5-23: Comparison of all selected wavelengths for JMDFS and ReliefF of 2013 and 2015.....	135
Figure 5-24: Comparison of the original selection of the wavelengths (plot a)) with the adjusted version (plot b)) of 2013.....	138
Figure 5-25: Comparison of the original selection of the wavelengths with (plot a)) with the adjusted version (plot b)) of 2015.....	139
Figure A-1: Shellfish bed classification results from TSX obtained with the hierarchical knowledge-based decision tree.....	170

Figure A-2: Salt marsh classifications obtained with the hierarchical knowledge-based decision tree.....	172
Figure A-3: Change maps of the salt marsh distribution obtained with the hierarchical knowledge-based decision tree.....	173
Figure A-4: Sediment maps obtained with the hierarchical knowledge-based decision tree.....	175
Figure A-5: Change maps of the four sediment classifications obtained with the hierarchical knowledge-based decision tree.....	178
Figure A-6: Representative areas for the channel extraction evaluation. The green polygons represent sand flat areas and the yellow polygons mudflat areas.....	180
Figure A-7: Results of the random forest land cover classifications. Plot a) has only a single dataset as input (RE), whereas plots b) to d) have two datasets as input (RE and TSX).....	182
Figure A-8: Change maps of the four sediment classification derived with the random forest classification approach.....	185
Figure A-9: Changes of the salt marsh distribution between 25 April 2010 and 27 June 2011 (a)), 27 June 2011 and 11 July 2011 (b)) and 11 July 2011 and 22 October 2011 (c)). The results are obtained with the random forest classification algorithm.....	187
Figure A-10: Chosen wavelengths applying the method ‘peaks’ and ‘ranges’ to the spectrometric data of 2013 and 2015.....	190
Figure A-11: Plots a) and b) represents the selected wavelengths from JMDFS with method ‘peaks’ and ‘ranges’ of the mean spectra of 2013 compared with all wavelengths in plot b). The discrete spectral band values of plots a) and b) were linked for better comparison.....	191
Figure A-12: Plot a) and b) represents the selected wavelengths from JMDFS with methods ‘peaks’ and ‘ranges’ of the mean spectra of 2015 compared with all wavelengths in plot b). The discrete spectral band values of plots a) and b) were linked for better comparison.....	192
Figure A-13: Plot a) and b) represents the selected wavelengths from ReliefF with method ‘peaks’ and ‘ranges’ of the spectra of 2013 compared with all wavelengths in plot b). The discrete spectral band values of plots a) and b) were linked for better comparison...	193
Figure A-14: Plot a) and b) represents the selected wavelengths from ReliefF with method ‘peaks’ and ‘ranges’ of the spectra of 2015 compared with all wavelengths in plot b). The discrete spectral band values of plots a) and b) were linked for better comparison...	194
Figure A-15: Objected-based water classification of the LiDAR DEM from 2010.....	195

Figure A-16: Objected-based water classification of the LiDAR DEM from 2012. 196

Figure A-17: Objected-based water classification of the LiDAR DEM tiles from 2013..... 197

List of tables

Table 3-1: Data acquisition dates, tide and weather conditions and spatial resolution of RE, TSX, LiDAR and aerial photos ((X)=partial coverage of the study area).....	17
Table 3-2: Technical information of the LiDAR data and flights.....	24
Table 3-3: Number of measured spectra for each class.....	27
Table 3-4: Overview of the ground truth data.....	30
Table 4-1: Sediment properties (after Janke & Kremer 2011).....	34
Table 4-2: Station ID's and their corresponding RMSE value of the two Spectralon® measurements.....	48
Table 4-3: Upper (UT) and lower (LT) threshold values for the sediment classification.....	56
Table 4-4: Chosen parameters for the object-based classification of the tidal channels and their values for the data of 2010.....	61
Table 4-5: Class ID's and class names for the spectrometer data of 2013 and 2015.....	82
Table 5-1: Radiometric improvement with the decrease of the heterogeneity of the pixel values in a water polygon of the RE image from 27 June 2011.....	87
Table 5-2: Spatial comparison of the shellfish bed classifications and the corresponding reference data using the hierarchical knowledge-based decision tree.....	94
Table 5-3: Accuracy measures for the shellfish bed classifications with the hierarchical knowledge-based decision tree.....	95
Table 5-4: Spatial comparison of the salt marsh classifications and the corresponding reference data using the hierarchical knowledge-based decision tree.....	99
Table 5-5: Accuracy measures for the salt marsh classifications with the hierarchical knowledge-based decision tree.....	100
Table 5-6: Accuracy measures for the sediment classifications with the hierarchical knowledge-based decision tree.....	102
Table 5-7: Euclidean distances between the sediment classifications.....	107
Table 5-8: Classification accuracy of the object-based water classification.....	110
Table 5-9: Detailed classification accuracy (mud and sand) of the object-based water classification.....	111
Table 5-10: Accuracy measures for the intertidal channel extraction with the hierarchical knowledge-based decision tree.....	113

Table 5-11: The number of confluences within the polygons of Figure 5-14 compared with the number of confluences derived with the applied method and the percentage.	114
Table 5-12: Correlation coefficient of the extracted geometric parameters and calculated ratios. Symbols are described in the text above.....	116
Table 5-13: Accuracy results of the 20 RF classifications with randomly chosen ROI's.....	117
Table 5-14: Confusion matrix of the final sediment classification of the LiDAR data.	118
Table 5-15: Accuracy measures for the sediment classifications with the hierarchical knowledge-based decision tree and the additional information derived from LiDAR data.....	120
Table 5-16: Accuracy assessment for the supervised random forest sediment classifications.....	121
Table 5-17: Euclidean distances between the sediment classifications of the RF approach.	122
Table 5-18: Spatial comparison of the salt marsh classifications and the corresponding reference data using random forest.....	123
Table 5-19: Accuracy assessment for the supervised random forest salt marsh classifications.....	124
Table 5-20: Spatial comparison of the shellfish bed classifications and the corresponding reference data using random forest.....	125
Table 5-21: Accuracy assessment for the supervised random forest shellfish bed classifications.....	126
Table 5-22: Selected wavelengths in [nm] from JMDFS and ReliefF applying 'peaks' and 'ranges' to the data of 2013 and 2015.	135
Table 5-23: Overall accuracies in percentage of the spectrometric data classifications with <i>RF</i> . The best results are highlighted in green colour. The value after the slash is the result of the adjusted version that explained after the table.	136
Table 5-24: Comparison of the accuracy measurements between the random forest approach, the hierarchical knowledge-based decision tree without and with LiDAR data. Details are described in the text.....	142

List of abbreviations

ALS	Airborne Laser Scanner Systems
ANN	Artificial Neural Network
AOI	Area of Interest
ASCS	Acoustic Seabed Classification System
ATCOR	Atmospheric Correction algorithm
BIL	Band-Interleaved-by-Line
BIP	Band-Interleaved-by-Pixel
BNR	Band number
CASI	Compact Airborne Spectrographic Imager
CCD	Charge-coupled Device
CFS	Correlation-Based Feature Selection
CIR	Colour Infrared
DEM	Digital Elevation Model
DLR	German Aerospace Center
DN	Digital Numbers
DT	Decision Tree
ED	Euclidean Distance
EPS	Extracellular Polymeric Secretions
GEDI	Global Ecosystem Dynamics Investigation Lidar
GIS	Geographic Information System
GPS	Global Positioning System
FFH	Fauna-Flora-Habitat
FFT	Fast Fourier Transformation
FLAASH	Fast Line-of-Sight Atmospheric Analysis of Spectral Hypercubes
FN	False Negative
FOV	Field of View
FP	False Positive
FWHM	Full Width Half Maximum
ha	Hectare
HH	Horizontal-Horizontal
IDL	Interactive Data Language
I_w	Intensity values

JMD	Jeffries-Matusita Distance
JMDFE	Jeffries-Matusita Distance based Feature Extraction
K	Cohen`s Kappa Coefficient
km	Kilometre
km ²	Square Kilometres
LiDAR	Light Detection and Ranging
m	Meter
mm	Millimetre
MCARI	Modified Chlorophyll Absorption Ratio Index
MF	Morphologic Filter
MFD	Multiple Flow Direction
MGD	Second Modified Triangular Vegetation Index
MLC	Maximum Likelihood Classification
MMAIQ	Maximal Minimal Associated Index
MNF	Minimum Noise Fraction Transform
MR	Multiple Regression
mRMR	Minimal-Redundancy-Maximal-Relevance Criterion
MSAVI	Modified Soil Adjusted Vegetation Index
MSI	Multispectral Instrument
NASA	National Aeronautics and Space Administration
NDWI	Normalized Difference Water Index
NIR	Near-Infrared
NPV	Negative Predicted Value
OA	Overall Accuracy
OBIA	Object-Based Image Analysis
OSARI	Optimized Soil Adjusted Vegetation Index
OSM	Open Street Map
P	Precision
PA	Producer Accuracy
PCA	Principal Component Analysis
P _r	Prevalence
R ²	Coefficient of determination
RADAR	Radio Detection and Ranging
RAR	Real Aperture Radar

RE	RapidEye
RF	Random Forest
RMS	Root Mean Square
RMSE	Root Mean Square Error
ROI	Regions of Interest
SAC	Special Areas of Conversation
SAR	Synthetic Aperture Radar
SFFS	Sequential Floating Forward Selection Algorithm
SMM	Spectral Mixture Model
SNR	Signal-to-Noise ratio
SRA	Simple Regression Analysis
SE	Spatial Enhanced
Stdev	Standard Deviation
SVM	Support Vector Machine
SWIR	Short Wave Infrared
TCARI	Transformed Chlorophyll Absorption Reflectance Index
TMAP	Trilateral Monitoring Assessment Program
TNR	True Negative Rate
TOAR	Top of Atmosphere Radiance
TP	True Positive
TPR	True Positive Rate
TSX	Terra SAR-X
UA	User Accuracy
VNIR	Visible and Near-Infrared
VV	Vertical-Vertical
UNESCO	United Nations Educational, Scientific and Cultural Organization
WiMo	Wissenschaftliche Monitoringkonzepte für die Deutsche Bucht

1 Introduction

Observing the earth, especially vulnerable ecosystems (e.g., coastal wetlands), with remote sensing sensors is becoming increasingly important in today's society. Coastal zones have a morphology that varies from cliffs, beaches and mangrove forests to low-lying coastal salt marshes. The impact of waves, tidal currents and the motion of sediments, change the coastal zone morphology constantly (Beijma, Comber and Lamb 2014). Intertidal flats like the German Wadden Sea are a part of such dynamic and diverse ecosystems that have a high economic and ecological value (Park et al. 2010; Van der Wal & Herman 2007). Despite the importance of these ecosystems, they are at risk due to climate change, sea level rise, algae blooms, invasive species (e.g., Pacific oyster) and marine pollution (CWSS 2013a; Troost 2010; Lee et al. 2012; Park et al. 2010; Klemas 2013). Rising seas, for instance, intensify coastal flooding and increase the erosion along barrier islands, which leading to greater probability of overwash during storm events (Klemas 2013). Recently, there has been much attention for the detection of emerging changes (e.g., shift of species) and the potential loss of the natural or semi-natural ecosystems accompanied by a decrease in water quality. Especially for the monitoring of big areas, time and cost saving applications are needed. Also the accessibility both from sea and land is very poor which makes monitoring and mapping of tidal flat environments from in situ measurements very difficult (Park et al. 2010). In this context, automatic or semi-automatic processing systems are preferable to manual interpretation. In monitoring the tidal flats of the German Wadden Sea, the focus of interest is shifting from a general overall classification to a more detailed classification and identification of specific habitats. Quick and detailed results are needed after extreme events such as winter storms. These information are going to be used to preserve a good ecological status of the environment (Farke 2011). Remote sensing sensors and applications can be very helpful for these tasks due to their provision of a large spatial coverage and non-intrusive measurements of the Earth's surface (Foody 2002). Along with sensor and image quality improvements over the last decades, the requirements for the accuracy of the results and image process efficiency are also becoming much higher.

1.1 Motivation and problem statement

The largest intertidal flats can be found on the German, Danish and Dutch North Sea coast and on the western coast of Korea (Gade et al. 2014). The trilateral Wadden Sea (Germany, Denmark and Netherland) is a large intertidal transition zone between terrestrial and marine

environment in the southeastern part of the North Sea with tidal flats, barrier islands, channels, gullies and salt marshes. It is one of the last remaining natural large-scale intertidal ecosystems, where natural processes continue to function largely undisturbed. The multitude of transitions between land and sea, salt- and freshwater, are the basis for a highly adapted, partly endemic flora and fauna. The productivity of biomass is one of the highest in the world, demonstrated by the numbers of fishes, shellfishes and birds (CWSS 2013b; Beijma, Comber and Lamb 2014). In 2009, the Dutch and German parts of the Wadden Sea were entered onto the UNESCO World Heritage List (Farke 2011). Changes in temperature and the variety of species, harmful algae blooms and the reduction of the fish population, as well as changes in the morphology in the Wadden Sea, are examples of the effect of global climate change, changes in the environment and anthropogenic pressure (CWSS 2013a). Furthermore, the long-lasting use by large ship transports and offshore industries have an impact on the entire ecosystem (CWSS 2013a). The emerging change and potential loss of the natural or semi-natural ecosystem, accompanied by a decrease in water quality, caused the European Union to implement various directives, such as the Habitats Directive (Council Directive 92/43/EEC), the Water Framework Directive (Directive 2000/60/EC) and the Marine Strategy Framework Directive (Directive 2008/56/EC). These directives formulate objectives, such as achieving or maintaining a good environmental and conservation status within a given time (EU 1992; EU 2000; EU 2008; Farke 2011; Buck et al. 2013). As a consequence, the Ministry of Environment, Energy and Climate Protection and the Ministry of Science and Culture of the Federal State of Lower Saxony launched a cooperative research project called ‘Scientific monitoring concepts for the German Bight’ (German acronym WiMo). The proposed methods and results of this thesis were achieved within this project.

The temporal and spatial evolution of habitats in coastal areas depends on a variety of biotic and abiotic parameters. Changes take place both seasonal and event-coupled and over a long time. The quality of prediction of such changes for the valuation of ecosystems in the coastal areas, such as island platforms, wadden systems and estuaries depends on the spatial density of the data and frequency of their acquisition. Besides stationary point measurements there are especially spatial measurements with short temporal frequencies which are the best basis for a comprehensive view of the habitat structures and their interactions in the coastal zone. For the sublittoral, for instance, it is common to use hydroacoustic methods, while in the eulittoral or intertidal area, the use of aerial and satellite based remote sensing data is common. Changes in the environment of the Wadden Sea, natural or anthropogenic origin, cannot be monitored by the standard measurement methods alone (e.g., on-site measurements), because large-area

surveys of the intertidal flats are often difficult due to tides, tidal channels and unstable underground. For this reason, remote sensing offers effective monitoring tools.

1.2 Goals and scientific contribution

This thesis is focused on the development of automatic and semi-automatic classification methods for monitoring concepts of tidal lands in the German bight. At various points of the procedure some methods are termed semi-automatic, because the human operator is called upon for assistance (e.g., parameterization of the sediment classification). The data input will be a combination out of different remote sensing sensors such as multispectral, hyperspectral, radar and LiDAR. It is important to pre-process and adapt the different spatial and temporal resolutions in previous steps to get a matching dataset. The analysis of their quality and suitability is essential. The main questions to be answered are the following:

- How good is the quality (e.g., temporal, spatial and spectral resolution) of the remote sensors for tidal flat applications?
- How can the different sensors be used for a classification of tidal flats?
- Have all sensors to be applied or can some been neglected?
- What are the benefits of a hierarchical multi-sensor application in comparison to a standard supervised classification?
- Which classes of the classification can be separated and in which quality?
- With the available data, which parts of the procedure can be developed in an automatic or semi-automatic manner to be part of a monitoring concept?
- What wavelengths should be used or be available for approaches in tidal flats?

Both visual and numerical evaluation strategies will be used in this work to exhaustively analyse the quality of the classification result from different spaceborne sensors and one terrestrial sensor. Assessments are performed with ancillary vector data of the defined land cover classes. The results of the classification quality assessment lead to a better understanding of the necessary sensors and wavelengths for classification and provide decision guidance on their potential usability for monitoring concepts in the tidal flats of the German bight.

A major advantage of working with multi-sensor data is that each sensor can deliver the necessary information for different land covers in high quality. After pre-processing each remote sensing data for itself, the images are examined for their spatial overlap and if

necessary are co-registered. The spatial resolution will be adapted to the coarsest one. Therefore, four different sensors (multispectral, hyperspectral, radar and LiDAR) for classifying tidal flats in the German bight are going to be used in this thesis. Each of them is focused on classifying different land covers of the study area. The multispectral sensor RapidEye (RE) will be focused on classifying water, sediments and vegetation, while the shellfish beds will be estimated by the radar sensor TerraSAR-X (TSX). Basis for the classification is a combined analysis of both remote sensing data coupled with ancillary vector data. It is based on a decision tree and a set of hierarchically structured algorithms which use object and texture features (i.e., spatial context). The third sensor LiDAR will be used to estimate the potential to improve the sediment classification of the electro-optical sensor RE. Geometry information derived from LiDAR data of the tidal inlets and channels will identify areas of muddy or sandy sediments. The last sensor is a spectroradiometer with a hyperspectral camera. The spectral information of different sediments of intertidal areas is often very similar. Hence, an analysis of the spectral separability will take place. The high number of bands will help to identify useful wavelengths for further sensor developments for intertidal areas.

To study the behaviour of the proposed sensors and methods, they are tested on the same area at different times. The data will differ in their water level, due to their acquisition time. The extracted classifications are visually and numerically compared with the reference data provided. Thus, the suitability of the proposed approaches to various datasets can be analysed. The correct and false detections are further studied. Thus, the requirement and potential of the multi-sensor approach of monitoring tidal lands in the German bight are evaluated in detail.

1.3 Organisation of the dissertation

Chapter 2 reviews the different methods that have been used for land cover classification in intertidal flats in the last 30 years. It is arranged in a thematic point of view (e.g., sediments, vegetation and shellfish beds) and points out important studies using electro-optical, radar, LiDAR and hyperspectral data for each thematic topic. Furthermore, alternative methods and applications in intertidal flats and feature selection methods will be discussed.

Chapter 3 presents a detailed description of the study area and the remote sensing and ground truth data that are available for this dissertation. Furthermore, the advantages, disadvantages, sensor theory and target influences on the reflectance and backscatter, in terms of intertidal flats, will be discussed.

Chapter 4 comprises a description of the classes used for the land cover classification and will discuss their ecological value. It also describes the pre-processing methods used as well as the developed and applied land cover classification and feature selection methods in detail.

The developed methods are evaluated with the given ground truth data and are compared to established remote sensing techniques in chapter 5 (e.g., random forest and ReliefF). The experimental results are described in detail and a discussion is included at the end of this chapter.

Chapter 6 and 7 close this thesis with conclusions obtained from the present work, along with an outlook of the future work.

2 Review of classification applications in tidal flats and feature selection methods

2.1 Introduction

As a precondition for the preservation of a sustainable ecological condition of the Wadden Sea, monitoring data is required that is based on reliable and automated techniques for accurate classification of the present state as well as the detection of changes. Due to the large geographic area of the Wadden Sea (appr. 10,000 km²), satellite remote sensing offers a cost efficient and fast way to gather high-resolution information and to detect long-term developments. This advantage, however, has so far been impeded by the fact that data of the intertidal flats can only be obtained at low tide. For a long time satellites could not guarantee an image during low tide due to their repetition cycle of several days or even weeks. But improving the temporal resolution is an essential issue of remote sensing of coastal environment due to the highly dynamic changes in morphological and sedimentary processes of intertidal areas (Park et al. 2010).

The purpose of land cover classification is to automatically identify the land cover of large areas, which are difficult to map by foot or are not even accessible. This has always been one of the most heavily investigated topics in satellite image applications. Numerous classification methods and many kinds of remote sensing sensors have been used according to the different applications and user requirements (Yates et al. 1993; Thomson et al. 1998; Rainey et al. 2003; Van der Wal & Herman 2007; Gade et al. 2014). Among these applications, the land cover of interest can be of any possible class or only pertaining to specific targets, such as shellfish beds. The applied classification methods can be broadly divided into pixel- and object-based methods.

Hereafter, the most important applications in classifying the land cover of intertidal flats are reviewed. The chapters will focus on the classes that will be of interest.

2.2 Sediments

The ability to map intertidal sediments or surfaces through different remote sensing systems (airborne or satellite-based) has been demonstrated by various researchers in the last 30 years. Their focus has been on distinguishing between sand and mud or different grain sizes, as well as examining the influence of water or biofilm. One great interest in the field of morpho-

dynamics and sedimentary processes of coastal environments is the distribution of sediments of a given particle size (Park et al. 2010). Yates et al. (1993) used three different classification methods (maximum likelihood classification (MLC), multiple regression (MR) and spectral mixture model (SMM)) on Landsat 5 TM data to identify surface sediment distribution. All methods produced high accuracies for muddy sites (MLC: 83%, MR: 93%, SMM: 94%) and lower accuracies for sandy sites (MLC: 68%, MR: 59%, SMM: 21%). They state that the lower accuracies for sandy sediments are probably a result of a veneer of muddy sediments covering some sandy sediments and the surface film of water retaining on sand in the study area. Rainey et al. (2000) used a series of in situ and laboratory reflectance experiments to investigate the complexity of intertidal sediments. They showed that the interstitial moisture influences the spectral contrast between sediments of contrasting grain size. They state, that satellite data should be collected after a prolonged period of exposure to summer drying conditions which ensures that the spectral influence of moisture is minimized and the spectral contrast is maximized. In a subsequent study, Rainey et al. (2003) took an image with the Daedalus 1268 Airborne Thematic Mapper after a drying period. They improved the image calibration significantly with a recombination of the sub-pixel end-member abundances through multivariate regression analysis for dry and wet conditions. Decho et al. (2003) analysed the influence of microbial mats on the sediment reflectance signatures. They found that the presence of microbial mats reduce the sediment reflectance signatures by 10% to 20%. A decrease in reflectance near 444nm and 678nm could be attributed to absorbance by photopigments. The decreases of the reflectance in a wide spectral range (400nm – 750nm) are a result of the extracellular polymeric secretions (EPS) which are produced by the microbial mats. Sørensen et al. (2006) classified four different sediment classes (mudflat, mixed flat, low sand flat and high sand flat) using Landsat ETM+ and texture measures (e.g., dissimilarity and homogeneity) derived from orthophotos. They concluded that a single-image approach has some limitations and that ground truth measurements have to be done at the time of the image acquisition. Ryu et al. (2004) investigated a new critical grain size effective for Landsat ETM+ data. The study indicated using the Landsat ETM+ 4 band and a target critical grain size of 0.25mm for intertidal sediment investigations. Van der Wal, Herman & Wielemaker-van den Dool (2005) used synthetic aperture radar (SAR – ERS-1 and ERS-2) to relate the backscatter coefficient to field measurements of surface roughness, moisture conditions and surface texture. They found a negative correlation between the surface roughness and the mud content, which can be used in a regression model to distinguish mud from sand. In addition, they showed that a high moisture content negatively effects the

correlation between the surface texture and the volumetric moisture content. Van der Wal & Herman (2007) showed that a combination of radar (C-Band), visible, near-infrared and shortwave infrared data was best for sediment grain size monitoring of intertidal flats. They found that a regression-based algorithm with a combination of SAR backscattering coefficient of ERS-1 and ERS-2, green band and SWIR band of Landsat TM provides the best results in estimating the distribution of mud flats. Gade et al. (2008) elaborated a method of extracting roughness parameters of sand ripples on exposed tidal flats for a coarse sediment classification (sandy, mixed and mixed/muddy). A comparison with an available sediment map showed promising results. Based on their results from 2008, Gade et al. (2014) found that multi-frequency SAR data of multiple satellites acquired at low tide provides additional information (e.g., RMS height and autocorrelation length) that can be used in monitoring systems. The RMS heights varied only slightly within the test sites, but the autocorrelation length was largest in sandy areas. Thomson et al. (1998) examined, with the use of Compact Airborne Spectrographic Imager (CASI) data, what spectral band definition is the best to distinguish between sand, mud and six different salt marsh types. They concluded that general bandsets are suitable for generating an overview map, while for distinctive surface types to be mapped the bandsets have to be adjusted to the specific spectral features. Dolch and Reise (2010) visually interpreted a time series of aerial photographs for mapping large sandy bedforms, seagrass and mussels. They demonstrated the effect of the movement of sandy bedforms on the distribution of seagrass and mussel beds. Stelzer et al. (2010) used a wide variety of optical and SAR satellite sensors (Landsat TM, SPOT 2, SPOT 4, SPOT 5, RapidEye, ALOS PALSAR, Envisat ASAR, ERS-2 SAR, TerraSAR-X) to classify sand, mixed sediments, mud, vegetation and mussels in different areas of the German Wadden Sea. They showed that a combination of different sensors is favourable to improve the classification accuracy.

Nonetheless, the classification of intertidal sediments using spectral information, SAR backscatter, roughness or texture measures, can still be considered as a challenge with electro-optical and SAR imagery. In comparison to the studies above, Eom et al. (2012) and Ryu et al. (2010) extract the geometric information of tidal channels from an aerial photograph to distinguish sediment types. They found that a higher sand percentage results in a lower tidal channel density. Furthermore, mud flat areas are more complex with a dendritic pattern. Both studies suggest using geometric features in a sedimentary facies classification. Yang and Morris (2008) developed a semi-automatic method for tidal stream network extraction from high resolution remote sensing imagery. They could successfully predict the major streams

and many small streams, but the limitations of the method are mainly with some of the small streams whose centerlines are not preserved or broken. Mason et al. (2006) developed a semi-automatic technique for extracting tidal channel networks from high-resolution LiDAR data. For their first study site (river Ems) they reach an error of omission of 26% and an error of commission of 11%. For their second study site (Venice Lagoon) they reached an error of omission of 14% and an error of commission of 42%. Choi et al (2011) estimated the spatial relationship between surface sedimentary facies distribution and topography, including channel networks (e.g., channel density and distance from channels) and an intertidal digital elevation model (DEM). The DEM was generated by a waterline method using Landsat ETM+ images and the reference map of the surface sediment distribution was produced from sediment samples. They found that fine-grained mud flat facies occur mainly in areas of complex tidal channels and elevated areas that have a high spectral reflectance. Coarse-grained sand flat areas are concentrated in areas of sparse tidal channels, whereas mixed flat areas have an intermediate level of complexity. That implies a spatial relationship between topographic feature of the tidal flats and the distribution of sediments.

2.3 Tidal vegetation

Studies dealing with vegetation classification in intertidal areas are very limited, especially studies concerning algae in tidal flats. Most of them are analysing salt marshes or seagrass as they are of very high ecological importance (Lee et al. 2014; Natura2000 n.d.). Belluco et al. (2006) applied multi-and hyperspectral data (e.g., CASI, IKONOS and Quickbird) to unsupervised and supervised classification methods (e.g., K-means and Spectral Angle Mapper). They were able to achieve accuracies between 75%-97% applying four different salt marsh classes, a soil and a water class. Lee et al. (2012) investigated the polarimetric SAR data of TerraSAR-X (TSX) to distinguish between two different kinds of salt marsh plants (annual plants and perennial plants). They concluded that winter is the best season for distinguishing between the two different species and that summer is ideal for analysing the distribution changes of annual plants in salt marshes. Furthermore, they found that the radar backscatter of TSX from wetlands is stronger in horizontal (HH) than in vertical (VV) polarization. Lee et al. (2014) analysed the disappearance of a large salt marsh patch due to anthropogenic impacts on the tidal flats. In comparison to the results of Lee et al. (2012), Gao & Zhang (2006) proposed autumn as best season to distinguish between four different salt marsh communities in China. They measured the spectral characteristics in the seasons of spring, summer and autumn using a FieldSpecTM Pro JR spectroradiometer. The four

communities had different and rather unique spectral characteristics during the three seasons, related to the growing season, the community type and its phenology.

Due to their natural pattern, seagrass meadows and algae are hard to detect with spatial resolution lower than or equal to 5m. Therefore, Henning et al. (2007) used an airborne spectrometer (Reflective Optics System Imaging Spectrometer) to classify intertidal macrophyte vegetation (e.g., brown algae, green algae, red algae, etc.) and general intertidal structures. They obtained an overall accuracy of 75.9% and producer's accuracies ranging from 64.9% to 100% and user's accuracies ranging from 59.4% to 100%. Quite often, seagrass is classified in combination with other land covers, such as in the study of Dolch and Reise (2010), which was reviewed in the chapter before. They could show that sandy bedforms have expanded and that they have displaced seagrass beds. Dehouck et al. (2011) analysed TSX and optical satellite data (SPOT-5 and FORMOSAT-2) to classify sediments, seagrass meadows and oyster beds. They state that the combination of SAR and optical data appears to be useful to improve the discrimination of various sediment and vegetation covers (e.g., seagrass and salt marsh). For further approaches of tidal vegetation classification, the author of this thesis refers to Klemas (2013), who reviews remote sensing approaches for seagrass estimation in the last 30 years.

2.4 Shellfish beds, blue mussel and oyster beds

Shellfish beds, blue mussels or oyster beds have been classified all over the world in the last decades. For instance, Choe et al. (2012) analysed full polarimetric RADARSAT-2 (C-band) and ALOS PALSAR (L-band) imagery to distinguish exposed oyster reefs from mud or sand flats on the west coast of the Korean peninsula. With C-band SAR data a stronger volume scattering and depolarization effects over oyster reef areas occur. The use of a multi-frequency polarimetric SAR system showed that the naturally distributed oyster reefs in the tidal flats could be detected. Nieuwhof et al. (2015) analysed dual-polarized TSX (X-band) and RADARSAT-2 (C-band) to estimate the contours, density and species of the Pacific oyster and blue mussel. They found that SAR imagery can be used for monitoring of the mussel contours, but not for estimating the density and distinguishing the species. Grizzle et al. (2002) distinguished dead oyster reef from living oyster reefs by their colour with the use of aerial photographs. Dead oyster reefs are highly reflected light-coloured areas in comparison to darker coloured living oyster reefs. Dehouck et al. (2011) analysed TSX and optical satellite data (SPOT-5 and FORMOSAT-2) to classify sediments, seagrass and oyster beds. They found that oyster beds and salt marshes have particular SAR signatures. Schill et

al. (2006) applied hyperspectral imagery to map the spatial distribution of intertidal oyster reefs. They used the difference of the spectral reflectance between oyster reefs and mudflats. But they had difficulties with the characterization of the spectral signature of oyster reefs, due to a considerable spectral variability. Furthermore, they used high resolution LiDAR data to identify oyster reefs. They found that the intensity returns of LiDAR were more diffused in oyster reefs in comparison to the surrounding area. But the vertical accuracy was not good enough to distinguish the roughness differences between oyster and mud.

2.5 Alternative methods and applications in intertidal flat areas

The monitoring methods of the intertidal flats are not only focused on sediment, vegetation or mussel bed classifications with spaceborne or airborne-based remote sensing data. Various authors developed methods for the determination of shorelines or waterlines. Waterline extraction is potentially one of the most effective satellite remote sensing tools to estimate changes in tidal flat environments and coastlines (Ryu et al. 2002). Even digital elevation models (DEM) can be derived from these waterline models. Mason & Davenport (1996) developed a semi-automatic method for the shoreline determination using ERS SAR imagery. Niedermeier et al. (2000) and Heygster et al. (2010) determined waterlines in the Elbe estuary using a wavelet-based edge-detection algorithm on ERS SAR data. Next to the comparison of polarimetric SAR signatures of salt marshes with ground truth radar measurements, Won (2009) also extracted waterlines from TSX imagery. Ryu et al. (2002) investigated the selection of a proper band for waterline extraction under various conditions with Landsat TM and ASTER data. No single band of Landsat TM (NIR or SWIR) and ASTER (TIR) can accommodate all aspects of the tidal flat environment. Ryu et al. (2008) used Landsat TM data from 1991 to 2000 to extract waterlines. These waterlines were the input for a DEM generation to quantitatively estimate morphologic changes and to evaluate their migration over the time. The results complied with the general rules of sedimentology and demonstrated that satellite remote sensing data is an efficient and effective tool for long-term morphologic change estimation in tidal flats. Others authors used acoustic technologies to observe estuarine and coastal benthic habitats. These technologies can be compared with SAR systems as they use the reflected sound energy to identify surface objects, texture and density discontinuities. Smith et al. (2001) analysed the ability of subbottom profiling systems, side scan sonar and acoustic seabed classification systems (ASCS) to assess oyster habitat in the Chesapeake Bay. They showed that ASCS technology is highly suited for the identification and charting of oyster shell as well as distinguishing among different combinations of shell and fine

sediments. But echo sounding is not feasible for large areas, due to the large point spacing, the limitation to a sufficient water depth and rather small coverage per day (slow speed of vessel) (Brzank et al. 2008). Kim et al. (2011) used polarimetric SAR imagery (TSX and RADARSAT-2) to detect water puddles on the west coast of Korea. They could relate the distribution of water puddles to the discharge of groundwater and proposed SAR data as an effective tool for observing and determining the areal distributions of possible groundwater discharge in large tidal flats.

2.6 Feature selection

Recently, band selection approaches based on search algorithms has received a lot of attention. Several approaches have been developed by various researchers to select the best bands for hyperspectral imagery using different kinds of methods. Choi and Lee (2003) present a feature extraction method by utilizing an error estimation equation based on the Bhattacharyya distance. They state that the proposed method compares favourably with conventional feature extraction methods, such as Foley-Sammon or principal component analysis (PCA). Venkataraman et al. (2006) proposed an unsupervised feature selection technique that integrates the Jeffries-Matusita distance during the feature selection process so that only the most distinct bands are selected. The total number of bands used in a Mahalanobis classifier is estimated using a thresholding technique. They compare the classification accuracies when all bands, the selected bands and randomly chosen bands are applied. The accuracies using all bands were slightly higher, which shows the potential of the proposed method. Ibrahim et al. (2009) used a very simple feature selection approach called sequential floating forward selection algorithm (SFFS) and they manually have chosen four and five different bands of specific parts of the electromagnetic spectrum. Li et al. (2014) propose an effective band selection method from the novel perspective of spectral shape similarity analysis with key points extraction, which retains physical information of hyperspectral remote sensing images. They took all bands of the hyperspectral data as time series. First, all trainings samples are clustered and a set of initial candidates is obtained based on extraction of key points. Finally, filtering contiguous bands according to conditional mutual information and branch and bound search are further performed sequentially. They state that the classification accuracy is comparable to others, while the computational complexity is lower.

Also, observing high correlations between the adjacent bands, band grouping and selection had been proposed by several researchers. Gomez-Chova et al. 2003 used the local

correlation, but with a subsequent selection of the most discriminative features based on a SFFS algorithm. They could identify five important bands for discriminating crops in their six hyperspectral images. Datta, Ghosh and Ghosh (2014) propose an unsupervised band elimination method for hyperpsectral imagery, which iteratively eliminates one band from the pair of most correlated neighbouring bands depending on the discriminating capability of the bands. The correlation is calculated over partitioned band images and the capacity discrimination is applied to measure the discrimination capability of a band image. Several evaluation measures, such as classification accuracy, kappa coefficient, class separability and entropy were calculated. The proposed method was compared to popular state-of-the-art approaches (ReliefF, information divergence and Wards linkage strategy using divergence) and showed promising results.

Another aspect in feature selection is the comparison of the proposed and popular state-of-the-art approaches. Bajwa et al. (2003) compared five different methods (information entropy, first spectral derivative, second spectral derivative, PCA and artificial neural network) using an airborne hyperspectral image. None of these methods could be identified as the best. They all had their advantages in different topics. Wu et al. (2013) compare different filter-based feature selection models, such as maximal minimal associated index (MMAIQ), mutual information-based max-dependency criterion (mRMR), ReliefF and correlation-based feature selection (CFS) for hyperpsectral band selection. The evaluation is based on several measuring indices, such as class separability, feature entropy, feature stability, feature redundancy and classification accuracy. They state MMAIQ as the best feature selection method.

2.7 Summary

This chapter has presented a review of the available literature in the field of land cover classification of coastal areas, alternative approaches in intertidal flats and feature selection methods.

Most of the land cover classification studies demonstrate the difficulties in classifying vegetation, shellfish beds and different sediments in the tidal flats. For sediments, the distinction between general classes (e.g., dry sand or wet sand) is possible (Small et al. 2009). Problems exist for the classification of mixed sediments and mud, especially if they are influenced by water (Verpoorter et al. 2014). Besides water, the reflectance of sediments is also influenced by properties like grain size, organic matter content, iron oxide, cyanobacteria and mineralogy as well as satellite-based properties like sensor characteristics and

illumination geometry (Han and Rundquist 1996; Rainey et al. 2000; Vaudour et al. 2008; Small et al. 2009; Decho et al. 2003; Mulder et al. 2011). The same problems occur for the classification of vegetation and shellfish beds that are influenced by water, macroalgae or their natural pattern. The vegetation classification requires either a high spatial resolution or a high spectral resolution. Shellfish beds, on the other hand, require information about the roughness, to be distinguished from vegetation (Gade et al. 2014).

Another challenge is the combined analysis of the ground truth measurements and the satellite data for the classification validation. Tidal areas are highly dynamic, with short-term variations over a tidal cycle or seasonal variations with respect to hydrological, biological and morphological conditions. This means, that for a combined analysis the measurement of the ground truth data and the satellite image, acquisition has to take place simultaneously during low tide (Sørensen et al. 2006). With this requirement, however, constant monitoring is not feasible. A robust algorithm is needed for long-term monitoring. The first promising results were published by Stelzer et al. (2010) and Geißler et al. (2011) as they incorporated satellite data into monitoring concepts.

Furthermore, different measurement systems (e.g., ASCS) or different approaches (e.g., waterline extraction) can be used to add ancillary information to the existing remote sensing methods, if remote sensing data or ground truth data is not available.

Various new applications in the field of feature selection have emerged in the recent years using different datasets and applications. Among them, the most fundamental and challenging problems for feature selection are stability, optimal redundancy removal, and the exploitation of auxiliary data (Wu et al. 2013). Just one of the feature selection methods, which are reviewed in this chapter, are applied to coastal areas or concerns tidal flat sediments in combination with feature selection of hyperpsectral data. Due to this lack in the remote sensing community, a feature selection method was developed and applied to spectrometric data of intertidal flats.

Despite the intensive efforts on land cover classification and feature selection, it remains a hot topic for remote sensing research. Overall, it can be stated that more work is needed to develop useful, automatic and robust land cover classifications and feature selection approaches. As a consequence, a classification method was developed that includes pre-processing and a hierarchical knowledge-based decision tree with a set of hierarchically structured algorithms using the satellite sensors of the following chapter.

3 Study area and datasets

3.1 Study area ‘Norderney’

The study area ‘Norderney’ is part of the German National Park Lower Saxony Wadden Sea, in the south-western part of the German North Sea, south of the barrier island ‘Norderney’ with a size of approximately 50km² (Figure 3-1).

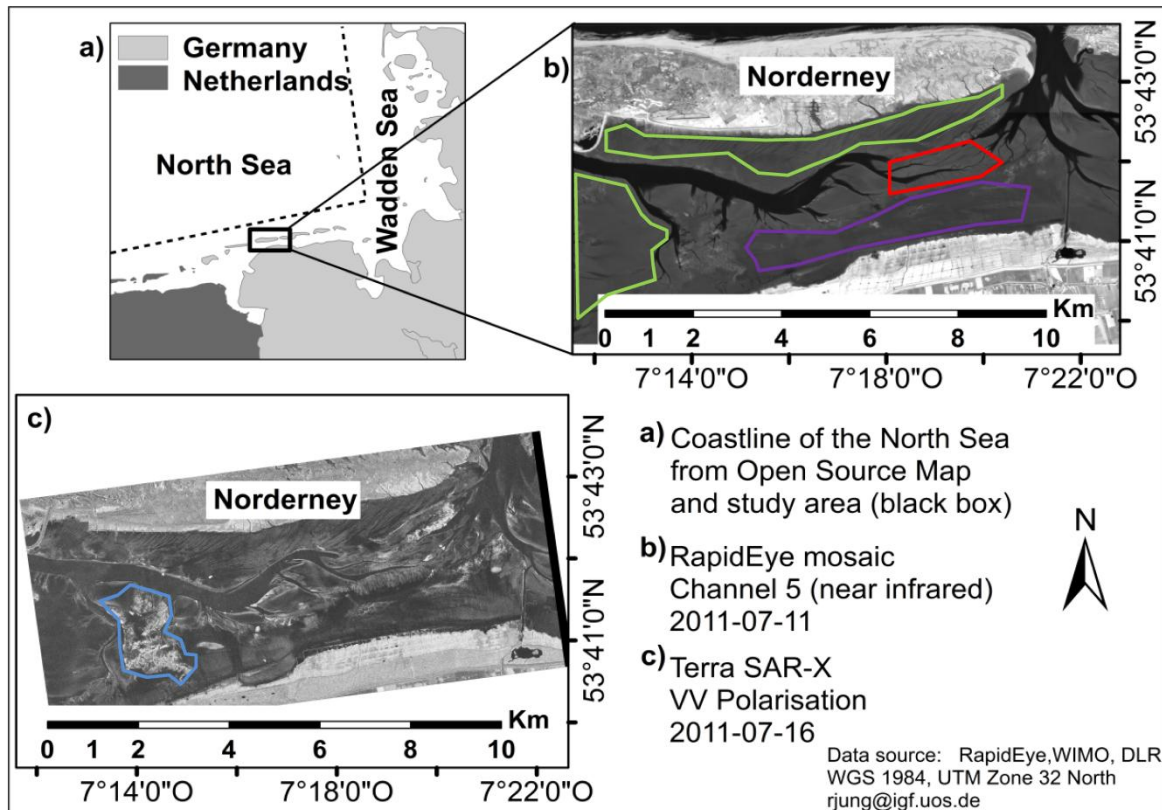


Figure 3-1: Location of the study area in the German bight (a) and an example of a RapidEye image (b) and TerraSAR-X image (c). The green polygons represent areas of sandy sediments, the red polygon represents an area of muddy sediments, the purple polygon represents an area of mixed sediments and the blue polygon represents an extended shellfish bed consisting of blue mussels and Pacific oysters.

The intertidal flat is traversed by two permanently water-covered tidal inlets. They emerge in the east and enter the North Sea on either sides of ‘Norderney’. These areas are the inlets ‘Riffgat’ in the west and ‘Ostbalje’ in the east. The sediment distribution has a strong spatial variation of different sediment types ranging from clay to fine/partly medium sand, shellfish beds and vegetation, such as algae and salt marsh plants. Near the island and in the western part of the study area are sandy sediments predominant (green polygon in plot b) of Figure 3-1), whereas muddy sediments are predominant near the origin of the traversing tidal inlets (red polygon in plot b) of Figure 3-1). All kinds of mixtures of sandy and muddy sediments

are present over the whole study area, characterized by a gradual transition (purple polygon in plot b) of Figure 3-1). In general the surface types are seldom separated by sharp boundaries. Very often, the sediments are covered by a thin layer of diatoms, small brownish microalgae or congregations of macrophytes and shellfish beds (Brockmann and Stelzer 2008). The sediment supply of the area originates from several sources, e.g. North Sea, fluvial sources, atmospheric deposition, primary production or erosion of nearby salt marshes (Sørensen et al. 2006). The most prominent peculiarity of the ‘Norderney’ study site, is the extended shellfish bed of blue mussels and Pacific oysters in the western part framed by two tidal creeks (blue polygon in plot c) of Figure 3-1).

3.2 RapidEye

The electro-optical satellite data for the Wadden Sea were acquired by the German RapidEye (RE) satellite constellation. This constellation is composed of five identical satellites (designated as RE1, RE2, RE3, RE4 and RE5) and was launched on August 29, 2008. Each RE spacecraft carries the Multispectral-Imager (MSI) push-broom imaging sensor containing five linear charge-coupled device (CCD) arrays, which observe the Earth in five discrete spectral bands (blue: 440-510 nm, green: 520-590 nm, red: 630-685 nm, red-edge: 690-730 nm and near infrared (NIR): 760-850 nm) at a spatial resolution of 6.5 m (resampled to 5 m) at nadir. The sensors have a swath width of nearly 77 km and acquire the data from a nominal altitude of 630 km. The satellites are phased in a sun-synchronous orbit plane with an inclination angle of 97.8 degrees. Due to the constellation of five satellites the potential repetition rate of RE is only one day (off-nadir) (Naughton et al. 2011). This increases the possibility of obtaining cloud free images during low tide. This advantage is clearly demonstrated by the fact that between the years 2010 and 2012 a total number of 403 RE scenes for the German Wadden Sea were acquired. The provider of the RE data sets a maximum cloud coverage of 20% for each 25 km x 25 km tile. Greater cloud coverage is not accepted, and this means no image acquisition. For this study, ‘cloud-free’ means that the area where the study site is located is covered by less than 5%, independently of the overall cloud coverage of one tile. All the images used in this study are fully cloud-free. Weather conditions as well as the dependency on sunlight limits the application of electro-optical sensors in tidal flats during low tide. Unfortunately, in 2013, the data policy was changed by the data provider. Since that year, Germany is now covered by RE only every 45 days, which reduces the number of suitable low tide data from the coast significantly.

Due to its image size of 25 km x 25 km and its location, more than one RE image is required to cover the study area. Table 3-1 shows the RE IDs for the two images in brackets and the acquisition date and weather information for each satellite dataset. The difference between the acquisition time and the low-tide time ranges from a few minutes to nearly two hours. This implies higher water coverage and water saturation of the sediments in all RE images except for the image of October 22, 2011, which was acquired near low tide. Furthermore, the different water levels will affect the classification results. In addition, the wind direction has an effect on the retaining water. During the acquisition of the RE image of July 11, 2011, a moderate wind from north-north-west was predominant. This will slow down the drainage of the water in the southern part of the study area. The RE images were delivered as RapidEye 3A Ortho Product, which offer the highest processing level with respect to radiometric, sensor and geometric corrections. This implies that the digital numbers (DNs) of the RE image pixels represent absolutely calibrated radiance values (BlackBridge 2013). The RE satellites cover an area of approximately 50 km² of the back barrier intertidal flat. The disadvantages of the electro-optical systems are the dependencies on weather conditions and sunlight.

Table 3-1: Data acquisition dates, tide and weather conditions and spatial resolution of RE, TSX, LiDAR and aerial photos ((X)=partial coverage of the study area).

	RE (3263910; 3263810)	TSX	LiDAR	Aerial photos
Acquisition date and time [CET]	25 April 2010 – 13:38 27 June 2011 – 13:42 11 July 2011 – 13:36 22 Oct. 2011 – 13:40	02 June 2011 – 19:18 16 July 2011 – 19:18 28 Oct. 2011 – 19:27 (X)	May 2010 April 2012 March 2013 (X)	30 Sep. 2010 02 Sep. 2011
Low tide time [CET]	25 April 2010 – 15:31 27 June 2011 – 14:50 11 July 2011 – 14:25 22 Oct. 2011 – 13:45	02 June 2011 – 19:05 16 July 2011 – 19:45 28 Oct. 2011 – 19:35	During low tide	N/A
High tide time [CET]	25 April 2010 – 09:21 27 June 2011 – 08:40 11 July 2011 – 08:10 22 Oct. 2011 – 07:15	02 June 2011 – 12:40 16 July 2011 – 13:15 28 Oct. 2011 – 13:10	N/A	N/A
Wind speed [m/s] and direction	25 April 2010 – 4.5, 155° (SSE) 27 June 2011 – 4.2, 145° (SSE) 11 July 2011 – 3.2, 340° (NNW) 22 Oct. 2011 – 4.9, 155° (SSE)	02 June 2011 – 5.6, 15° (NNE) 16 July 2011 – 6.3, 175° (SSE) 28 Oct. 2011 – 1.0, 205° (SSW)	N/A	N/A
Precipitation [mm]	none	16 July 2011 – 1.3	N/A	N/A
Spatial resolution [m]	5	1	1	0.3

Besides these dependencies, the spectral information of electro-optical sensors are influenced also by target properties such as grain size, organic matter content, moisture content, iron oxide, cyanobacteria and mineralogy. The effects have been studied extensively in laboratory and in field conditions by various authors. For instance, Small et al. (2009) estimates the influence of water under laboratory conditions. They state that moisture content account for more than 98% of the spectral variance, which was observed in their samples. Ibrahim et al. (2009) analysed three different sediment types:

- Type 1: saturated, muddy sediment with high amount of chlorophyll a (*chl a*) and high organic matter content
- Type 2: wet, mixed sediments with medium amount of *chl a* and high organic matter content
- Type 3: dry, sandy sediment with low amount of *chl a* and low organic matter content

The sediment types differ in their grain size, moisture, *chl a* and organic matter content. They could show that type 1 and 2 are nearly spectral identical with only some minor differences, due to their different amount of *chl a* and organic matter. The amount of *chl a* influences the spectral reflectance in the wavelengths between 600nm and 720nm. The absorption at wavelength 670nm to 690nm increases (i.e., the reflectance decreases) with increasing *chl a* content. The reflectance values between 400nm to 2500nm decreases as the organic matter content increases. The influence of the moisture content is clearly represented by the sediment type 3. The reflectance values of the whole spectrum decrease if the moisture content increases. The change of the longer wavelengths is stronger compared to the shorter wavelengths. The mud content is highly correlated to the moisture content. Therefore, the effect of mud content would be incorporated indirectly with the effect of moisture content. Both lead to changes in the overall brightness. In contrast, Verpoorten et al. (2014) estimated the influence of grain size on beach sands. They show an overall decrease of the reflectance values with increasing grain sizes. They state that the increase of grain size affect surface scattering and translate into a decrease of the relative proportion of volume scattering. Decho et al. (2003) analysed the influence of microbial communities on the spectral reflectance of intertidal sediments. The overall characteristics of sediments with microbial mats and without are the same, but a decrease of 10%-20% of the spectral signature occurs. The decrease near 444nm and 678nm could be attributed primarily to absorbance by photopigments. A decrease of a wide spectral range (400nm-750nm) could be explained by the extracellular polymeric secretions (EPS) of the microbial mats. A great amount of EPS increases the relative spacing

of sediment grains. This process permits light to penetrate deeper into sediments. Furthermore, it results in a more efficient capture of photons, which decreases the spectral reflectance.

3.3 TerraSAR-X

Although the repetition time of RE is short, cloud-free images remain rare due to the typical weather conditions (e.g., clouds and rain) in northern Germany. In comparison to the optical sensor, radar images are independent of weather conditions and the time of day (Henderson & Lewis 1998; Herold 2000; Knuth 2008, Hajsek 2001, Lusch 1999; Choe et al. 2012). Hence, additional radar images from the German satellite TerraSAR-X (TSX) (3 cm wavelength) with 1 m spatial resolution (later resampled with the nearest neighbour method to 5m), VV polarization, and a swath width of 10 km were available and incorporated into the proposed concept. The satellite was launched on June 15, 2007 and has a general revisit cycle of 11 days which can, however, be shortened to two-and-a-half or two days, depending on the acquisition mode at a nominal altitude of 514 km (DLR 2010). All TSX images were acquired in high-resolution spotlight mode and as Multi Look Ground Range Detected (MGD) product type (see Table 3-1). They are all classified as spatial enhanced (SE) and have a cover of 10 x 5km.

According to Table 3-1, the acquisition time of all the TSX images differs by only a few minutes from the low-tide time. This means that a low water level can be considered. An exception is the image of 02 June 2011, where a wind direction from north-north-east was predominant. As already explained for the RE image in the chapter before, the wind direction can affect the drainage of the water. The image of 28 October 2011 covers only the eastern part of the study area (labelled by an (X) in Table 3-1) and is the only acquisition with very low wind conditions. For this particular image, a smoothing process of the surface from the retaining water will be assumed. For the other two, an increase of the backscatter from the retaining water will be accepted. At the acquisition time of the image from 16 July 2011, a precipitation of 1.3 mm was measured. This parameter is a sum of the measured values between 7 and 8 pm. This moderate precipitation will not affect the radar measurement itself, but it will moisten the surface and affect the backscatter.

Chapter 2 showed that SAR systems have become a promising tool for quantitatively estimating the physical characteristics of the earth's surface. The returning signal (i.e., radar backscatter) is thereby strongly affected by target parameters such as surface roughness, dielectric constant and moisture content of surface materials as well as sensor parameters such

as wavelength, incidence angle and polarization (Henderson & Lewis 1998; Herold 2000; Knuth 2008; Hajnsek 2001; Lusch 1999; Choe et al. 2012). The following paragraphs give a short summary of the SAR theory and the impact of the target parameters in terms of Wadden Sea.

The word Radar itself is an acronym and stands for radio detection and ranging. In general, there are two different types of remote sensing imaging systems: passive and active (Lusch 1999). Both system types operate in the microwave portion of the electromagnetic spectrum at wavelengths of 1mm to 1.3m (Figure 3-2). The passive system uses the natural emitted, reflected or scattered radiation of the earth. But these systems often suffer from low spatial resolution which reduces their use in modern remote sensing applications (Lusch 1999). In the remote sensing community it is common to use the term radar as a synonym for an active radar system. Active radar systems emit their own electromagnetic wave in the direction of the target and measure the received the backscatter intensity. In the following, this thesis will address only active systems.

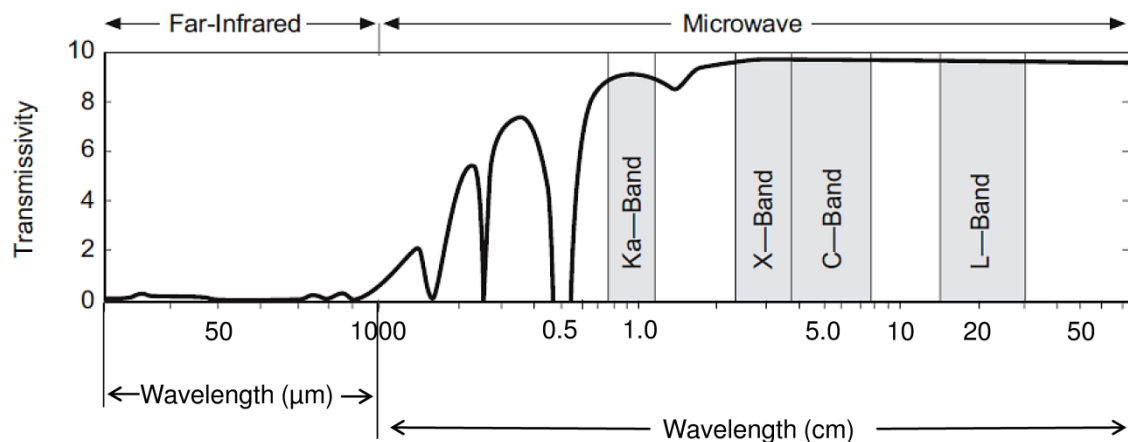


Figure 3-2: The electromagnetic spectrum with the microwave portion of radar systems (changed after Lusch 1999).

At the beginning of radar systems it was common to use a so-called real aperture radar (RAR). These radar systems were characterized by an azimuth resolution (i.e., spatial resolution along the flight track) depending on the wavelength, the size of the real antenna and the distance between the sensor and the target to be imaged. The disadvantages were technical limits for the size of the antenna and the transmitted wavelength. Therefore, only poor spatial resolutions, which varied inside the image, were achievable. To solve these problems a concept called synthetic aperture radar (SAR) was invented. This concept basically uses a small real antenna with a large beamwidth moving along the flight direction to simulate a very long antenna with a small beamwidth (Figure 3-3). A coherent integration of the received signals along the flight track allows synthesizing of a long virtual antenna.

This leads to images with high spatial azimuth resolution independent of the operating frequency and the distance to the scene (Henderson & Lewis 1998; Hajnsek 2001). Figure 3-3 illustrates the SAR concept.

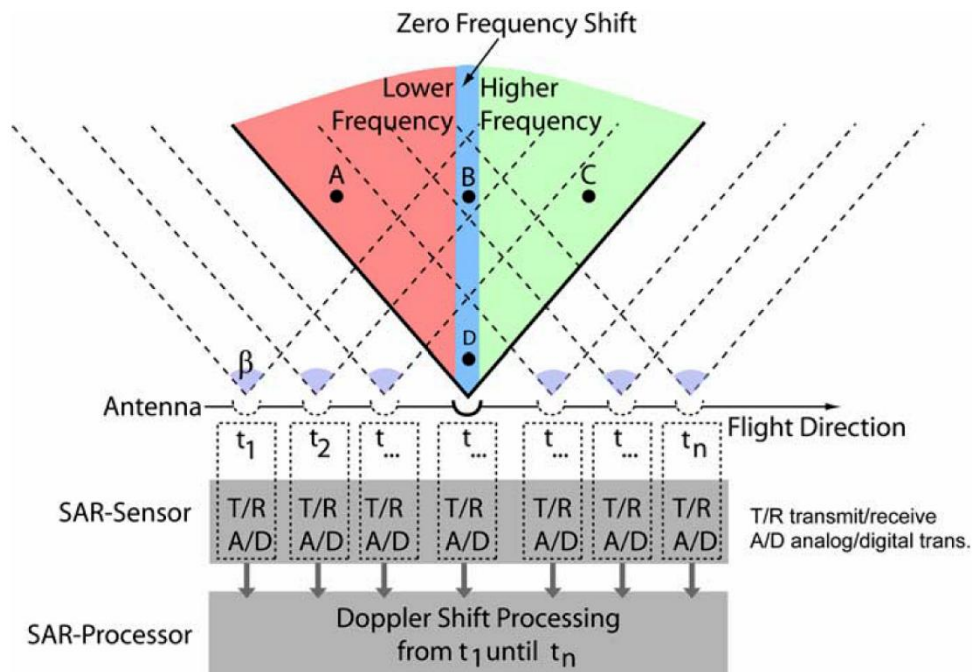


Figure 3-3: Concept of the SAR (Knuth 2008).

The movement of the system leads to a multiple recording of targets (due to the large beamwidth) and creates a Doppler effect between the target and the sensor. The Doppler effect enables the system to discriminate between different targets. Targets ahead of the sensor will have higher frequencies (target C in Figure 3-3), whereas targets behind the sensor will have lower frequencies (target A). Targets near the centre of the beamwidth will show nearly no frequency shift at all (target B and D). In addition, targets further away (i.e., far range) from the sensor are illuminated more often than targets near to the sensor (i.e., near range). For example target B gets recorded three times, whereas target D gets recorded only once (Knuth 2008; Thiel 2004; Herold 2000).

The length of the synthesized antenna is equal to the way of the real antenna while illuminating one target. Thus, the length of the synthetic antenna increases proportional with the distance to the target (Thiel 2004; Richards 2009). This makes the resolution in azimuth of a SAR, as already mentioned, independent of the distance to the targets. The half length of the real antenna defines the smallest spatial resolution in azimuth (Klausing & Holpp 2000; Sabins 1997; Richards 2009). But the length of the antenna is limited. Smaller antennas lead to a lower signal-to-noise ratio (SNR) and the amount of transmitted and received energy decreases (Thiel 2004; Börner 2000).

The dielectric constant (ϵ) is a very important parameter within the monitoring of intertidal areas. It describes the ability of a material to absorb or reflect electromagnetic waves. If the difference of ϵ between two materials is very high then the electromagnetic wave will be reflected from the border between those two materials. If the difference is low then the major part of the wave will be transmitted into the second material. This so-called penetration depth of an electromagnetic wave depends on the wavelength (λ), the scattering element density and the difference of ϵ (Lusch 1999). For a fixed wavelength the penetration depth into a medium decreases with an increasing difference in ϵ . The element with the highest value of ϵ is liquid water ($\epsilon \approx 80$ at a wavelength of 30cm). Air has the lowest value of approximately 1. Dry soils or rocks have a value of 3 to 8. The Organic matter of vegetation or the mineral components of soils have also low values for ϵ (Lusch 1999). The value of ϵ is depended on the wavelength. That means water has a value of 60 at a wavelength of 3cm (e.g., Terra SAR-X). The highest differences occur if water is part of the material or target (e.g., intertidal surface), due to the fact that the emitted electromagnetic wave propagates through the atmosphere. So the difference of ϵ of two materials has a huge impact on the backscatter intensity. This is the reason why radar systems are very sensitive towards soil moisture content or water coverage of soils and other targets (e.g., vegetation, houses, streets, etc.). This fact is important in respect to the monitoring of the intertidal flats of the Wadden Sea. The surface of the intertidal flats is not totally dry during low tide. It remains a high level of soil moisture and even water on top of the surface which results in a high specular reflection (Park et al. 2010), due to a high difference in ϵ between water and air and the side-looking geometry of a SAR. Furthermore the surface roughness of the sediments is, in respect to the TSX sensor ($\lambda=3\text{cm}$), very low. In addition, recordable height differences can be smoothed to a plane if they are covered by water, which decreases the backscatter. Therefore, a low backscatter intensity from the sediments are expected. This assumption applies only under no-wind or very low-wind conditions. With high winds, it can even increase the backscatter compared to no-water-covered sediments. This means that the wind has to be taken into account if an SAR image of the tidal flats is interpreted (Table 3-1). In contrast to the sediments, a high backscatter can be expected from the shellfish beds. They have a rough surface and a lower moisture content (Lusch 1999; Cartus 2010; Herold 2000; Van der Sanden 1997; Hajnsek 2001). In Addition, sensor parameters like wavelength, incidence angle and polarization determine also the backscatter intensity (Henderson & Lewis 1998; Herold 2000; Knuth 2008, Hajnsek 2001, Lusch 1999; Lee et al. 2012). For more information about radar sensor such as radar geometry, resolution in range and azimuth, concept of SAR, speckle, impact of sensor

parameters and object parameters on backscatter intensity look up references such as Henderson & Lewis (1998), Börner (2000), Hajnsek (2001), Lusch (1999), Klausing & Holpp (2000), Sabins (1997), Richards (2009), Lillesand et al. (2008), Thiel (2004), Knuth (2008), Lillesand & Kiefer (1994) and CCRS (2014).

3.4 LiDAR

The airborne LiDAR datasets were acquired during a flight in May, 2010, April, 2012 and March, 2013. Hence, low tide and cloud-free weather conditions can be assumed (see Table 3-1). Figure 3-4 shows the image boundaries of every acquisition.

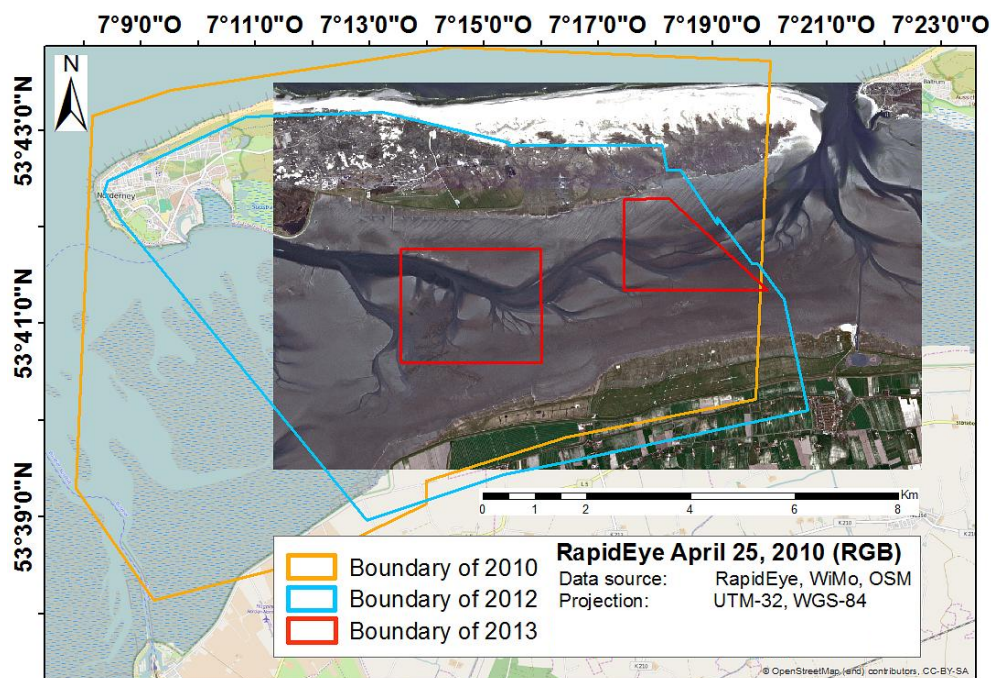


Figure 3-4: Boundaries of the LiDAR data from 2010, 2012 and 2013 with a RE image and OSM data in the background.

They were distributed by the data provider as text files with pre-processed 3D information. This information was further converted into a digital elevation model (DEM) (see chapter 4.3.3) for the improvement of the later sediment classification. The technical details of the LiDAR sensors and flights are summarized in Table 3-2.

The word LiDAR is an acronym and stands for light detection and ranging. It is an active optical remote sensing technology that measures scattered light and operates generally in the near infrared (Brzank et al. 2008; Lillesand & Kiefer 1994³). It is most commonly mounted on an airplane, which always implicates a cost intensive flight and only several images a year.

Table 3-2: Technical information of the LiDAR data and flights.

	May, 2010	April, 2012	March, 2013
Sensor	LMS-Q 560	LMS-Q 560	LMS-Q 680i
Laser wavelength	Near-infrared	Near-infrared	Near-infrared
Travel speed [km/h]	198	259	259
Flight altitude [m]	400	650	650
Measurement rate [kHz]	150	100	≤ 266
Field of view [degree]	45	30-60	30-60
Beam deflection	Rotating polygon mirror	Rotating polygon mirror	Rotating polygon mirror
Range resolution [cm]	2	2	2
Vertical accuracy [cm]	< 15	< 15	< 15
Horizontal accuracy [cm]	< 25	< 25	< 15

Such as radar, the target is determined by measuring the time delay between transmission of a pulse and detection of a reflected signal (Beraldin et al. 2010; Baltsavias 1999). Parts of the pulse can be reflected (e.g., specular, diffuse or a mixture of both), absorbed or transmitted depending on the characteristics of the target. After traversing the atmosphere two times, in general, only a small fraction of the emitted and reflected pulse is received at the sensor. This is similar to radar technology, but instead of using microwave energy, LiDAR uses much shorter wavelengths of the electromagnetic spectrum (e.g., ultraviolet, visible or near-infrared range). Due to the similarity, the radar equation is also valid for LiDAR data (Brzank et al. 2008; Lillesand & Kiefer 1994³).

$$P_R = \frac{P_E D_R^2}{4\pi R^4 \gamma^2} \eta_{sys} \eta_{Atm} \sigma \quad (3-1)$$

where

P_E	emitted power [W]
R	distance between emitter and target [m]
γ	beam divergence [radian]
η_{Atm}	atmospheric transmission factor
P_R	received power [W]
D_R	aperture diameter of receiver [m]
η_{sys}	system transmission factor
σ	backscatter cross section [m ²]

Such as radar, the returning signal of a LiDAR is dependent on various sensor and object-based parameters. For example, a return echo from a low reflecting target will have a lower amplitude and therefore simple pulse detectors tend to put out longer ranges. For instance, white markings (high reflection) will hover above the runway in a range image, due to the low reflectivity of the asphalt. In addition, the form and orientation of the target has an effect on the shape of the returned signal. The theory of LiDAR is based on surfaces that are opaque, diffusely reflecting and uniform, and that the surroundings do not have an influence. Even objects with sharp discontinuities such as holes or edges have an influence. Thus, the quality

of the measured data can decrease. Airborne laser scanner systems (ALS) operate, in general, at wavelengths between 800nm and 1,550nm. Not all wavelengths are equally applicable for different surfaces. Wavelengths close to the visible part of the spectrum have a high absorption at water. Hence, water will rarely be seen. However, ice and snow have a low reflectivity at 1,550nm, therefore such scanner would not be the perfect choice when surveying snow fields (Beraldin et al. 2010).

The point density of an ALS is dependent on the pulse repetition frequencies, the cruising speed of the plane, the survey height and the scan angle. To gain the highest point density possible, the pulse repetition frequencies are high, the cruising speed and survey height is low and the scan angle is small. Due to the scan pattern and topography, the point density is not homogenous (Beraldin et al. 2010).

Another similarity with radar, which is important in terms of Wadden Sea, is the interaction with calm water surface. Near-infrared laser pulses cannot penetrate water (Table 3-1). Hence, the measured elevations represent the water surface. Afterwards, these areas can be adapted with additional data such as side scan sonar (Schmidt et al. 2014). Water can behave like a mirror and thus specular reflection occurs. To receive a signal and to estimate a distance in such cases, the local incidence angle has to be close to zero, which can be assumed for the intertidal flats of the Wadden Sea. Otherwise the received intensity cannot be distinguished from the background noise. Even mudflats with a smooth surface can result in similar specular reflection behaviour. Furthermore, the absorption of water is significantly higher compared to soil, which leads to a lower received power of water points. This results in a significantly lower point density within water areas than within land areas (Brzank et al. 2008). Furthermore, the atmospheric condition such as water vapour, dust particles, carbon dioxide and smoke reduce the detection capability. It cannot penetrate cloud, fog and dense vegetation (Beraldin et al. 2010). To avoid this, LiDAR systems use infrared wavelengths with high atmospheric transmission. Even the daylight decreases the measuring quality, which leads to the perfect condition that has a cool, dry and clear atmosphere at night (Beraldin et al. 2010; Baltsavias 1999). Suchlike conditions cannot not be assumed at any time in the intertidal flats of the Wadden Sea. For a more detailed description of the basic relations and formulas look up Baltsavias (1999) and Beraldin et al. (2010).

The LiDAR technology allows the direct measurement of three-dimensional structures and the underlying terrain. Measurements can be of very high resolution (e.g., five points per meter), which is one of the principal advantages over conventional optical instruments (ESRI 2010). Next to the three-dimensional information the intensity of each return is captured by the

LiDAR sensors. The intensity represents the returned signal strength reflected back from the targets to the sensor and can be used as a pseudoimage (i.e., amplitude image) to provide context of the LiDAR acquisition, if no conventional aerial photography is available (Beraldin et al. 2010; ESRI 2010). In general, an additional multispectral image is acquired during a flight. But for the Wadden Sea the flight has to be performed during low tide and the weather conditions has to be adequate for multispectral data acquisition. Those time windows are rather rare and small, which leads to relatively high costs and forcing customers to order only LiDAR data (Brzank et al. 2008). Due to this, only LiDAR data of the above mentioned dates are available.

3.5 Spectrometry data

Spectrometry sensors (i.e., hyperspectral sensors) gives us the opportunity to measure the reflection of the landscape as a continuous spectral pattern for each pixel of an image built from dozen to hundreds of narrow spectral bands. This reveals a high potential to measure unique spectral responses of different ecological conditions (Henning et al. 2007).

In this study, hyperspectral ground measurements were made with the field portable spectroradiometer SVC HR-1024i from June 03 to 06, 2013 and on June 11, 2015. During the measurements in June 03 to 06, 2013, the cloud coverage changed. Figure 3-5 shows examples for the cloud coverage at the specific dates. The cloud coverage on June 03, 2013 was really dense over the whole measurement period. An influence on the resulting spectra can be assumed, thus these spectra are eliminated from the analysis. On June 04, 2013 the cloud coverage got lesser and thinner. There were periods of no cloud impact on the measurements. The weather condition on June 05, 2013 was cloud-free. On the last day some thin cloud layers could be seen, but they did not influence the measurements. On June 11, 2015 no clouds were visible over the whole measurement period.

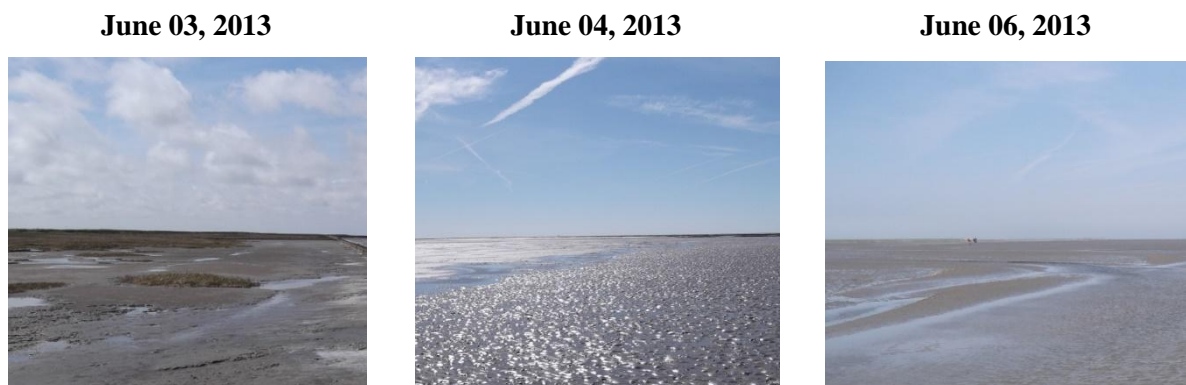


Figure 3-5: Cloud coverage during the spectrometric measurements in 03 June 2013, 04 June 2013 and 06 June 2013.

Table 3-3 shows an overview of the number of measured spectra for each land cover class and date. The number of samples of each class is not identical, due to varying weather conditions and different measurement areas. Some of these land cover classes are influenced by vegetation, shellfish, water, biofilms or varying illumination conditions (see table 4-5). The influence of the illumination on the analysis is described in chapter 4.3.4.

Table 3-3: Number of measured spectra for each class.

Date/Class	Sand	Mixed Sediments	Mud	Water	Shellfish bed	Calibration
June04, 2013	3	N/A	10	N/A	N/A	N/A
June05, 2013	2	7	5	4	N/A	N/A
June06, 2013	5	2	1	2	N/A	N/A
June 11, 2015	6	3	5	N/A	1	7

All measurements (2013 and 2015) were made to obtain further insight in the spectral properties of sediments of intertidal flats. During the measurements in the intertidal flats, the spectrometer device was connected to a sealed fiber-optic cable with a nominal conical field of view (FOV) of 25°. The measurements took place between one hour before and one two hours after low tide level. For the calibration measurements on the mainland a foreoptic with a FOV of 14° was used. The SVC instrument uses three separate spectrometers to measure radiance between 350nm to 2,500nm. The Visible/Near Infrared (VNIR = 350nm to 1,000nm) spectrometer uses a 512 band silicon photodiode array that provides a nominal spectral resolution (full width at half maximum or FWHM) of 3.5nm at 700nm. The Shortwave Infrared (SWIR = 1,000 to 2,500nm) portion of the spectrum is acquired with two scanning spectrometers (each 256 bands) using indium gallium arsenide (InGaAs) detectors with a spectral resolution of 9.5nm at 1,500nm and 6.5nm at 2,100nm (Spectravista 2015). The surface was viewed from the nadir position in a height of approximately 1m. Upwelling spectral radiance from the sediment surface and from a clean white Spectralon® were measured. The Spectralon® from the company ‘SphereOptics’ is a clean white plate and nearly an ideal lambertian scatterer with a reflectance of 99% constantly over the wavelength range 250nm – 2,450nm (SphereOptics 2015). The measurement of a surface ensues always the following steps:

1. Calibration of the device with a Spectralon®
2. First measurement of the Spectralon® (i.e., illumination conditions)
3. Three times measurement of the surface
4. Second measurement of the Spectralon® (i.e., illumination conditions)

Each surface reflectance spectra were used in the further analysis. The second and fourth step enables the analysis of the illumination conditions before and after the surface measurements. If the results in reflectance values differ significantly between each measurement than different illumination conditions can be assumed and the surface reflectance spectra will vary for the same surface. Figure 3-6 shows the locations of each station from 2013 and 2015.

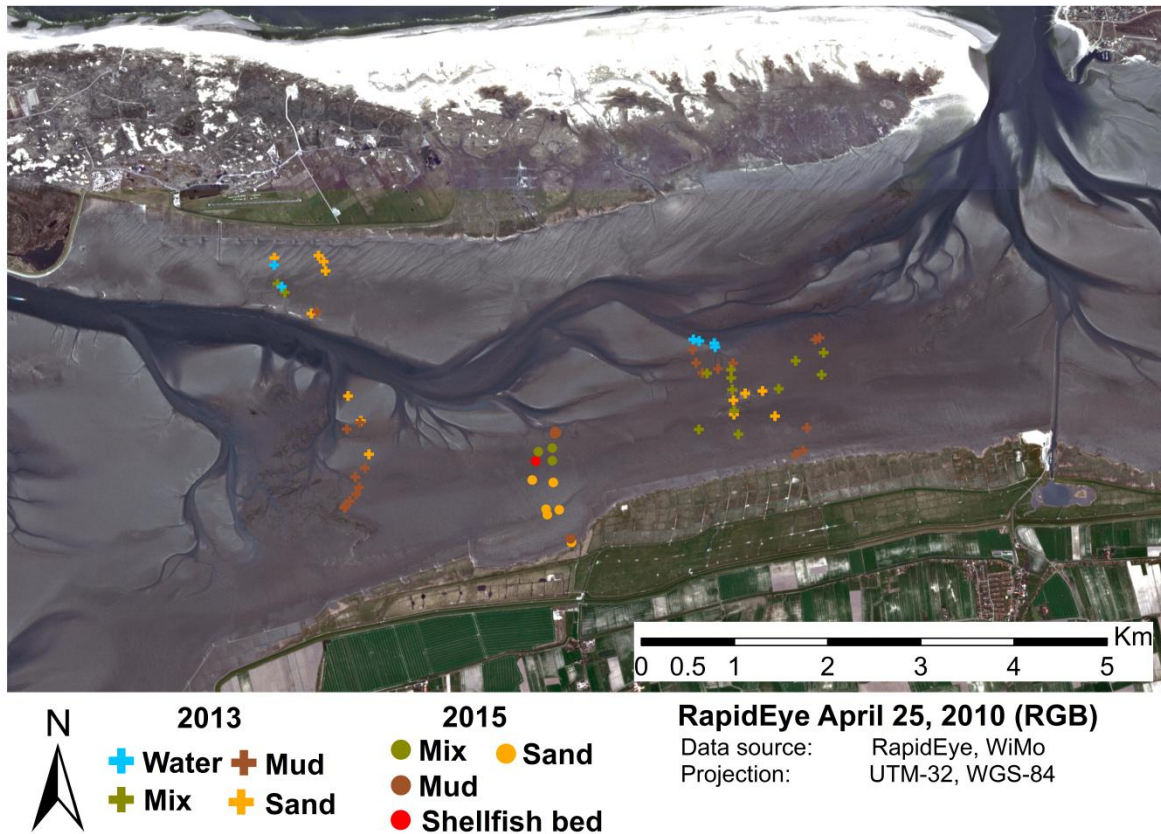


Figure 3-6: Distribution of the stations from 03 – 06 June 2013 and 11 June 2015 of the spectrometric measurements.

3.6 Other ground truth data

In addition, in situ data (point measurements and areal data) with information on the distribution of sediments (2008/2009), seagrass (2003-2008), shellfish beds (1999-2011) and the location of the coastline (2010, 2011; from OpenStreetMap) were available (Table 3-4), and were used for the training and accuracy assessment of the classification procedure (Farke 2011; NPWS 2010a; NPWS 2010b).

The sediment types were classified by specialists of the DeMarine project on site in a raster of 300m between each measurement (Figure 3-7; reference of 2008/2009). During three measurement campaigns of the project WiMo in May 2011, July 2012 and June 2013, additional ground truth data about the sediment distribution were collected on site. To locate

the measurement points, a Global Positioning System (GPS) hand-held from Garmin® (Etrex 30) with a location measurement error of about 5 m was used.

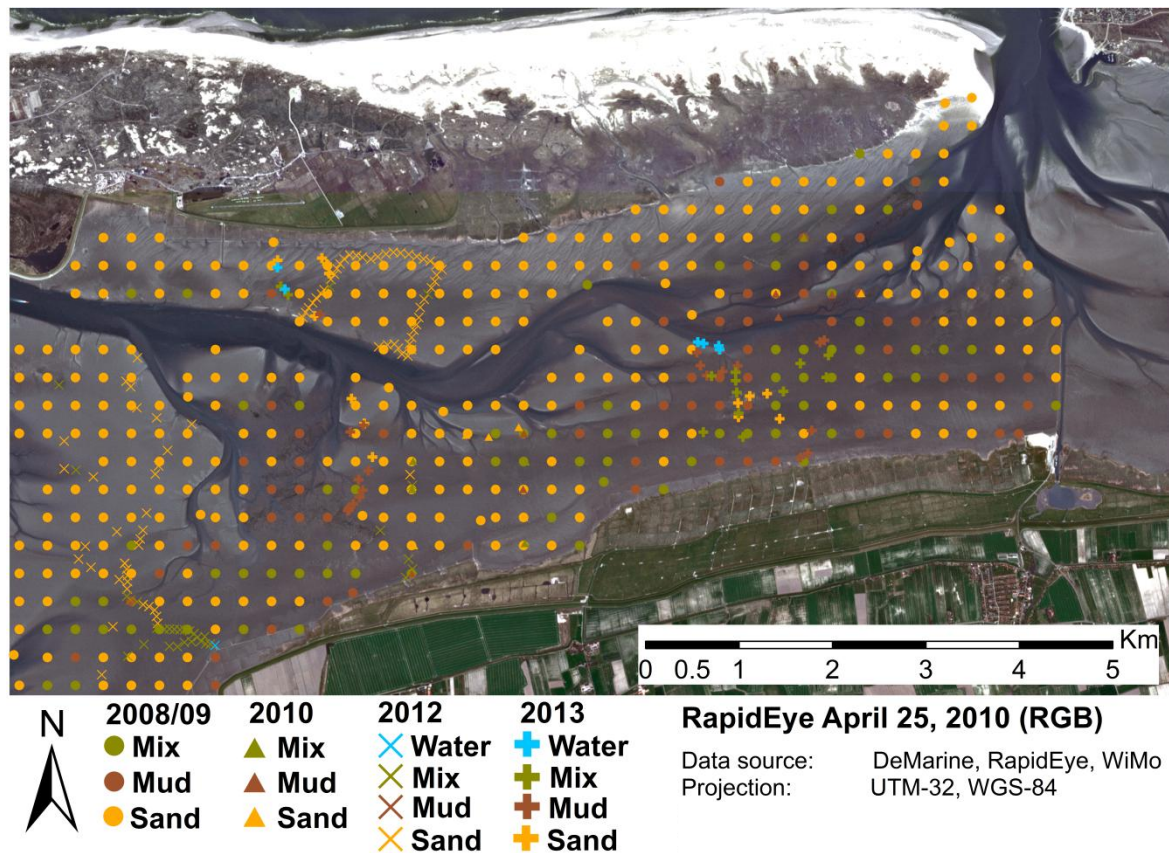


Figure 3-7: A map of ground truth data representing sediments with an underlying pre-processed image of RE from 25 April 2010. The different markers represent different years of ground truth measuring. The ground truth measurements of 2008/09 were acquired by the project DeMarine.

The areal information of seagrass and shellfish beds was generated by two institutions of Lower Saxony (National Park Wadden Sea and the Lower Saxony Water Management, Coastal Defence and Nature Conservation Agency). On the one hand, they digitized high-resolution orthophotos (e.g., stereoscopy) and on the other hand they conduct ground truth measurements. The ground truth mapping of the seagrass and shellfish boundaries were carried out on an international level following the recommendations of the Trilateral Monitoring Assessment Program (TMAP). The monitoring protocol aims to map the seagrass/shellfish patches by walking the circumferences of the patch. A coverage of more than 5% and a distance of maximum 10m between single patches defines a seagrass meadow or shellfish patch. Areas with lower coverage are defined as single, sparse grown patches (Nieuwhof et al. 2015; NLKWN 2011; NLWKN 2010).

Coastline information was obtained from the OpenStreetMap (OSM) project which provided the most accurate and up-to-date input. In addition to the in situ data, true colour (RGB) and colour infrared (CIR) aerial photos from 2010 and 2011 have been included in the accuracy

assessment. The aerial photos were acquired by the company ‘Weser Airborne Sensing’. These measurements were ordered, which implies a flight during low tide, no precipitation and cloud-free weather.

256 real time kinematic measurements (RTK) in the intertidal flats were carried out during a measurement campaign of the project WiMo in 2012, to be applied as high resolution reference data for the DEM validation (derived from the LiDAR data).

It has to be considered that one disadvantage might be the differences between the acquisition dates of the satellite images and the in situ data. This could lead to problems in the combined analysis and accuracy assessment. This specific problem will be discussed in chapter 5.2.2.3. Furthermore, the ecosystem and sediment distributions are very dynamic during the seasons. With remote sensing techniques, only the upper millimetre of the surface is detected. For example, a calm weather period can influence the surface sediments (i.e., sandy sediments can be covered by a thin, muddy layer), which can lead to misclassifications (Brockmann and Stelzer 2008). This implies that occurring errors between the reference and the classification results are a combination of natural changes and false allocation, which have to be considered during the interpretation of the results.

Table 3-4: Overview of the ground truth data.

Reference	Shellfish beds [areal]	Seagrass [areal]	Sediments [points]	RTK [points]	OSM [areal]
Year	1999 - 2011	2003 - 2008	2008/2009, 2010, 2012 and 2013	2012	2013

3.7 Summary

The previous chapter 3 described the study area south of the barrier island ‘Norderney’, summarized the datasets that are available, discussed the influence of the surface on the applied remote sensing sensors, explained the basic theory of two remote sensing sensor (radar and LiDAR) and stated the advantages and disadvantages of all of them in terms of tidal flats. It could be shown that none of the sensors for itself is best appropriate to classify or monitor the intertidal flats of the Wadden Sea. For instance, the electro-optical sensors are dependent on the weather conditions, the daylight and target properties (e.g., water content, grain size, etc). ALS sensors are also dependent on daylight and weather conditions, but in a slightly different way than the electro-optical sensors. The radar sensor as well as the LiDAR sensor interact strongly with the soil moisture and water coverage of the tidal flats. These surface conditions can lead to specular backscatter or reflection, respectively and therefore to

a decrease in the returned signal. The spectrometric data and the other ground truth data are very important additional information for the satellite data and are the most reliable. But, the accessibility both from sea and land is very poor, which makes the monitoring and mapping of tidal flat environments from in situ measurements very difficult, very cost- and time-intensive and only a very small area can be covered during low tide. Even more the result is dependent on the operator (i.e., subjective opinion).

To overcome the disadvantages and to bring together the advantages, a multi-sensor concept was developed in this study for classifying the land cover of the tidal flats in the Wadden Sea.

4 Methodology

4.1 Introduction

To investigate the distribution of shellfish beds, seagrass, salt marsh, algae and sediments, an extensive field work would be necessary. However, this kind of accurate data collection on intertidal flats is often costly, inefficient, or even unattainable. Airborne sensors, for instance, can be a possibility of acquiring remote sensing data at low tide, because they can be scheduled for specific dates (e.g., LiDAR). Although, such sensors and their data are valuable and powerful, a flight campaign is relatively expensive leading to only a few occasional acquisitions. Furthermore, due to the nature of an airplane (e.g., roll, pitch and yaw), image processing is complex and the covered area is quite small. Spaceborne sensors widen the possibilities of remote sensing applications in studying and monitoring intertidal flats. They provide data in a wide range of spectral, spatial and temporal resolutions, while their cost is relatively low and their spatial coverage is large. As already mentioned in chapter 2, various authors have used optical, SAR or LiDAR data for sediment and habitat classifications on intertidal flats. Promising results have been achieved through the classification of sediment types, mussel beds and vegetation. Existing classification systems of sediments and vegetation of intertidal flats are usually based on single remote sensing data (Lee et al. 2012; Gade et al. 2008; Sørensen et al. 2006; Schill et al. 2006). Integrating both electro-optical and SAR data to provide opportunities for a more comprehensive understanding of land cover and change has been investigated a lot. However, as yet relatively few studies have combined more than these two sensor types. In this context, the objective of this study is to determine the effectiveness of high-resolution electro-optical, SAR and LiDAR data for land cover mapping in the German Wadden Sea. Hereafter, the land cover classes and each method applied to the datasets is explained in detail.

4.2 Class definition and ecological value

Some of the following labels of the land cover classes are based on the fauna and flora habitat directives (FFH; Council Directive 92/43/EEC), which define the natural habitats that occur in Germany. FFH areas are also called Special Areas of Conservation (SAC). Various attachments on these directives describe species and habitat types that are particularly worthy of protection. Their conservation should be secured by the system of protected areas of Natura

2000 (Natura2000 n.d.; Buck et al. 2013). The equivalent habitat types of the FFH directives to the land cover classes of the study are:

- FFH 1140 – vegetation-free sand, mud and mixed flat →thesis – sediments
- FFH 1320 – seagrass →thesis – seagrass
- FFH 1330 – Atlantic salt marshes →thesis – salt marsh

The other two labels left (i.e., shellfish bed and algae) are defined by literature. In general, seagrass meadows, shellfish beds and microphytobenthos (i.e., microalgae) are bio-stabilisers that modify the habitat by reducing turbidity, increasing light penetration and enhancing sedimentation processes (Schückel et al. 2013).

4.2.1 Sediments

The land cover class ‘sediments’ describes intertidal flats that fall dry at low tide and that consist of sand, mud or a mixture of both sediments (Natura2000 n.d.). The salt concentration is high over the whole year and changes very little. Mudflats and mixed flats are always water saturated (even at low tide) and are abundant with nutrients. Sand flats have less nutrients and their solum is ventilated daily (Scheffer & Schachtschabel 2010; Ryu et al. 2004). Vegetation is almost absent except for sparse seagrass patches. The sediments of the intertidal flats are an important habitat for marine fish species in their juvenile stage and moreover they supply food for waterfowls and migrating birds (Natura2000 n.d.). The sediment type and the corresponding properties are an important factor in estuarine systems and are of significance for coastal zone management. They influence the hydrodynamics, morphological changes and the pathway of nutrients and pollutants due to their grain size and mud content. A change in mud content of estuarine intertidal flats, for instance, can have affects to the food chain. That includes primary production by microphytobenthos, recruitment, survival and growth of benthic species, flatfish and (wading) birds. The sediment grain size was also identified as a key parameter to define habitats, in particular of benthic fauna. Besides the ecological value, sediment properties are relevant when evaluating the effects of engineering work, such as dredging and dredge spoil dumping (Van der Wal & Herman 2007). Remote sensing data can satisfy the deficiency of high resolution and synoptic information on sediment grain size of intertidal flats to monitor the distribution and mud content. Table 4-1 shows an overview of the sediment properties.

Table 4-1: Sediment properties (after Janke & Kremer 2011).

Properties	Sand	Mixed sediments	Mud
Amount of sand [%]	85 – 100	50 – 85	15 – 50
Amount of mud [%]	0 – 5	5 – 50	50 – 85
Soil water content	Low	Moderate	high
Amount of organic matter	Low	Moderate	high
Reduction layer [cm]	5 – 10	1 – 2	~ 0.3
surface	Rough with ripples	Smooth and greasy	Shiny and silky
Accessibility	Solid underground	Sink to the ankles	Sink to the knees and further

4.2.2 Tidal vegetation

Salt marshes, with respect to their composition, develop in the upper intertidal zone and are influenced by tides and salinity at the transition point between tidal flats and inland. They are dominated by halophytic herbaceous plants and have different ecological functions (Lee et al. 2014; Natura2000 n.d.; Belluco et al. 2006). For example, they act like a buffer zone from storms and contaminations through pollutants (e.g., heavy metals). However, they are also exchange materials between tidal flats and open water. As a third example they remove a high amount of carbon dioxide from the atmosphere and convert it into organic carbon (Lee et al. 2012; Lee et al. 2014). In comparison to freshwater marshes, which emit methane, salt marshes release only negligible quantity of methane and store a higher quantity of organic carbon per unit area (Lee et al. 2014). Salt marshes are separated in vertical zones and are spatially segregated, which is based on plant competition and physical gradient characteristics of the habitat such as salinity, water level and exposure time. The distribution and vertical zonation can be disturbed by sea level changes (related to exposure time), the rate of marsh accretion, sediment supply and anthropogenic modifications (Lee et al. 2012). The high marshes are dominated by competitively superior plants. They are located in the high tidal zones which are affected by land. This results in more than 10 days where they are continuously exposed. However, stress-tolerant plants dominate the low marshes. These areas are inundated for an average of more than 360 days yearly (Lee et al. 2014). One of the major driving forces of losing salt marsh is the imbalance between sea level rise and sediment accretion. This is why alteration and demarcation of salt marsh vegetation is an important environmental indicator of sea level changes (Lee et al. 2012). With rising sea level, the salt marshes will also rise, which causes a landwards migration (Lee et al. 2014). The vulnerability and the high dynamic of salt marshes gives rise to the need of up to date spatial information for their biodiversity conservation and management. The use of remote sensing

data can help to map the salt marsh areas over a large spatial extent and to monitor their temporal change (Gao & Zhang 2006).

Seagrass (*Zostera noltii* and *Zostera marina*) is the dominant vegetation species of shallow sandy bottoms on coastal areas around the world and they are of high ecological importance in the intertidal ecosystem (Natura2000 n.d.; NLWKN 2010; Dolch & Reise 2010). In general, they grow in dense patches that slow down the water current, improve water quality, stabilize the sediments, cycle nutrients and build productive biotopes that are habitat and food resources for different faunal species (NLWKN 2010; Young et al. 2010; Klemas 2013). “[...] Most of the beds are to be found in the mid to upper tidal zone along the leeside of islands and high sand bars, as well as along sheltered parts of the mainland coast” (CWSS 2013a). The best substrate for their roots is clay and peat of marsh soils submerged long ago. That means seagrass occurs in areas where islands generate areas of protection and firm substrates occur to safe seagrass from getting uprooted by wave erosion (CWSS 2013a). In the northern part of the Wadden Sea, extensive areas of dense seagrass meadows exist, while just a few patches occur in the southern and central part. To what extent the uneven distribution is natural or caused by eutrophication and other disturbances is still not clear. Climate effects can be neglected, because seagrass beds of the two species *Zostera noltii* and *Zostera marina* thrive all along the Atlantic shore from Scandinavia to northern Africa (CWSS 2013b). In the study area of ‘Norderney’ seagrass grows in very sparse patches (see Figure 4-1). Seagrass is a very sensible plant and reacts with vanishing if, for instance, sediments are changing. Also the increase of nutrient loads stresses the seagrass meadows, because they are best adapted to oligotrophic conditions (CWSS 2013b). This shows that seagrass is a suitable indicator for the water quality or ecosystem quality and thus is part of the Water Framework Directive (NLWKN 2010). Although, some of the stress factors such as nutrient loads (i.e., eutrophication), strong hydrodynamics (currents and waves), changes in salinity or sediments, and dredging and dumping of sediments (i.e., turbidity) are already discovered, research is still needed for understanding the seagrass meadow development (CWSS 2013b; Dolch & Reise 2010; Klemas 2013).

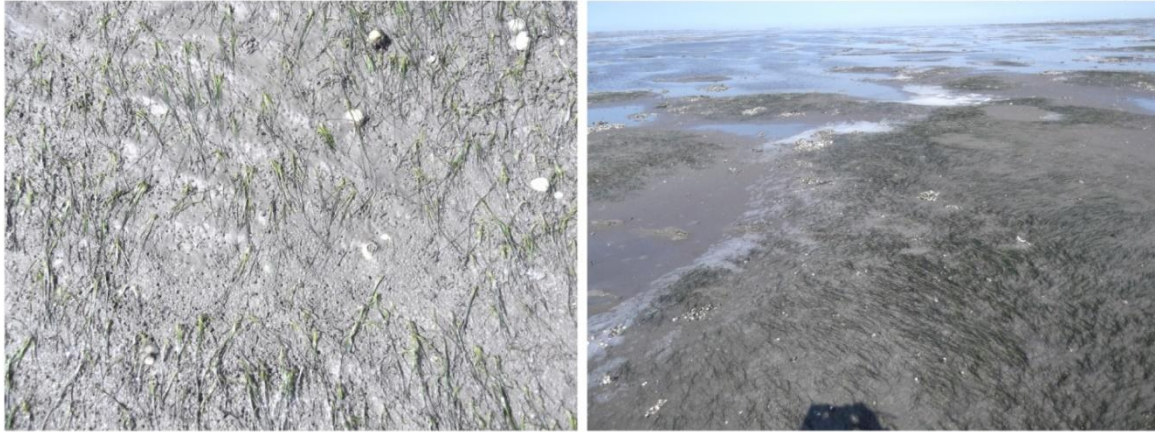


Figure 4-1: Example for a dense seagrass patch in the study area.

Algae do not play a major role in this study, because they cannot be separated from seagrass by remote sensing methods with the available data. Furthermore, no ground truth data is available and due to their appearance an estimation of reference data from the remote sensing data is not possible. However, they have an important role in the intertidal environment and for separating sediments from each other. Hence, they will be described in short. In general, algae have to be separated into micro- (i.e. diatoms) and macroalgae.

Diatoms are very small (up to one million per square meter) and have a strong influence on the spectral reflectance of the sediments (see chapter 5.3). Although, they can only be noticed as very thin reddish or brownish layer on top of the sediments, they produce more oxygen than grassland of the same size. This high productivity is caused by their fast reproduction. They can duplicate their amount within one day. This makes them the predominant species in the intertidal flats. Algae blooms of diatoms can lead to a rapid degradation of oxygen and thus to widespread deaths of fauna. During an algae bloom, lot of dead algae sink to the bottom of the ocean where they are decomposed by bacteria. This process dissipates a lot of oxygen and animals which are not fast enough for leaving this area pass away. Algae blooms are coupled with the climate change and the increasing eutrophication (Bund n.d.).

Examples for macroalgae in the German Wadden Sea are brown algae, red algae and green algae. Due to their missing roots, macroalgae needs a solid underground (e.g., mussels, oysters or rocks) to settle down. They build a dense community, which gives shelter to juvenile fishes and other marine species. Brown algae are suffering particularly from eutrophication. They grow very slow in comparison to other algae species and thus can be overgrown. However, also the climate change has an influence on the macroalgae. Despite their ecological value, macroalgae is also used in the economy (e.g., cosmetics) (Bund n.d.).

4.2.3 Blue mussel/oyster beds

Shellfish species such as the blue mussels (*Mytilus edulis*) and the Pacific oysters (*Crassostrea gigas*) are exposed above the sediment and unlike other shellfish species they can form a rough reef or bed structures on soft bottom sediments which are quite distinct from mudflat and sand flat areas (Nieuwhof et al. 2015; Choe et al. 2012; Gade et al. 2014). Blue mussels, for instance, have the ability to attach to each other by byssal threads. These aggregates can resist translocation by waves and currents (CWSS 2013a). Next to economical values (e.g. coastal shellfish industry) blue mussels and oysters have a high ecological value and provide a myriad of ecosystem services (Nieuwhof et al. 2015). They play a major role in nutrient cycling, water filtration, shoreline protection and providing a habitat for many other marine organisms (Nieuwhof et al. 2015; Choe et al. 2012; Folmer 2012). Changes in the direct environment, such as more frequent extreme weather events, global warming, sea level rise, changes in nutrient concentration and coastal erosion, are affecting the shellfish communities (Oliver et al. 2008). But also human activities, such as overfishing or water pollution have an influence (Nieuwhof et al. 2015; Dolch & Reise 2010). The Pacific oyster was introduced the German Wadden Sea due to their high suitability for mariculture. However, with the global warming it becomes invasive (Troost 2010; Gade et al. 2014). In the Wadden Sea the first observations were made about 30 years ago, and a structural relevant expansion started only in the first decade of the 21st century (Diederich et al. 2005). The former mussel beds have developed into hybrid beds (mixed beds of oysters and blue mussel). Furthermore, the expansion of the oyster alters the community composition locally and may also alters the ecosystem functioning (Nieuwhof et al. 2015). However, more research has to be carried out to find out what the combined impacts of non-native oysters and global change will be (Nieuwhof et al. 2015). In the study area not all mussel beds are dominated by oysters (Gade et al. 2014). This makes the monitoring of mussel beds in general very important. In situ measurements can be one opportunity, but due to the tidal cycle an access to the tidal flats is temporary limited. Remote sensing systems can be an efficient, accurate and cost-efficient tool for monitoring and mapping the spatial distribution of blue mussel beds and oyster beds (Nieuwhof et al. 2015; Choe et al. 2012). In the further process of this study the term ‘shellfish beds’ will comprise both blue mussel and oyster.

4.3 Data pre-processing

The image quality directly influences the performance of any feature detection and thus classification and change detection. Multi-temporal images that are used for classification and change detections are often acquired by different sensors under different atmospheric conditions. Thus, a radiometric and geometric co-registration is necessary to make these images comparable. In general, pre-processing involves (1) radiometric calibration, (2) atmospheric calibration between multi-temporal images and (3) geometric co-registration. Since this study uses remote sensing images from different dates and sensors, several pre-processing methods have to be applied. The RE data has constant artefacts, which were eliminated by a Fast Fourier Transformation (FFT) followed by a Minimum Noise Fraction transformation (MNF) to reduce noise. Subsequently, an atmospheric correction with ENVI's FLAASH (ENVI 2009) was carried out to obtain comparable spectral reflectance values. The airborne LiDAR data were provided as 3D point information in a text file, which was transformed into a DEM for further analysis and processing. The overlaps of the spectrometric detectors were corrected, the spectra were calibrated to a white plate reference, the SNR and the illumination conditions of spectrometric data were analysed for their application in the further process. A geometric co-registration between the satellite images and the reference data was not necessary, because they already matched perfectly.

4.3.1 RapidEye

The RE data are acquired by different sensors (RE1, RE3 and RE4) and therefore display a different number of artefacts and a different kind of spectral variety at each acquisition date. These artefacts (i.e., striped texture) are part of the image noise that occurs in the blue band over dark and homogenous areas. This effect is well known and cannot be prevented (Black Bridge, Email of 22 February 2013). In this study, 'spectral variety' means that an area of homogenous land cover (e.g., water) has a wide range of values, which implies heterogeneity. In a first pre-processing step, a Fast Fourier Transformation (FFT) is applied to eliminate those artefacts that are most likely sensor anomalies. The Fourier transform is a linear transformation and is used to convert a raster image from the spatial domain into the frequency domain. The image will be decomposed into sines and cosines of varying amplitudes and phases, which reveal repeating patterns within the image (Schott 1997). As a result of the transformation we obtain a magnitude and phase image. A binary filtering process that eliminates the frequencies - which are responsible for the artefacts in the image -

is then applied to the Fourier coefficients to eliminate the artefacts in the satellite data. The green rectangles in Figure 4-2 represent the applied filter. All the frequencies covered by the filter were removed. Once the binary filter was created on the FFT result of April 25, 2010, it could also be applied to the other three RE images, as well. An inverse FFT transforms the image back into the spatial domain.

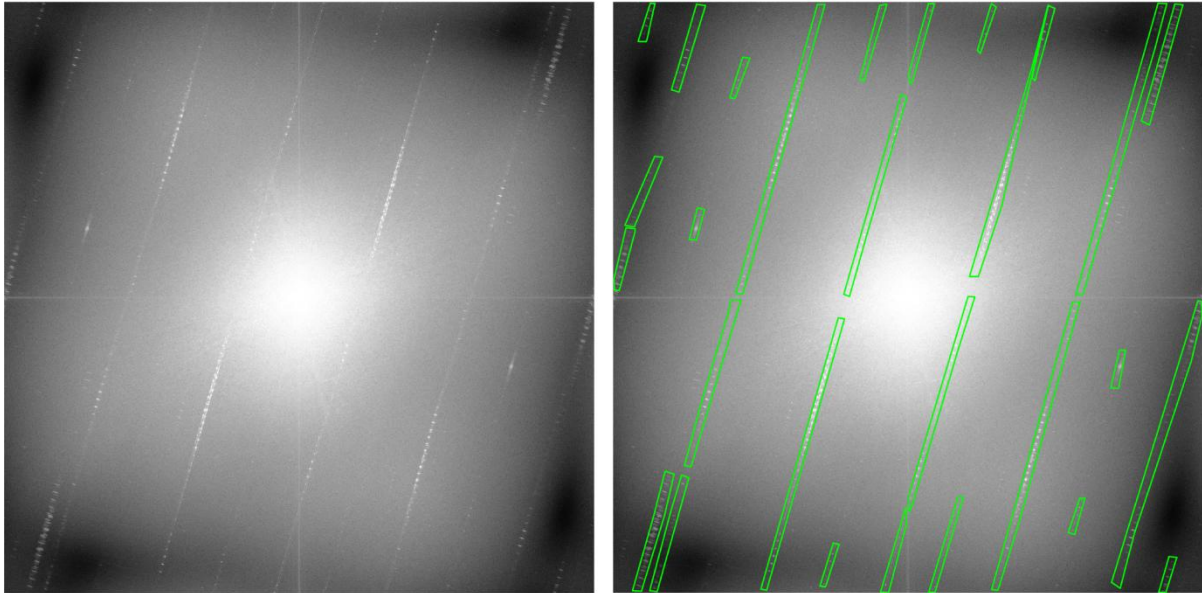


Figure 4-2: The magnitude image of April 2010 (left) and the binary filter (right) of the FFT process. The green polygons on the right side represent the applied filter.

Afterwards, a Minimum Noise Fraction (MNF) transform is used to segregate noise in the data and to reduce the computational requirements for subsequent processing (Green et al. 1988). It is in principle a two cascaded Principal Component Analysis (PCA) transformation which determines the inherent dimensionality of the data by the eigenvalues. The first PCA transformation uses an estimated noise covariance matrix to decorrelate and rescale the noise in the data (Green et al. 1988). The result is a transformed dataset in which the noise has unit variance and no band-to-band correlation. The second transformation is a standard PCA transformation of the noise-whitened data. The inherent dimensionality of the data is determined by examination of the final eigenvalues and the associated images. This implies that images with low or near-unity eigenvalues are noise-dominated. Large eigenvalues, however, generate coherent images which are noise separated (Green et al. 1988). The MNF procedure was applied to each data separately. The first three MNF images were selected for the inverse MNF transformation to reduce most of the remaining spectral variety in the image bands. The MNF bands four and five are not chosen because of their low signal-to-noise ratio (SNR) in the tidal area. Theoretically, band 4 could have been used as well, but it only contained information of areas on the mainland which are not of interest in this study.

The use of a multi-temporal dataset requires an atmospheric correction. Subsequent to the radiometric improvement, an atmospheric correction is carried out. Various researchers have investigated the effects of different atmospheric correction methods for satellites like Landsat TM (Janzen et al. 2006; Watmough et al. 2011), Ikonos (Xu and Huang 2008), SPOT (Vaudour et al. 2008), Quickbird (Wu et al. 2005), ALI and Hyperion (Yuan and Niu 2008). In general, methods using a radiative transfer model combined with satellite imagery retrieve target reflectance values with high accuracy. Nevertheless, to work in the best way, they require information about the atmospheric conditions at the time of the satellite overflight. This information are sometimes difficult to obtain (Manakos et al. 2011). A recent study by Manakos et al. (2011) compared the widely used Atmospheric Correction algorithm (ATCOR) with Fast Line-of-Sight Atmospheric Analysis of Spectral Hypercubes (FLAASH) and a Simple Regression Analysis (SRA). They demonstrated that all approaches generate plausible reflectance values with a small advantage for the SRA due to the ground truth data and the fact that it is an empirical-statistical model. FLAASH produced better results than ATCOR. Manakos et al. (2011) referred this result to the fixed assumptions about the atmosphere (e.g., water quantity) and surface materials on the ground over the entire scene. ATCOR, FLAASH and any other algorithm (but not SRA) that involves radiative transfer modelling rely on these assumptions. Another study by Matthew et al. (2002) evaluated the results of FLAASH on AVIRIS data. Matthew et al. (2002) describe the workflow of FLAASH in detail and demonstrate the usability of this atmospheric correction algorithm. Due to missing ground truth data for the SRA, the second best atmospheric correction method referring to Manakos et al. (2011) was applied in this study. ENVI's FLAASH atmospheric correction module is based on the radiative transfer model MODTRAN4 and has special requirements on the input data (Matthew et al. 2002; Wang et al. 2013). Without corresponding ground truth data, the output of FLAASH assumed reflectance values. Afterwards, the atmospherically corrected RE images are used to produce a mosaic image and to subset the area of interest (AOI).

The digital numbers (DN) of the RE bands were converted into surface reflectance values taking into account the scale factor, conversion of units, solar angle, zenith angle and azimuth angle. Before the atmospheric correction can be executed, the satellite images have to be converted into top of atmosphere radiance (TOAR) and into the image format Band-Interleaved-by-Line (BIL) or Band-Interleaved-by-Pixel (BIP) (ENVI 2009). The calculation of TOAR is the fundamental step putting image data into a common radiometric scale. This is

achieved by using the scale factor, which is stated in the metadata file, in the following equation:

$$TOAR = DN * scale\ factor \quad (4-1)$$

The resulting unit of TOAR is $W/(m^2 \mu m sr)$, but ENVI's FLAASH requires input data to be in floating-point values in units $\mu W/(cm^2 nm sr)$. To obtain the correct unit the following universal equation is applied:

$$TOAR = DN * (scale\ factor * unit\ conversion\ factor) \quad (4-2)$$

For all four RE images the scale factor is 0.01 and the unit conversion factor is 0.1 which converges into a RE specific equation of:

$$TOAR[\mu W/(cm^2 nm sr)] = DN * 0.001 \quad (4-3)$$

Furthermore, the input images should contain information of the wavelength of each band in the header file or a separate wavelength file has to be defined (ENVI 2009). To perform the actual atmospheric correction additional parameters such as, flight time, zenith angle, azimuth angle, etc. have to be specified. A part of the required information can be looked up in the metadata file (e.g., scene centre location, flight date or flight time). The correct 'Atmospheric Model' and 'Aerosol Model' and their impact have to be looked up in the reference ENVI (2009). The 'Initial Visibility' cannot be calculated compared with ATCOR. Different values ranging from 0.1km to 100km were analysed, but no distinctive differences in the resulting reflectance values were noticed. Due to cloud- and haze-free weather condition in the four RE images a high visibility of 30km was selected.

Furthermore, the advanced settings have to be specified (Figure 4-3). The suggested values of ENVI (2009) were applied for the parameters on the left side in Figure 4-3. The feature 'Use Tiled Processing' has to be set to 'No' and the 'Output Reflectance Scale Factor' has to be set to 10,000, otherwise incorrect reflectance values will be the result. After the successful performance of an atmospheric correction, the resulting reflectance values that are lower than 0 or greater than 10,000 were set to 0 or 1, respectively. Values between 0 and 10,000 were divided by 10,000 to obtain a value range between 0 and 1. Some of the required parameters in the advanced settings, such as the zenith angle or azimuth angle, have to be calculated.

The zenith angle and the azimuth angle for FLAASH can be calculated using information from the metadata file. The reference ENVI (2009) has an explanation how to calculate both angles, but does not cite any equations. This means that the equations have to be derived from those explanations. In the following both explanations are cited:

"For instruments that use a non-nadir viewing geometry, you must specify the zenith and azimuth angles. The zenith angle is defined at the sensor as the angle between the line of sight

and the zenith (180 for nadir-viewing sensors). Zenith angles must be positive and between 90 and 180 degrees. The azimuth angle is defined as the azimuth (the angle between the line of sight and due North) of the sensor as viewed from the ground. This angle is arbitrary for nadir-viewing sensors. Azimuth values must be between -180 and 180 degrees. For example, if your azimuth from the sensor is 90 degrees (due east), then the azimuth from the ground is -90 degrees (due west)” (ENVI 2009).

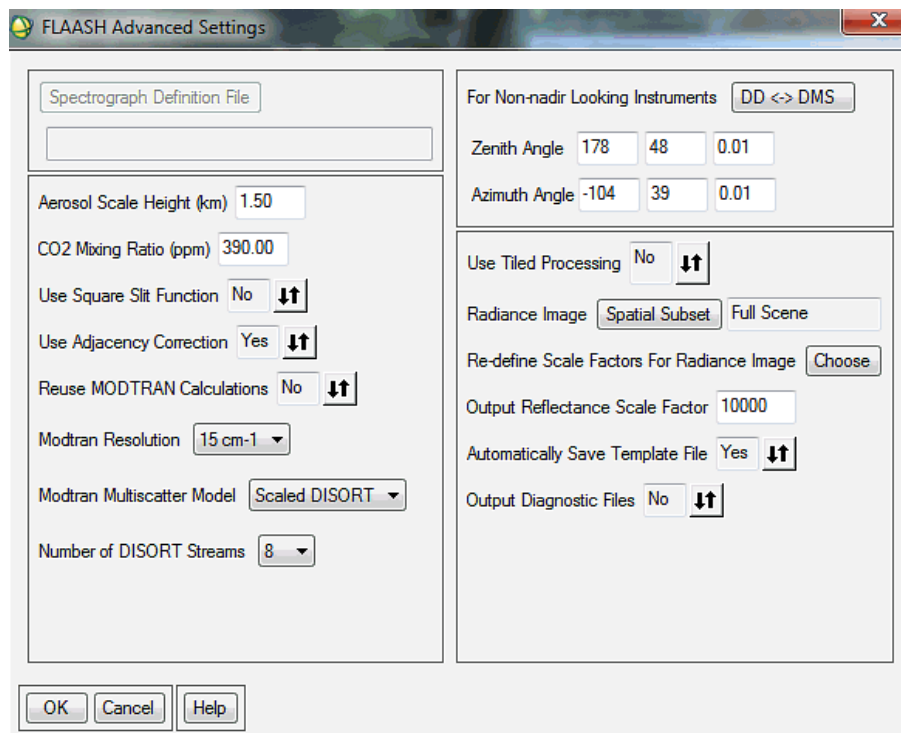


Figure 4-3: Advanced parameters for FLAASH.

Figure 4-4 illustrates both interpreted calculations, which were applied to achieve the zenith and azimuth angle. The red question mark on the left side in plot a) represents the wanted zenith angle for FLAASH (F_{za}). This parameter has, according to ENVI (2009), a range from 90°-180° and is derived from the incidence angle (δ) of the satellite system (i.e., ‘eop:incidenceAngle’ in the metadata file). The azimuth angle for FLAASH (F_{az}) is derived from the azimuth angle of the satellite system (S_{az}), which is stated in the metadata file (‘re:azimuthAngle’), and ranges from -180°-180°. Two examples of calculating F_{az} are shown in plot b) of Figure 4-4.

The result of FLAASH are assumed reflectance values and without corresponding ground truth data, a validation of the results was not possible. Nevertheless, the literature describes FLAASH as a method that estimates plausible reflectance values (Manakos et al. 2011; Matthew et al. 2002).

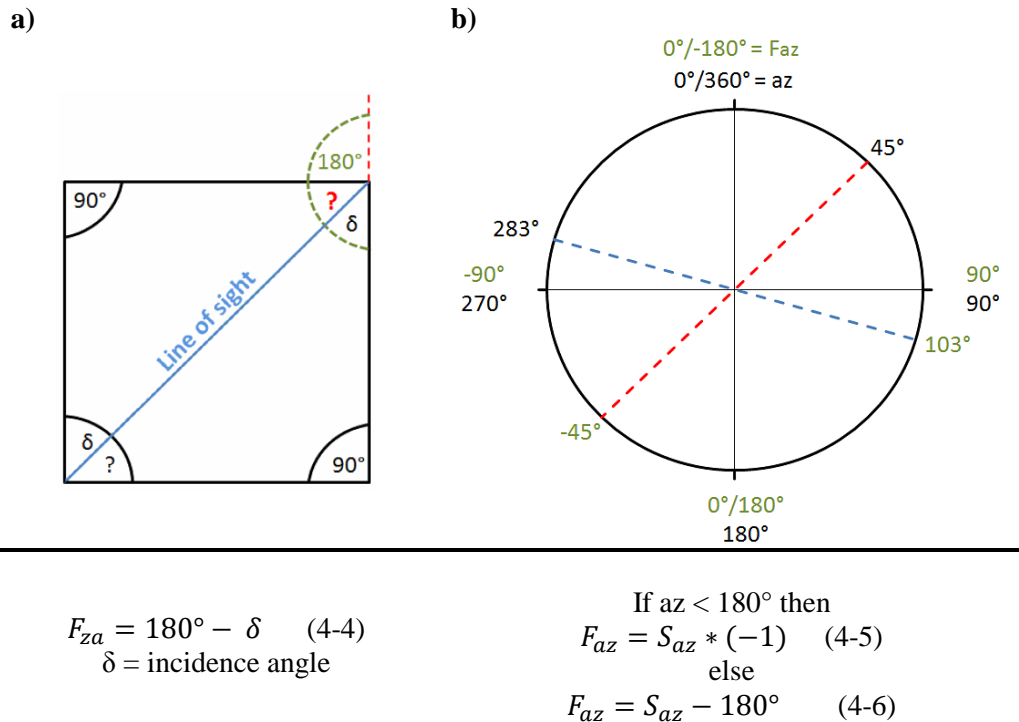


Figure 4-4: Calculation of zenith and azimuth angle for FLAASH.

4.3.2 TerraSAR-X

The TSX data were used as they were delivered by the German Aerospace Center (DLR), with DN's ranging from 0 to 255. Furthermore, the images were resampled to 5m with the nearest neighbour method to eliminate some of the noise and to fit the spatial resolution with the RE data. For the presented TSX data, no further geospatial matching to the RE data was necessary.

4.3.3 LiDAR

The data was available for the years 2010, 2011 and 2012 as point information (location and height) stored in a text file. First, the dataset is converted into a digital elevation model (DEM). This was done in ArcMap following the methodology described in a white paper of ESRI (ESRI 2010). This comprises the transformation of the text file into a 3-D feature class (3D-ASCII in Feature-Class) and their rasterization (Point to Raster) to obtain a DEM with a spatial resolution of 1m.

4.3.4 Spectrometry data

First, the pre-processing procedure (see Figure 4-6) comprises a radiometric correction that can be carried out with the software delivered along with the spectroradiometer SCV HR-1024i. During the radiometric correction, the overlapping detector transitions at 985nm and 1,900nm are eliminated. Figure 4-5 shows the details for the parameterization. Afterwards, a correction for a non-ideal white plate reflectance to the spectra is carried out. The necessary information is given by the provider of the spectroradiometer.

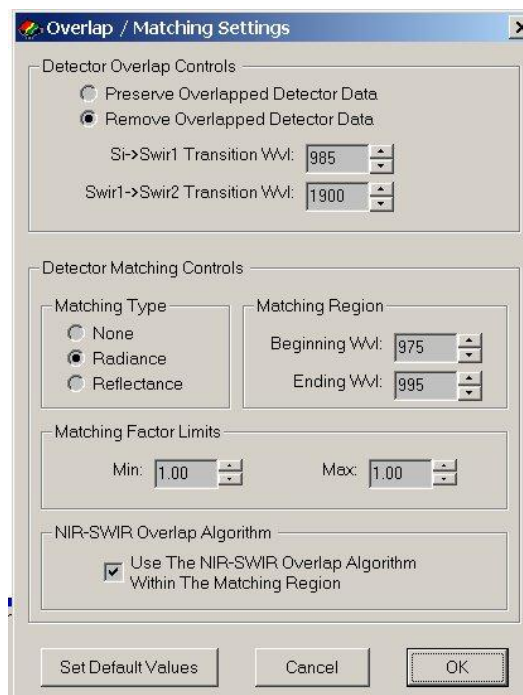


Figure 4-5: Detailed description of the overlap removal.

Subsequent to the radiometric correction, the spectra are applied to an automatic process (written in IDL) that comprises the removal of the water absorption bands between 1,352nm to 1,452nm, 1,802nm to 1,979nm and 2,403nm to 2,500nm (defined by the user), a spectrum smoothing with the Savitzky-Golay filter and, if desired, a resampling to the spectral resolution of a specific sensor configuration (e.g., RapidEye, WorldView-2, Landsat 8, etc.).

In general, the Savitzky-Golay filter is used to smooth a noisy signal (King et al. 1999). The filter is a simplified least squares-fit convolution for smoothing and computes derivatives of a set of consecutive values (e.g., a spectrum) (Savitzky and Golay 1964). The convolution is defined as a weighted moving average filter with weighting given as a polynomial of a certain degree. If the returned weight coefficients are applied to a signal, they perform a polynomial least-squares fit within the filter window. This polynomial is designed to reduce the bias introduced by the filter and to preserve higher moments within the data. There exist a few

requirements for this filter. First, it can be applied to any consecutive data, if the points of the data are at a fixed and uniform interval along the chosen abscissa. Secondly, the curves formed by displaying the points must be continuous and more or less smooth. In general, the heights and widths of the curves are preserved (Chen et al. 2004; Exelis VIS 2015a). Due to the nature of smoothing filters, the data input loses some data points at the beginning and end of the spectrum (King et al. 1999), in this case even at the location of the eliminated water absorption bands. Overall these are $3*((L-1)/2)$ samples that are lost for a given filter length L , while it is defined as

$$L = (2 * width) + 1 \quad (4-7)$$

For the smoothing technique, two functions of the software ENVI/IDL ('SAVGOL' and 'CONVOL') were used. "The SAVGOL function returns the coefficients of a Savitzky-Golay smoothing filter, which can then be applied using the CONVOL function" (Exelis VIS 2015a). "The CONVOL function convolves an array [(e.g., reflectance values)] with a kernel [(e.g., coefficients of SAVGOL)], and returns [for instance, a smoothed spectrum]" (Exelis VIS 2015b). Some parameters (e.g., width, degree and order) for the SAVGOL function have to be defined.

The parameter *width* is an integer value specifying the number of data points to the left and right of each point to be included in the filter. Usually, a larger value for width produces a smoother result at the expense of flattening sharp peaks. This means that too-small values may cause difficulties in capturing the spectral trend and too-large values may neglect some important variations of the spectrum. Values between four and seven can be considered as appropriate (Chen et al. 2004; Exelis VIS 2015a).

The parameter *degree* is an integer specifying the degree of smoothing polynomial. Lower values will produce smoother results but may introduce bias, whereas higher values will reduce the filter bias but may overfit the data and give a noisier result. Typical values are two or four (Chen et al. 2004). It should be noted that the parameter *degree* must be lower than the filter *width*.

Order specifies the order of the derivative desired and must be lower than or equal to the value specified for the parameter *degree*. For smoothing, the *order* must be set to zero (Exelis VIS 2015a).

Consequently, there are 12 combinations of the parameter *width* and *degree*, when both are set to typical values. All combinations were tested and the most reasonable result was obtained with the combination of *width* equals seven and *degree* equals four. The parameter *order* was set to zero, due to smoothing of the spectra.

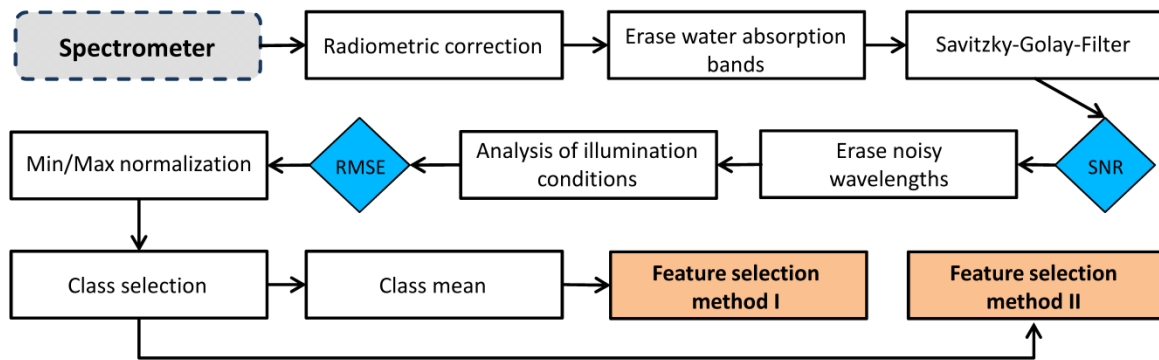
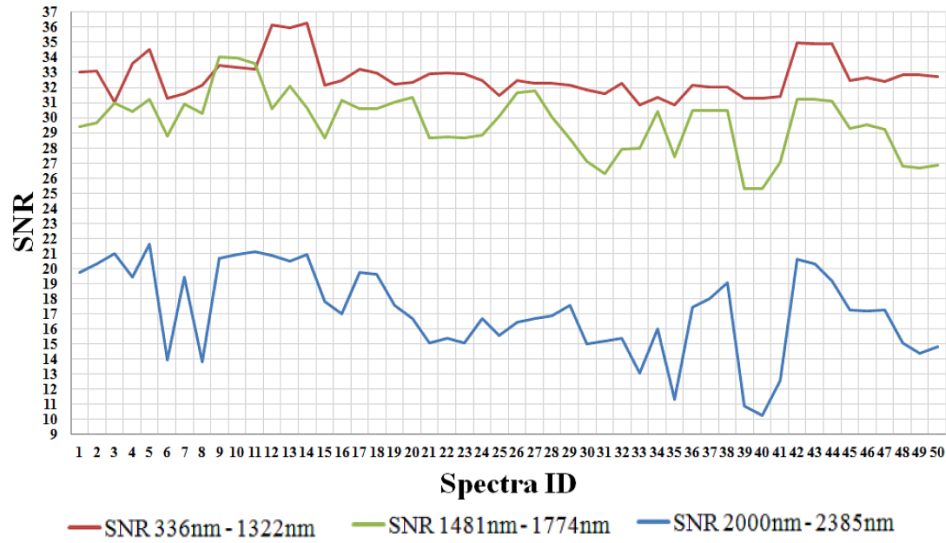


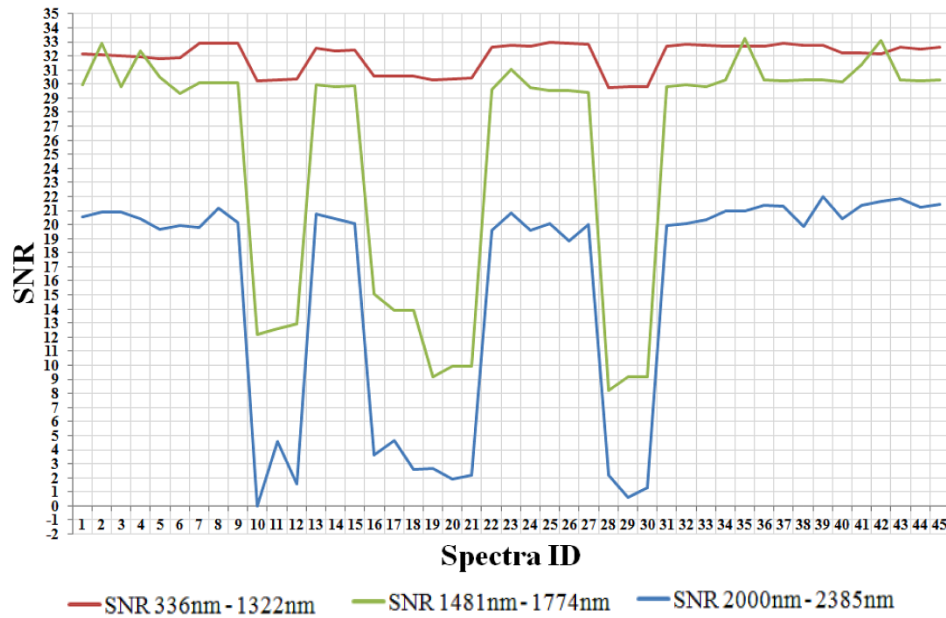
Figure 4-6: Flow chart for the pre-processing of the spectrometer data.

Subsequent to the Savitzky-Golay filter, an analysis of the signal-to-noise ratio (SNR) of each spectrum was carried out by applying the calculation of Stoehr (2007) and Stoehr et al. (2008). The results are expressed in dB using $SNR[dB] = 10\log_{10}(SNR)$. They show that the wavelengths between 2,000nm and 2,385nm are very noisy (i.e., low SNR). Figure 4-7 plots a) and b) summarize the SNR values for every spectrometric measurement of 2013 and 2015 in the corresponding wavelength ranges separated by the water absorption bands. In general, sediments in tidal flats reflect a low amount of energy (i.e., low reflectance values) (Verpoorter et al. 2014; Stelzer, Brockmann & Geißler 2009; Small et al. 2009; Decho et al. 2003; Rainey et al. 2000). Simultaneously, the second scanning spectrometer of SVC HR-1024i (see chapter 3.5) needs a lot of energy for generating a signal with a low amount of noise. This can be achieved in laboratory conditions and with high reflecting materials. However, in the intertidal flats, these requirements cannot be achieved. This is shown by the blue lines of Figure 4-7 plot a) and plot b), which represent the SNR values of the wavelengths from 2,000 nm to 2,385 nm. The SNR is clearly lower in comparison with the other wavelength ranges. The drops in the SNR values in the data of 2015 are a result of water coverage. The corresponding measurements can be seen in Figure 4-7 plot c). The water absorbs nearly all the energy and only the noise was detected by the spectrometer (Schmidt & Skidmore 2003). Therefore, only the spectral range between 336nm to 1,774nm was analysed, with a gap at the water absorption band (1,352nm-1,452nm), leaving a total of 703 bands for analysis.

a) 2013



b) 2015



c) 2015

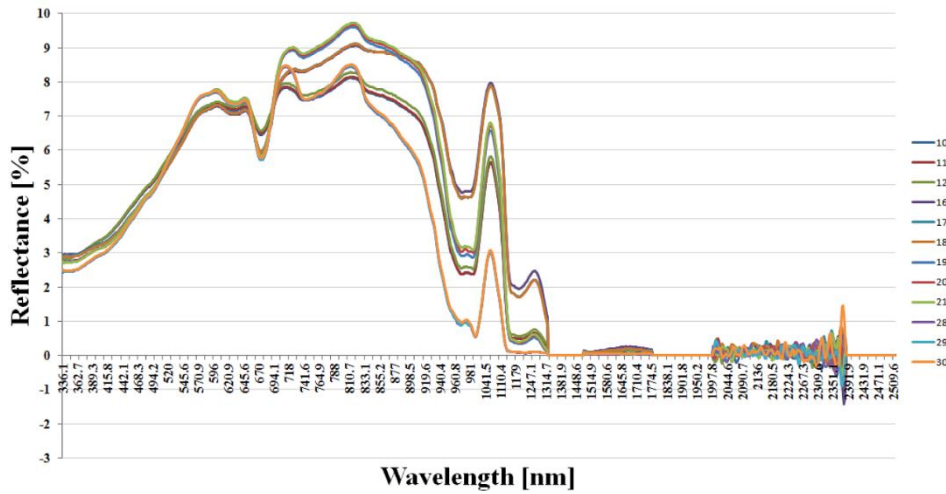


Figure 4-7: SNR values in dB of specific wavelength ranges from 2013 (plot a) and 2015 (plot b)). Plot c) represents distinctive spectra that create a very low SNR in the data of 2015.

A further pre-processing step is the estimation of the illumination condition at the beginning and end of each measurement at each station. Changing illumination conditions during the measurements would result in differences between measurements of the same surface at the same station, which is inexplicable. In general, the atmospheric conditions and thus the illumination conditions of the Wadden Sea can change very quickly, due to the great amount of water vapour, clouds and the strong winds. To estimate this effect, the Spectralon® was measured twice (see chapter 3.5) and the root mean square error (RMSE) between those two spectra was calculated (see Table 4-2 and Figure 4-8). For station 15 of 2013, the spectrum of the second Spectralon® is missing.

Table 4-2: Station ID's and their corresponding RMSE value of the two Spectralon® measurements.

Station-ID	RMSE - 2013	RMSE - 2015
S1	2.17	1.08
S2	2.42	3.59
S3	8.4	9.36
S4	5.04	0.4
S5	12.06	8.81
S6	0.86	0.44
S7	5.98	7.86
S8	3.33	0.59
S9	1.48	0.51
S10	4.25	4.06
S11	1.31	5.46
S12	2.81	1.53
S13	4.72	2.21
S14	3.59	4.47
S15	NA	2.48
S16	5.46	
S17	1.31	

The calculated RMSE of Table 4-2 shows partially very high values, ranging from 0.86 to 12.09 (mean 4.07) for the spectra of 2013 and from 0.4 to 9.36 (mean of 3.5) for the spectra of 2015. Figure 4-8 gives an illustrative example for the best and worst RMSE of 2013 and 2015. Most of the differences are very high, so that a significant change in the illumination condition during the measurements has to be considered. Experiments with laboratory conditions have proven that the same material has a different measured spectrum if the illumination conditions are changed. Due to the RMSE, most spectra would not be useable in the further analysis. This would drastically reduce the amount of data. To eliminate the influence of the illumination, the measured spectra are normalized by their minimum and maximum value with the following equation:

$$S_{Norm} = (i_{max} - i_{min}) / (S_{max} - S_{min}) * (S - S_{min}) + i_{min} \quad (4-8)$$

with $i_{max} = 1$ and $i_{min} = 0$

where i_{min} and i_{max} are the lower and higher boundaries of the normalized values. S_{max} and S_{min} are the maximum and minimum values of the measured spectra (S). Due to the normalization, all spectra are independent of illumination and can be applied to the feature selection methods.

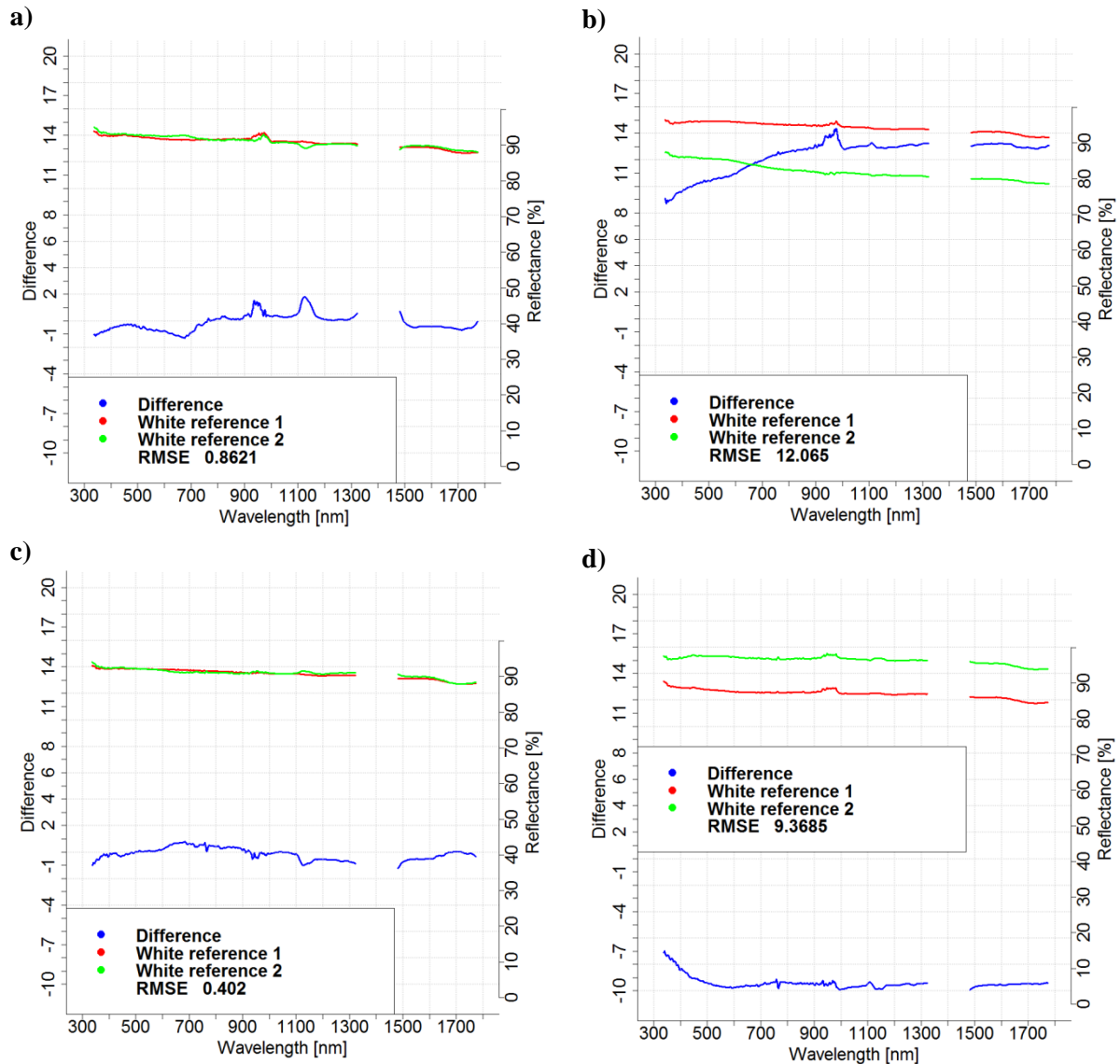


Figure 4-8: Examples for the analysis of the changing illumination conditions. Plot a) represents the lowest RMSE of 2013, plot b) the highest RMSE of 2013, plot c) the lowest RMSE of 2015 and plot d) the highest RMSE of 2015.

4.4 Classification

4.4.1 Hierarchical knowledge-based classification

As already described in chapter 2, different techniques have been used for mapping sediment properties, channel geometries, vegetation and shellfish beds. Yates et al. (1993) or Thomson et al. (1998) applied supervised classification methods, such as the maximum likelihood

classification. The quality of the results of supervised classifications relies on the validity of the training sets used to define the classes and their statistical separability. Unsupervised classification methods (e.g., ISODATA, PCA or K-Means), on the other hand, maximize the separability with only a little user interaction involved. Optimal statistical clustering of data leads not always to meaningful classes (Daniels 2006). Additional ground truth data is needed for labelling the classes. If there is no ground truth data available, the assignment of the resulting classes is rather difficult. Further disadvantages are the input parameters (e.g., number of cluster or allowable dispersion around cluster means) which could produce different final classes for the same dataset or between scenes. Furthermore, the spectral signatures for the supervised classification can overlap, making effective discrimination unachievable based on reflectance characteristics alone. Both methods use sharp boundaries to define the classes (Van der Wal & Herman 2007; Daniels 2006).

Van der Wal & Herman (2007) further describe the method of spectral un-mixing and regression modelling as an appropriate choice for more heterogeneous areas with diffuse boundaries, such as intertidal areas. This method calculates the proportion of the various components present in each pixel. It is based on the spectral characteristics of the surface using spectral end-members which represent pure spectral statistics of one class. These end-members have to be identified using ground truth data or spectral plots of the satellite image (i.e., expert knowledge). In this study only a few ground truth datasets were available and no pure spectral statistics could be identified using the optical satellite data.

A third kind of mapping of land covers is the regression modelling with hyperspectral data. This method is able, such as spectral un-mixing, to show the variable of interest on a ratio scale, allowing detection of subtle differences. For this method also ground truth data is required, which is regressed against surface reflectance in a number of key wavelengths. The resulting linear or non-linear regression equation is applied to the image to obtain a classification map. A great disadvantage is the limited number of wavelengths (i.e., bands) that can be used to obtain significant regression models and that many wavelengths of hyperspectral data are highly correlated. Due to missing spectrometric ground truth data of the land cover for 2010 and 2011, as well as missing hyperspectral imagery, the method was not chosen.

In the context of the above mentioned disadvantages that arise with some classification methods and due to the lack of necessary information, this study uses a kind of decision tree classifier. Lee et al. (2012) describe the decision tree classifier as an efficient tool for mapping pattern in data and give some advantages:

1. no assumption is required for data distribution or feature independence
2. nonlinear and hierarchical associations can be utilized
3. easy to interpret with all measurement scales

Also Wang et al. (2013) describe the decision tree method as a more accurate, convenient and efficient way to solve basic classification problems.

In general, a decision tree is based on a hierarchical decision scheme, which is composed of a root node containing all data, a set of internal nodes (splits) and a set of terminal nodes (leaves) (Wang et al. 2013). At each node of the hierarchical decision scheme, a binary decision is made that separates the target variables (e.g., land cover classes) from each other. The processing starts at the first decision and ends when every leaf node was reached. A decision tree splits a complex decision into several simpler decisions, which are easier to interpret (Wang et al. 2013).

In this study a hierarchical knowledge-based decision tree was designed for mapping sediments, shellfish beds and different kind of tidal vegetation by integrating indices and spectral statistics from electro-optical data (RE), backscatter values from SAR data (TSX) and geometrical information derived from LiDAR data. It also comprises object and texture based analysis (Figure 4-9), because a considerable amount of information held in remotely sensed data lies in spatial context. The algorithm is based on previous work of Klonus and Ehlers (2012) and was already published (Jung et al. 2015). The hierarchy of the decision tree follows the numeration in Figure 4-9.

As a first step, the vector information of the coastline (OSM) is used to mask the mainland as well as the island of Norderney. Using this approach, the AOI within the pre-processed RE data can be isolated. The island of Norderney as well as the mainland represent a potentially large source of misclassification. During this first step, the normalized difference water index (NDWI) (McFeeters 1996) with a threshold value greater than or equal to 0.2 for the RE image of April 25, 2010, and a threshold value greater than or equal to 0.0 for the other RE images, was applied to separate water from the tidal flats. These different threshold values result from a different water level at each acquisition time (April: 457 cm, June: 384 cm, July: 374 cm and October: 401 cm) and were derived empirically from the images.

$$NDWI = \frac{Green - NIR}{Green + NIR} \quad (4-9)$$

The second step contains the shellfish bed classification. The class 'shellfish bed' is classified using a thresholding technique using texture features derived from backscatter values of TSX, morphologic filters (MF) and an exclusion criterion, as they are not part of the area that was

classified as water. In the study area, they do not grow near the coast and must have a minimum size. During the third step, the modified soil adjusted vegetation index (MSAVI) (Chehbouni et al. 1994) was used to separate sediments from vegetation.

$$MSAVI = \frac{2NIR+1-\sqrt{(2NIR+1)^2-8(NIR-RED)}}{2} \quad (4-10)$$

The class ‘vegetation’ is divided into ‘sea grass/algae’ and ‘salt marsh’. These classes are part of the tidal flats, but areas that are already classified as water or shellfish are not considered. ‘Salt marsh’ is classified as vegetation that is connected to the land in a 25 m buffer zone. ‘Sea grass/algae’ comprises all the vegetation that is not connected to the land. During the fourth step, the remaining area - which is not classified yet - is defined as the class ‘sediments’. This class is further separated into the sediment types ‘sand’, ‘mud’ and ‘mixture’ with the help of the spectral properties of RE and the MSAVI. As a last step, the LiDAR data are analysed for the potential to improve the sediment classification result of RE by deriving the geometric properties of the tidal inlets. At every step, the analysed area gets smaller by eliminating the area of the respective classes in the hierarchy level before.

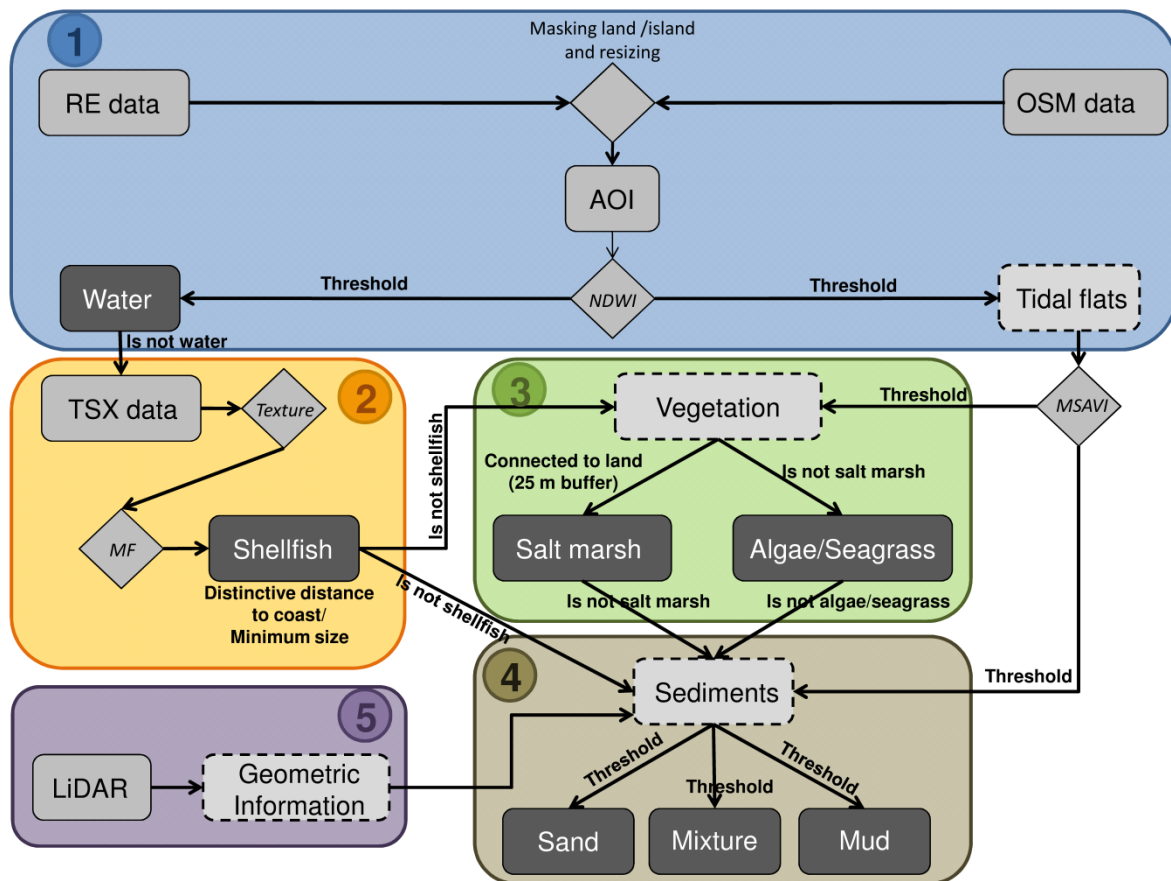


Figure 4-9: Workflow of the hierarchical classification procedure (see text for explanations).

4.4.1.1 Classification of shellfish beds based on TerraSAR-X

In this study area, shellfish beds are actually a mixture of oysters and blue mussels. With RE data alone, the detection of shellfish beds is difficult (see Figure A-7 plot a)). Shellfish beds have a highly inhomogeneous appearance and are therefore difficult to detect spectrally with optical sensors. Other surface types (e.g., wet sand, dry mud, green algae or seagrass) can have similar spectral reflectance values (Brockmann and Stelzer 2008). Shellfish beds can even be covered by other surface types which change their spectral reflectance. Older and well-developed shellfish beds can be detected, but small or young shellfish beds are not visible with electro-optical sensors. They can be overgrown partially by vegetation (e.g., algae) or else vegetation may grow nearby (e.g., seagrass). This makes the separation of shellfish beds and vegetation more difficult with electro-optical sensors. In Figure 4-10, a subset of both datasets is displayed. The bright pixels of the TSX image represent the shellfish beds which can be seen (next to other land cover types) as dark, brownish pixels in the RE image. Due to this fact, an approach was developed based on two datasets (RE and TSX) for the classification of the shellfish beds and vegetation. As shellfish beds have a larger surface roughness than the sediments and water areas, radar images are an excellent tool to identify shellfish beds. First, the Haralick texture measure ‘contrast’ in a 3x3 window and one pixel distance from the DN of TSX is calculated (Haralick et al. 1973). The result was separated by a threshold of 20 into two classes: ‘shellfish bed’ and ‘no shellfish bed’. The threshold was derived empirically from the texture measure. Furthermore, a filter process was applied. The procedure starts with the MF closing, followed by a majority filter and a dilate filter. All the filters use a window size of three. The resulting adjacent shellfish bed pixels are combined into one area. The resulting areas are examined according to their size and objects smaller than 200 m² are erased. The area-based parameter is chosen to reduce the number of false classifications. These occur due to those roughness effects which are not caused by shellfish beds (e.g., dead shell fish patches, areas of steep slope). The disadvantage of this procedure, however, is that small shellfish bed areas are also erased. To avoid the effect whereby the edges of tidal rivers are assigned to the class ‘shellfish bed’, a buffer of 5 m is defined around water areas derived from RE in each dataset. The RE data were used, because the acquisition times of all the RE images are further away from the low tide in comparison with the TSX images. This indicates a higher water level, and this implies no area that was covered with water in the RE image is taken into account for the shellfish bed classification.

Due to missing TSX data for the optical data of April 25, 2010, a manual delineation of the shellfish bed borders was carried out.

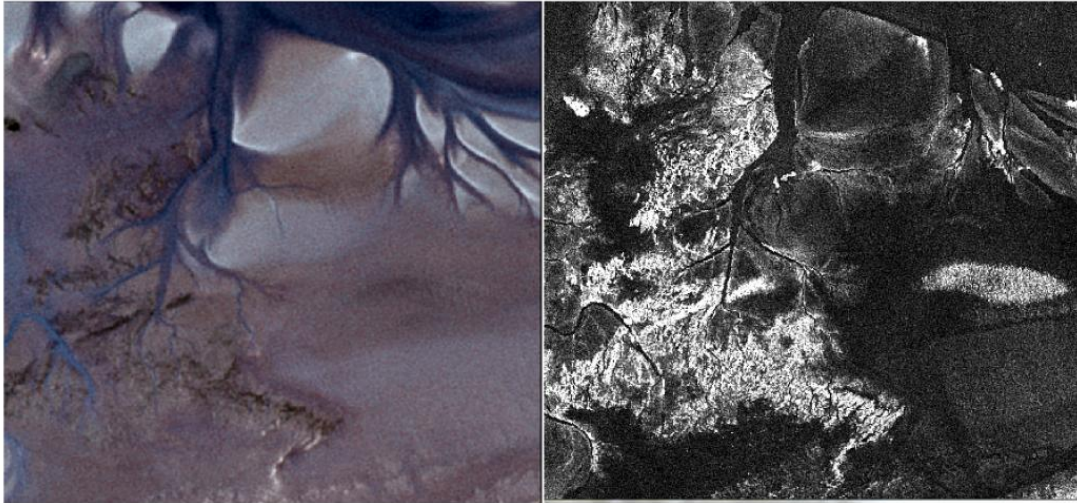


Figure 4-10: Subset of a RE image (left, RGB of 27 June 2011) and a TSX image (right, 16 July 2011) of an old and well developed shellfish bed and a small shellfish bed. The bright pixels in the TSX image represent the shellfish beds which can be seen partly as dark brownish pixels in the RE image.

4.4.1.2 Classification of tidal vegetation based on RapidEye

The spectral index MSAVI and a thresholding technique were applied to separate vegetated areas from non-vegetated areas. The result of the MSAVI calculation is rearranged to the value range of 0 to 255 by the following equation:

$$f(i, j) = \left(\frac{\text{value}_{i,j} - \text{minimum}}{\text{maximum}} \right) * 256 \quad (4-11)$$

where:

$$\text{minimum} = \text{mean} - (2 * \text{stdev})$$

$$\text{maximum} = \text{mean} + (2 * \text{stdev})$$

Any values that are greater than the maximum or lower than the minimum are automatically set to 255 or 0. In this study area, vegetated areas have a value greater than 30. The reference data from 2003-2008 were analysed to find areas where seagrass occurs every time. The corresponding threshold was derived empirically at these locations in the images.

The vegetated areas are further separated into the following classes: ‘sea grass/algae’ and ‘salt marsh’, which are determined by the fauna and flora habitat directives (FFH; Council Directive 92/43/EEC). The directives determine the natural habitats that occur in Germany. Salt marshes form the transition zone between the tidal flats and the mainland on the one side, and the dunes of the island on the other side. Although they are not the focus of the study - and thus will not play a part in the further analysis - they are classified by an object- and

neighbourhood-based analysis and are used as additional information (i.e., exclusion criterion). Salt marshes are in general connected to the coastline (especially in this study site). Thus, all vegetation areas within a 25 m buffer zone of the coast are classified as salt marsh. Within this buffer zone seagrass also grows, which is then classified as the class 'salt marsh'. The class 'salt marsh' is used as an exclusion criterion later on. The remaining vegetated areas of the class 'vegetation' are labelled as 'sea grass/algae'.

4.4.1.3 Classification of sediments based on RapidEye

A hierarchical decision tree (DT) based on the spectral properties of sediments and MSAVI values is used for the sediment classification (sand, mud and mixed sediments) (Figure 4-11). The labelling of the class 'sediments' is based on the fauna and flora habitat directives (FFH; Council Directive 92/43/EEC). The sediment classes are distinguished by defining their spectral range with two thresholds for each class and each spectral band. As an initial point, the geographic coordinates of the ground truth data are used to extract spectral information (mean and standard deviation) directly from the satellite images at this location. Furthermore, different locations were evaluated to adjust the extracted threshold values (i.e., expert knowledge of the study area was applied). With this approach, the entire spectral range of each sediment class was covered. In addition to the spectral information, the spectral index MSAVI was used to improve the separation of wet sand (low values) and mud (high values). Table 4-3 shows the threshold values for the sediment classification. The order of the column 'Class/Band' represents simultaneously the decision hierarchy. Three different hierarchies are necessary. A transfer of the thresholds was not possible because of the different spectral properties for the sediment classes in each image. These differences emerge from the fact that the images were acquired in different seasons (e.g., spring, summer or autumn) or years (e.g., 2010 or 2011). The only exceptions are the images of 27 June 2011 and 11 July 2011, which are acquired in the same season within a 14-day interval. Furthermore, the information from the spectral index MSAVI was enough to distinguish between 'wet sand' and 'mud'.

Applying a threshold approach, some pixels will not be assigned to any class. A majority filter with a window size of 7x7 pixels is then used to eliminate unclassified pixels.

Table 4-3: Upper (UT) and lower (LT) threshold values for the sediment classification.

Acquisition date	Class/Band	1	2	3	4	5	MSAVI
25 April 2010	Wet sand (LT)	0.069	0.085	0.08	0.08	0.09	0
	Wet sand (UT)	0.1	0.12	0.11	0.11	0.11	0.055
	Dry sand	0.08	0.1	0.1	0.1	0.1	---
	Mixed sediments (LT)	0.06	0.078	0.07	0.072	0.07	---
	Mixed sediments (UT)	0.1	0.14	0.12	0.1072	0.125	---
	Mud (LT)	0.05	0.07	0.06	0.06	0.07	0.055
	Mud (UT)	0.08	0.1	0.095	0.11	0.15	1
27 June 2011 11 July 2011	Dry sand	0.065	0.09	0.1	0.1	0.1	---
	Mud (LT)	---	---	---	---	---	0.055
	Mud (UT)	---	---	---	---	---	1
	Mixed sediments (LT)	0.025	0.05	0.055	0.06	0.06	---
	Mixed sediments (UT)	0.048	0.062	0.069	0.085	0.1	---
	Wet sand (LT)	---	---	---	---	---	0
	Wet sand (UT)	---	---	---	---	---	0.055
22 Oct. 2011	Dry sand	0.06	0.1	0.1	0.1	0.1	---
	Mixed sediments (LT)	0	0.05	0.055	0.06	0.06	---
	Mixed sediments (UT)	0.04	0.075	0.08	0.1	0.1	---
	Mud (LT)	0.04	0.07	0.07	0.09	0.1	0.1
	Mud (UT)	0.047	0.079	0.082	0.1	0.12	1
	Wet sand (LT)	0.04	0.07	0.06	0.08	0.08	0
	Wet sand (UT)	0.1	0.1	0.1	0.14	0.15	0.1

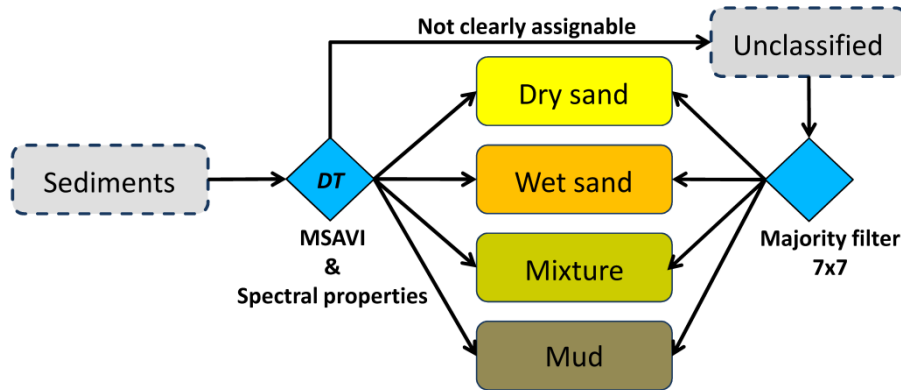


Figure 4-11: Scheme of the hierarchical decision tree classification of the sediments.

4.4.1.4 Improvement of sediment classification with LiDAR

Several studies have used remote sensing data from various sensors to estimate sediment types based on reflectance values, which are affected, for example, by grain size, water content and organic matter. Just a few studies have considered the spatial distribution of tidal channels and their geometric features in sediment classification. Tidal channels are filled with water during low tide and generate various patterns, which are influenced by wind, water current and the tide (Mason et al. 2006; Ryu et al. 2010; Choi et al. 2011; Eom et al. 2012). However, LiDAR data are very valuable for feature extraction. The perception of humans relies extensively on contextual information to identify features. For instance, we are able to

perceive depth in a 2D image through the use of visual cues such as shadowing, or we recognize features through their shape, such as rivers or buildings. To transfer these attributes to an automated method is very difficult, if only electro-optical images and pixel-based approaches are applied (O'Neil-Dunne et al. 2013).

In this context, the proposed improvement of the sediment classification is based on the geometric information (e.g., number of confluences and number of flow direction changes) derived from an object-based classification of the intertidal stream network. In general, stream networks can be mapped in two different ways, 1) through ground surveys or 2) remote sensing data. The advantages of ground surveys are their accurate measurements, but they often suffer from serious logistical constraints. With remote sensing data, stream networks can be delineated by using either manual or automated approaches (Yang & Morris 2008; Mason et al. 2006). The manual approach needs a digitizer and can be quite labour-intensive (Heine et al. 2004; Novakowski et al. 2004). The automatic approach can be based on different input datasets, as already discussed in chapter 2. Figure 5-8 shows the poor separability of the sediments sand, mud and mixed sediments, as an example. This implies the need for additional information to estimate the distribution of sediments. Choi et al. (2011) and Eom et al. (2010) describe in their studies that the tidal channels (i.e., streams) should be part of a sediment classification. Mason et al. (2006) showed the importance of tidal channels as a key factor for propagation and evolution of tidal flats. The sediment exchanges between intertidal flats and sea are governed by the channels. Furthermore, their morphological behaviour can control the evolution and hydrodynamics of the intertidal flat and thus the distribution of sediments (Fagherazzi et al. 1999). During low tide they drain the marshes, while during flood tides they act as conduits. The incoming water fills them prior to flooding the areas around them when the channels are overtopped (Mason et al. 2006). With the development of the tidal channel network, the morphodynamics of the intertidal flats and the distribution of the sediment facies also change as well (Eom et al. 2012). A lot of work has already been done by various authors analysing the geometry of intertidal channels and describing their origin and development (Marani et al. 2002; Temmerman et al. 2007), or discussing the relationship of intertidal channel hydrodynamics to the geomorphic structure of salt marshes (Fagherazzi et al. 2008). Figure 4-12 demonstrates the difference in geometry of two sediment types, whereby plot a) represents a sand flat and plot b) represents a mudflat. Muddy areas generate subtler channels, which change their flow direction quite often. They meander like terrestrial rivers, but there are fundamental differences between tidal and terrestrial channels, the most important being the bi-directional flow that occurs only in tidal

channels (Mason et al. 2006). Furthermore, the number of channels in muddy areas, which evolve from a bigger channel or tidal inlet, is clearly higher. These kinds of channels are in the focus of the further analysis. Bigger channels cannot be examined due to the result of the applied channel network extraction algorithm (see Figure 4-21).

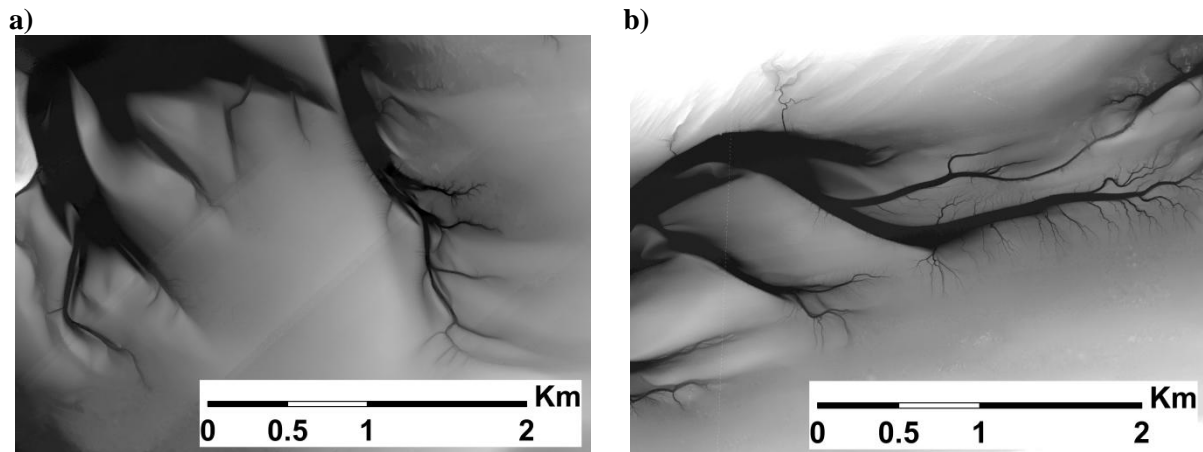


Figure 4-12: Two subsets of the LiDAR DEM from 2010 showing the differences of the channel geometry in relation to the underlying sediment type. On the left hand side is an example for a sandy area and on the right hand side an example for a muddy area.

Only one overlap in acquisition between the RE data and LiDAR data took place in 2010, with only a one-month difference (see Table 3-1). Hence, the integration of the LiDAR dataset from 2010 into the sediment classification scheme of RE will be illustrated in further paragraphs (Figure 4-13).

First, the water coverage was classified with an object-based method. Second, the channel network structure was derived from the water cover classification with the software ‘GRASS GIS’. Finally, several geometric features (e.g., number of confluences and number of flow direction changes) were extracted to define the pattern of the channel distribution. The patterns were analysed for several sub-channel stream networks in terms of sediment types. Figure 4-19 shows a subset of the derived DEM from the LiDAR data. This subset represents a muddy area and will be the example for the implementation of the object-based classification and the extraction of geometric features in the further descriptions. In chapter 5 a second area is introduced, representing a sand flat for comparison. The results of the whole dataset are presented in the appendix (Figure A-15 to Figure A-17).

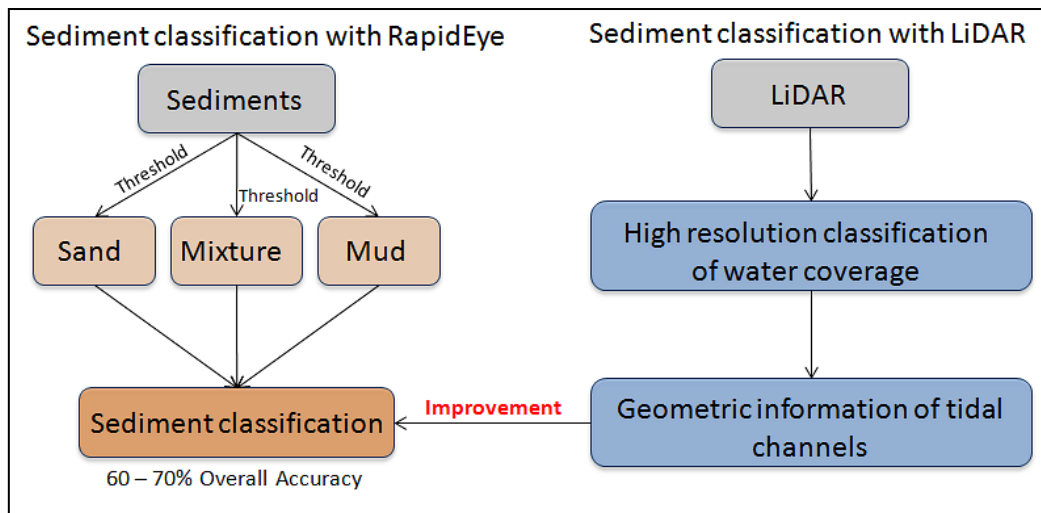


Figure 4-13: Integration of LiDAR data into the existing sediment classification scheme of RE.

4.4.1.4.1 Object-based water classification

Various studies have shown that Object-Based Image Analysis (OBIA) techniques are superior to pixel-based approaches for feature extraction of very high spatial resolution images (Gao et al. 2006; Myint et al. 2011). However, an object-based classification is always based on a segmentation procedure. In this study the multiresolution segmentation procedure of ‘eCognition Developer’ was used. “The multiresolution segmentation creates objects using an iterative algorithm, whereby objects (starting with individual pixels) are grouped until a threshold representing the upper object variance is reached. The variance threshold (scale parameter) is weighted with shape parameters (with discrimination of shape and compactness parameters) to minimize the fractal borders of the objects. By increasing the variance threshold, larger objects will be created although their exact size and dimensions is dependent on the underlying data” (Landmap n.d.). Figure 4-14 illustrates the algorithm. First, the algorithm finds a seed point and uses the homogeneity criteria to determine the best neighbourhood to merge with (red arrow in Figure 4-14 plot a)). If the first seed point has no best neighbour, the algorithm moves on (Figure 4-14 plot b)), with the second seed point finding the best neighbour. This is repeated until mutual best-fitting partners are found (Figure 4-14 plots c) – e)). If the homogeneity of the new image object does not exceed the scale parameter, the two adjacent pixels are merged (Figure 4-14 plot f)). The procedure continues with another seed point or image object best neighbour. It stops if no further image object can be merged without harming the maximum-allowed homogeneity criteria of an image object (Definiens 2010). A more detailed description of the algorithm can be found in Definiens (2010).

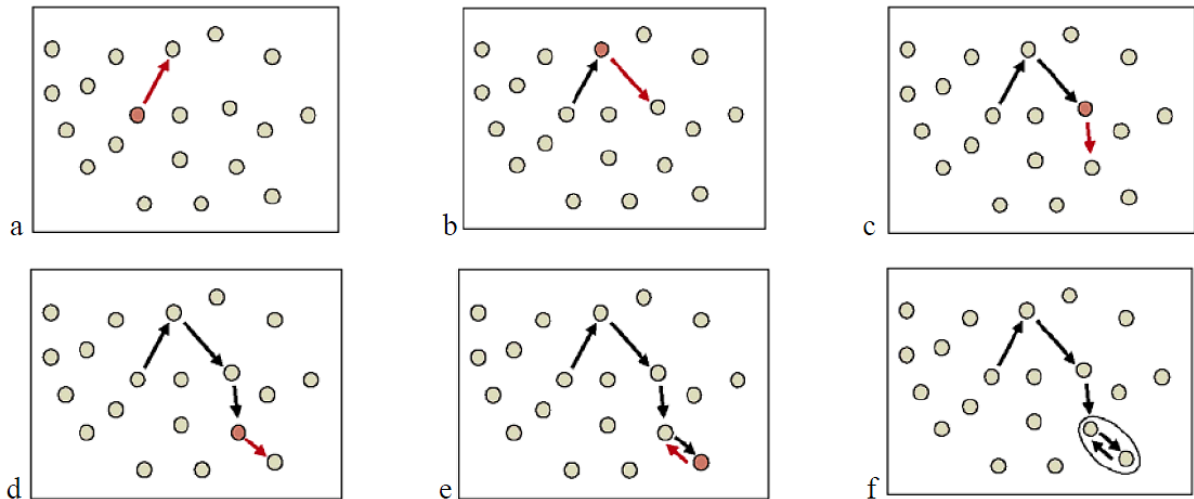


Figure 4-14: The multiresolution segmentation algorithm in a nutshell (Definiens 2010).

The multiresolution segmentation algorithm belongs to the region growing techniques, which are the most complex. As such, the values for the parameters of the segmentation have to be found by trial and error concept. The multiresolution segmentation algorithm in ‘eCognition developer’ uses the parameters ‘scale’, ‘shape’ and ‘compactness’ to define the homogeneity criteria for each image object (Figure 4-15).

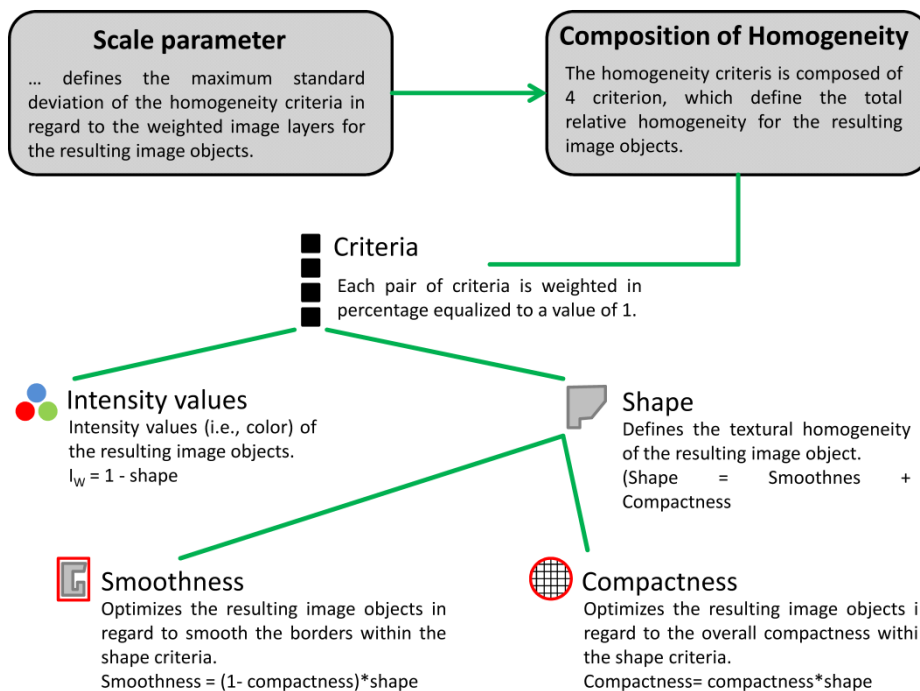


Figure 4-15: Relationship between the parameters of the multiresolution segmentation algorithm (after Definiens 2010).

Scale defines the acceptable standard deviation within objects (i.e., amount of spectral variation within objects) and therefore their resulting size. *Shape* defines the weighting of the object shape, which is simultaneously the antagonist of the intensity values (i.e., colour). This means that the weighting of the intensity values (I_w) is $I_w = 1 - \text{shape}$. If *shape* equals zero,

only the intensity value is considered, whereas if *shape* is greater than zero, the object's shape along with the intensity value is considered and therefore fewer fractal boundaries are produced. The third parameter, *compactness*, specifies how compact the objects are. As antagonist to the *compactness*, the *smoothness* ($1 - compactness$) is defined simultaneously. It specifies how fractured the object borders can be (Landmap n.d.; Definiens 2010).

Subsequent to the segmentation process, the software 'eCognition Developer' holds various object- and pixel-based parameters to define the target objects and assign them to a class. Table 4-4 lists the classes, the related parameters and the left and right border of their membership function applied in the object-based water classification of 2010. All membership functions are 'full range' membership functions (Definiens 2007).

Table 4-4: Chosen parameters for the object-based classification of the tidal channels and their values for the data of 2010.

Class	Parameters	Membership function
Prewater	Mean difference to neighbours layer 1	-6 to -0.05
	Mean layer 1	-6 to -0.9
	Not compactness	9 to 10
	Border contrast layer 1	BC_min to -0.035
Copy of water	Mean difference to neighbours layer 1	-6 to -0-06
	Mean layer 1	Layer1_min to -1.25
	Mean lee sigma	0.005 to 0.045
	Border contrast layer 1	BC_min to -0.035
Water	Mean difference to neighbours layer 1	-6 to -0-06
	Mean layer 1	Layer1_min to -1.25
	Mean lee sigma	0.005 to 0.045
Gaps	Number of pixels	0 to 50
	Number of water	1.9 to 4

A single rule set was developed to extract the stream network of the whole study site using the DEM derived from the LiDAR data of 2010. This classification is performed with the software 'eCognition Developer' from the company 'Trimble'. The rule set was developed largely through a trial and error process using a subset of the DEM. Figure 4-16 shows the original DEM compared with the subset used in the rule set.

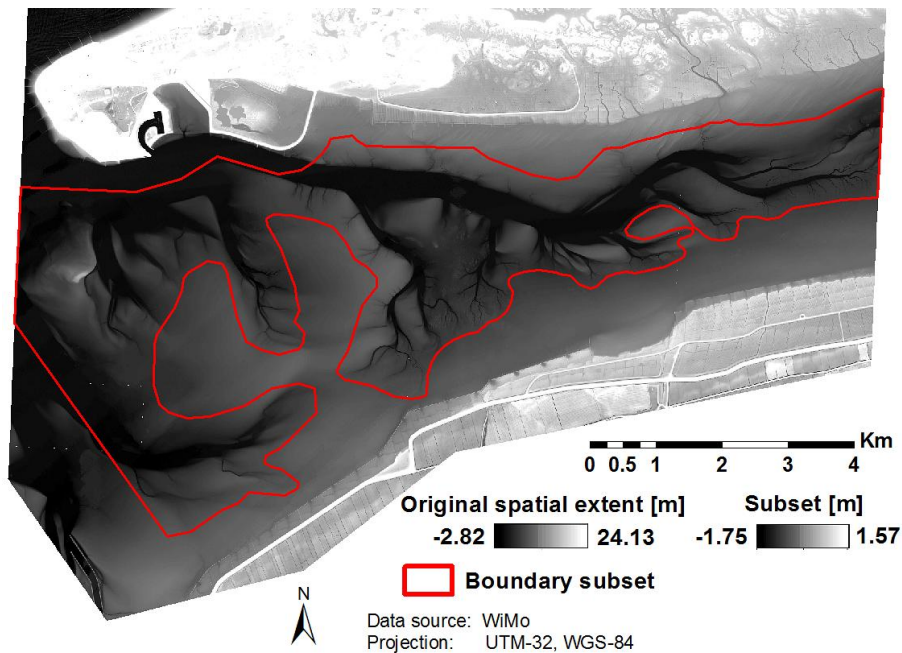


Figure 4-16: Original spatial extent of the DEM of 2010 compared to the subset (red polygon) used for the development of the rule set.

The subset expedited the rule set building by permitting more rapid executions. The rule set was modified in an iterative process, resulting in four major parts. A growing strategy (i.e., bottom-up strategy) was applied, which focuses on creating initial image objects and assigning a portion of them to temporary classes. Additionally, multiresolution segmentations and classification procedures were constrained to the unclassified image objects, reducing the number of new image objects created at each part of the rule set. Starting with large image objects and focusing the detailed analysis on just a few image objects will reduce the computational complexity and thus place less strain on system resources. Figure 4-17 illustrates an example of the growing strategy, whereas plot a) is a subset of the DEM, plot b) to plot d) represent the different parts of the rule set.

Figure 4-18 represents the applied rule set. In the first part, large features were isolated using a threshold of lower or equal to -1.15m . These image objects are assigned to the temporary class ‘prewater’. In the second part, the class ‘prewater’ is extended using the parameters represented in Table 4-4. The resulting objects are copied and merged to the class ‘water’. All objects with a number of pixels lower or equal to 3,500 are erased from the classification to avoid false allocations. In the third part, an edge detection filter called ‘lee sigma’ and additional parameters are calculated (see Table 4-4). The mode ‘dark’ of the edge detection filter was applied, which extracts edges of darker objects (Definiens 2010). This information is used to assign the image objects to another temporary class called ‘copy of water’. All image objects of that class are merged and image objects with a number of pixels lower or equal to 40 are erased to avoid false allocations. The resulting image objects are assigned to

the class 'water'. The final part comprises the closing of small gaps between image objects of the class 'water'.

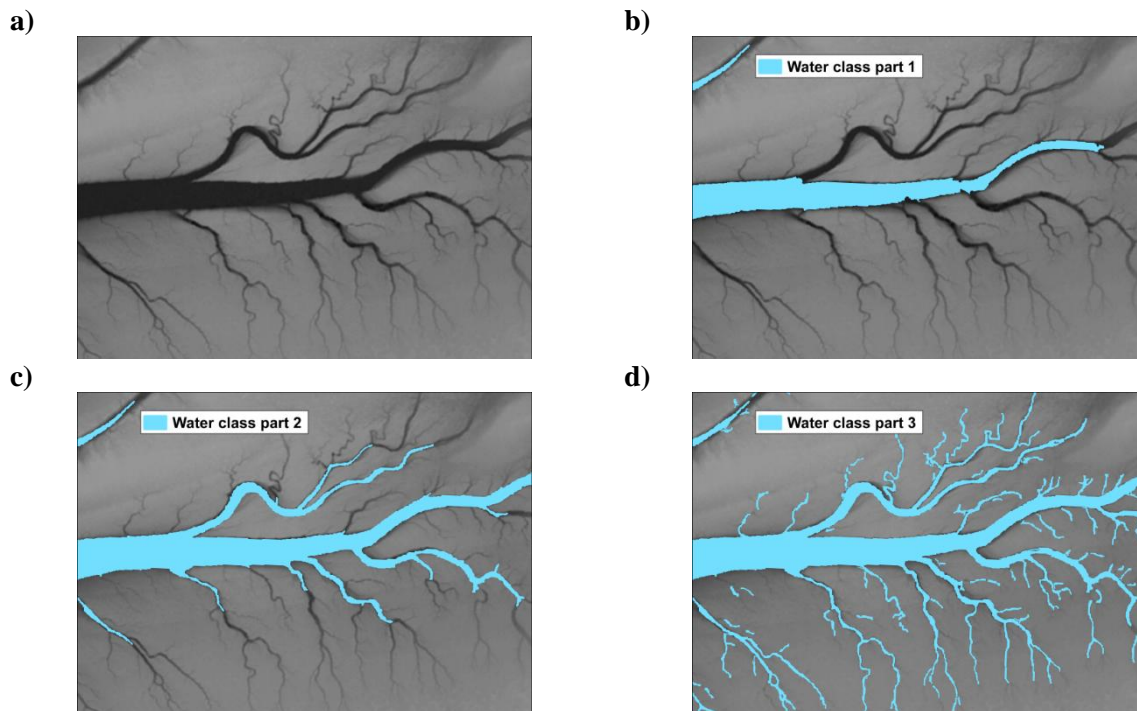


Figure 4-17: Plot a) represents a subset of the DEM and plot b) to d) illustrates the growing strategy.

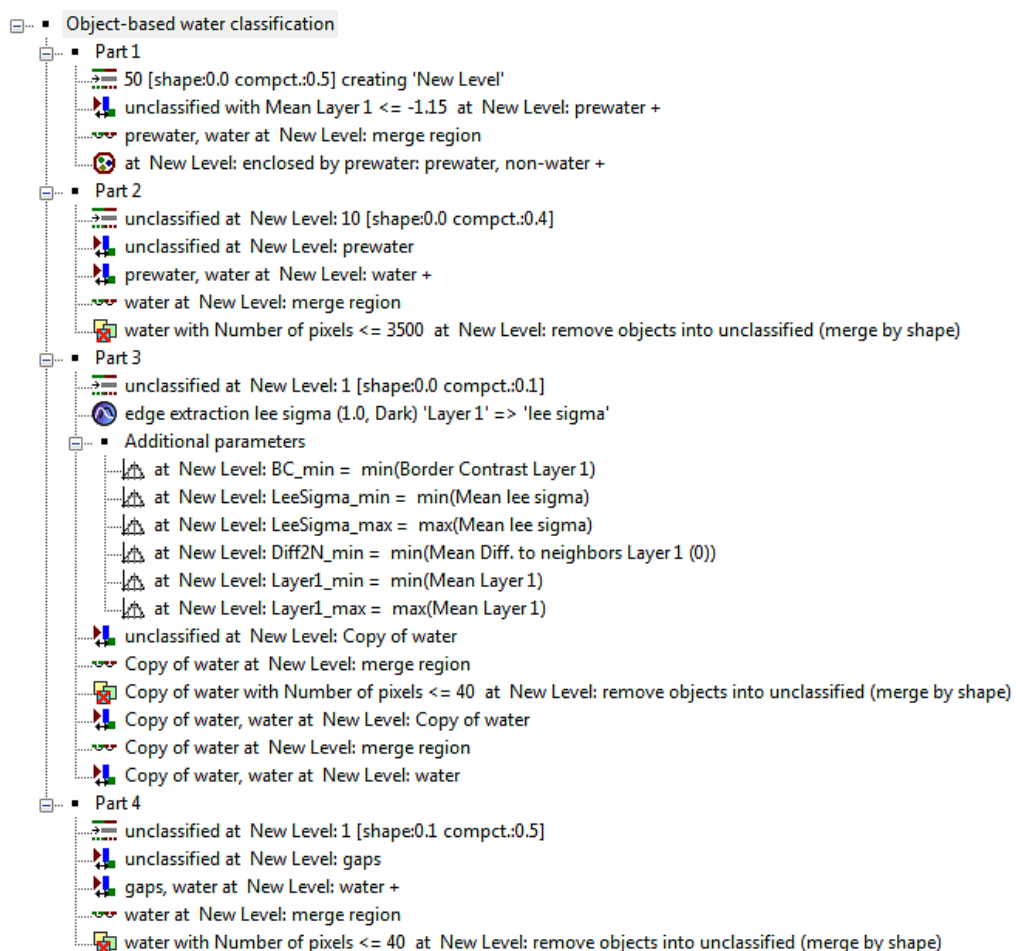


Figure 4-18: Rule set of the object-based water classification.

4.4.1.4.2 Extraction of the tidal channel network and geometric features

A subset of the resulting classification can be seen in Figure 4-19. The parameter *scale*, *shape* and *compactness* of the several multiresolution segmentations and borders of the membership functions are derived through a trial and error process from the image objects.

The analysis of the robustness of the proposed rule set was conducted by applying the rule set to the DEM of 2012 and 2013.

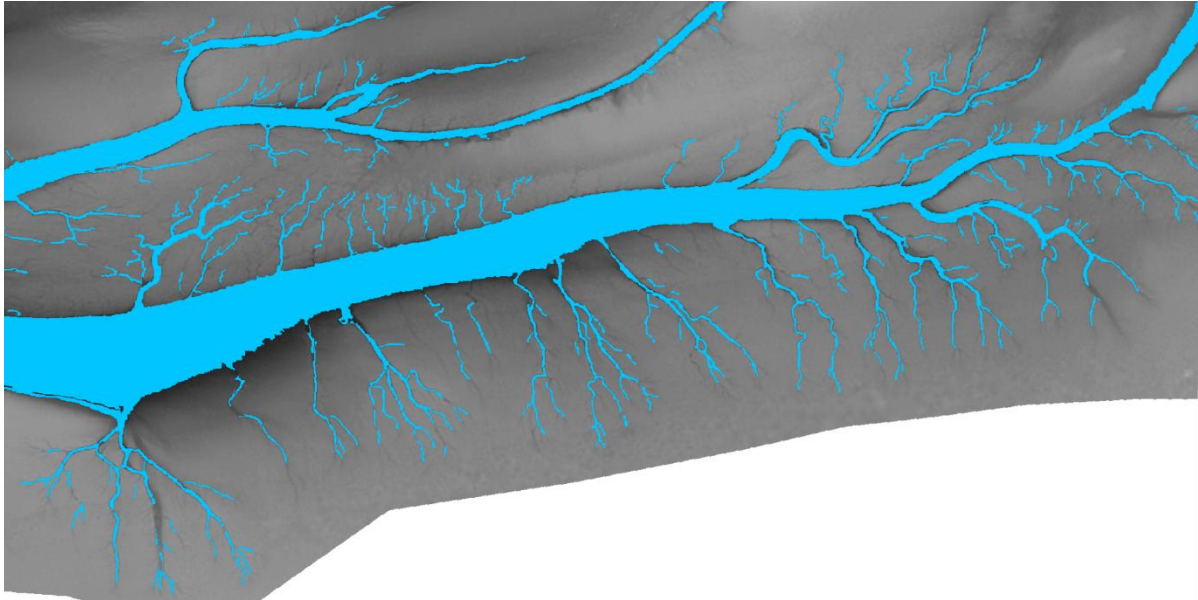


Figure 4-19: Subset of the object-based tidal channel classification result from the LiDAR data of 2010.

4.4.1.4.2 Extraction of the tidal channel network and geometric features

Subsequent to the classification of the tidal channels, an extraction of the tidal channel network as a one-pixel-wide linear structure was carried out. The prior classification acts as a mask to reduce the false channel network estimations. Without this masking, the algorithm would fail in extracting tidal channels, due to the very flat terrain of the Wadden Sea. The algorithm ‘*r.stream.extract*’ from the toolkit ‘*r.stream*’ implemented in the open-source software ‘GRASS GIS’ was applied with the following expressions:

- (1) `g.region -p rast= LiDAR_DEM @mapset`
- (2) `r.stream.extract elevation=LiDAR_DEM@mapset threshold=300 stream_length=3 stream_rast=outputname -overwrite`

The first expression manages the boundary definitions for the geographic region and the second expression performs the extraction of the tidal channel networks (GRASS 2011). ‘GRASS GIS’ was chosen as it is a leading open-source GIS (geographic information system) software and it enables the possibility of processing calculations on very large raster maps that could not be performed simultaneously in memory, since a DEM derived from LiDAR

4.4.1.4.2 Extraction of the tidal channel network and geometric features

data can consist of hundreds of millions of grid cells (Jasiewicz & Metz 2011). The following explanation of the module ‘r.stream.extract’ is a summary of the study from Jasiewicz and Metz (2011), who have developed the module.

The purpose of ‘r.stream.extract’ is the extraction of topologically correct, dendritic stream networks. The algorithm calculates the flow accumulation as the number of cells draining through a current cell using the elevation map as input data. This calculation is done by a hydrological analysis called multiple flow direction method (MFD or FD8) after Holmgren (1994) (GRASS 2014; Jasiewicz & Metz 2011). In general, MFD means that the surface flow (i.e., runoff) of one cell can partially flow between two of the common eight directions (Figure 4-20 plot a)). Hence, the flow is distributed proportionally to the slope gradient in each direction (Figure 4-20 plot d)). In comparison, the one-direction flow method (D8) directs all runoff to the lowest of eight neighbours (Figure 4-20 plot c)). The method D8 results in a narrow flow pattern, where the runoff quickly aggregates into stream shapes and a divergent flow is impossible (Holmgren 1994). The flow proportion for each cell can be calculated as follows:

$$f_i = \frac{(\tan\beta_i)^x}{\sum_{j=1}^8 (\tan\beta_j)^x} \quad \text{for all } \tan\beta > 0 \quad (4-12)$$

where i, j are the possible flow directions (1 – 8), f_i represents the flow proportions between 0 and 1 in direction i , $\tan\beta_i$ is the slope between the central cell and the cell in direction i and x is a variable exponent. If x equals 1, the function represents the MFD method and when $x \rightarrow \infty$ the distribution will move towards D8 (Holmgren 1994). The recommended value for x is 4 – 6, but no statement was made for the module ‘r.stream.extract’, which defines x (ESRI 2014; Holmgren 1994).

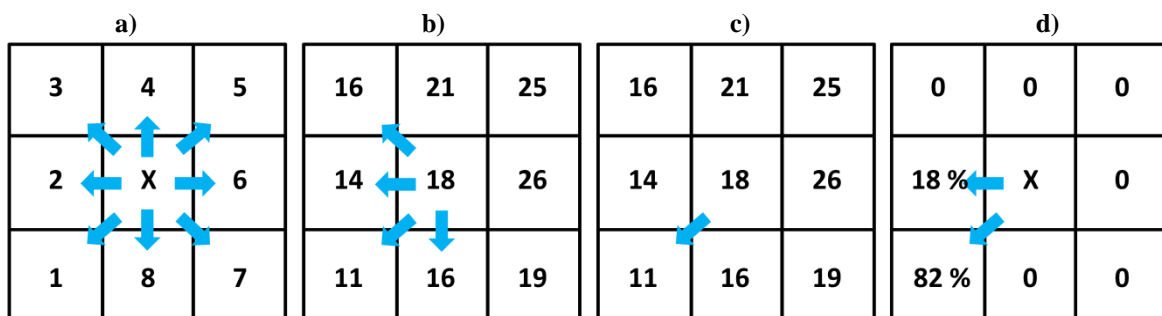


Figure 4-20: Plot a) represents the eight possible flow directions from a grid cell, plot b) is an example for heights of an DEM with the possible downhill directions, plot c) shows the resulting runoff of the D8 method and plot d) shows the resulting runoff of the MFD method (after Holmgren 1994).

After calculating the accumulation map from the elevation raster, the algorithm discriminates between stream initiation and stream tracing. First, it starts with finding sources of stream or stream heads only and does not attempt to find all stream cells. The stream initiation is

4.4.1.4.2 Extraction of the tidal channel network and geometric features

strongly dependent on the local morphology and the spatial heterogeneity of the exposed lithology, vegetation cover or dominating erosional mechanisms, which could lead to a basic map that merely indicates the location of stream heads. To overcome this disadvantage, the module 'r.stream.extract' has the possibility to add additional information such as rainfall, direct field observations or soil moisture (Jasiewicz and Metz 2011). In this study no additional information was available.

Stream tracing follows the main drainage direction, which is determined using flow accumulation and elevation. First, the grid cells are sorted according to elevation using the A^T search algorithm (i.e., least cost search) as per Ehlschlaeger (1989). He derives stream networks from a DEM by computing the shortest paths in a graph, which contains a node for each grid cell of the DEM and an edge for each two adjacent cells. The decision for a path can be based on various parameters such as distance, elevation, the cost of traversing a cell or a combination of criteria organized around a set of rules. In terms of stream network extraction, it is elevation.

An advantage of the module 'r.stream.extract' is the independence of hydrologically conditioned elevation maps, because the search heuristic is very robust in handling depressions (Jasiewicz & Metz 2011). "The main drainage direction is then set for each cell toward the downstream cell with the highest flow accumulation. The initially assigned drainage direction is used as main drainage direction when several downstream cells including the one pointed to by the initial direction share the same highest flow accumulation" (Jasiewicz & Metz 2011). The method is very flexible. If there is insufficient information in the accumulation map to unambiguously determine predominant drainage direction, the module can provide a channel initiation map that is only used to initiate streams and then the elevation map is used to trace streams. The results are always thin, one-cell-wide streams also extracted from broader stream tubes and they are independent of the surface flow accumulation method (e.g., D8, FD8, D-Inf, DEMON, etc.) used. The flow directions are provided in D8 manner (eight principal directions separated by 45° ; Figure 4-20 plot a)), which allows the calculation of other hydrogeomorphological parameters (Jasiewicz & Metz 2011).

The parameter *threshold* of the module 'r.stream.extract' defines the minimum flow accumulation value for initiating a new stream (i.e., determines the number of streams and the detail of the stream network) and the parameter *stream_length* defines the minimum stream length in number of cells for first-order stream segments. If the flow accumulation reaches or exceeds the value for *threshold*, a new stream is initiated and traced down to its outlet point

4.4.1.4.2 Extraction of the tidal channel network and geometric features

(GRASS 2014). Streams are only initiated if all grid cells contributing to the current grid cell have a surface flow accumulation below the given *threshold* and if no other adjacent grid cell has already been identified as an initial stream or stream cell (Jasiewicz and Metz 2011). Smaller *threshold* values create a less diverse channel network with only the bigger channels integrated. Higher values generate several minor tributaries that do not exist in the classification result.

The value for *threshold* was set to 300 and the *stream_length* was set to three. The parameterization has to be done by trial and error, such as the parameterization in the multiresolution segmentation. The stream segments must be longer than three pixels, because this eliminates artefacts generated by the parameter *threshold*. Figure 4-21 shows a subset of the channel network extraction.

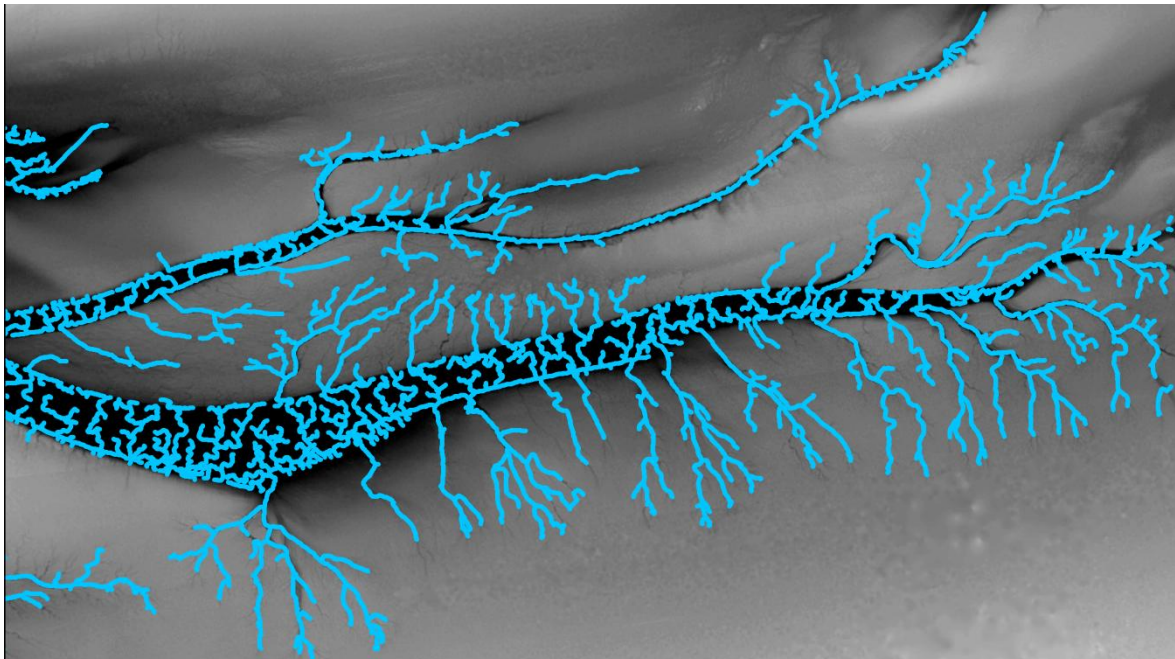


Figure 4-21: Subset of the channel network extraction (blue lines) from the LiDAR data of 2010.

In Figure 4-21 several minor channel networks (i.e., sub-channel stream networks) could be detected (see Figure 4-22). A quantitative estimation of the pattern of the tidal channel distribution within the sub-channel stream networks was carried out by extracting the geometric features (e.g., confluences and flow direction). The geometric properties of these sub-channel stream networks are analysed to define whether muddy sediment or sandy sediment is predominant. In the literature, parameters such as channel density, frequency of change in flow direction and the number of channels in a network are proposed as indicators for the underlying sediment type (Choi et al. 2011). Muddy sediments or mudflats are characterized by a high number of channels that change their flow directions very often (Choi et al. 2011; Eom et al. 2012; Mason et al. 2006). This means that the number of confluences

4.4.1.4.2 Extraction of the tidal channel network and geometric features

and channels, as well as the number of flow direction changes, can be used as indicator of the sediment type. In the further description, the sub-channel stream network at the bottom left corner of Figure 4-22 (light green dashed polygon) will be the example area to represent the developed methodologies used for the extraction of the geometric features.

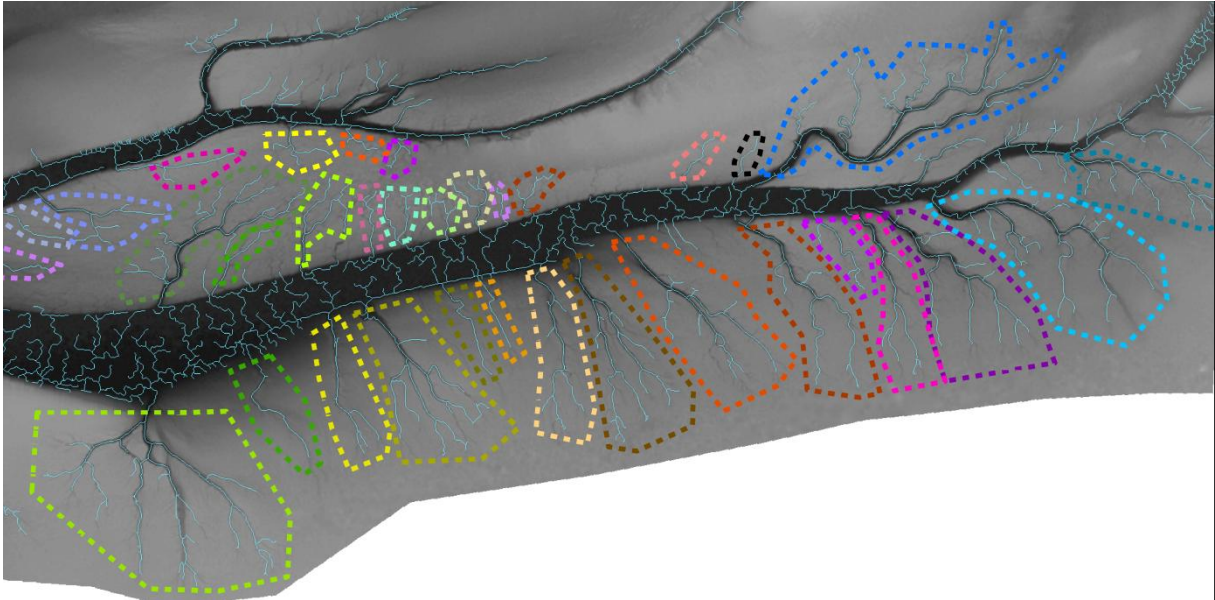


Figure 4-22: Sub-channel stream networks that are detected after the network extraction with 'GRASS GIS'.

In the first algorithm, the number of confluences in a tidal channel network is extracted. Confluences define locations where a tidal channel splits into several – sometimes smaller – tidal channels. To find the confluences, a 3x3 array is used (see Figure 4-23). If the number of stream network pixels is greater than three, then this location is marked as a confluence.

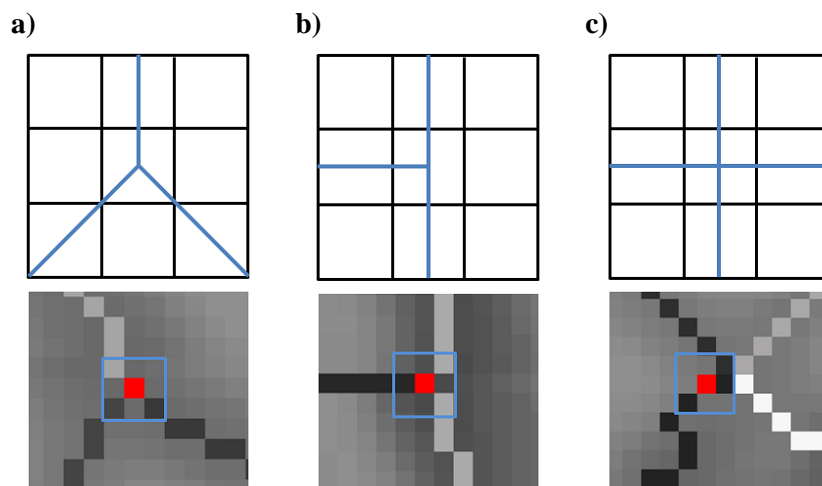


Figure 4-23: Schematic examples of the search for confluences using a 3x3 array. The red square represents a confluence.

Some kinds of confluence can create an error, such as Figure 4-24 illustrates. If they consist of four or more adjacent pixels, the search algorithm finds more than one possible result. To eliminate these redundant confluences, a 5x5 array is used subsequently. This array finds one

4.4.1.4.2 Extraction of the tidal channel network and geometric features

of the redundant confluences and deletes all other confluences in the neighbourhood of a 5x5 pixel array. This might result in the wrong location of the confluence, but the correct location is not of interest in this study. In the following, the number of confluences is used to discriminate mudflat and sand flat.

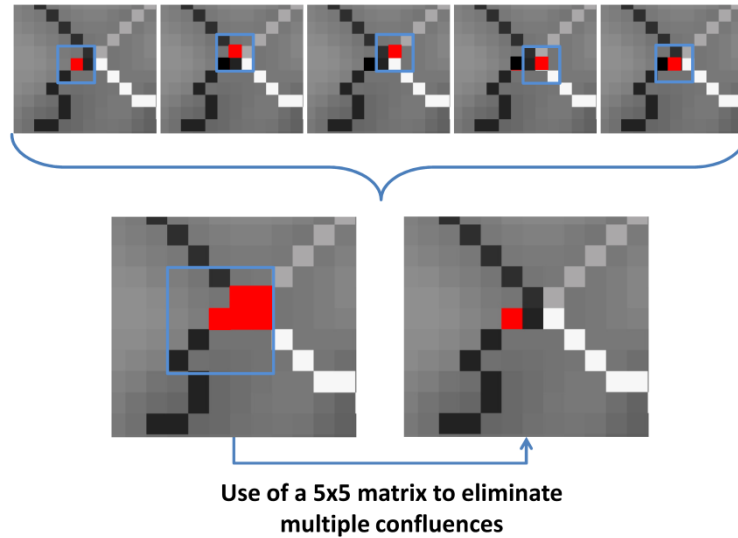


Figure 4-24: Schematic example for the elimination of redundant confluence results.

The second approach is the extraction of the flow direction and its change. First of all, a 3x3 array is used to extract the flow direction of each pixel. The array finds a channel network pixel and examines the direct neighbourhood for other network pixels. These neighbours get a flow direction based on their location in relation to the pixel in the centre of the array. All channel network pixels that already have a direction value are bypassed. Figure 4-25 shows the algorithm in detail for the four possible flow directions.

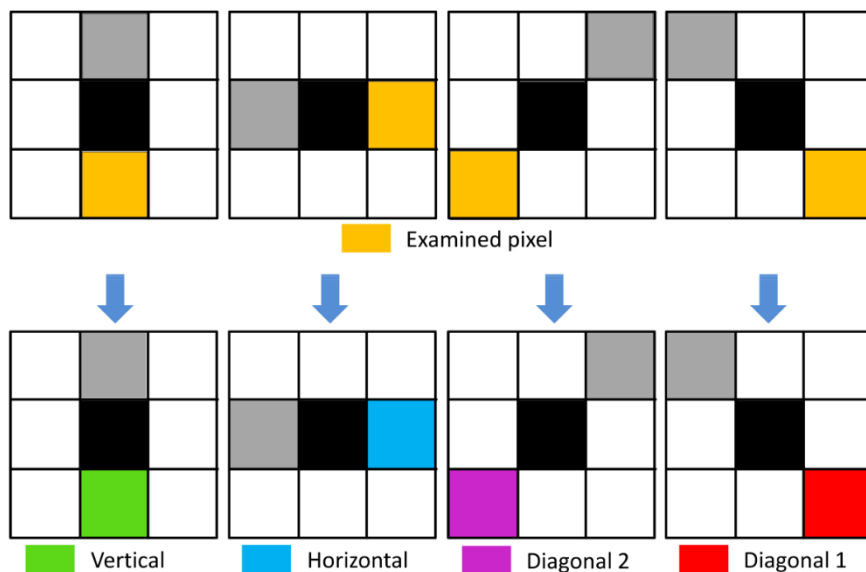


Figure 4-25: Schematic example for the definition of flow direction for every adjacent channel network pixel.

4.4.1.4.2 Extraction of the tidal channel network and geometric features

The grey squares represent the pixels that are bypassed, the black squares are the current channel network pixels that were found and the orange squares are the network pixels found in the neighbourhood. The orange squares are assigned to one of four possible flow directions based on their location in relation to the current network pixel in the centre.

The same method is used to calculate the number of flow direction changes in a sub-channel stream network. However, instead of assigning flow directions, the procedure examines the type of flow direction in the direct neighbourhood (i.e., in a 3x3 array). The examples of Figure 4-25 represent no flow direction changes in comparison with Figure 4-26, which shows four examples of flow direction changes. The orange squares are the current network pixels that are examined. If the adjacent pixels have a different flow direction assigned, then the current network pixel is marked as a flow direction change (black square). If an adjacent pixel is already marked as a flow direction change, then the current network pixel is skipped to avoid a redundant selection of one change.

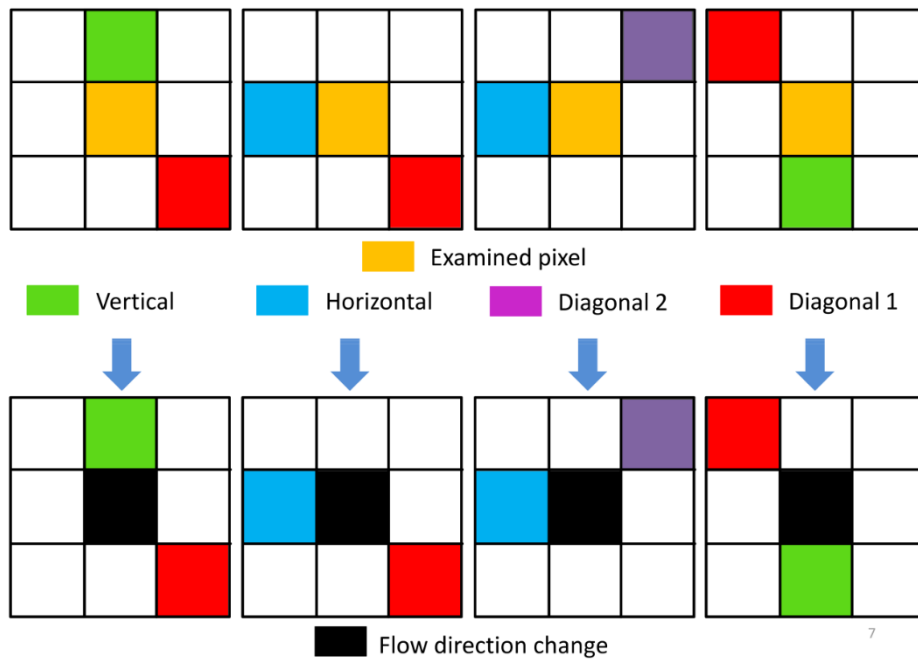


Figure 4-26: Examples of flow direction changes.

Furthermore, the extracted geometric parameters (e.g., the number of confluences and number of flow direction changes) are applied to the following ratios:

$$Ratio_{stream} = \frac{P_{ex}}{N(P_{stream})} \quad (4-13)$$

$$Ratio_{class} = \frac{P_{ex}}{N(P_{class})} \quad (4-14)$$

$$normRatio_{stream} = \frac{|P_{ex} - N(P_{stream})|}{P_{ex} + N(P_{stream})} \quad (4-15)$$

$$normRatio_{class} = \frac{|P_{ex} - N(P_{class})|}{P_{ex} + N(P_{class})} \quad (4-16)$$

4.4.1.4.2 Extraction of the tidal channel network and geometric features

where P_{ex} is an extracted parameter, $N(P_{stream})$ represents the number of pixels of the extracted tidal channel network and $N(P_{class})$ represents the number of pixels of the object-based classification.

To assign whether the sub-channel stream network is located in a muddy area or sandy area, the extracted parameters and ratios are used in a random forest classification (RF). This classification method is described in detail in the next chapter. Altogether, 48 sub-channel stream networks could be identified in the study area (Figure 4-27), some of which are located on mudflats (35) and others are located on sand flats (13). The selection of the areas is based on the result of the stream network extraction (see chapter 5.2.2.4.2). In this context, some sub-channel networks that can be seen in plot a) of Figure 4-27 are not part in the further analysis.

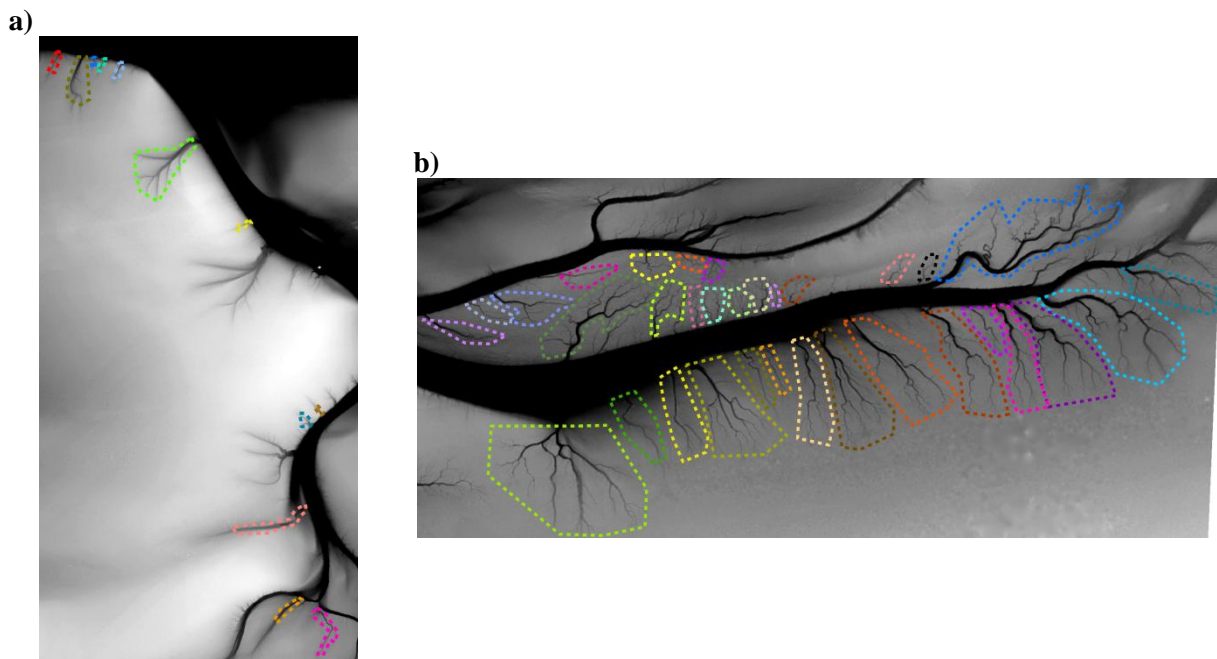


Figure 4-27: Identified sub-channel stream networks for sand flats (plot a) and mudflats (plot b)). One of each sub-channel stream networks for sand flats and mudflats are not shown, because they are out of the chosen subset boundary.

Due to the low sample sizes of 35 and 13, a 20-fold cross-validation was applied. The data was split into two nearly equally sized intervals, one representing the training dataset and the other representing the validation dataset. The selection of the variables for each training dataset takes place randomly. This means that the classification is repeated 20 times with randomly chosen sub-channel stream networks as the training dataset, while the remaining (i.e., not chosen) sub-channel stream networks represent the validation dataset (i.e., with no deletion for generating the next sample). Hence, some data may be used more than once in the training of classifiers and others may never be used. This makes the algorithm more robust when facing slight variations in input data and increases the accuracy at the same time (Cutler

et al. 2007). With this technique the problem of small sample size is reduced (Pudil and Somo 2008). The 20 obtained classification results are eventually averaged to estimate the range of accuracy. Finally, all classifications are condensed by majority voting to one final classification result.

4.4.2 Random Forest

Supervised classification can be used to cluster pixels in a dataset into classes corresponding to user-defined training classes (i.e., regions of interest). These regions of interest (ROI) are the basis for every supervised classification. The quality of the results relies on the validity of the ROI used to define the classes and their statistical separability (Yates et al. 1993; Thomson et al. 1998). Various classification methods, such as parametric supervised methods (e.g., maximum likelihood, mahalanobis distance or minimum distance), non-parametric supervised methods (e.g., parallelepiped or feature space), machine learning algorithms (e.g., artificial neural network, decision trees or support vector machine) and ensembles of classifiers (random forest, bagging and boosting) use those ROIs to determine if a specific pixel will be assigned to a class. Machine learning algorithms are very efficient, because they do not rely on data distribution assumptions (e.g., normal distribution). However, algorithms, such as the artificial neural network (ANN) or the support vector machine (SVM) are complicated due to the large number of adjustable parameters and they tend to overfit the data, unlike random forest (RF). The RF algorithm was developed to increase the classification accuracy and stability of classification trees (Rodriguez-Galiano et al. 2012). In this context, the proposed hierarchical knowledge-based classification method is compared with the common pixel-based, non-parametric, supervised classification called random forest, which was introduced by Breiman (2001), featuring the following advantages:

- Runs efficiently on large data
- Handles thousands of input variables without variable deletion
- Estimates which variables are important in the classification
- Generates an internal unbiased estimate of the generalization error (out-of-bag error)
- Computes proximities between pairs of cases that can be used in locating outliers
- Is relatively robust to noise and outliers
- Exhibits smaller computational complexity than other machine learning algorithms

Rodriguez-Galiano et al. (2012) state as further advantages the non-parametric nature and the high accuracy. Furthermore, it is well suited for classification of multi-source remote sensing and geographical data, including data sources recorded from different measurement scales (Beijma, Comber & Lamb 2014; Timm & McGarigal 2012). In the past, the RF classification has been applied successfully in coastal research (Jhonnerie et al. 2015; Beijma, Comber & Lamb 2014; Liu et al. 2014; Timm & McGarigal 2012), ecological research (Corcoran, Knight & Gallant 2013; Cutler et al. 2007) and land cover mapping (Rodriguez-Galiano et al. 2012; Gislason, Benediktsson & Sveinsson 2006).

A flow chart of the RF algorithm is shown in Figure 4-28. Briefly, RF is based on decision trees and fits a predefined number of them (e.g., 100) to a dataset where each decision tree contributes with a single vote for the assignment of the most frequent class to the input (i.e., majority voting) (Beijma, Comber and Lamb 2014; Rodriguez-Galiano et al. 2012). The algorithm begins by selecting many bootstrap samples from the original data and builds a decision tree for each in an ensemble. About two-thirds of the original data will be included in a bootstrap sample. Bootstrap aggregating resamples randomly the original dataset with replacement (i.e., with no deletion for generating the next sample). As already stated, this makes the algorithm more robust when facing slight variations in input data and increases the accuracy at the same time. The other one-third that is not included is called out-of-bag (OOB) observations and is formed for every bootstrap sample individually (Cutler et al. 2007; Rodriguez-Galiano et al. 2012; Liu et al. 2014). For every bootstrap sample, a classification tree is fitted and at each node a reduced number of randomly selected predictor variables (e.g., usually, and in this case, the square root of the total number of predictor variables) are used for the binary portioning of the classification trees, which simultaneously avoids overfitting of the model (Timm and McGarigal 2012; Waske et al. 2012; Cutler et al. 2007). As a measure for the best split selection, an RF usually (and in this case) uses the Gini index, which measures the impurity of a given element with respect to the rest of the classes (Breiman 2001; Cutler et al. 2007; Rodriguez-Galiano et al. 2012). The splitting process continues until a further subdivision no longer reduces the Gini index (Cutler et al. 2007). Each tree is fully grown and is used to predict its own OOB observations. Finally, all trees are aggregated to one single prediction by majority vote of the OOB predictions for that observation (Cutler et al. 2007; Rodriguez-Galiano et al. 2012; Liu et al. 2014). This implies that the RF algorithm produces multiple classifications of the same data and produces a probability of each class for every observation (Rodriguez-Galiano et al. 2012). Additional details concerning the RF

4.5 Analysis of the spectral discrimination of sediments with spectrometric data

algorithm can be found in Breiman (2001), Cutler et al. (2007), Rodriguez-Galiano et al. (2012) and Liu et al. (2014).

The classifications were performed in the ‘EnMAP Box’, a open source image classification tool developed at the Humboldt University Berlin. This toolbox has a number of in-built classification algorithms, such as RF.

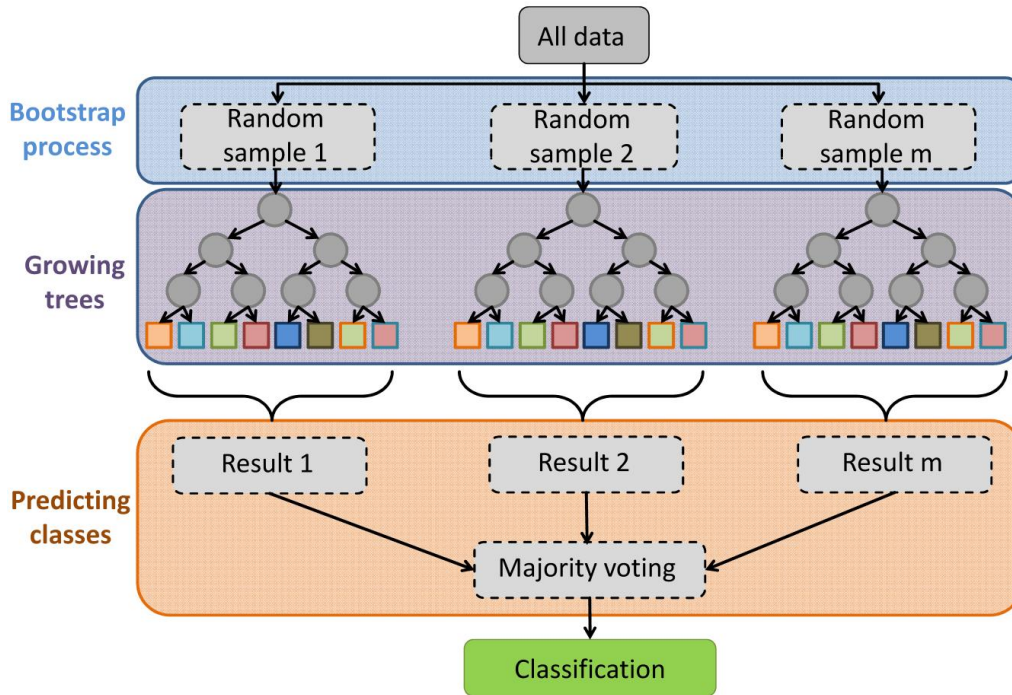


Figure 4-28: Flow chart of the RF algorithm.

4.5 Analysis of the spectral discrimination of sediments with spectrometric data

The spectral resolution of RE is very low (five spectral bands) and thus a detailed analysis of the sediment’s spectra is limited. To overcome this limitation, hyperspectral measurements of a spectrometer are used to estimate whether the sediments can be separated and which spectral wavelengths are necessary. The spectral resolution from visible to infrared regions of the electromagnetic spectrum with hundreds of narrow and contiguous bands (e.g., in this study from 0.35 μm to 2.5 μm with 1,024 spectral bands) enables the hyperspectral sensors to better discriminate among similar ground land cover classes than traditional multispectral sensors (Bajwa et al. 2004; Li et al. 2014; Datta, Ghosh & Ghosh 2014). Hyperspectral data contain information on the reflection, absorption and emission of the targets of certain wavelengths. Their composition and molecular structure enables the characterization and identification of the observed targets from their spectral curve (Clark 1999). Sometimes, different targets have nearly the same spectral curve, which makes discrimination difficult. To

4.5 Analysis of the spectral discrimination of sediments with spectrometric data

find features that can discriminate the two targets while preserving their characteristics is an important step in remote sensing, because the major problem for pattern recognition methods is the huge amount of data involved when processing hyperspectral data. They are sensitive to problems associated with high dimensionality feature spaces (i.e., Hughes phenomenon or curse of dimensionality), since classifications do not always improve beyond tens of bands (Richards 1993; Gomez-Chova et al. 2003; Robnik-Sikonja and Kononenko 2003; Wu et al. 2013; Datta, Ghosh and Ghosh 2014).

Alongside the spectral similarity between two different targets, there also exists a spectral correlation within a spectral curve. Hyperspectral datasets have a very high spectral resolution with narrow and contiguous bands. This leads to high correlation (i.e., spectral redundancy) between adjacent wavelengths (Gomez-Chova et al. 2003; Venkataraman et al. 2006). These redundant bands increase the computing complexity on one side and reduce classification accuracy on the other side (Jia & Richards 1999; Ibrahim et al. 2009; Wu et al. 2013). For the discrimination of two targets, it is desirable to preserve information needed for discrimination while erasing redundant information (e.g., between two spectra and within a spectrum). The contrast of reducing dimensionality without sacrificing the discriminating power among pattern classes, along with finding the feature vectors, has been studied extensively in the last decades (Benediktsson et al. 1995; Benediktsson & Sveinsson 1997; Choi & Lee 2001; Gomez-Chova et al. 2003; Verpoorter et al. 2014; Li et al. 2014; Datta, Ghosh & Ghosh 2014).

In the literature, feature extraction and feature selection are often employed for band decorrelation and dimensionality reduction (Pudil, Novovicova & Kittler 1994; Serpico & Bruzzone 2001; Kavzoglu & Mather 2002; Lee & Landgrebe 2003; Li, Zhang & Ogihara 2004; Kuo & Landgrebe 2004; Pal 2006). The aim of dimensionality reduction is to find a set of new features (d) based on the input set of D features (if possible $d < D$), so as to maximize (or minimize) an adopted criterion. Wu et al. (2013) and Datta, Ghosh & Ghosh (2014) give a good review of unsupervised band selection techniques. Both (extraction and selection) can be viewed as finding a set of vectors that represent an observation while reducing dimensionality. Feature extraction finds a transformation from higher dimensional feature space to a lower dimension feature space (ignoring the loss of originality of the data), whereas feature selection identifies a small subset of variables that ideally is necessary and sufficient to describe the target concept with respect to certain criteria (Richards 1993; Gomez-Chova et al. 2003; Li et al. 2014; Datta, Ghosh & Ghosh 2014). A drawback of feature extraction for this study is the transformation into a 'non-real' system. The specific features that give the

most contribution to the transformation are not traceable and thus the wavelengths that are most informative are not directly known. However, feature selection removes non-useful information, improves computational efficiency and can improve classification accuracy (Ibrahim et al. 2009). The main risk of both methods is the loss of information if the feature selection is wrong. The choice between feature extraction and feature selection depends on the application domain and the specific available training data.

In comparison with hyperspectral data, the application of best band algorithms to multispectral images is not a problem. They are typically neither contiguous nor do they possess spectral resolution equivalent to that of hyperspectral sensors. An exhaustive test of all band combinations is acceptable to verify the band selection algorithm since the spectral resolution is low (e.g., up to 11 bands). However, this method cannot be adapted to hyperspectral data (Venkataraman et al. 2006).

To make a decision on which features to preserve and which to discard, a reliable and efficient method for analysing their relevance is needed. Due to this importance, two different feature selection methods for extracting the necessary wavelengths while preserving the relevant information for posterior sediment classification are compared. Feature selection methods were chosen, since they have several advantages:

- Data transmission (only selected bands to be transmitted)
- Interpretability of the results (selected feature are spectral bands with physical meaning)
- Extrapolation of the results to other spectrometers or hyperspectral sensors

4.5.1 Jeffries-Matusita distance feature selection

The first method was developed within this study and is called 'Jeffries-Matusita Distance based feature selection' (JMDFS). According to Wu et al. (2013) and Datta, Ghosh & Ghosh (2014), the proposed method is a filter-based supervised band elimination technique. The basic idea is that if the spectra become more different from each other (i.e., less correlated), they are easier to discriminate. It is reasonable, therefore, to select as the feature space that subspace of the pattern in representation space in which the classes are the most discriminated. In general, the algorithm represents a reduction strategy that eliminates redundant information by means of local Euclidean distance (ED) between two vectors (i.e., classes or spectra) and a subsequent selection of the most discriminative features based on the

Jeffries-Matusita distance (JMD). The JMD is a transformation of the Bhattacharyya distance (α) from range $[0, \text{inf.}]$ to the fixed range $[0, 2]$.

$$JMD = \sqrt{2(1 - e^{-\alpha})} \quad (4-17)$$

in which

$$\alpha = \frac{1}{8}(\mu_i - \mu_j)^t \left\{ \frac{\Sigma_i + \Sigma_j}{2} \right\}^{-1} (\mu_i - \mu_j) + \frac{1}{2} \ln \left\{ \frac{|\Sigma_i + \Sigma_j|}{|\Sigma_i|^{1/2} |\Sigma_j|^{1/2}} \right\} \quad (4-18)$$

where μ_i and Σ_i are the mean vector and covariance matrix of class i , respectively (Bhattacharyya 1943). The principle of α can be simply described as follows: it increases with increasing the distance of class mean values and with decreasing the class variance. The JMD is a feature similarity measure and calculates the distance between a pair of probability functions and indicates the average distance between the two class density functions (Venkataraman et al. 2006; Richards 1993; Swain & Davis 1978). The JMD is normalized between zero and two which indicates either no separability or high separability, respectively (Richards 1993). A value of two implies that the within-group difference is smaller than the between-group difference. In order to find the best feature set (i.e., wavelengths) an iterative process searches the whole feature space to optimize the JMD using the smallest Euclidean distance of a wavelength pair. During each iteration the algorithm finds the wavelength pair with the smallest Euclidean distance and eliminates them from the set of wavelengths (i.e., reducing dimensionality). Afterwards, the JMD is calculated for the dimensionally reduced vectors. This procedure will be repeated until one of the stopping criteria is achieved. The selection approach belongs to the sequential backward selection methods (Pudil and Somo 2008). In this study the following stopping criteria are chosen (see Figure 4-29):

- JMD is greater than or equal to 1.9 (Exelis VIS 2015c)
- Fewer than four bands are left in the iteration process (BNR)

The parameter JMD was chosen, because it is robust against both the mean and covariance differences (Choi and Lee 2001). No statements or explanations are made in the literature regarding the JMD value at which two vectors are discriminable. Two references were found, with one stating a value greater than or equal to 1.8 as the best threshold (Ibrahim and Monbaliu 2010), with the other stating 1.9 as the best threshold (Exelis VIS 2015c). Neither discusses why they choose this threshold or even gives an explanation. Due to the higher probability of discrimination, which is the aim of this method, the threshold 1.9 was chosen. If the second criterion (BNR) is achieved, a discrimination of the two vectors can be neglected.

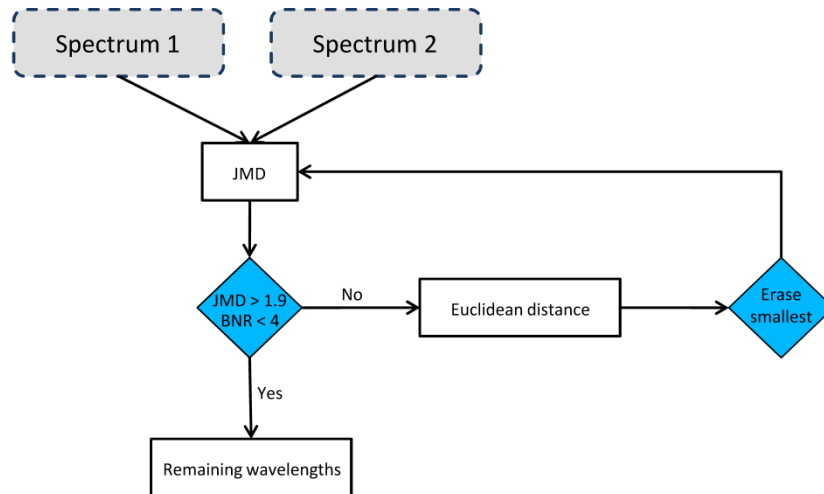


Figure 4-29: Stepwise execution of the ‘Jeffries-Matusita distance feature selection’ algorithm with the stopping criteria Jeffries-Matusita distance (JMD) and the number of bands left (BNR).

The remaining wavelengths and the resulting JMD for each comparison are illustrated in a separate plot for analysis. These plots show whether there are any common bands that can be used to separate the sediment’s spectra from each other. Figure 4-30 shows two plots for two contrary results, as an example. Plot a) represents the actual spectrum (black and bold dashed line) that is compared with all the others. In this example it is spectrum four. The remaining wavelengths of the JMDFS method are displayed by the black dots. Due to the high spectral resolution, the black dots look like a black line in many cases. The blue dashed lines are the wavelengths of the RE bands for comparison. This should help to estimate whether the RE bands are suitable for the discrimination of the sediments or not. Plot b) shows an artificial result, if common bands are found. It can be seen that, in every comparison, the wavelengths between 550nm, 1,000nm, 1,400nm and 2,000nm remained. This would indicate a wavelength range (red dots/lines) that is specific for discriminating the actual spectrum from all other sediment spectra. The analysis of the plots for all combinations showed that no common wavelengths exist (e.g., plot a)) that can be used to discriminate all spectra. In this context, a second analysis was carried out, which is described in chapter 5.3.

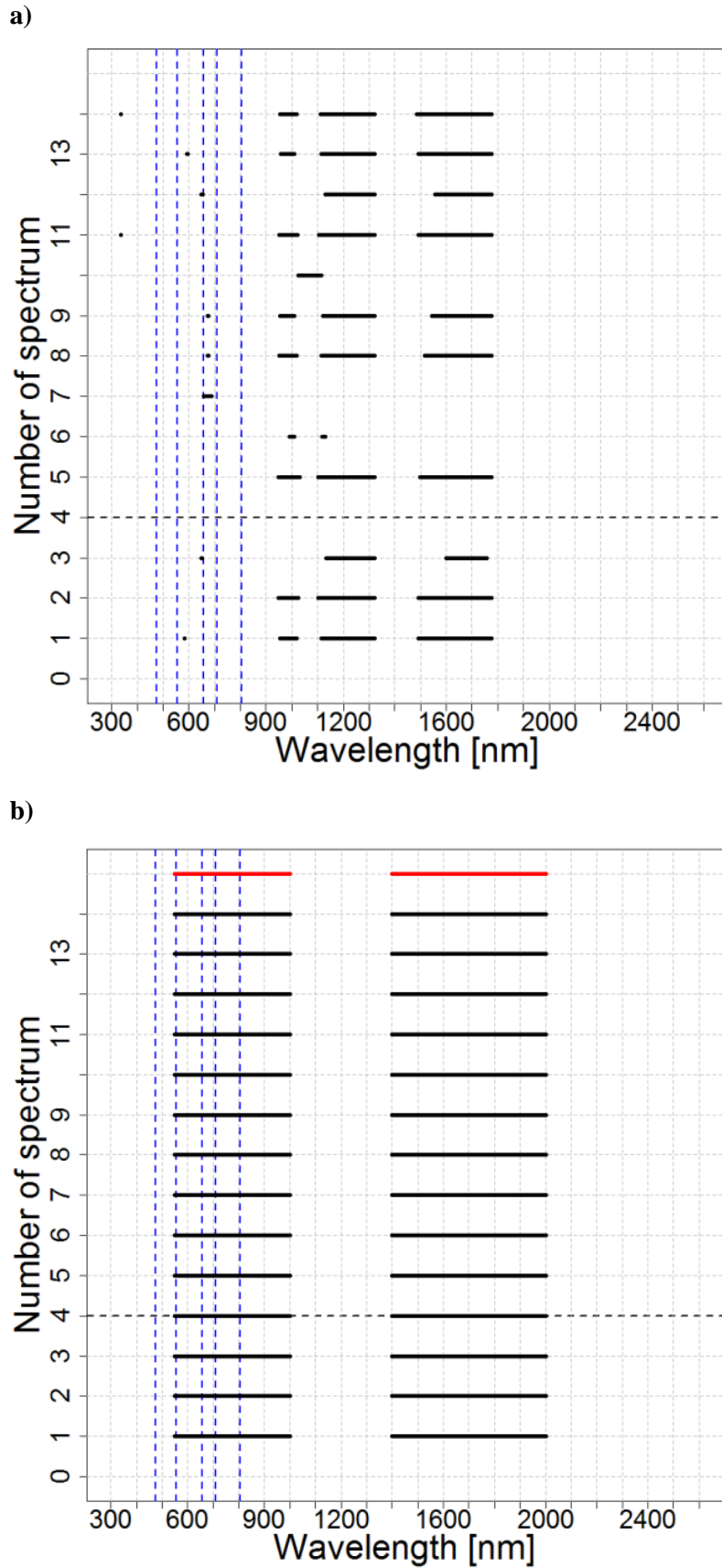


Figure 4-30: A result of the ‘Jeffries-Matusita Distance feature selection’ of 2015 (plot a)) and an artificial result (plot b)) in comparison. The horizontal black and bold dashed line is the actual spectrum that is compared with all the others, the black dots/lines represent the remaining wavelengths, the vertical blue dashed lines represent the wavelength of RE and the red dots/lines of plot b) are the resulting common wavelengths.

4.5.2 ReliefF

The second feature selection method is called ReliefF and is an implementation in the software ‘R Statistics’ (package ‘FSelector’). It was chosen because it is a popular state-of-the-art approach, which is part of many comparative studies of feature selection methods (Pudil and Somo 2008; Wu et al. 2013; Datta, Ghosh and Ghosh 2014). The following paragraph is a summary of the study of Robnik-Sikonja and Kononenko (2003), which describes the ‘ReliefF’ algorithm in detail. Other studies, such as Wu et al. (2013) or Datta, Ghosh and Ghosh (2014), also refer to this study and therefore only one reference is used for the description of the algorithm.

Relief algorithms (Relief, ReliefF and RReliefF) belong to the filter approaches in the feature selection domain. They are a general and successful feature estimator, which detects dependencies between features and can be used in regression and classification issues. It can exploit information locally, taking the context into account and providing the global view. In comparison with the majority of heuristic measures for feature selection, they do not assume the conditional independence of features. This means that they are more appropriate for problems that possibly involve much feature interaction. Regardless of the contextual information, they are efficient and can correctly estimate features in problems with strong dependencies between features. They are widely used in pre-processing steps before a model is learned, in decision or regression tree learning and in inductive logic programming. The algorithm ‘ReliefF’ itself can deal with multiclass problems and is an extension of the algorithm ‘Relief’, which is limited to two-class problems. It can even handle noisy and incomplete data. The basic idea of ‘ReliefF’ is to randomly select a class R and find k nearest neighbours of the same class H (nearest hits) and k nearest neighbours from each of the different classes M (nearest misses). The number of nearest neighbours k is defined by the user, controls the locality of the estimates and ensures greater robustness of the algorithm concerning noise. For all features F the quality estimation $W(F)$ is updated in the following way: if a feature F can be used to separate R from H , although they belong to the same class, then the quality estimation $W(F)$ is decreased. On the contrary, if a feature F can be used to separate R from M , then the quality estimation $W(F)$ is increased. The contribution of all the hits and all the misses is averaged and weighted with the *a priori* probability of the class. This procedure is repeated m times, where m is a user-defined parameter. Summarizing this to a short statement, the algorithm rewards features F for not separating similar classes and

punishes features F for not separating different classes. The outputs are weights indicating the importance of each feature.

Robnik-Sikonja and Kononenko (2003) stated in their study that the neighbours count can be safely set to 10 for most purposes, but in general it is problem dependent. If the value for the neighbours count goes too high, then the positive and negative updates of the quality estimation $W(F)$ become equiprobable and $W(F)$ reaches zero. The informative features become indistinguishable from the unimportant features. The number of iterations should be set between 20 and 50, while further iterations will always refine the estimates. They also state that the number of iterations is problem dependent.

Wu et al. 2013 summarizes the algorithm in the following equation:

$$R_f(x_i) = \frac{1}{m} \sum_{t=1}^m \left\{ -\frac{1}{k} \sum_{x_i \in H(y)} \text{diff}(x_{t,i}, x_{j,i}) + \sum_{x_j \in M(x_i,y)} \frac{P(y)}{k(1-P(y_i))} \text{diff}(x_{t,i}, x_{j,i}) \right\} \quad (4-19)$$

where R_f is the score of x_i , y_i is the class label of the sample x_t and $P(y)$ is the probability of the sample being from class y . The parameter $x_{t,i}$ denotes the values of x_t on feature x_i and $\text{diff}()$ is the function used to calculate the differences between $x_{t,i}$ and $x_{j,i}$. The number of nearest neighbours in $H(x_i,y)$ and $M(x_i,y)$ is pre-defined by k .

As already mentioned above, the feature selection method ‘ReliefF’ was implemented in the software ‘R Statistics’. Next to the spectrometric data, the algorithm requires a ‘sample size’ (i.e., m) and the ‘neighbours.count’ (i.e., k nearest neighbours of H and M), which were set to the overall sample size of the spectrometric data (e.g., 50 and 45) and to the smallest sample size (e.g., two and three) (Wu et al. 2013). According to Robnik-Sikonja and Kononenko (2003) and Wu et al. (2013), a value of 10 for the ‘neighbours.count’ would give good results, but due to the low sample size of some classes, the value was set to two and three, respectively. Because of the nature of ReliefF (randomly selecting a class R), the method was applied 50 times and the mean of all resulting weights was used for selecting the most important wavelengths for discriminating sediment spectra.

4.5.3 Selection of the most important wavelengths

The land cover class names for the feature selection and later classifications are listed in Table 4-5 (location can be seen in Figure 3-6). The names represent the composition of the land cover, while the numbers (i.e., 15 or 75) represent the coverage of microalgae in percentage in terms of 1m^2 . For instance, ‘Sand_Microalgae15_water_covered’ means there was sand covered by 15% of microalgae and it is completely covered by a water layer of minimum 2cm. The feature selection method ‘JMDFS’ needs the averaged spectra of each class as input

4.5.3 Selection of the most important wavelengths

(i.e., 14 different spectra), whereas the method ‘RelieFF’ uses all measured spectra of the 14 classes (i.e., 50 and 45 different spectra) (see Figure 4-31).

Table 4-5: Class ID's and class names for the spectrometer data of 2013 and 2015.

ID	2013	Sample size	2015	Sample size
C1	Mix_Greenalgae	3	Sand_dry	3
C2	Mix_Seagrass	3	Mud_wet	3
C3	Mix_Shellfish_Brownalgae	3	Sand_Seagrass_dry	3
C4	Mix_water_covered	3	Sand_Microalgae15_water_covered	3
C5	Sand	2	Mix_wet	6
C6	Sand_Schill	3	Mix_Microalgae15_water_covered	3
C7	Sand_Seagrass_dry	3	Mud_Microalgae75_water_covered	3
C8	Sand_water_covered	3	Mud_Microalgae100	3
C9	Sand_wet	2	Mud_Microalgae75	3
C10	Mud	10	Mud_Microalgae15_water_covered	3
C11	Mud_Macroalgae	3	Sand_Macroalgae_dry	3
C12	Mud_Schill	3	Sand_Seagrass_very_dry	3
C13	Mud_Shellfish	6	Sand_very_dry	3
C14	Mud_wet	3	Mud_very_dry	3
	Overall	50		45

Figure 4-31 shows the extended flow chart of the spectrometric data methodology. The pre-processed spectra were transformed to a synthetic image that is later classified with the remaining wavelengths for each feature selection method. Every measured spectrum represents one pixel in the image, resulting in a 10x5 pixel and a 9x5 pixel-sized image for 2013 and 2015, respectively. Spatial information was not taken into account to build the synthetic data. This means that the pixel was only described by its reflectance value per spectral band without considering the effect of neighbouring pixels. The number of bands varies depending on the feature selection result. In the classification process, 14 different classes from 2013 and 2015 were considered (see Table 4-5).

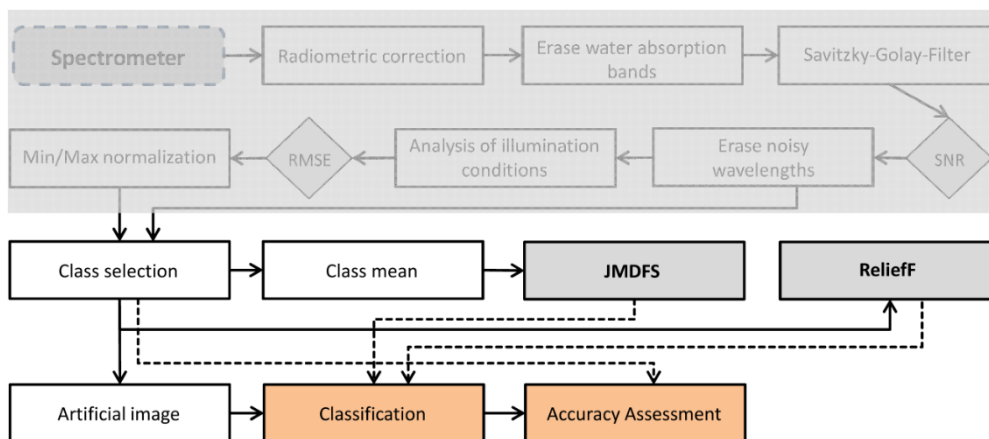


Figure 4-31: Extended flow chart for the methodology of the spectrometric data. The first part (pre-processing), which was already discussed in Figure 4-6, is greyed out.

Due to the low sample size for each class (see Table 4-5), a separation into a training-set and validation-set was very difficult. Since the majority of the classes have three samples, a three-fold cross-validation was applied. In three-fold cross-validation, the data is split into three equally sized intervals (i.e., one sample). The classification is repeated three times with two data intervals (i.e., two samples or two pixels) used for training and one for validation (each interval used once for validation during the three classifications). The three obtained classification results are eventually averaged to get the final result. With this technique the problem of small sample size is reduced. Most of the data are used as a training dataset to obtain better classification accuracies. There are some exceptions for the two given datasets: in the case of class 'C5' and 'C9' of 2013, only one sample is used as a training and validation dataset. For class 'C10' and 'C13' of 2013, six or four randomly chosen samples result in an interval. In the dataset of 2015, only class 'C5' has a different interval of four randomly chosen samples for the training dataset.

The resulting training and validation datasets are applied to the popular state-of-the-art classification algorithm RF. The 'EnMAP box' requires some parameters, such as the number of trees, the number of features (i.e., reduced number of randomly selected predictor variables) and the impurity function (e.g., Gini index). Due to the proposed number of trees in the literature ranging from 100 – 500 (Jhonnerie et al. 2015; Rodriguez-Galiano et al. 2012; Timm & McGarigal 2012; Waske et al. 2012; Breiman 2001), the out-of-bag-Accuracy for every classification and 500 trees was analysed. The out-of-bag-Accuracy is a plot that can be generated in the 'EnMAP box' and which shows the accuracies of the OOB predictions changing with increasing number of trees. The accuracies of all classifications did not increase significantly after 100 trees. Hence, the number of trees was set to 100 for the eventual classifications. With respect to Breiman (2001), Cutler et al. (2007) and Rodriguez-Galiano et al. (2012), the Gini index was used as an impurity function.

The input data for the classifications are on the one hand all pre-processed wavelengths (e.g., 703 bands) and on the other hand the results of the feature selection methods. To select the most important features from the results of the feature selection methods, two approaches are applied. The first approach, called 'peaks', uses all local peaks and the second approach, called 'ranges', defines ranges of wavelengths. Both approaches are illustrated in Figure 4-32 and Figure 4-33 shows two examples. Local peaks mean that wavelengths were chosen where the importance increases to a local maximum, regardless of the global importance. The approach 'ranges' uses the local peaks and searches from this location the nearest local minimum. The distance between the local peak and the nearest local minimum is divided by

two and represents the range that is added and subtracted from the local peak to obtain a range of wavelengths.

The classification results are validated with the help of two performance measures, which are the overall accuracy and the Kappa coefficient. The classes of Table 4-5 are used as reference data.

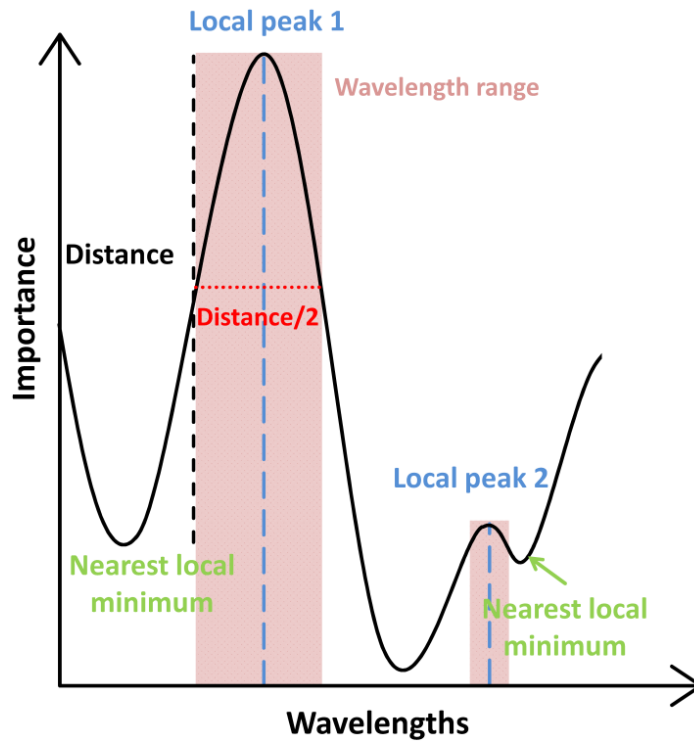
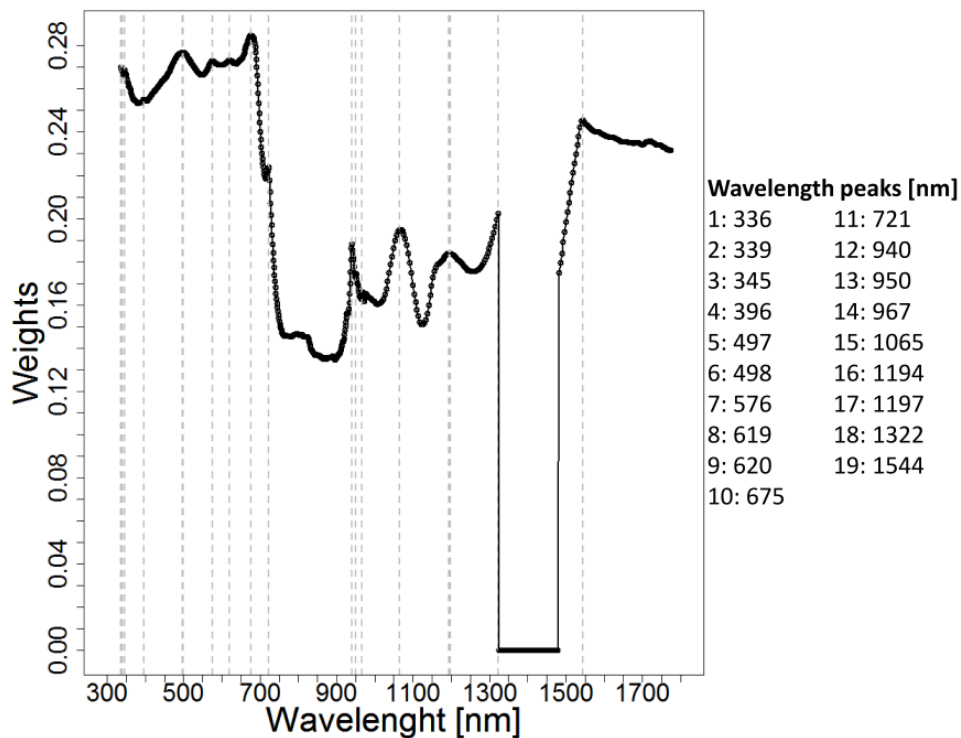


Figure 4-32: Schematic example for the two wavelength selection approaches ‘peaks’ and ‘ranges’.

a) 2013 ReliefF ‘peaks’



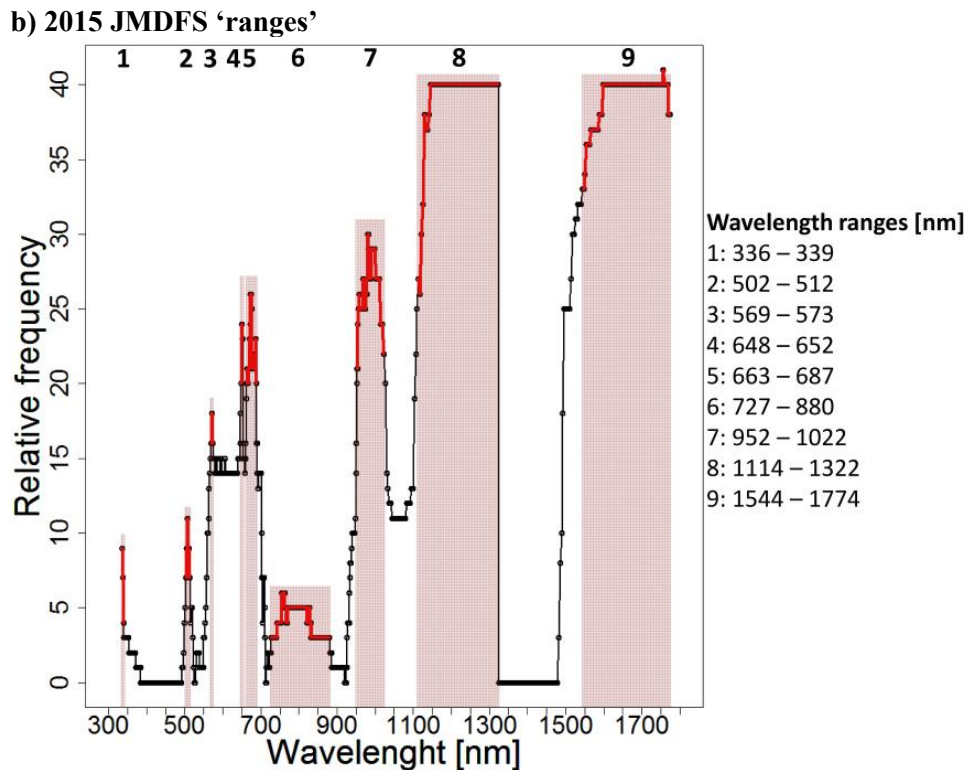


Figure 4-33: Two examples for obtaining the most important wavelengths from both feature selection methods (JMDFS and ReliefF). Plot a) represents the method ‘peaks’ and plot b) represents the method ‘ranges’. The obtained wavelengths are displayed next to the plots.

4.6 Summary

In this chapter, the land cover classes were described and their ecological value was discussed. Furthermore, the data pre-processing, classification approaches, feature selection methods and initial results were introduced. The flow chart of the hierarchical knowledge-based classification can be seen in Figure 4-9. It was shown how the various satellite datasets were used to estimate the land cover in the study area. The land cover water, sediments and tidal vegetation are classified with RE data, shellfish beds will be estimated with the backscatter intensity of TSX and the geometric information, extracted from the LiDAR data, is applied to improve the sediment classification. A new feature selection method (JMDFS) for hyperspectral data was proposed in chapter 4.5.1 (Figure 4-29). Two different methods of extracting the most important features from the feature selection methods were introduced. Additionally, a popular state-of-the-art classification method (RF) and a selection feature method (ReliefF) were described, which will be used as reference in the validation process.

5 Results

5.1 Data pre-processing

5.1.1 RapidEye

The image of 27 June 2011, exhibited the strongest influence of artefacts and noise in all bands. The artefacts appear periodically over the whole image and can be seen equally in all bands. This striped texture is part of the image noise that occurs in the blue band over dark and homogenous areas. This effect is well known and cannot be prevented (Black Bridge, Email). For this reason, we selected the blue band for the comparison of the original dataset with the result of the FFT-based filtering and the MNF transformation. A subset of the blue band is represented in Figure 5-1, which shows the efficiency of the filter process by comparing the subset of the original satellite data with the results of the transformations. The subset is located in the western part of the large tidal inlet.

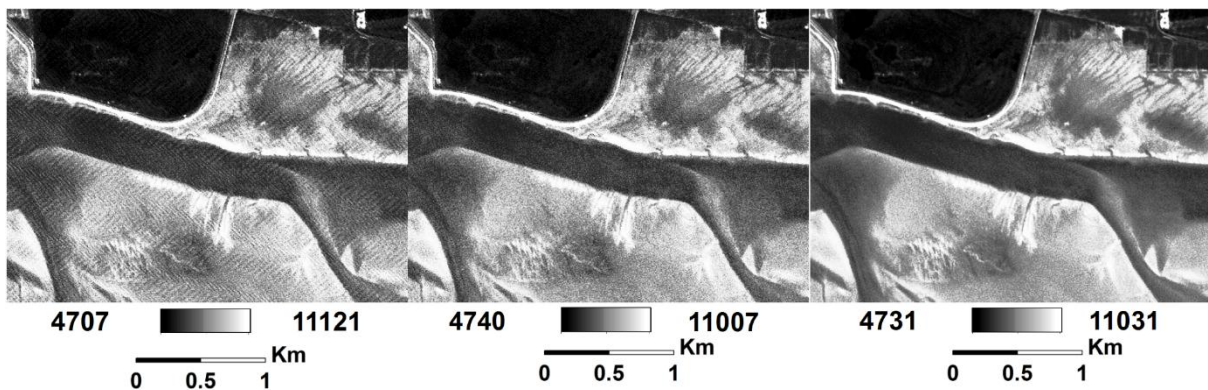


Figure 5-1: The original RE image with noise and artefacts (left), the result of the Fourier transform based filter (centre) and the result after the MNF transform (right).

With the FFT transformation, the artefacts were completely erased over the entire subset and the entire study area. Nevertheless, there remained high spectral variability in the image which was visible in the water channel in the upper part of the subset. A subsequent MNF transformation produced a more homogenous appearance (Figure 5-1). Water is expected to be the most homogenous image class with respect to the spectral features in the study area and should therefore have the lowest standard deviation (stdev) and SNR. The SNR was carried out by applying the calculation of Stoehr (2007) and Stoehr et al. (2008). Table 5-1 lists the stdev and SNR values of the original data after FFT and after the MNF transform for an area of deep water (13,560 m²). Deep water defines an area of water within a channel with a water column deep enough such that the underlying terrain does not influence the spectral signal. The results confirmed the positive effects of the radiometric pre-processing methods applied

indicated by the stdev and SNR (Stoehr 2007; Stoehr et al. 2008). The strongest improvements appeared in the first three bands. As expected, the NIR band and the Red Edge band show only slight improvement. Nevertheless, the calculated stdev still seem higher than expected for a homogenous area such as water. This is related to the properties of the water in the channels, being enriched with algae, suspended matter, phytoplankton and other organic and inorganic matter, as well as its movement, which leads to fluctuating spectral signals. Nevertheless, the decreasing stdev and increasing SNR indicate an improvement in radiometric quality. The spectral variability from the original bands is significantly reduced by the pre-processing algorithm.

Table 5-1: Radiometric improvement with the decrease of the heterogeneity of the pixel values in a water polygon of the RE image from 27 June 2011.

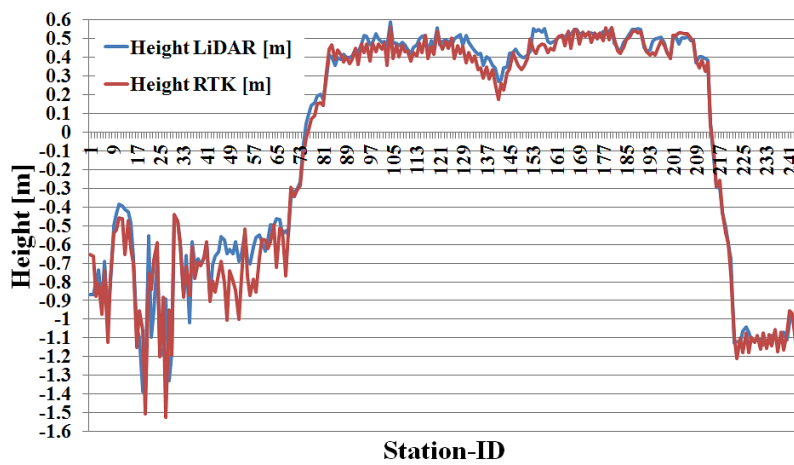
<i>Water</i>	Original RE data		FFT		MNF	
Band	Stdev [DN]	SNR [dB]	Stdev[DN]	SNR [dB]	Stdev[DN]	SNR [dB]
Blue	171.62	16.04	130.67	17.01	69.35	19.97
Green	112.3	16.93	105.72	16.93	55.46	19.37
Red	71.76	16.94	68.23	16.75	61.47	17.33
Red-Edge	86.5	14.14	84.83	14.3	82.35	14.14
NIR	51.3	14.09	47.45	14.45	51.27	13.99

5.1.2 LiDAR

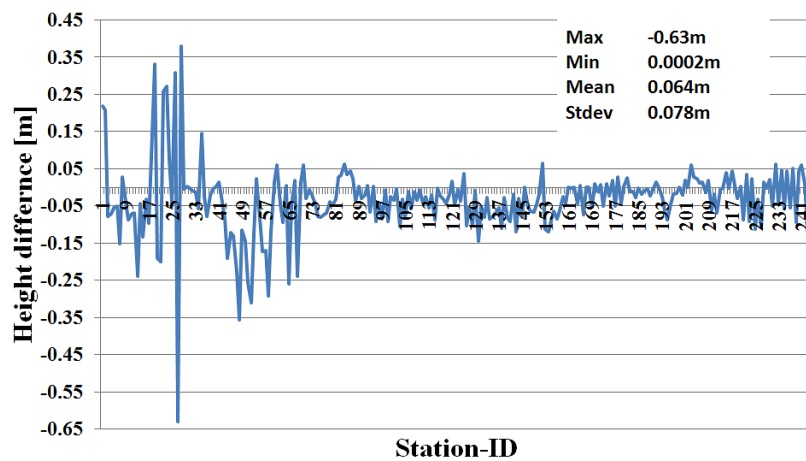
For the LiDAR data of 2010, 2012 and 2013, no reference data were available. Due to this, a numerical comparison (e.g., difference, RMSE and R^2) of RTK measurements from 2012 with a DEM, derived from LiDAR data of 2012 using the method explained in chapter 4.3.3, was carried out. Plots a)-c) of Figure 5-2 show the direct comparison of the height values, the difference in statistical parameters and the result of the linear regression with R^2 and the RMSE. It can be seen that the height values of the DEM are slightly higher at most of the stations. The differences are vary from a maximum of -63cm to a minimum of 0.02cm with a mean of 6.4cm and a stdev of 7.8cm. Except for a few outliers, all differences are lower than 15cm. These outliers are located in or near intertidal creeks, which are filled with water or influenced by water. A LiDAR system using near-infrared laser pulses cannot penetrate water, as already mentioned in chapter 3.4. In this context, high differences between the RTK measurements (under water) and the LiDAR measurement have to be expected at such locations. Minor differences can be a result of the time gap between both measurements, due to the highly dynamic environment. This means that the derived height values from the

LiDAR data are, basically, very precise, which is also confirmed by the R^2 of 0.97 and the RMSE of 0.101.

a)



b)



c)

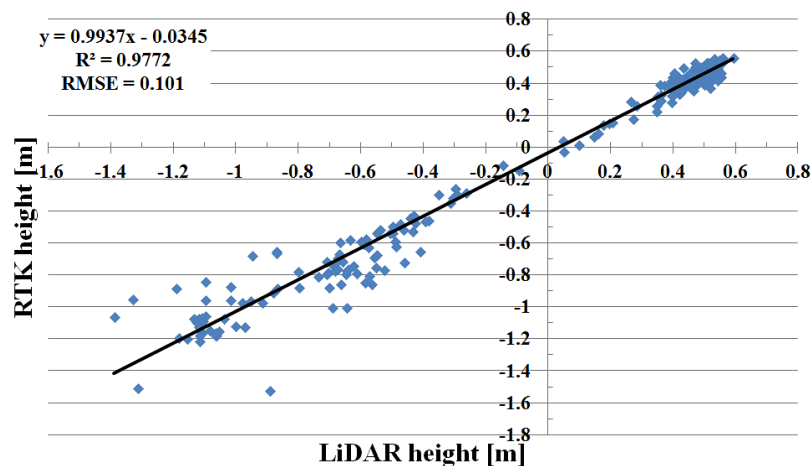


Figure 5-2: Comparison of the height values derived from the LiDAR data of 2012 with the RTK measurements of 2012. Plot a) shows the height values for both measurements, plot b) represents the difference in height and plot c) shows the accordance using a linear regression.

5.2 Classifications

5.2.1 Evaluation methods

In order to evaluate the effectiveness of the proposed methods for the classifications of the land cover types and the water coverage in tidal flats, the results obtained are compared with reference data, if available. The reference data are either part of the ground truth data of chapter 3.6 or were specifically digitized (e.g., seagrass). The evaluation is performed for each land cover type using the described methods. The accuracy assessment of the classification is carried out at the pixel level and is displayed in terms of a confusion matrix. A confusion matrix is a simple cross-tabulation of the mapped class label against reference data (i.e., ground truth data) for a sample of cases at specific locations. Such a matrix can help to display interclass confusion that could be resolved with the use of additional discriminatory information (Foody 2002). To assess the accuracy of the introduced procedures, the following measures are involved:

- Overall Accuracy (OA):
$$OA = \frac{\sum_{i=1}^r x_{ii}}{n} \quad (5-1)$$

where r is the number of rows, x_{ii} are the correct classified pixels and n is the total number of pixels. The overall accuracy is an average value that gives an overview of the accuracy of the entire classification (i.e., percentage of cases correctly allocated). It does not reveal, however, whether an error is evenly distributed between classes or not. Although many other accuracy measures exist (Pontius and Millones 2011), the OA was used because it is the simplest and one of the most popular accuracy measures (Congalton 1991), which is also recommended for use as a primary measure (Liu, Frazier and Kumar 2007).

To focus on the accuracy of individual classes, the producers' and users' accuracy is included in the evaluation.

- Producer Accuracy (PA)

The producers' accuracy describes the probability that a pixel is correctly classified with regard to all pixels of that ground truth class (i.e., error of omission). For each class of ground truth pixels, the number of correctly classified pixels is divided by the total number of ground truth pixels (Mullin & Seigel 2009; Foody 2002). The parameter states how much of the reference area was estimated (a lower value means less reference area was classified).

- User Accuracy (*UA*)

The users' accuracy describes the fraction of correctly classified pixels with regard to all pixels classified as this class in the classified image (i.e., error of commission). It defines how accurate the map is from the perspective of the user. For each class in the classified image, the number of correctly classified pixels is divided by the total number of pixels that were classified as this class (Mullin and Seigel 2009; Foody 2002). The parameter states how much of the classified area is falsely allocated (a lower value means more false allocations).

In any classification there occurs a certain random allocation. The Kappa coefficient models and represents the degree of randomness with a range between -1 and 1. In other words, it is essentially a measure of how well the classifier performed compared with how well it would have performed simply by chance. A low Kappa coefficient characterizes the result of the overall accuracy as random (Cohen 1960; Hudson and Ramm 1987; Foody 2002; Datta, Ghosh and Ghosh 2014).

- Cohen's Kappa coefficient (Cohen 1960):
$$K = \frac{n \sum_{i=1}^r x_{ii} - \sum_{i=1}^r x_{i+} * x_{+i}}{n^2 - \sum_{i=1}^r x_{i+} * x_{+i}} \quad (5-2)$$

where x_{i+} is the sum of pixels in a row and x_{+i} is the sum of pixels in a column. Another definition is the following (Congalton 1991):

$$K = \frac{P_o - P_e}{1 - P_e} \quad (5-3)$$

The parameter P_o is the relative observed agreement between the extracted results and the reference data. It is calculated in the same way as *OA*, while

$$P_e = \frac{\sum_{i=1}^r x_{i+} * x_{+i}}{n^2} \quad (5-4)$$

P_e represents the hypothetical probability of the agreement between the extracted result and reference data. In this study, the original equation (5-2) of Cohen (1960) was applied.

For the object-based water classification, the pixel-based channel network extraction, shellfish bed and salt marsh classifications, a binary confusion matrix was carried out. The following specific measures are involved. The term 'shellfish bed' can be replaced by one of the other classes (e.g., salt marsh or water).

- True Positive (*TP*): The number of shellfish bed pixels correctly detected as shellfish bed (i.e., correctly recognized class examples).
- True Negative (*TN*): The number of no shellfish bed pixels correctly detected as no shellfish bed (i.e., correctly recognized class examples that do not belong to the class).

- False Positive (*FP*): The number of no shellfish bed pixels incorrectly detected as shellfish bed (i.e., examples that were incorrectly assigned to this class).
- False Negative (*FN*): The number of shellfish bed pixels incorrectly detected as no shellfish bed (i.e., examples that were not recognized as class examples).
- True Positive Rate: $TPR = \frac{TP}{TP+FN}$ (5-5)
- True Negative Rate: $TNR = \frac{TN}{TN+FP}$ (5-6)

The measure *TPR* is also known as ‘sensitivity’ and defines the proportion of true positives (i.e., shellfish bed) that are correctly identified as such (i.e., effectiveness of a classifier to identify positive labels). The measure *TNR* (i.e., specificity) defines the proportion of the true negatives (i.e., no shell fish bed) that are correctly identified as such. Both are equivalent to the *PA* of a multi-class confusion matrix (Sokolova & Lapalme 2009).

- Precision: $P = \frac{TP}{TP+FP}$ (5-7)

- Negative Predicted Value: $NPV = \frac{TN}{TN+FN}$ (5-8)

The parameter *P* (precision) measures the class agreement of the reference labels with the positive labels (i.e., shellfish bed) given by the classifier and the parameter *NPV* or ‘specificity’ measures how effectively a classifier identifies negative labels (i.e., no shellfish bed). Both are equivalent to the *UA* of a multi-class confusion matrix (Sokolova & Lapalme 2009).

- Prevalence: $P_r = \frac{TP+FN}{n}$ (5-9)

The parameter *P_r* measures how often a class, for instance shellfish bed, actually occurs in the sample and thus measures the reliability of the *OA*.

The interpretability of a confusion matrix is strongly dependent on the sampling design and amount of reference data available. A confusion matrix only represents a comparison at the location of the reference data and the classification result. This means that it lacks interpretability if only a small amount of reference data are available or if they are unevenly distributed (see *P_r*) (Foody 2002).

As already mentioned in chapter 4.4.1.4.2 and 4.5.3, a cross-validation for the sediment classification results of the LiDAR data and spectrometric data will be carried out.

The derived results of the proposed methods are compared with results of the popular state-of-the-art classification (RF) and the feature selection (ReliefF) approach. This helps to properly describe and interpret the achieved accuracies.

5.2.2 Hierarchical decision tree

5.2.2.1 Blue mussel/oyster beds

Figure 5-3 shows a subset of the classification result with the superimposed reference vector layer for a detailed description of the result. The vector layer, which was partly digitized from an aerial photo of 2011, represents the border without the internal structure of the shellfish beds. This work was performed by the ‘National Park Wadden Sea of Lower Saxony’. They also measured the ground truth data on site by surrounding the shellfish beds. With this method, blank spaces in the shellfish beds were not taken into account. They also measured areas where new shellfish beds evolve.

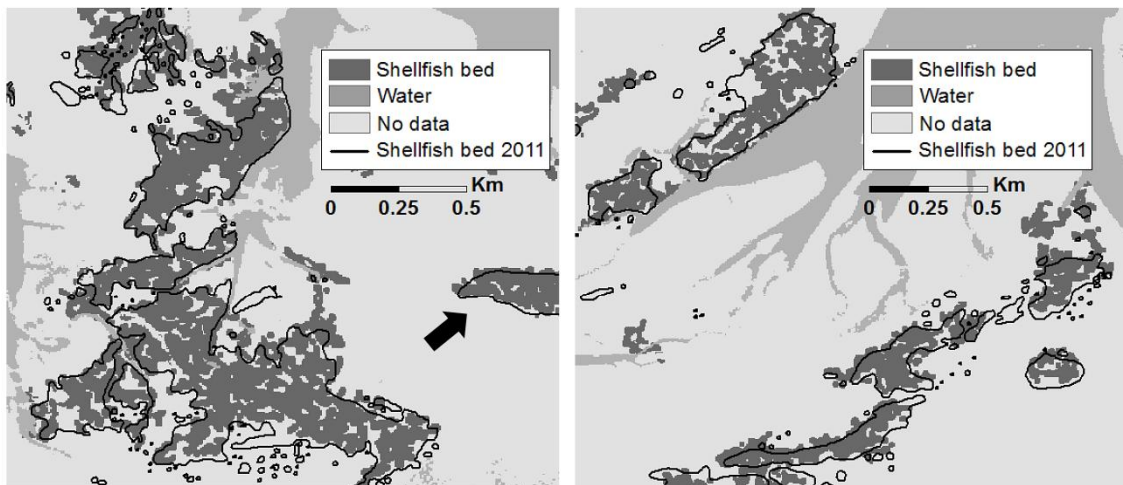


Figure 5-3: Subset of the combined shellfish bed and water classification from 16 July 2011 (TSX data) and 11 July 2011 (RE data) in the western part (left) and the eastern part (right) of the study area superimposed with the vector layer of 2011. The arrow shows a young mussel bed which cannot be detected with electro-optical satellite data alone.

The correspondence between the two layers can be seen easily. The reference data on the left side of Figure 5-3 have an overall area of 0.78km² and the classification result has an overall area of 0.87km². In this part, areas with shells of dead mussels exist that are classified as shellfish beds and therefore increase the classified area. On the right-hand side, the reference data have an overall area of 0.54km² and the classification result has an overall area of 0.53km². Although the difference in the overall area is less, there is a misalignment between the spatial location of the reference polygons and the classification (see Figure 5-3). Similar

results are obtained by Geißler et al. (2011). Some of the classified parts, however, are not shellfish beds in the reference data (i.e., *false positives, FP*). These areas have a bright backscatter in the radar data (see Figure 4-10), which could be a result of a steep slope that occurs at the tidal inlet borders, or shells of dead mussels, and which therefore were not digitized in the reference data. Other parts are not classified as shellfish beds, although they are mapped as shellfish beds in the reference dataset (i.e., *false negatives, FN*). This misalignment is a result of prospective shellfish beds that were also digitized in the reference data. These shellfish beds consist of small and isolated mussels. Sometimes shellfish beds are covered by sediments or vegetation. Small and partly covered shellfish beds generate a smoother surface in regard to the satellite sensor and thus a lower backscatter occurs. They cannot be dissolved with the wavelength and the spatial resolution of TSX, due to their size and the extent of the settlement area. Another reason is the chosen minimum size in the classification algorithm, which eliminates small shellfish beds. Young shellfish beds that start growing have a very low level of surface roughness and thus cannot be detected with radar sensors.

The advantage of using radar data for shellfish bed detection can be seen in the isolated shellfish bed on the left-hand side in Figure 5-3 (arrow). Due to the mixture of the spectral signature of mussels and sediments, this shellfish bed cannot be detected using the electro-optical data alone (see Figure 4-10). This shellfish bed can only be detected and classified with the help of radar data. For this reason, a multi-sensor approach for classifying shellfish beds was applied.

Figure A-1 gives an overview of the classification results from the satellite images of TSX for the whole study area. Among them, plot c) shows only a partial coverage of the study, which is caused by the partial coverage of the TSX satellite image (see Table 3-1). At first glance, the algorithm seems to fit most of the reference areas. The difference in the overall area of plot a) is 0.37km², with an area of 2.05km² for the classification result and an area of 1.68km² for the reference data. The difference in the overall area of plot b) is 0.26km², with an area of 1.94km² for the classification result and an area of 1.68km² for the reference data. The smallest difference occurs in plot c) with 0.04km², while the classification area is 0.52km² and the reference area is 0.56km². The *FP* have an area of 1.05km² for plot a), 0.88km² for plot b) and 0.24km² for plot c). They are mostly located at areas of steep slopes or rough surfaces, which could not be eliminated by the algorithm. The first two results have a tendency to over-classify, whereas the last result is balanced leading to a small difference. All values are summarized in Table 5-2.

Table 5-2: Spatial comparison of the shellfish bed classifications and the corresponding reference data using the hierarchical knowledge-based decision tree.

Acquisition date	Overall area [km ²]	Ref. Area [km ²]	Diff. [km ²]	FP [km ²]	FN [km ²]
02 June 2011	2.05	1.68	0.37	1.05	0.68
16 July 2011	1.94	1.68	0.26	0.88	0.62
28 October 2011	0.52	0.56	0.04	0.24	0.28

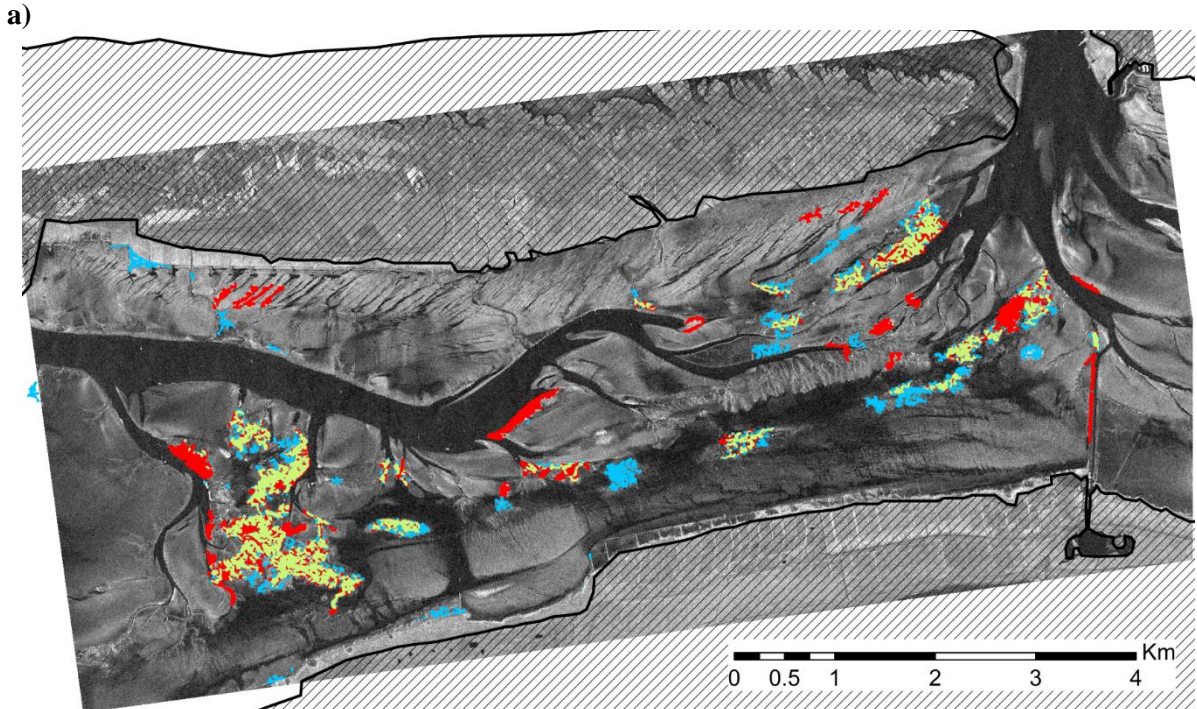
An example for a steep slope is shown in Figure A-1 plot a) on the right-hand side, where a linear shellfish bed is classified at the channel of the ferry boats. Rough surfaces occur, for instance, in the northern part of the study area where sandy sediment generates bedforms that are characterized by crests and troughs. Overall, plot a) misses 0.68km² of the reference area, plot b) 0.62km² and plot c) 0.28km². This means that the classifications of 02 June 2011 and 16 July 2015 tend to classify too many shellfish beds. This is compensated for by the *FN*, which results in quite low differences in the overall area. For the result of 28 October 2011, the *FP* and the *FN* balance each other out, resulting in a very low value for the overall difference. Most of the reference polygons were met by the classification algorithm, but they were not always fully filled, especially at the borders. Towards the borders, the shellfish beds tend to get smaller and sparser, because they are less protected from the tide and less evolved, which makes the detection with TSX more difficult.

Table 5-3 shows the results of the accuracy assessment in a binary confusion matrix for each acquisition date. To obtain the number of pixels, the reference polygons were transformed to raster images. The explanation of the accuracy parameters can be looked up in chapter 5.2.1. Although an *OA* between 95-97% is achieved, some misclassifications can be seen in Figure A-1. The high *OA* is a result of the unbalanced area ratio between the classes ‘shellfish bed’ and ‘no shellfish bed’ (see P_r ranging from 2.8-4.2). Therefore, additional parameters are needed to estimate the accuracy, such as *TPR*, *P* and P_r . A closer look at *TPR* and *P* reveals the true accuracy. For *TPR* the algorithm results in 48-63% accuracy and for *P*, 48-54%. The statistics of Table 5-3 reflect the previous assumption that the results of 02 June 2011 and 16 July 2011 tend to an over-classification, while the result of 28 October 2011 is balanced. Furthermore, the results show that a higher accuracy from the perspective of the user and a lower accuracy for a correct classification of the reference can be assumed for the results of 02 June 2011 and 16 July 2011. This means that the probability of finding a shellfish bed with these maps is higher than that of having a reference area classified as a shellfish bed. The accuracies for the class ‘no shellfish bed’ (i.e., *TNR* and *NPV*) are very high, due to the unbalanced area ratio (see P_r).

Table 5-3: Accuracy measures for the shellfish bed classifications with the hierarchical knowledge-based decision tree.

Classification of TSX from 02 June 2011				
		No shellfish	Shellfish	Sum
Reference of 2011	No shellfish	1469986	42190	1512176
	Shellfish	27080	40204	67284
	Sum	1497066	82394	1579460
	<i>OA [%]</i>	95.61	<i>P_r [%]</i>	4.25
	<i>TPR [%]</i>	59.75	<i>P [%]</i>	48.79
	<i>TNR [%]</i>	97.2	<i>NPV [%]</i>	98.19
Classification of TSX from 16 July 2011				
		No shellfish	Shellfish	Sum
Reference of 2011	No shellfish	1476974	35202	1512176
	Shellfish	24873	42411	67284
	Sum	1501847	77613	1579460
	<i>OA [%]</i>	96.2	<i>P_r [%]</i>	4.26
	<i>TPR [%]</i>	63.03	<i>P [%]</i>	54.64
	<i>TNR [%]</i>	98.00	<i>NPV [%]</i>	98.34
Classification of TSX from 28 October 2011				
		No shellfish	Shellfish	Sum
Reference of 2011	No shellfish	762293	9940	772233
	Shellfish	11588	10855	22443
	Sum	773881	20795	794676
	<i>OA [%]</i>	97.29	<i>P_r [%]</i>	2.82
	<i>TPR [%]</i>	48.36	<i>P [%]</i>	52.2
	<i>TNR [%]</i>	98.71	<i>NPV [%]</i>	98.5

Figure 5-4 represents the spatial changes of the shellfish beds derived with the decision tree approach. The difference in the spatial coverage between plot a) and plot b) is a result of the partial coverage of the TSX data from 28 October 2011. Based on the obtained accuracies, the results have to be treated with caution. The changes occur very randomly and most of them are accompanied by *FP* of the classification results (see Figure A-1). If those areas are neglected, then the change is focused on the three big shellfish beds in the western and eastern part of the study area between June and July 2011. At these areas, the shellfish beds get bigger in their spatial extent while simultaneously generating blank spaces in their community, which results in a more or less similar spatial coverage. In contrast, the spatial coverage decreases from July to October 2011.

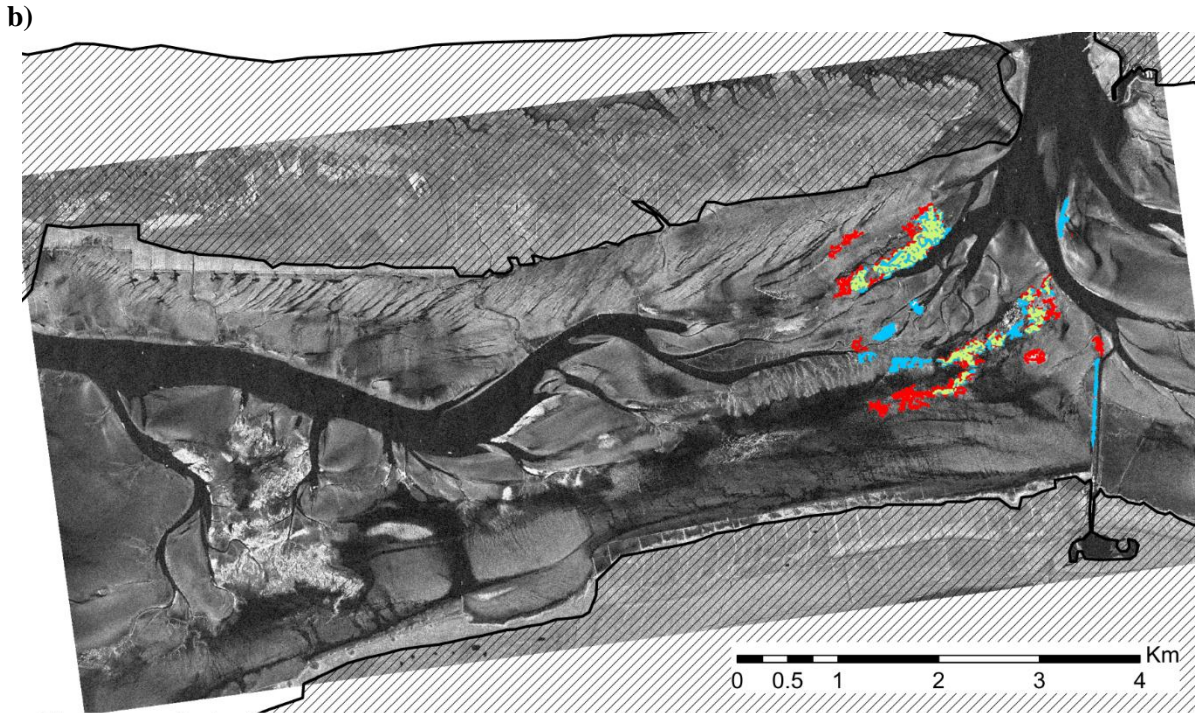


Change of shellfish bed distribution from June 2, 2011 to July 16, 2011

N

Decrease	Increase
No change	Mainland/Island

Data source: DLR, WiMo
Projection: UTM-32, WGS-84



Change of shellfish bed distribution from July 16, 2011 to October 28, 2011

N

Decrease	Increase
No change	Mainland/Island

Data source: DLR, WiMo
Projection: UTM-32, WGS-84

Figure 5-4: Change of the shellfish bed distribution derived with the decision tree approach. Plot b) represents only a small area of change, due to the TSX image of 28 October 2011 that covers only the eastern part of the study area.

5.2.2.2 Vegetation (salt marsh, algae and seagrass)

For the accuracy assessment of the vegetation classification, only ground truth data of seagrass from 2003-2008 was available. To perform an accuracy assessment anyway, aerial photos for visual interpretation and self-generated reference data for the accuracy assessment of the salt marsh classification were applied. For the self-generated reference data, the salt marsh areas were manually digitized using pseudo-colour RE images (R: NIR, G: Red, B: Green). These polygons are the input for a binary confusion matrix. The coverage of the class 'algae/seagrass' could not be clearly estimated from the datasets. The seagrass grows very sparse, which made the manual delineation from the orthophotos very difficult. Moreover, a manual discrimination between algae and shellfish bed could not be carried out, because algae have no roots, in comparison to seagrass, and need a solid foundation (e.g., mussel shells) to settle down. Therefore, in regard to the hierarchical method, the area where algae could occur is already assigned to the class 'shellfish bed'. Hence, neither reference data could be generated nor a numeric accuracy assessment was possible or carried out for the class 'algae/seagrass'.

The time gap between the two datasets (vector layer and satellite data) representing seagrass is too large for a numerical evaluation of the classification accuracy. Because of this, a part of the study area was chosen where it is known from in situ measurements that seagrass occurs every year. Figure 5-5 shows this area with the vector layer of the seagrass from 2008 superimposed. The seagrass areas can be seen in the very high-resolution CIR photos of 2011 (0.3m) as reddish areas in the intertidal flats close to the shore. The reddish brown parts north of the shore belong to a shellfish bed with attached algae. In the RE image, only a very small part of the possible seagrass area could be classified in comparison with the reference data and the CIR photos. This underestimation can be explained by the natural surface pattern of seagrass areas. Seagrass often grows very sparsely in the study area, which, with respect to the spatial and spectral resolution of RE, leads to a mixture of the spectral signal of sediment and seagrass (Figure 5-6). In this context, a differentiation between these two land covers is very difficult.

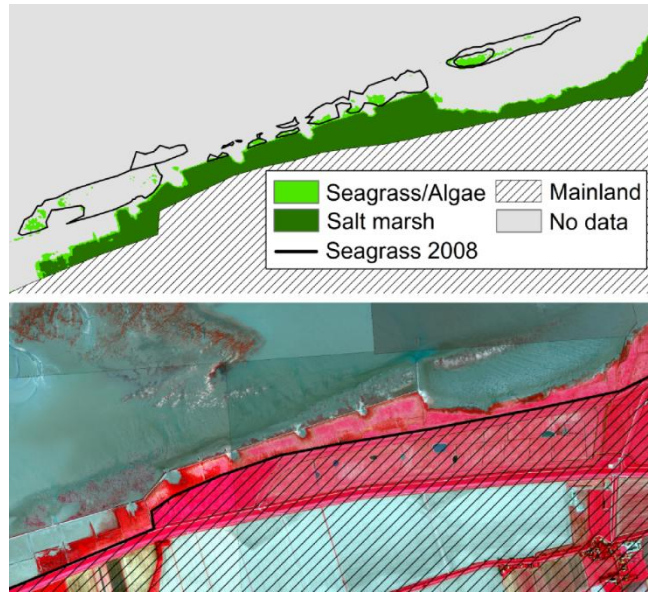
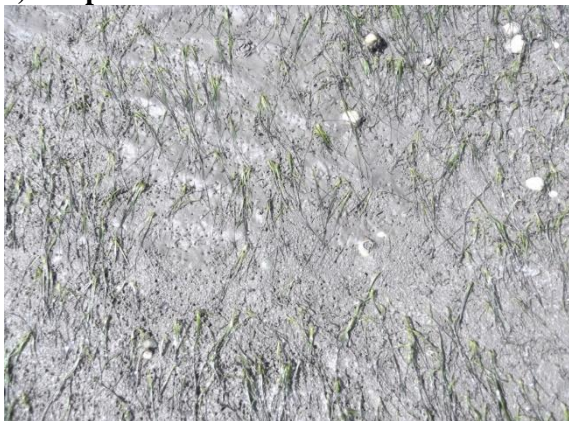


Figure 5-5: Subset of the seagrass/algae and salt marsh classification from 11 July 2011 (above) and the corresponding CIR aerial photos of September 2011 (below).

a) Topview



b) Oblique view



Figure 5-6: Two examples for the sparse seagrass meadows in the study area. One is taken from topview and one from oblique view.

Figure A-2 shows an overview of the salt marsh classification results from the satellite images of RE for the whole study area. It can be seen that most of the reference data are also classified by the algorithm. Table 5-4 shows the differences in the overall area, the area of *FP*, the area of *FN*, the overall area of the classification and the reference. The differences between the overall area of the classifications and the reference data are very small. The worst result is achieved with the data from 25 April 2010, which is still an acceptable result. Furthermore, it is the only result with *FP* being the predominant error. This is a result of the manual digitalization, because it was not always easy to clearly identify the salt marsh border in the north of the image of 25 April 2010. Most of the *FN* are located at the shore in the eastern part of the study area. These parts are sparsely vegetated, which leads to a mixture of the spectral signature of sediments and salt marsh. Therefore, the *MSAVI* value is lower than the applied threshold. In this study area, a lower threshold or a bigger buffer zone would

increase the classified area, but this would also enclose areas of seagrass, which grow nearby the shore (see Figure 5-5). This means that the threshold and the buffer zone have to be adjusted according to the study area.

Table 5-4: Spatial comparison of the salt marsh classifications and the corresponding reference data using the hierarchical knowledge-based decision tree.

Acquisition date	Overall area [km ²]	Ref. Area [km ²]	Diff. [km ²]	FP [km ²]	FN [km ²]
25 April 2010	0.75	0.62	0.13	0.14	0.02
27 June 2011	1.02	1.11	0.09	0.04	0.12
11 July 2011	1.06	1.08	0.02	0.05	0.07
22 October 2011	1.05	1.10	0.05	0.05	0.10

The assumptions of the areal comparison are confirmed by the binary confusion matrices of Table 5-5.

The lowest P is achieved with the image of 25 April 2010, which is equivalent to the area of FP . On the other hand, the value of TPR is the highest, due to the lowest area of FN . The OA is always 99%, which is due to the unevenly distributed reference data (see P_r). Nevertheless, the values for TPR (88-96%) and P (80-95%) are also very high, which shows the high quality of the results. The best result is obtained with the data of 11 July 2011. Due to the high accuracies achieved, a detailed description or error explanation, such as Figure 5-3 shows for the shellfish beds, was not carried out. Just like the shellfish bed classification, the accuracies for the class ‘no salt marsh’ (e.g., TNR and NPV) are very high.

Due to the very high accuracy result, a post-classification comparison as change detection approach was carried out (Lillesand and Kiefer 1994³; Liu and Zhou 2004). The change maps can be found in the appendix (Figure A-3). Figure 5-7 summarizes the areal change in a bar chart. Between 25 April 2010 and 27 June 2011, there is a large increase in the salt marsh areas, which are mainly located at the shore of the island ‘Norderney’. On the other hand, the changes in the subsequent acquisitions are very low. In this context, a stable distribution of the salt marshes during the months June, July and October of 2011 can be assumed. In general, the salt marsh areas are disturbed by winter storms, which as a consequence causes some areas to disappear. This means that the increase from 25 April 2010 to 27 June 2011 is not an effect of an overall increasing of the salt marsh areas, but rather an effect of the season (i.e., growing season) or an effect of retrieval. Because of the season, the salt marsh areas have decreased by 22 October 2011. To approve this hypothesis, satellite images from the winter and directly before and after a winter storm would be necessary.

Table 5-5: Accuracy measures for the salt marsh classifications with the hierarchical knowledge-based decision tree.

Classification of RE from 25 April 2010				
		No salt marsh	Salt marsh	Sum
Reference	No salt marsh	1548514	5847	1554361
	Salt marsh	840	24259	25099
	Sum	1549354	30106	1579460
	<i>OA [%]</i>	99.58	<i>P_r [%]</i>	1.59
	<i>TPR [%]</i>	96.65	<i>P [%]</i>	80.58
	<i>TNR [%]</i>	99.62	<i>NPV [%]</i>	99.94
Classification of RE from 27 June 2011				
		No salt marsh	Salt marsh	Sum
Reference	No salt marsh	1533230	1830	1535060
	Salt marsh	5063	39337	44400
	Sum	1538293	41167	1579460
	<i>OA [%]</i>	99.56	<i>P_r [%]</i>	2.81
	<i>TPR [%]</i>	88.59	<i>P [%]</i>	95.55
	<i>TNR [%]</i>	99.88	<i>NPV [%]</i>	99.67
Classification of RE from 11 July 2011				
		No salt marsh	Salt marsh	Sum
Reference	No salt marsh	1533763	2121	1535884
	Salt marsh	2992	40584	43576
	Sum	1536755	42705	1579460
	<i>OA [%]</i>	99.67	<i>P_r [%]</i>	2.75
	<i>TPR [%]</i>	93.13	<i>P [%]</i>	95.03
	<i>TNR [%]</i>	99.86	<i>NPV [%]</i>	99.80
Classification of RE from 22 October 2011				
		No salt marsh	Salt marsh	Sum
Reference	No salt marsh	1532914	2337	1535251
	Salt marsh	4271	39938	44209
	Sum	1537185	42275	1579460
	<i>OA [%]</i>	99.58	<i>P_r [%]</i>	2.71
	<i>TPR [%]</i>	90.33	<i>P [%]</i>	94.47
	<i>TNR [%]</i>	99.84	<i>NPV [%]</i>	99.72

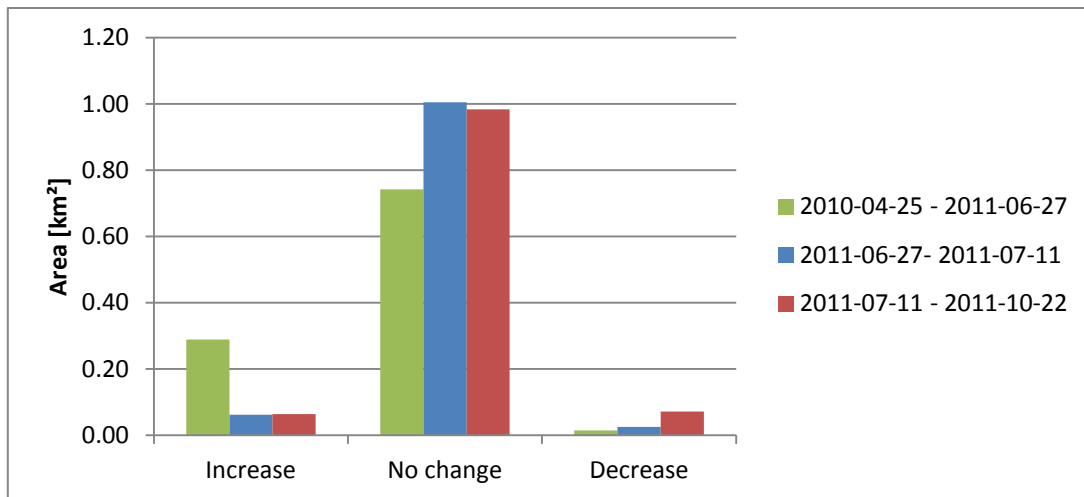


Figure 5-7: Bar chart of the salt marsh changes in km² from 25April 2010 to 27 June 2011, from 27 June 2011 to 11 July 2011 and from 11 July 2011 to 22 October 2011. These are results of the hierarchical knowledge-based decision tree classifications.

5.2.2.3 Sediments with RapidEye

Table 5-6 shows the accuracy assessment for the sediment classification with respect to the ground truth data of 2008/2009, 2010 and 2012. No data values occurred when the ground truth data positions were covered by water or located outside the defined sediment area. All the pixels of the class ‘sand’ exhibited 76-78% UA. For the classes ‘mixture’ and ‘mud’, very low UA of between 38-42% and 20-28%, respectively, is obtained. This is related to the already-mentioned strong similarity of the spectral signature influenced by water, iron oxide, grain size or organic matter. If sediments like sand contain a large amount of water, the spectral reflectance of all wavelengths decreases (especially in the longer wavelengths) (Small et al. 2009; Ibrahim et al. 2009). Due to their greater pore volume in comparison with mud, they less frequently develop a water layer on the surface. Areas of mud are saturated longer with water and can generate a water layer on the surface with increasing moisture (Table 4-1; Scheffer & Schachtschabel 2010; Janke & Kremer 2011). This water layer creates a specular surface and increases the spectral reflectance of mud in the shorter wavelengths. Sand has, in general, higher reflectance values over the entire wavelength range of RE in comparison with mud. Sand appears brighter than mud (Stelzer, Brockmann & Geißler 2009). However, the decreasing effect for sand and the increasing effect for mud raised by water cause similarities and therefore create overlaps in the spectral space (see Figure 5-8) (Small et al. 2009; Ibrahim et al. 2009). The class allocation becomes random, as proven by the Kappa coefficient. For the class ‘sand’, the *PA* ranges from 82-86%, for the class ‘mixture’ from 28-50% and for the class ‘mud’ from 4-23%. The *UA* and *PA* show that, with decreasing grain size, the accuracy

decreases with the proposed knowledge-based decision tree approach. There is a strong tendency to classify ‘mud’ as ‘sand’ or as ‘mixture’.

Table 5-6: Accuracy measures for the sediment classifications with the hierarchical knowledge-based decision tree.

25 April 2010		Ground truth			Classified	UA [%]
		Sand	Mixture	Mud		
Classes	Sand	191	27	22	240	79.58
	Mixture	30	30	20	80	37.5
	Mud	3	2	2	7	28.57
Ground truth		224	59	44	327	
PA [%]		85.27	50.85	4.55		
OA [%]	68.20	Kappa	0.29	No data	101	
27 June 2011		Ground truth			Classified	UA [%]
		Sand	Mixture	Mud		
Classes	Sand	220	33	29	282	78.01
	Mixture	14	17	10	41	41.46
	Mud	20	10	12	42	28.57
Ground truth		254	60	51	365	
PA [%]		86.61	28.33	23.53		
OA [%]	68.22	Kappa	0.26	No data	32	
11 July 2011		Ground truth			Classified	UA [%]
		Sand	Mixture	Mud		
Classes	Sand	208	29	27	264	78.79
	Mixture	18	22	12	52	42.31
	Mud	26	8	12	46	26.09
Ground truth		252	59	51	362	
PA [%]		82.54	37.29	23.53		
OA [%]	66.85	Kappa	0.26	No data	40	
22 October 2011		Ground truth			Classified	UA [%]
		Sand	Mixture	Mud		
Classes	Sand	212	34	31	277	76.53
	Mixture	17	21	17	55	38.18
	Mud	26	8	9	43	20.93
Ground truth		255	63	57	375	
PA [%]		83.14	33.33	15.79		
OA [%]	64.53	Kappa	0.22	No data	23	

The *OA* of the sediment classifications ranges from 64-68% and the Cohen’s Kappa coefficient ranges from 0.22-0.29. This low overall accuracy could be a result of conservative bias. The conservative bias describes the errors in the reference data (e.g., incorrect class assignment or change in land cover type) of location and scale that could arise with the use of ground truth data (Verblya and Hammond 1995). First of all, there is the time component, which, as regards this study, is the most important one. The ground truth data that are used in

this study were acquired both two years before and one year after the satellite images were acquired. Between these dates, changes occurred, which were recognized by comparing the recorded sediments of some ground truth measurement locations between 2008/2009 and 2012. These changes could be a result of the small-scale changes between the acquisition time of the satellite image and ground truth data (e.g., temporal cover of different sediments or weathering processes). An error of location can be neglected because the ground truth data were taken in a large area of the same sediment and the GPS handhelds had an error of 3-5m. The last part of the conservative bias is the difference in scale of the ground truth data and the satellite image. In this case, the ground truth data are a point measurement with the information of the sediment type, in comparison with a satellite pixel that represents an area of 25m². The data of 2008/2009 are based on a systematic sampling scheme of 300m distance between adjacent points. The data of 2012 were randomly sampled at interesting areas. For both datasets, the information about the sediment type was estimated onsite. Due to the difference in scale, the sediment measurement of a ground truth point and the spectral response of a satellite pixel can significantly differ from each other. One pixel of the satellite can cover a transition between different sediments that is not represented by the ground truth (Verblya and Hammond 1995; Foody 2002). As already mentioned in chapter 3.1, intertidal flats are characterized by gradual transitions between the different sediment types. The phenomenon of transition zones and the use of static thresholds led to higher errors in these areas. An improvement of the sediment classification with the integration of radar data was analysed but, due to the acquisition mode - especially the single polarization - no relation between the backscatter and the sediment types could be detected.

In intertidal flats, the spectral response of sediments depends strongly on the amount of water in the upper layer and on the occurrence of water coverage or vegetation (micro- and macro-vegetation) (Small et al. 2009; Rainey et al. 2000). Water causes a lower reflectance, especially in the longer wavelengths (>700nm) (Ibrahim et al. 2009). In contrast, organic matter (e.g., chlorophyll a or microbial mats) has a great influence on the shorter and longer wavelengths (see chapter 3.2 and 5.3). With increasing amounts of organic matter, the spectral reflectance decreases (Ibrahim et al. 2009; Decho et al. 2003). Due to this effect, the similarity of the sediments increases and the probability of distinguishing the sediments decreases. Therefore, the system of RE, with its spectral resolution, is not perfectly suited for classifying sediments in intertidal areas. Additional spectral information of longer wavelength (e.g., NIR or SWIR) is needed to improve the quality of the sediment classification, which is proven by the results of chapter 5.3 (Sørensen et al. 2006; Van der Wal & Herman 2007). Despite the

spectral limitation of RE, classification accuracies of 64% and better were achieved (see Table 5-6). Rainey et al. (2000) have shown, with in situ and laboratory-based reflectance experiments, that satellite data should be collected after a prolonged period of exposure to summer drying conditions, which ensures that the spectral influence of moisture is minimized and the spectral contrast is maximized. This would enhance the capacity for spectral distinction between coarser sand- and finer mud-dominated sediment fractions. Ryu et al. (2004) and Choi et al. (2011) confirm this conclusion. Due to this, an image acquisition at exactly the moment of low tide, or up to 30min later (depending on the topography), would increase the probability of distinguishing the sediments in this study area. In this study, the difference between the acquisition time and the low tide time ranges from a few minutes to nearly two hours (see Table 3-1). With a repetition rate of one day for RE, images during the period of the driest conditions can be obtained. This means the water is drained off and that the surface was dried by the sun.

In addition to the accuracy assessments, a separability analysis of the spectral signatures was carried out. First of all, the spectral signatures of each class were compared by their absolute values and the root mean square error (RMSE) (Figure 5-8). The comparison comprises a dry-sand polygon, a wet-sand polygon, a mud polygon and a mixed-sediments polygon in parts of the study area with high reliabilities for the selected sediment classes. Each polygon comprises 100 spectra and is represented by its mean, maximum (max), minimum (min) and standard deviation (stdev) in Figure 5-8. In plot a) of Figure 5-8 are very similar spectra showing approximately the same range of reflectance values and a low RMSE value. This is a result of the water content, which reduces the reflectance values of sand on one side and raises the reflectance values for mud (specular surface) at the same time. The narrow spectral signature space between wet sand and mud makes the separation difficult and thus often leads to a mix-up of the classes and to a false allocation (Brockmann & Stelzer 2008). The same applies for plots b) and d), where mixed sediments get mixed up with mud or wet sand. In general, these sediment types have a high water content, which influences the spectral reflectance. Only the spectrum of dry sand can be separated clearly from all the other spectra, which is represented by the higher RMSE value. In plots c), e) and f) of Figure 5-8 the spectral differences are stronger, which is also represented by a higher RMSE value. The results show that some class-pairs have greater potential of being separated with the introduced classification algorithm. However, it also demonstrates the need for additional information to improve the sediment classification. The selected sediment classes cannot be classified with high accuracy by their spectral properties alone. The results show that the

spectral resolution and the wavelength domain of the RE data are quite limited for the classification of such similar land covers (i.e., sediment types). Hyperspectral data (e.g., EnMap, HyMap, PRISM, HICO, etc.) have a higher spectral resolution, which could help in separating sediment types. As mentioned above, additional bands such as SWIR or SWIR2 can bring benefits. Furthermore, they are an indicator for water, which will help to identify water-covered sediments (Yates et al. 1993; Thomson et al. 1998; Sørensen et al. 2006; Van der Wal and Herman 2007; Stelzer et al. 2010). This hypothesis will be analysed in chapter 5.3.

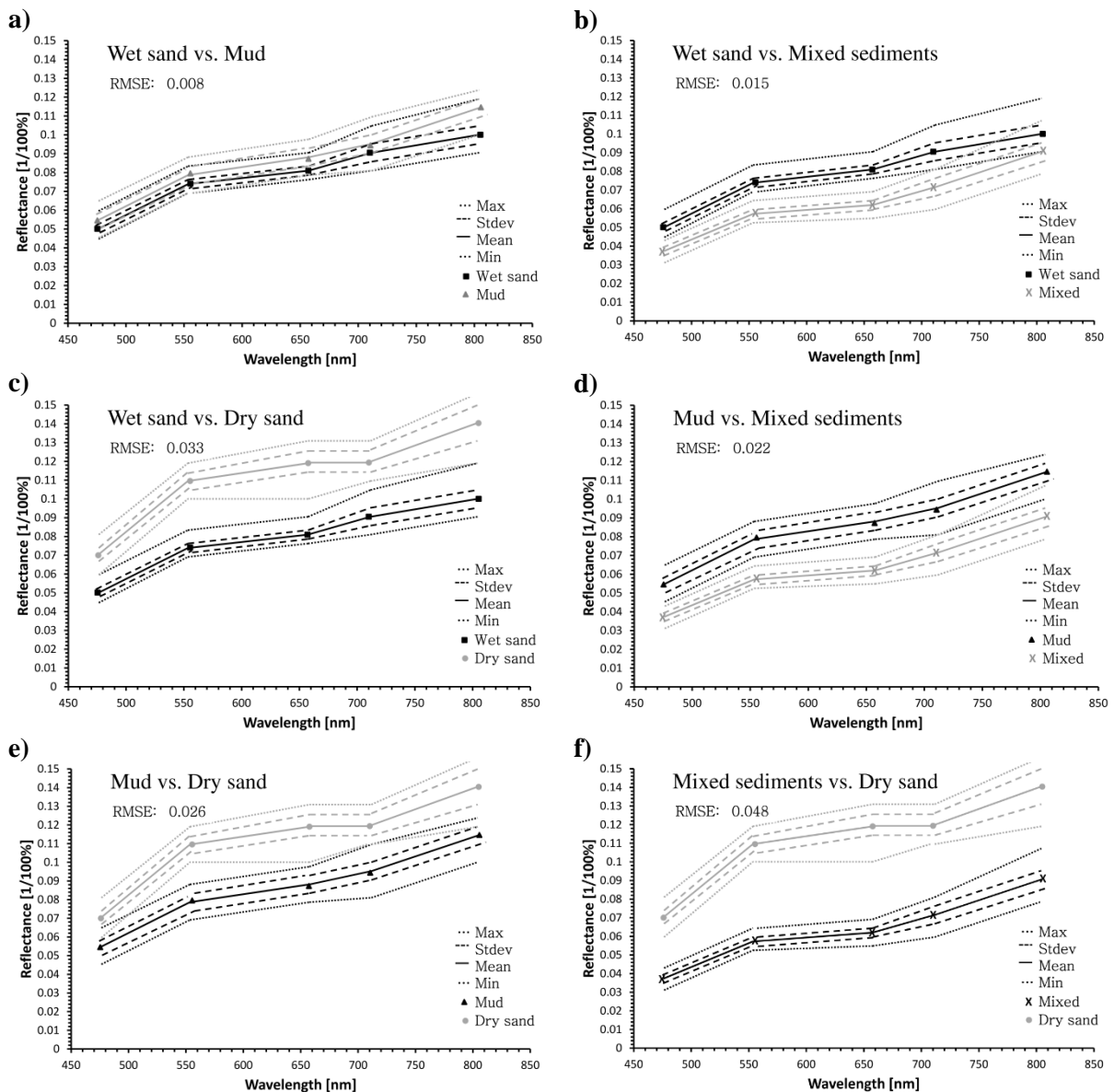


Figure 5-8: The plots a) to f) show comparison of the statistical parameters (mean, maximum, minimum, stdev and RMSE) of spectra from wet-sand polygon, dry-sand polygon, mud polygon and mixed-sediment polygon. All the polygons comprise 100 samples. The different lines represent the minimum (bottom dotted line), stdev (dashed lines), mean (solid line) and maximum (top dotted line). Discrete spectral band values (symbolized by squares, triangles, circles and crosses) were linked for better comparison.

Figure A-4 shows the sediment map for all four acquisition dates. The general distribution of the sediments looks similar throughout the images. There are dry and wet sands predominant in the north and the west. In the south are some large areas of mixed sediments, with mud occurring near the tidal inlets. On the map of 11 July 2011 (plot c) in Figure A-4), one can see a larger area of water in the south that does not exist on the other maps. At that time, a wind from the north was predominant. This pushed the water into its position. At this location, depressions are also located that encourage this event. The equality of the sediment distributions would imply a low-sediment dynamic from one year to another as well as from one season to another, which would be contrary to the general statements in the literature (Van der Wal et al. 2005; Sørensen et al. 2006; Van der Wal & Herman 2007; Park et al. 2010; Brockmann & Stelzer 2008; Nieuwhof et al. 2015). Thus, a more detailed comparison analysis with change statistics (Euclidean distance) and change maps was carried out to analyse this hypothesis. Table 5-7 shows the lowest Euclidean distance (Malik and Baharudin 2013) between the sediment classification of 25 April 2010 and 11 July 2011. The highest distance occurs between 27 June 2011 and 22 October 2011. As expected, the distance between 27 June 2011 and 22 July 2011 is low. Figure A-5 shows in blue where changes of sediments occur. It is often the same area that is changed throughout the images. This shows that the most dynamic areas are located in the southeastern part of the study area. This location also has a lower height and a flat terrain in comparison with its surroundings, which enables the accumulation of sediments with smaller grain sizes. This accumulated sediment layer can be washed away during higher flow velocities, which can expose a different sediment type (e.g., sand). In the northern part of the study area, the slopes are steeper near the island and flatten towards the large tidal inlet (i.e., in a southern direction). This generates higher flow velocities and therefore prevents the accumulation of sediments with smaller grain sizes in most of the northern parts. The change in the north at the shore of the study area shows only a shift from wet sand to dry sand, which is not a significant change. Near this area some muddy areas occur in the RE images of 2011. This is where the slope flattens and where sediments with smaller grain sizes can accumulate. The classification results (Figure A-4) in combination with the change maps (Figure A-5), show that the tidal flat South of Norderney is very dynamic by changing the grain size of the sediment (e.g., eastern part), but that there are also highly stable parts in the study area, where only the moisture content is changing (e.g., northern or western part). A change such as sand being replaced by mud or mixed sediments and vice versa does not take place. It seems to be the case that sediments with

smaller grain sizes are moving on top of sand at specific locations, which can be a result of different water currents at each acquisition date.

Table 5-7: Euclidean distances between the sediment classifications.

	25 April 2010	27 June 2011	11 July 2011	22 October 2011
25 April 2010	---	1971	1891	2099
27 June 2011	1971	---	1936	2362
11 July 2011	1891	1936	---	2337
22 October 2011	2099	2362	2337	---

5.2.2.4 Improvement of sediment classification with LiDAR

It is important for the classification and estimation of the intertidal stream network that the smallest streams and their confluences and connections to the intertidal inlets are classified with high accuracy. The large intertidal inlets are not further analysed and thus errors of large tidal inlets are accepted and their classification accuracy is not considered in this thesis. In this context, an analysis of the smaller intertidal streams will be carried out and the intertidal inlets will be omitted. The smallest streams, however, are typically a metre or less in width. Although the topographic data is measured in high spatial resolution (i.e., 1m), it is likely that such features will be missed. The subsequent analysis and description of the results is based on the small streams and the ability of the proposed algorithms to properly identify them.

5.2.2.4.1 Object-based water classification

No reference data were available for the validation of the object-based water classification. Therefore, the reference data (i.e., pixels) were generated by a specific sampling design. The most important aspect for the validation of the object-based methodology was to examine the accuracy in a balanced way, including small intertidal streams and confluences. To satisfy this requirement, the references were set equally on intertidal inlets, confluences and very small intertidal streams.

Figure 5-9 shows some examples. This evenly distributed sampling design generates a confusion matrix that is meaningful in terms of accuracy. A sampling design ignoring the smallest intertidal streams or confluences would result in very high accuracies, which do not represent the reality. The same applies if only very small streams or confluences are selected. Such a sampling design would result in very low accuracies.

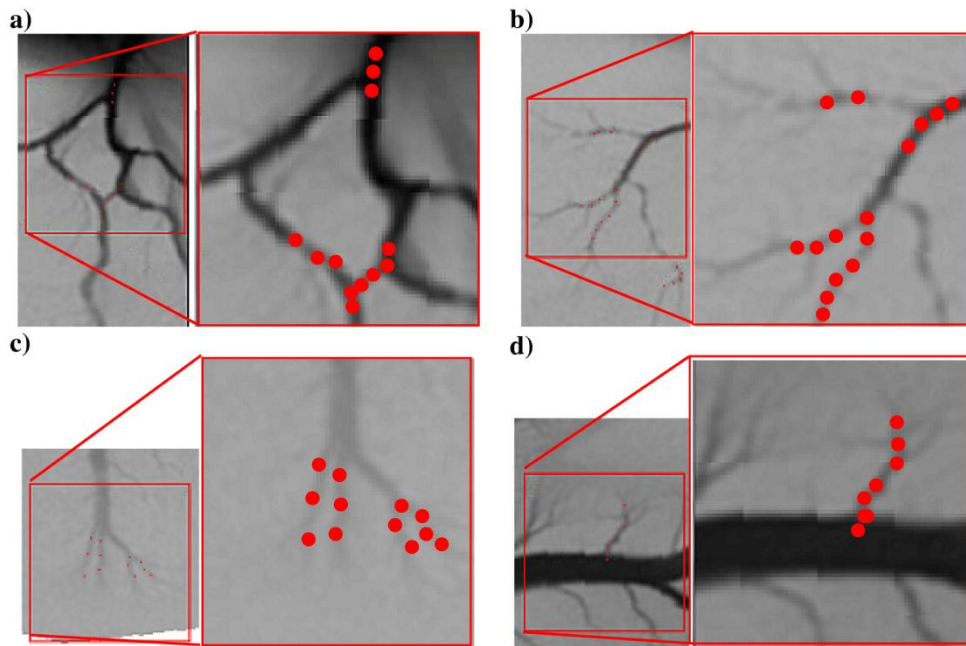


Figure 5-9: Examples of the balanced sampling design of the accuracy assessment. The red dots represent reference pixel for the class ‘water’.

Although this method is able to capture the general stream structure, it misses sometimes to properly characterize important connectivity properties at the fine and very fine scales, especially in the higher zones of the basin (see Figure 5-12). If the segmentation is set to generate smaller objects, the method is able to identify finer and more elevated branches of the network, but at the same time it will incorrectly include portions of intertidal flats in the stream subset. This is especially the case if the intertidal streams start near to, or in, shellfish beds. This can be seen in the Figure 5-10. In the centre is located a shellfish bed, which generates fictive streams. These areas are very flat with a low height, except for the shellfish beds. These height differences act like an intertidal stream. As already mentioned in chapter 5.2.2.1, shellfish beds create blank spaces between each other (i.e., it is not a solid surface), which result in a similar object geometry, compared with intertidal streams, after the segmentation procedure. In this context, they are assigned to the class ‘water’, although they belong to the intertidal flat.

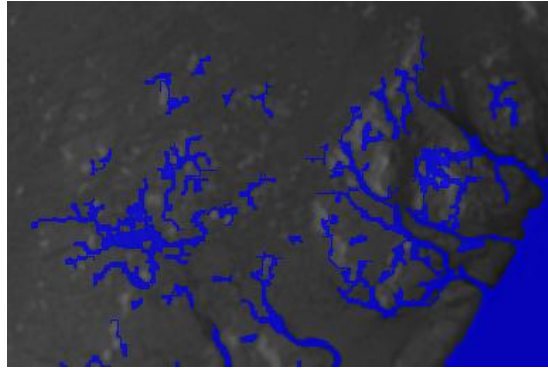


Figure 5-10: A subset of the object-based water classification (blue area) from 2010 showing a shellfish bed in the centre and the influence on the classification result.

The errors of broken streams, missing confluences or even whole streams are somewhat connected to sand flats (see Table 5-9). A reason for this could be the difference in erosion that occurs in comparison with small intertidal streams on mudflats. In general, sand is heavier, more compact and needs more energy (i.e., higher water current) to erode. This leads to shallower intertidal streams and a lower height ratio between the water surface and the boundary of the intertidal stream at low tide. The homogeneity criterion of the segmentation is not exceeded and thus the adjacent pixels (e.g., intertidal stream and intertidal flat) are merged (see chapter 4.4.1.4.1). Therefore, most of the smaller intertidal streams on sand flats are difficult to identify, even for the human eye. Figure 5-11 compares small intertidal streams of sand flats with those of mudflats and their schematic profile. Bigger and wider intertidal streams can be identified very well, due to the higher water current (i.e., energy).

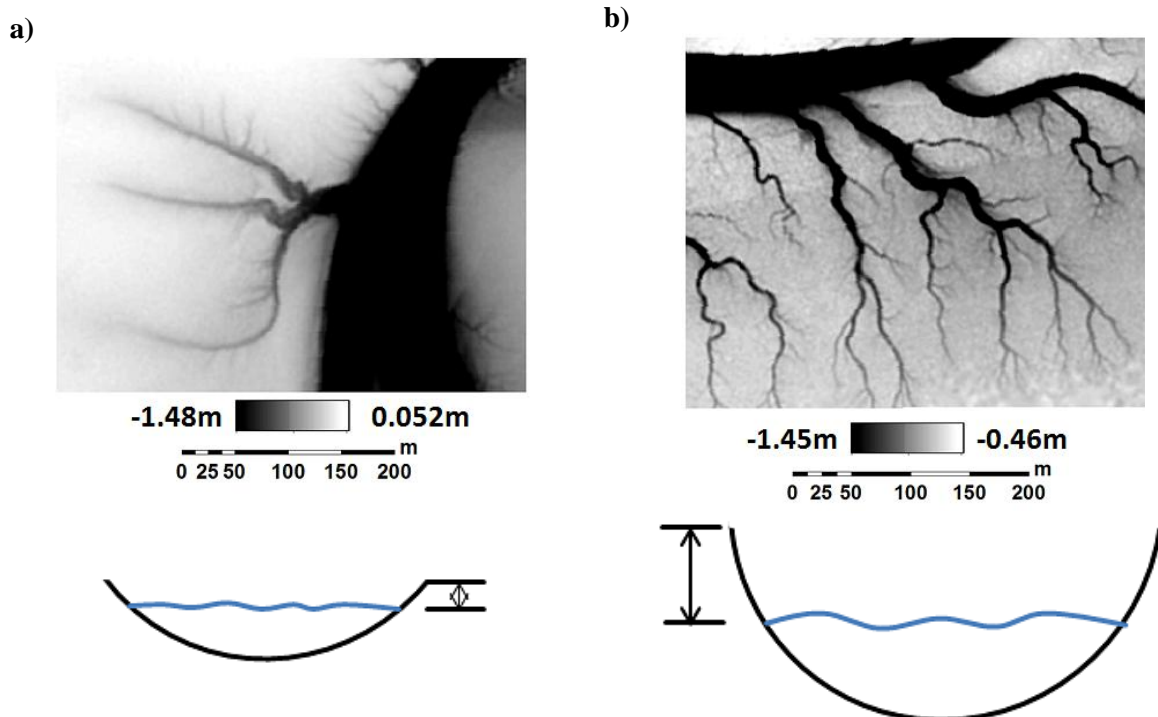


Figure 5-11: Comparison of the visibility of small intertidal streams on a) sand flats and b) mudflats with the corresponding schematic profile.

Table 5-8 shows the overall accuracy (79.58%) of the object-based water classification. This time the *OA* is reliable, due to the high value of *P_r* (79.21%). This means that approximately 80% of the intertidal stream network was identified correctly. Furthermore, the precision *P* of 99.68% shows no tendency of over-classification. In contrast, the value of *TPR* (74.46%) shows the source of error. The classification tends to miss the reference. Due to the lower height ratio between the water surface and the boundary of the intertidal stream at the beginning of each intertidal stream, the classification fails to identify those parts.

Table 5-8: Classification accuracy of the object-based water classification.

Object-based water classification from 2010				
		No water	Water	Sum
Reference	No water	218	2	220
	Water	214	624	838
	Sum	432	626	1058
	<i>OA</i> [%]	79.58	<i>P_r</i> [%]	79.21
	<i>TPR</i> [%]	74.46	<i>P</i> [%]	99.68
	<i>TNR</i> [%]	99.09	<i>NPV</i> [%]	50.46

Table 5-9 compares the accuracy of the classification for mudflats and sand flats separately. The same sampling design described above was applied with one exception. The reference was specifically set for mudflats and sand flats, respectively. The *OA* (92.20%) for mudflats is very high, as is *TPR* (99.13%). In comparison, the result for sand flats has a lower *OA* (72.83%) and a distinctively lower *TPR* (58.06%). Both have a very high *P* (99.13% and 99.13%). This means that both results are reliable, but they tend to miss reference areas. The results prove the ability of the classification to identify intertidal streams on mudflats and to fail in classifying intertidal streams on sand flats.

A further analysis of the rule set showed the transferability of the approach to the other DEM's, with some restrictions. The parameter *scale* for the segmentation in part one and part three of Figure 4-18 has to be set to specific values for 2012 (15 and one) and for 2013 (25 and two), respectively. With these adaptations, the data of 2012 (n=1,015) achieves an *OA* of 91.23%, a *TPR* of 91.11%, a *P* of 94.56%, a *TNR* of 91.43% and an *NPV* of 86.27%, while the data of 2013 tile one (n=478) achieves an *OA* of 94.56%, a *TPR* of 95.04%, a *P* of 97.31%, a *TNR* of 93.33% and a *NPV* of 88.11%. Tile two of 2013 (n=392) achieves an *OA* of 86.73%, a *TPR* of 89.85%, a *P* of 92.14%, a *TNR* of 78.85% and an *NPV* of 73.21%. All three results have an equal capability of identifying mudflats and sand flats. This shows the advantage of

5.2.2.4.2 Extraction of the tidal stream network and geometric features

the stepwise segmentation and classification approach. During each step (i.e., part), the result can be analysed and an appropriate change can be carried out.

Table 5-9: Detailed classification accuracy (mud and sand) of the object-based water classification.

Object-based water classification from 2010 of mudflats				
		No water	Water	Sum
Reference	No water	218	2	220
	Water	50	397	447
	Sum	268	399	667
<i>OA [%]</i>		92.20	<i>P_r [%]</i>	67.02
<i>TPR [%]</i>		88.81	<i>P [%]</i>	99.50
<i>TNR [%]</i>		99.09	<i>NPV [%]</i>	81.34
Object-based water classification from 2010 of sand flats				
		No water	Water	Sum
Reference	No water	218	2	220
	Water	164	227	391
	Sum	382	229	611
<i>OA [%]</i>		72.83	<i>P_r [%]</i>	63.99
<i>TPR [%]</i>		58.06	<i>P [%]</i>	99.13
<i>TNR [%]</i>		99.09	<i>NPV [%]</i>	57.06

5.2.2.4.2 Extraction of the tidal stream network and geometric features

Different subsets of the derived stream network are shown in Figures 4-21 and 5-12. It is clearly visible that most of the streams can be derived with some drawbacks. These drawbacks can be thought of as advantages and disadvantages. Due to the shortest path algorithm, some streams that belong to each other and, on the other hand, streams that do not belong to each other, become connected. These kinds of ‘errors’ occur mostly at very narrow and shallow intertidal streams that cannot be classified by the object-based algorithm. Figure 5-12 shows two examples: Plot a) in the first row represents the generation of fictive streams that do not exist like this; Plot b) represents the same process, but this time parts of one stream, which belong to each other, get united to a consistent intertidal stream. Many of these broken streams cannot be united, resulting in an incomplete representation of the stream network, especially for sand flats (described in the previous chapter). Furthermore, the algorithm does not work in bigger or wider intertidal inlets (see Figure 4-21). It creates several minor streams instead of one representing the whole intertidal inlet. These streams are the result of the very flat surface and the height differences generated by the near-infrared laser over water (see chapter 3.4). As mentioned earlier, this error or disadvantage has no effect on the further analysis, because in this study only the small streams, evolving in the intertidal flat and flowing into the bigger intertidal inlets, are from interest. The introduced

advantages and disadvantages are mostly related to the result of the object-based classification and to the intertidal inlet morphology, such as the bi-directional flow or the very flat surface (i.e., small slope). Basically, the algorithm was designed for the extraction of inland river systems, which have a different morphology.

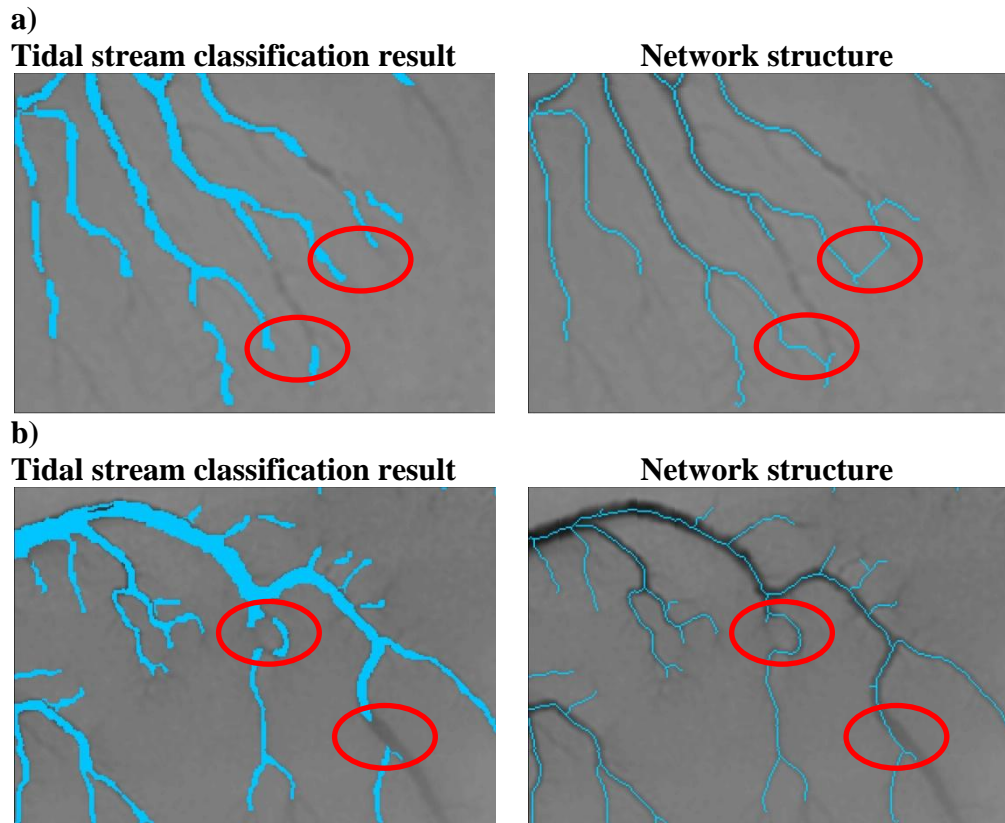


Figure 5-12: Plot a) shows an example for errors that occur during the stream network extraction. Plot b) shows the same process as an advantage. The errors and advantages are highlighted by the red polygons.

In addition to the visual interpretation, a binary accuracy assessment based on the approach described in Rutzinger, Höfle and Kringer (2012) was carried out. For the accuracy assessment, the automatically extracted streams are compared with reference data that were digitized using the DEM. Due to the size of the DEM, representative regions for mud and sand (see Figure A-6) were chosen for the evaluation. The evaluation procedure is based on an analysis of the reference and stream extraction result on a pixel basis. Pixels from both datasets are accepted as matching (*true positives*, TP) if they share a defined search radius of 1m or 5m and if the derived or reference stream is located in this specific area (Figure 5-13). Pixels that have no corresponding reference are classified as *false positives* (FP) and pixels of the reference with no corresponding pixel in the derived stream network are counted as *false negatives* (FN). The search radius of 1m or 5m represents the average width of the smallest and biggest channels, respectively.

5.2.2.4.2 Extraction of the tidal stream network and geometric features

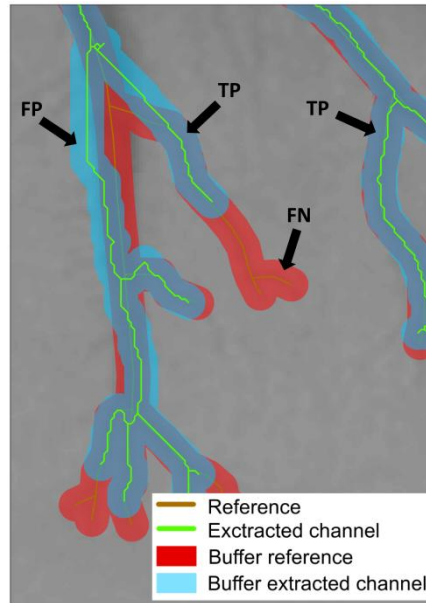


Figure 5-13: Classification of the derived and reference channel network into true positives (TP), false positives (FP) and false negatives (FN).

The percentages of the achieved accuracies are shown in Table 5-10. It shows high values for *OA* (75%-82%), *TPR* (82%-87%) and *P* (90%-93%). This means that the automatically derived channel network is very precise and tends to miss the reference pixels (low *TPR*) instead of generating an *FP* (i.e., high *P*). This is especially so if small channels have been estimated.

Table 5-10: Accuracy measures for the intertidal channel extraction with the hierarchical knowledge-based decision tree.

Channel extraction of LiDAR DEM 2010 – 1m buffer				
		No	Yes	Sum
Reference	No	0	927	927
	Yes	2004	9146	11150
	Sum	2004	10073	12077
	<i>OA</i> [%]	75.73	<i>P</i> [%]	90.80
		<i>TPR</i> [%]	82.03	
Channel extraction of LiDAR DEM 2010 – 5m buffer				
		No	Yes	Sum
Reference	No	0	743	743
	Yes	1483	9851	11334
	Sum	1483	10594	12077
	<i>OA</i> [%]	81.56	<i>P</i> [%]	92.99
		<i>TPR</i> [%]	86.92	

Looking at the values of Table 5-10 in detail, it can be seen that the derived channels are shorter than the reference ($FN=1,483-2,004$) and that fewer additional channels ($FP=743-927$) are derived. This is related to the previous object-based classification. A more detailed water

5.2.2.4.2 Extraction of the tidal stream network and geometric features

classification would decrease the amount of *FN* and maybe increase the amount of *FP*. This shows that, within the given area of the object-based water classification, the channel extraction algorithm achieves satisfying results.

Based on the channel extraction, two geometric parameters (confluences and flow direction) were derived. To evaluate the result of the number of confluences, five subsets, representing a different pattern of confluences, were defined. Figure 5-14 shows the chosen areas, which are located on sand flats and mudflats and Table 5-11 represents the corresponding accuracy. In general, the applied method tends to underestimate the number of confluences slightly. Only once is the derived number higher than the reference (i.e., blue area). In the purple area all confluences were found. This shows that, regardless of the pattern and the number of confluences, the applied method achieves high accuracies.

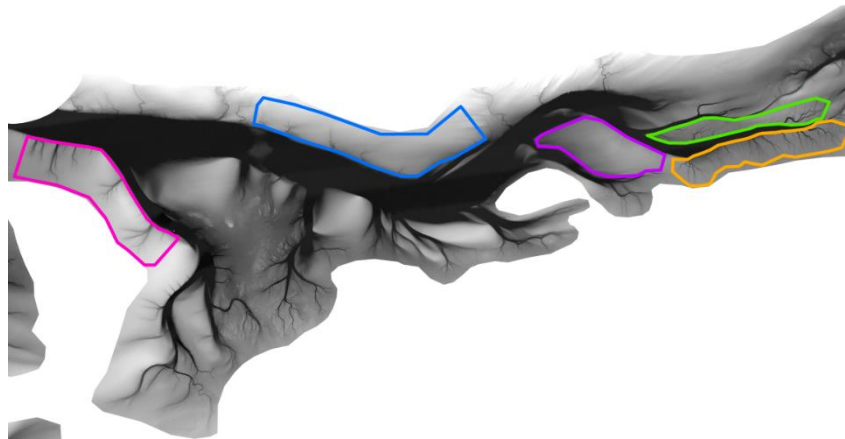


Figure 5-14: Representative channel network areas to validate the search for confluences approach.

Table 5-11: The number of confluences within the polygons of Figure 5-14 compared with the number of confluences derived with the applied method and the percentage.

Area	Confluence	Derived	Percentage
Orange	132	130	98,5
Green	65	64	98,5
Purple	8	8	100
Blue	24	26	108,3
Pink	53	49	93,5

The next parameter that has to be analysed is the flow direction and its change. To do so, a sub-channel stream network was chosen that exhibits several flow direction changes and all flow directions (e.g., horizontal, vertical, diagonal one and diagonal two). Figure 5-15 shows this subset. The reference data were manually generated by assigning one of the four flow directions to each pixel of the stream network result and marking flow direction changes. The proposed algorithms for the flow direction and flow direction change achieved 100%

5.2.2.4.2 Extraction of the tidal stream network and geometric features

accordance with the references. Three examples of the extracted flow direction change are shown in Figure 5-16.

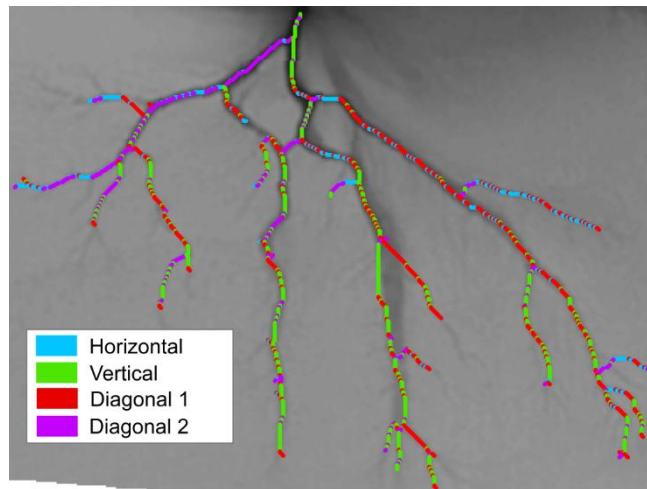


Figure 5-15: Example for the extraction of the flow direction from a channel network

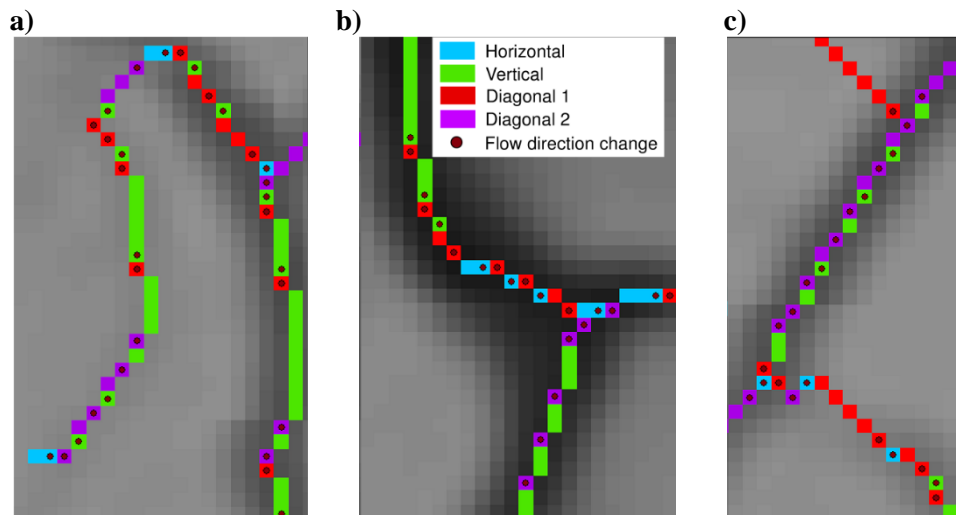


Figure 5-16: Three examples for the extraction of the flow direction change on a mudflat.

The extraction of the parameters ‘confluences’, ‘flow direction’ and ‘flow direction change’ was carried out for 35 sub-channel systems representing muddy areas and for 13 sub-channel systems referring to sandy areas. As mentioned earlier, many stream networks have broken streams, resulting in an incomplete representation of the sub-channel network, especially for sand flats. Due to this, the choice of sub-channel networks, which are representative, was limited.

A correlation analysis was carried out to determine which of the extracted parameters and calculated ratios are best suited as input data for the subsequent supervised classification random forest. Table 5-12 shows the correlation coefficient between all parameters. Although the number of pixels in a sub-channel stream network (#SP) is highly correlated with the number of flow direction changes (#FDC), the parameter #FDC cannot replace the other, because they describe totally different geometric properties. The same applies for the

5.2.2.4.2 Extraction of the tidal stream network and geometric features

parameter #CP (number of water pixels derived from the object-based classification) and #C (number of confluences). Parameters Rel1 to Rel4 are the results with #C as input parameter for the equations (4-13) to (4-16) in chapter 4.4.1.4.2. Parameters Rel5 to Rel8 have the parameter #FDC as input for the same equations. Rel1 to Rel4 have high correlations between each other, which means that only one of them should be used in the further analysis. Rel6 and Rel8 are the only relative parameters that are neither correlated to each other nor to the other parameters, such as #SP, #CP, #C, #FDC and Rel2.

Table 5-12: Correlation coefficient of the extracted geometric parameters and calculated ratios. Symbols are described in the text above.

	#SP	#CP	#C	Rel1	Rel2	Rel3	Rel4	#FDC	Rel5	Rel6	Rel7	Rel8
#SP	--	0.88	0.95	0.2	-0.2	0.03	-0.03	0.99	0.15	-0.17	-0.23	0.24
#CP		--	0.79	0.13	-0.13	-0.13	0.13	0.9	0.21	-0.23	-0.46	0.47
#C			--	0.38	-0.38	0.22	-0.22	0.94	0.16	-0.17	-0.16	0.16
Rel1				--	-0.99	0.87	-0.87	0.2	0.13	-0.15	0.07	-0.08
Rel2					--	-0.87	0.87	-0.2	-0.13	0.15	-0.06	0.07
Rel3						--	-0.99	0.009	-0.05	0.04	0.41	-0.42
Rel4							--	-0.01	0.05	-0.04	-0.4	0.4
#FDC								--	0.22	-0.24	-0.25	0.26
Rel5									--	-0.99	0.05	-0.05
Rel6										--	-0.02	0.02
Rel7											--	-0.99
Rel8												--

Depending on the results of Table 5-12, the input data for the supervised classification (i.e., RF) are the following:

- Number of pixels in a sub-channel stream network (#SP)
- Number of water pixels derived from the object-based classification (#CP)
- Number of confluences (#C)
- Number of flow direction changes (#FDC)
- $\text{normRatio}_{\text{stream}}$ (Rel2)
- $\text{normRatio}_{\text{class}}$ (Rel6, Rel8)

Due to the low sample size, a 20-fold cross-validation was applied. Thus, 17 sub-channels for muddy areas and seven sub-channels for sandy areas were randomly chosen 20 times as trainings data. The remaining 18 or 6 sub-channel systems, respectively, were used for the validation of the accuracy. In this context, 20 RF classifications with a corresponding accuracy assessment were carried out. As already stated in chapter 4.5.3, different numbers of trees are proposed in the literature. In this context, the same analysis of the *OOB* accuracy

5.2.2.4.2 Extraction of the tidal stream network and geometric features

was carried out. Nearly identical results were achieved, leading to a parameterization of 100 trees and the Gini index as an impurity function. Table 5-13 shows the *OA*, *UA*, *PA*, Kappa coefficient, the corresponding mean value and stdev for every classification. For all classifications, a mean *OA* of 79% with a stdev of 3.5% is achieved. The mean *PA* of the mudflats is very high, with 89.55% ($\pm 8.3\%$) in comparison with sand flats (46.4% $\pm 17.62\%$). The same applies to the *UA*, where mudflats have a high mean of 83.5% (± 4.82) and sand flats have a mean of 66.45% ($\pm 18.76\%$). What is also noteworthy is the stdev, which is clearly higher for sand flats. Hence, mudflats can be derived with high accuracy. The Kappa coefficient has a mean of 0.39 and a stdev of 0.1. This shows that all 20 classifications are not a result of a random allocation process and that the classifications are very robust.

Table 5-13: Accuracy results of the 20 RF classifications with randomly chosen ROI's.

# Sample	OA [%]	PA Mud [%]	UA Mud [%]	PA Sand [%]	UA Sand [%]	Kappa.
1	79	94	80	33	66	0.33
2	75	88	80	33	50	0.25
3	79	83	88	66	57	0.47
4	83	100	81	33	100	0.42
5	79	88	84	50	60	0.41
6	83	88	88	66	66	0.55
7	83	100	81	33	100	0.42
8	83	100	81	33	100	0.42
9	75	83	83	50	50	0.33
10	75	88	80	33	50	0.25
11	79	94	80	33	66	0.33
12	79	83	88	66	57	0.47
13	75	83	93	50	50	0.33
14	75	66	100	100	50	0.5
15	79	94	80	33	66	0.33
16	75	88	80	33	50	0.25
17	79	94	80	33	66	0.33
18	83	94	85	50	75	0.5
19	87	100	85	50	100	0.6
20	75	83	83	50	50	0.33
Mean	79	89.55	83.5	46.4	66.45	0.39
Stdev	3.67	8.32	4.82	17.62	18.76	0.1

To extract a final classification from these 20 classifications, a majority analysis was carried out. This means that the class that was frequently assigned to a sub-channel system is assigned to the same sub-channel system in the final classification. However, a simple majority analysis cannot be used in this context (i.e., training data were randomly chosen), because a sub-channel system can be used 15 times or more in the 20 classifications, which would result automatically in a majority. To avoid this, an adapted majority was calculated by applying the following equations:

5.2.2.4.2 Extraction of the tidal stream network and geometric features

$$P_{class} = \frac{N_{poss}}{N_{act}} * 100 \quad (5-10)$$

P_{class} is the proportion of a class for the actual sub-channel system that defines which class is assigned to the sub-channel system. If the result is greater than or equal to 50%, the corresponding class is assigned. It is calculated by dividing the number of possible classifications (N_{poss}) by the number of actual classifications (N_{act}).

$$N_{poss} = n - N_{ROI} \quad (5-11)$$

The number of possible classifications defines how many of the classification results for a sub-channel system (e.g., $n=20$) are not influenced by an ROI (N_{ROI}).

$$N_{act} = Maj_{class} - N_{ROI} \quad (5-12)$$

The number of actual classifications defines how many of the possible classifications are achieved. The majority of a class (Maj_{class}) for each sub-channel system being assigned (e.g., sand or mud) is derived and the number of selection as an ROI in a classification is subtracted.

The following example applies to sub-channel system five. After the 20 classifications ($n=20$), the sub-channel system five was classified 20 times as mudflats and was used 10 times as an ROI ($N_{ROI}=10$). In this context, the number of possible classifications (N_{poss}) is 10 (i.e., 10 out of 20 classifications were not influenced by an ROI). In every classification, this sub-channel system was classified as muddy area ($Maj_{class}=20$); thus the number of actual classifications equals 10. This means that of 10 possible classifications that were not influenced by an ROI, 10 classifications were still classified as mudflat. This sub-channel system is then assigned to the class ‘mud’ in the final classification. This procedure was done for every sub-channel system to assign the class ‘mud’ or ‘sand’.

The accuracy assessment of the final classification is shown in Table 5-14. It can be clearly seen by the PA and UA that the mudflats were classified with high accuracy.

Table 5-14: Confusion matrix of the final sediment classification of the LiDAR data.

LiDAR – 2010	Ground truth		Classified	UA [%]	
	Mud	Sand			
Classes	Mud	30	6	36	83.33
	Sand	5	7	12	58.33
Ground truth		35	13	48	
PA [%]		85.71	53.85		
OA[%]	77.08	Kappa	0.40	No data	0

The proposed method misses to classify sand flats, but this disadvantage is compensated for by the sediment classification with RE in the hierarchical knowledge-based decision tree (see

5.2.2.4.2 Extraction of the tidal stream network and geometric features

Table 5-6; PA: 82-86% and UA: 76-80% for the class ‘sand’). In this context, only the information of the mudflats, derived from the LiDAR data, is added to the whole classification procedure.

The sub-channel systems that were assigned to the class ‘mud’ are modified by a buffer area. This buffer area has a diameter of 60m and defines the muddy area around the extracted stream network. The size of the diameter is set by expert knowledge, which is gained through several measurement campaigns in this study area. Figure 5-17 shows a subset as an example of a completely muddy area. It can be seen that just five out of 34 muddy sub-channel systems were not classified as ‘mud’.

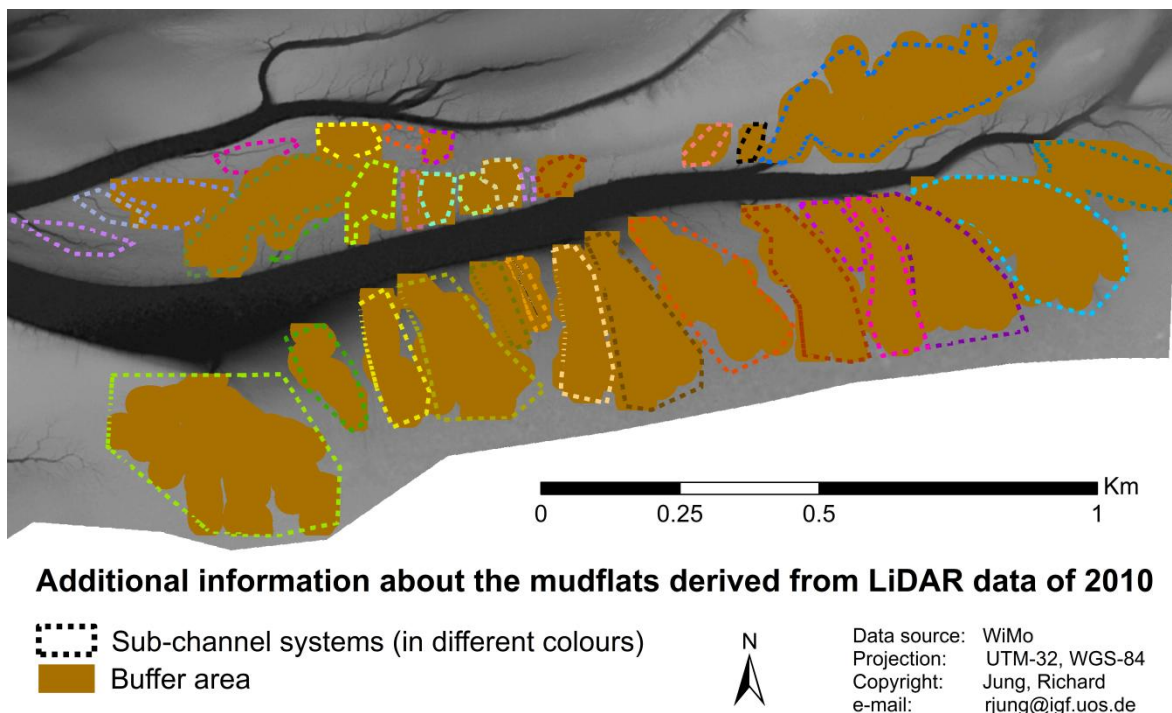


Figure 5-17: A subset of classified mudflats using geometric information derived from LiDAR data.

The derived information about the mudflat distribution was added to the existing hierarchical sediment classification from RE and a reanalysis of the classification accuracy was carried out. Table 5-15 shows that all values could be improved (bold green values) with the exception that the *UA* of ‘sand’ and the *PA* of ‘mixture’ decreases slightly. Of note is the improvement of the accuracies for the class ‘mud’, especially the *PA*. Even the Kappa coefficient doubles its value, which results in an accuracy that is definitely not randomly achieved. The *OA* increases by about 2.5%. The consistently accurate values for the classes ‘sand’ and ‘mixture’ show the high suitability of the derived geometric information for improving the classification of mudflats without harming the other sediment classes.

Table 5-15: Accuracy measures for the sediment classifications with the hierarchical knowledge-based decision tree and the additional information derived from LiDAR data.

RE of 25 April 2010 and LiDAR 2010		Ground truth			Classified	UA [%]
		Sand	Mixture	Mud		
Classes	Sand	261	38	29	328	79.57
	Mixture	33	46	11	90	51.11
	Mud	12	16	29	57	50.88
Ground truth		306	100	69	475	
PA [%]		85.29	46.00	42.03		
OA [%]		70.74	Kappa	0.41	No data	101

5.2.3 Intertidal classification with Random Forest

The input data for the RF classifications are identical to those of the hierarchical knowledge-based decision tree approach (e.g., RE, NDWI, MSAVI, TSX and texture parameter). Table 5-16 shows the accuracies for the sediment classification using RE and TSX in the RF classification approach with respect to the ground truth data of 2008/2009, 2010 and 2012. All results show moderate accuracies. The highest *OA* (66.31%) is obtained with the RE data of 11 July 2011 and TSX data of 16 July 2011 in combination. The results emphasize that the classifications using both RE and TSX can obtain on the one hand better results compared with one single data as input (*OA*=56%; 25 April 2010), but can also obtain worse results on the other hand (*OA* between 56% and 66%). The confusion matrices indicate moderate *PA* and *UA* for ‘sand’ (62-75% and 77-89%) and sometimes ‘mixture’ (54-72% and 30-33%), whereas the remaining class ‘mud’ has very low values of between 10-23% and 16-69%, respectively. The *UA* and *PA* show that, with decreasing grain size, the accuracy decreases with the RF classification approach. There is a strong tendency to confuse ‘mud’ with ‘sand’ or with ‘mixture’ and ‘sand’ with ‘mixture’. The low values are again the result of the strong similarity of the spectral signature influenced by water, mineral content, grain size or organic matter, as already explained in chapter 5.2.2.3. The accuracies of all three classifications show that the additional information of the radar data does not necessarily improve the classification result.

Figure A-7 shows the classification maps comprising all land cover classes. The general distribution or location of the sediments looks similar throughout the images. There are dry and wet sands predominant in the north and the west. Mixed sediments are most often located in the southern part of the study area. Differences can be seen in the size of the classified area. In the result of 27 June 2011 the borders of the TSX data can be seen very clearly, represented by the class ‘mixture’ in the southwestern part of the study area. A noticeable difference

between all images is the classification of ‘dry sand’. Every result has its own distribution and size of this class. The class ‘mud’ is located near the tidal inlets and shellfish beds on the classification maps of 25 April 2010 and 27 June 2011, whereas this class has almost disappeared by 11 July 2011. On the map of 22 October 2011 the class ‘mud’ is most often located in the northern part of the study area.

Table 5-16: Accuracy assessment for the supervised random forest sediment classifications.

April 2010		Ground truth			Classified	UA [%]
		Sand	Mixture	Mud		
Classes	Sand	146	8	9	163	89.57
	Mixture	66	45	36	147	30.61
	Mud	23	9	7	39	17.95
Ground truth		235	62	52	327	
PA [%]		62.13	72.58	13.46		
OA [%]	56.73	Kappa	0.27			
June 2011		Ground truth			Classified	UA [%]
		Sand	Mixture	Mud		
Classes	Sand	204	23	24	251	81.27
	Mixture	44	36	26	106	33.96
	Mud	22	7	15	44	34.09
Ground truth		270	66	65	365	
PA [%]		75.56	54.55	23.08		
OA [%]	63.59	Kappa	0.3			
July 2011		Ground truth			Classified	UA [%]
		Sand	Mixture	Mud		
Classes	Sand	199	17	21	237	83.97
	Mixture	59	42	26	127	33.07
	Mud	4	0	9	13	69.23
Ground truth		262	59	56	377	
PA [%]		75.59	71.19	16.07		
OA [%]	66.31	Kappa	0.33			
October 2011		Ground truth			Classified	UA [%]
		Sand	Mixture	Mud		
Classes	Sand	177	22	30	229	77.29
	Mixture	57	41	31	129	31.78
	Mud	33	3	7	43	16.28
Ground truth		267	66	68	401	
PA [%]		66.29	62.12	10.29		
OA [%]	56.11	Kappa	0.2			

The uneven distribution of the sediments implies a high dynamic between years as well as between the seasons, which would prove the general statements in the literature (Van der Wal et al. 2005; Sørensen et al. 2006; Van der Wal & Herman 2007; Park et al. 2010; Brockmann

& Stelzer 2008; Nieuwhof et al. 2015). For a better visualization and interpretation, a detailed comparison analysis with change statistics (Euclidean distance) and change maps was carried out. Table 5-17 shows the lowest Euclidean distance (Malik and Baharudin 2013) between the sediment classification of 27 June 2011 and 11 July 2011, which was as expected. They are acquired in the same season and year within a 14-day interval. The highest distance occurs between 27 June 2011 and 22 October 2011. Figure A-8 shows the sediment changes coloured blue. Most of the changes occur in the northern and western part, which simultaneously mark the ‘dynamic’ areas. In comparison with the results of the hierarchical knowledge-based decision tree, the dynamic is not based on flow velocities or the movement of the sediments. It is more likely based on the change of moisture, because most of the change occurs between ‘dry sand’ and ‘wet sand’. Only a few areas near the intertidal inlet and in the southeastern part really change their grain size (e.g., from mud to sand). This means that only a small amount of dynamic, in terms of sediment movement, can be seen, if Figure A-7 and A-8 are analysed in combination. This would imply that the tidal flats South of Norderney are highly stable, which is in contrast to the hierarchical knowledge-based decision tree and the opinion of the literature.

Table 5-17: Euclidean distances between the sediment classifications of the RF approach.

	April 2010	June 2011	July 2011	October 2011
25 April 2010	---	1931	1739	2126
27 June 2011	1931	---	1534	2279
11 July 2011	1739	1534	---	2024
22 October 2011	2126	2279	2024	---

In Figure A-7, the distribution of the class ‘salt marsh’ looks similar throughout all land cover maps. Most of the area is located at the south- and northwestern shore. A difference occurs in October 2011 in the northwestern part. There, the area of salt marsh is larger compared with the other results (see Figure A-9). In this context, a change of the salt marsh vegetation can be assumed. This assumption is revised by the areal comparison of the classification and reference in Table 5-18. The best result is obtained with the data of 25 April 2011 achieving a difference of 0.08km², 0.12km² of *FP* and 0.03km² of *FN*. This shows a tendency to over-classify the salt marsh distribution. In comparison, the other results tend to under-classify the salt marsh distribution, which is proven by the *FN* (0.23km²-0.4km²). Most of the *FN* are located at the southeastern and northwestern shoreline. At these areas, the RF classification is not able to discriminate between vegetation and sediments, due to a mixture of the spectral signature of both land covers. The value for *FN* decreases in October 2011 slightly, which

explains the increasing area of salt marsh in the northwestern part in plot d) of Figure A-7. This means that the increasing area of salt marsh in October 2011 is not an actual change, but a change due to a better classification result.

Table 5-18: Spatial comparison of the salt marsh classifications and the corresponding reference data using random forest.

Acquisition date	Overall area [km ²]	Ref. Area [km ²]	Diff. [km ²]	FP [km ²]	FN [km ²]
April 2010	0.70	0.62	0.08	0.12	0.03
June 2011	0.72	1.11	0.38	0.01	0.40
July 2011	0.76	1.08	0.32	0.02	0.34
October 2011	0.90	1.10	0.19	0.04	0.23

The assumptions of the areal comparison are confirmed by the binary confusion matrices of Table 5-19. The highest accuracies ($TPR=94.23\%$ and $P=82.5\%$) are obtained with the image of 25 April 2010, which confirms the tendency of over-classifying. In comparison, the other results obtain moderate values for TPR (63-78%) and very high values for P (95-97%), which approves the tendency to miss reference areas (i.e., FN). The OA is always 99%, which is due to the unevenly distributed amount of reference data (see P_r of Table 5-19). In this context, the accuracies for the class ‘no salt marsh’ (e.g., TNR and NPV) are very high. The accuracies show that mapping methods based on electro-optical data alone provide better results classifying salt marshes than including additional single polarized radar data (compare with Table 5-5). This finding is approved by Gebhardt et al. (2011), who compared TSX quadpol data with vegetation indices (e.g., $MCARI/MTVI2$, $TCARI/OSAVI$ and $NDVI$) derived from RE data. They state that significant correlation between multi-polarised radar backscattering and the $MCARI/MTVI2$, $TCARI/OSAVI$ could be found. Furthermore, Beijma, Comber & Lamb (2014) state that longer SAR wavelengths are more suited to vegetation mapping.

To compare the results with the hierarchical knowledge-based decision tree of chapter 5.2.2.2, a post-classification comparison as change detection was carried out, although moderate accuracies were achieved. Figure A-9 shows the change maps. Figure 5-18 summarizes the areal change in a bar chart. The increase and decrease in the area is almost the same from April 2010 to June 2011. From June 2011 to October 2011 the area successively increases (see OA of Table 5-18), which shows a totally different trend compared with Figure 5-7. This would mean that, even at the end of the growing season in October, the salt marsh vegetation still spreads.

Table 5-19: Accuracy assessment for the supervised random forest salt marsh classifications.

Classification of April 2010				
		No salt marsh	Salt marsh	Sum
Reference	No salt marsh	1549903	4923	1554826
	Salt marsh	1422	23212	24634
	Sum	1551325	28135	1579460
	<i>OA [%]</i>	99.60	<i>P_r [%]</i>	1.56
	<i>TPR [%]</i>	94.23	<i>P [%]</i>	82.50
	<i>TNR [%]</i>	99.68	<i>NPV [%]</i>	99.90
Classification of June 2011				
		No salt marsh	Salt marsh	Sum
Reference	No salt marsh	1534448	742	1535190
	Salt marsh	16045	28225	44270
	Sum	1550493	28967	1579460
	<i>OA [%]</i>	98.93	<i>P_r [%]</i>	2.80
	<i>TPR [%]</i>	63.75	<i>P [%]</i>	97.43
	<i>TNR [%]</i>	99.95	<i>NPV [%]</i>	98.96
Classification of July 2011				
		No salt marsh	Salt marsh	Sum
Reference	No salt marsh	1535126	800	1535926
	Salt marsh	13932	29602	43534
	Sum	1549058	30402	1579460
	<i>OA [%]</i>	99.06	<i>P_r [%]</i>	2.75
	<i>TPR [%]</i>	67.99	<i>P [%]</i>	97.36
	<i>TNR [%]</i>	99.94	<i>NPV [%]</i>	99.10
Classification of October 2011				
		No salt marsh	Salt marsh	Sum
Reference	No salt marsh	1533671	1645	1535316
	Salt marsh	9502	34642	44144
	Sum	1543173	36287	1579460
	<i>OA [%]</i>	99.29	<i>P_r [%]</i>	2.79
	<i>TPR [%]</i>	78.47	<i>P [%]</i>	95.46
	<i>TNR [%]</i>	99.89	<i>NPV [%]</i>	99.38

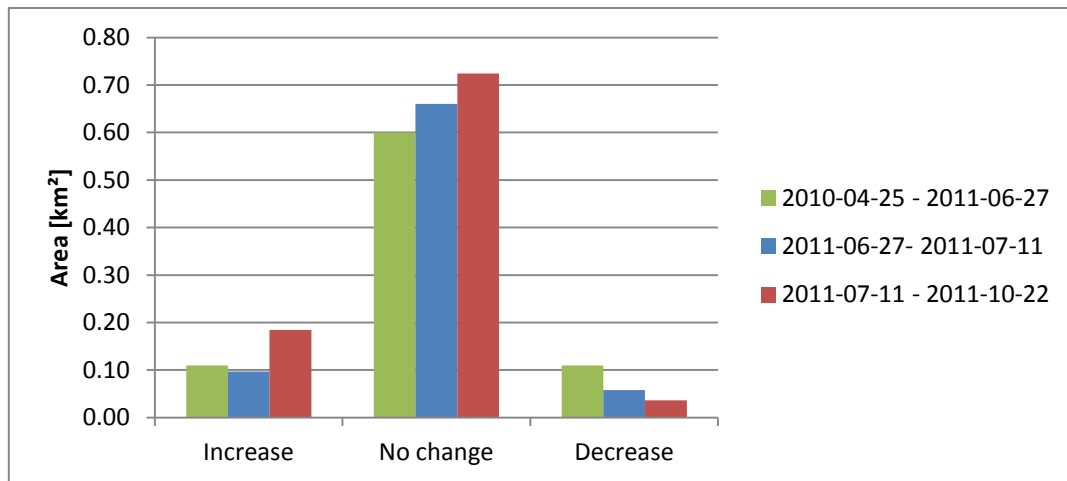


Figure 5-18: Bar chart of the salt marsh changes in km² from 25 April 2010 to 27 June 2011, from 27 June 2011 to 11 July 2011 and from 11 July 2011 to 22 October 2011. The results are obtained using the random forest classification.

The classification results of the shellfish beds in Figure A-7 are very diverse. Due to the missing radar data in April 2010, the area assigned as shellfish beds is very small (see Table 5-20). Even the big shellfish beds in the western and eastern part of the study area could not be estimated (displayed in Figure 5-3). In contrast, the result of July 2011 shows too many shellfish beds (FP=2.95km²), especially in the northern parts near the salt marshes or next to the tidal inlet. The false allocation near the salt marshes in the northern and southern part is also present in the classification results of June and October 2011 (FP=0.58km² and FP=0.68km²). Mapping methods for shellfish beds in intertidal flats in combination with electro-optical data often do not perform well because of the presence of macroalgae on shellfish beds (Dehouk et al. 2011). In general, macroalgae is settled down on top of shellfish beds, which leads, in combination, to a high MSAVI and backscatter value for this class. In this context, vegetated areas have a chance to be assigned to that class. Because of this possibility, the hierarchical knowledge-based decision tree uses only radar data to estimate shellfish beds. Table 5-20 summarizes the spatial extent of the classification results compared with the reference data. The result of July 2011 is the only one that tends to highly over-classify (e.g., false positives). The other results have the tendency to miss reference areas and overall to assign far too little.

Table 5-20: Spatial comparison of the shellfish bed classifications and the corresponding reference data using random forest.

Acquisition date	Overall area [km ²]	Ref. Area [km ²]	Diff. [km ²]	FP [km ²]	FN [km ²]
April 2010	0.26	1.68	1.42	0.07	1.50
June 2011	1.12	1.68	0.55	0.58	1.13
July 2011	3.84	1.68	2.16	2.95	0.79
October 2011	1.07	1.68	0.6	0.68	1.28

5.2.3 Intertidal classification with Random Forest

Table 5-21 proves the above described assumptions. For the parameter *TPR*, low to moderate values (11-53%) are obtained. This means that, in general, more than 50% of the reference data were not achieved (i.e., FN). The other areas, which were assigned to ‘shellfish beds’, are false allocations (i.e., FP), which is described by the parameter *P* (23-72%). This is especially the case for the results of July and October 2011 ($P=23\%$ and $P=36\%$), which exhibit between 77% and 64% of *FP*.

Due to the low to moderate values for the parameters *TPR* and *P* throughout all results, a change detection was not carried out.

Table 5-21: Accuracy assessment for the supervised random forest shellfish bed classifications.

Classification of RE from 25 April 2010				
Reference of 2011		No shellfish	Shellfish	Sum
		No shellfish	1509285	2891
	Shellfish	59784	7500	67284
	Sum	1569069	10391	1579460
	<i>OA</i> [%]	96.03	<i>P_r</i> [%]	4.26
	<i>TPR</i> [%]	11.15	<i>P</i> [%]	72.18
	<i>TNR</i> [%]	99.81	<i>NPV</i> [%]	96.18
Classification of RE from 27 June 2011 and TSX 02 June 2011				
Reference of 2011		No shellfish	Shellfish	Sum
		No shellfish	1488801	23375
	Shellfish	45524	21760	67284
	Sum	1534325	45135	1579460
	<i>OA</i> [%]	97.03	<i>P_r</i> [%]	4.25
	<i>TPR</i> [%]	32.34	<i>P</i> [%]	48.21
	<i>TNR</i> [%]	98.45	<i>NPV</i> [%]	97.03
Classification of RE from 11 July 2011 and TSX 16 July 2011				
Reference of 2011		No shellfish	Shellfish	Sum
		No shellfish	1393886	118290
	Shellfish	31693	35591	67284
	Sum	1425579	153881	1579460
	<i>OA</i> [%]	90.50	<i>P_r</i> [%]	4.25
	<i>TPR</i> [%]	52.89	<i>P</i> [%]	23.12
	<i>TNR</i> [%]	92.17	<i>NPV</i> [%]	97.77
Classification of RE from 22 Oct. 2011 and TSX 28 Oct. 2011				
Reference of 2011		No shellfish	Shellfish	Sum
		No shellfish	1484820	27356
	Shellfish	51478	15806	67284
	Sum	1536298	43162	1579460
	<i>OA</i> [%]	96.64	<i>P_r</i> [%]	4.25
	<i>TPR</i> [%]	23.49	<i>P</i> [%]	36.62
	<i>TNR</i> [%]	98.19	<i>NPV</i> [%]	96.64

5.3 Spectrometry data

The abovementioned results of the intertidal sediment classifications showed that mapping sediment remains difficult with electro-optical and LiDAR data. Therefore, hyperspectral sensors might improve the ability to distinguish between intertidal sediment types and define the necessary wavelengths. In order to identify sediments and map them, a basic underlying premise is that the sediment types are indeed spectrally separable. This means that the variance of the reflectance must be greater between types than within types (i.e., high Jeffries-Matusita distance). In this context, two feature selection methods (JMDFS and ReliefF) are applied and the results will be compared. Both approaches make the attempt to reduce dimensionality while preserving relevant information for posterior sediment classification. In general, feature selection methods have the following benefits (Gomez-Chavo et al. 2003; Li et al. 2014):

- They reduce high dimensionality of the feature spaces (i.e., Hughes phenomenon or curse of dimensionality) and thereby increase the performance of the classifier. Furthermore, it allows faster calculations and makes the training of iterative methods possible (e.g., neural network).
- The class discrimination can be increased.
- They identify physical meanings and relate them to the selected bands.

In order to guarantee a meaningful comparison between the different feature selection algorithms, an experimental protocol was designed to meet the following criteria: 1) in the stage of feature pre-processing, the inputs were kept identical and only the feature selection methods varied; 2) for each method, optimal parameters were carefully selected so that their best-case performance is evaluated (e.g., ‘peaks’ and ‘ranges’). From the second criterion arises a problem that still needs to be addressed, that of how to determine the optimal parameters for respective algorithms to achieve best possible performance. For that purpose, a supervised classification approach (RF) is used to evaluate the effectiveness of the two different feature selection methods. The analysis focuses on the comparison between the accuracies for classifications obtained when 1) all bands were included and 2) only a number of selected bands were included.

However, first the spectral features of the measurements by means of the data from 2015 will be discussed. Without a more detailed compositional analysis of the measurements, a relation between the spectral variations and features to geophysical or chemical properties, such as

grain size, water, chlorophyll or organic matter content, cannot be carried out in this thesis. In this context, the impact of the most specific reflection features on general vegetation and sediment properties will be described. Figure 5-19 shows the mean spectra of 2015 (i.e., 14 classes of 2015), which will be the example for the description.

In general, it is well accepted that with increasing moisture content the reflectance values decrease, whereas longer wavelengths are more affected than shorter wavelengths (Ibrahim et al. 2009; Baumgardner 1985; Verpoorter, Carrere & Combe 2014; Small et al. 2009). This is true until a certain moisture content is achieved and specular reflection occurs, which increases the reflectance (Ibrahim et al. 2009; Baumgardner 1985). Vice versa, the response of soil reflectance to the disappearance of water is not linear (Verpoorter, Carrere & Comber 2014). A specific effect of increasing moisture content can be seen in the absorption band of water at wavelengths 970nm and 1,200nm (Verpoorter, Carrere & Combe 2014; Bachmann 2007). There, a huge decrease in reflectance occurs if the sediment is covered by water. Both effects are clearly represented in Figure 5-19. Four classes have the suffix 'water' (see Table 4-5) with high reflectance values in the visible part of the electromagnetic spectrum (i.e., specular reflection) and low reflectance in the NIR region values at 970nm and 1,200nm (blue spectra in Figure 5-19). Verpoorter, Carrere & Comber (2014) state that the absorption feature at 970nm should be used to describe the hydration states of the sediments. Lobell & Asner (2002) confirm that longer wavelengths are more applicable, but state that the SWIR region (1,400nm-3,000nm) is more reliable to quantify water content than the visible light and NIR (VNIR) region. Between the wavelengths of 450nm-520nm (i.e., blue band) and 625-690nm (i.e., red band), plant specific absorption features occur, such as β -carotene, chlorophyll a and b (Bajwa et al. 2014; Schmidt & Skidmore 2003; Decho et al. 2003). Furthermore, biomats create a linear decrease of 10%-20% over the whole spectra (Decho et al. 2003). The high absorption of all spectra at approximately 674nm is accompanied by chlorophyll a. In general, it can be observed by small reflectance values in the absorption feature between 625nm-690nm (smallest reflectance at approximately 674nm). In addition, it is related to the moisture content. This means that, with increasing moisture content, the reflectance in the absorption feature increases (Ibrahim et al. 2009). This is also represented by the four mean spectra coloured blue in Figure 5-19, which have higher reflectance values in the wavelength range of 450nm-690nm. The two purple spectra with the lowest reflectance at 674nm have seagrass partially grown on top of the sediments. The shape of their spectral curve in the VNIR region looks like a standard vegetation spectrum. In general, red and NIR regions are more responsive to partially vegetated surfaces, due to the role of plant pigments in attenuating

visible light bands and of biomass (cell structure) in attenuating NIR wavelengths (Bajwa et al. 2004). This means high absorption between 450nm-520nm and 625nm-690nm and high reflectance between 520nm-625nm and after 690nm. After approximately 800nm, the spectral curve behaves like a soil spectrum, which, in general and depending on moisture content, increases with longer wavelengths until 1,300nm (Verpoorter, Caerre and Combe 2014; Hadjimitsis et al. 2013; Decho et al. 2003; Bachmann 2007). The spectral curve of the red spectra in Figure 5-19 is very similar to the once mentioned earlier (i.e., purple spectra). However, these spectra do not have macro-vegetation on top. They are only influenced by microalgae, such as diatoms. The microalgae have a very high absorption feature in the range of 650nm-690nm, due to chlorophyll, and a high reflectance in the red-edge and NIR region. Diatoms, for instance, use chlorophyll a and c to collect energy from the sun through photosynthesis. Furthermore, several mean spectra (coloured black) have almost the same shape as the red spectra, only distinguishable by their reflectance values between 650nm-1,250nm. They do not have any visible features, such as vegetation or microalgae, on top of the surface. In this context, the difference between 650nm-690nm is due to the missing vegetation and between 690nm-1,250nm due to the organic matter content that decreases all reflectance values in the range of 400nm-2,500nm (Ibrahim et al. 2009; Bajwa et al. 2004; Bachmann 2007). Nevertheless, there is absorption at 674nm, which shows the presence of microalgae. This means that this specific wavelength can be used to discriminate between different amounts of microalgae. The overall reflection of dry sediments increases with increasing mud content and the absorption at specific clay absorption features increases. Furthermore, mineral content such as iron, calcium and magnesium have an influence on the spectral curve in the visible light region. However, the high moisture content of intertidal sediments hampers the scattering of clay particles and mineral content; thus this effect can be neglected (Ibrahim et al. 2009; Bajwa et al. 2004). Shellfish beds or mussels have a very inhomogeneous appearance (e.g., covered by vegetation or sediments), which makes it difficult to define spectral features and to detect them spectrally (see Table 5-21). The assumptions made above cannot be approved, due to a lack of a detailed compositional analysis of the sediments. However, the spectral curves showed consistency with theoretical expectations and published research shows that VNIR (far red, red edge) and SWIR regions of the electromagnetic spectrum carry valuable information on vegetation and soil characteristics (Ibrahim et al. 2009; Verpoorter, Caerre & Combe 2014; Hadjimitsis et al. 2013; Decho et al. 2003; Baumgardner 1985; Small et al. 2009; Bajwa et al. 2004; Gao & Zhang 2006; Schmidt & Skidmore 2003; Brockmann & Stelzer 2008). The black dashed lines, representing the

bands of RE, clearly miss the important wavelengths of the spectral features. This shows the ineffectiveness of the RE sensor for mapping intertidal sediments, which was already revealed in chapter 5.2.2.3. Some additional bands between 550nm-650nm, at 674nm and at 970nm would enhance the discrimination capability.

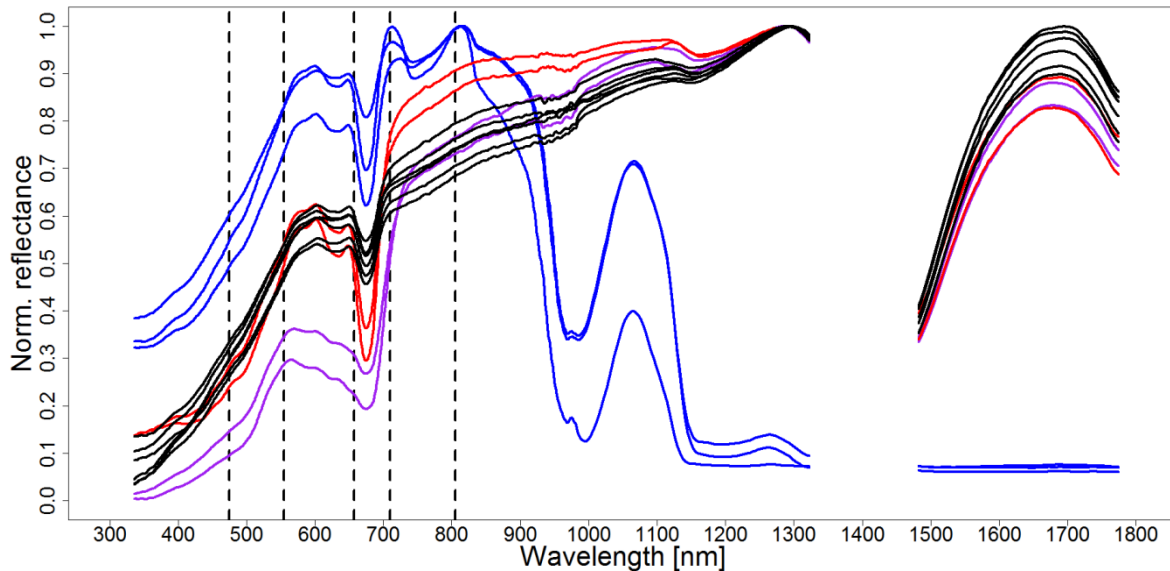


Figure 5-19: Normalized mean reflectance of the classes from 2015 coloured by their specific influences. The red spectra are influenced by microalgae, the blue by water, the purple by seagrass and the black by nothing specific. The black dashed lines are the wavelengths of the RE bands.

Subsequent to the execution of the JMDFS for discrimination of sediment spectra, three questions emerged: 1) Are there any common wavelengths between one spectrum and all the others that remain every time and which can be used to discriminate one spectrum with high accuracy? 2) Is there an overlap between these common wavelengths to define wavelengths that can be used to discriminate all sediment classes with high accuracy? 3) Do the common wavelengths match the theoretical expectations from the literature? To answer these questions, first the remaining wavelengths were plotted for each spectrum, such as that represented in Figure 4-30 or Figure 5-20.

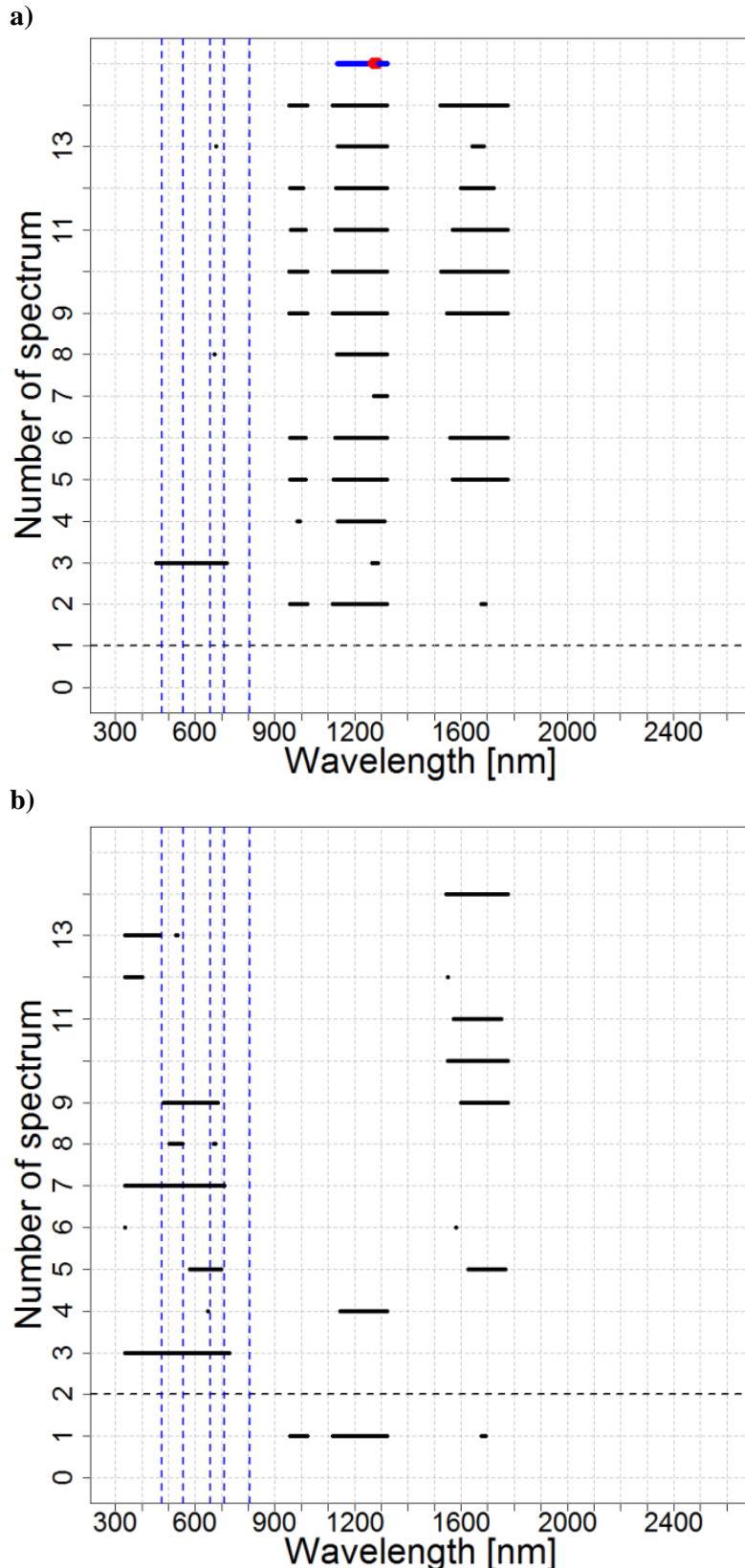


Figure 5-20: Two examples of 2013 for the analysis of the JMDFS for common wavelengths between all combinations of one spectrum to all the others. The black dots/lines representing the remaining wavelengths after achieving a JMD greater than 1.9, the red dots/ lines represent a 100% accordance between all combinations, the blue dots/ lines on plot a) represent an accordance greater than 80%, the blue dashed line are the wavelengths of RE and the black dashed line represents the actual spectrum that is compared with all the others. Plot a) represents the common wavelengths between spectrum 1 and all the others and plot b) represents the same for spectrum 2.

Plot a) compares, for instance, spectrum one ('Mix_Greenalgae'; Table 4-5) with all the other spectra. The remaining wavelengths (black dots), which generate a JMD greater than 1.9, were plotted, while the wavelengths that occur in every combination (red dots; appr. 1,250nm-1,300nm) and wavelengths with greater than 80% occurrence (blue dots; 1,000nm-1,300nm) were marked. The red and blue dots represent the common wavelengths. Plot b) compares spectrum two ('Mix_Seagrass'; Table 4-5) with all the others. In this example no common wavelengths could be found in any combination. Repeating this analysis for all of them revealed that in each comparison different wavelengths remained. Therefore, common bands with 100% accordance could be found only for one spectrum of 2013 and two spectra of 2015. If the threshold is lowered to greater than 80% accordance, then the result rises to three and four spectra for 2013 and 2015, respectively. These initial results revealed that far too few common bands were found, which could be used to discriminate the sediment spectra from each other. To overcome this drawback, the relative frequency of each remaining wavelength was calculated and displayed in a plot. Figure 5-21 shows the results for 2013 and 2015. The higher the relative frequency (red line), the higher the importance of the wavelength. Two totally different results were achieved for both spectra measurements using the JMDFS method. In 2013 the wavelengths between 440nm-711nm and 1,570nm-1,774nm have the highest relative frequency (>20%). These two wavelength ranges represent the visible light (appr. 390nm-700nm) and the SWIR part of the electromagnetic spectrum (e.g., Landsat-8). This means that these wavelengths responded to intertidal soil characteristics very well. Furthermore, there is a small increase in the NIR range between 959nm-1,010nm and 1,152nm-1,322nm. The result of 2015 is more diverse in terms of the relative frequency values, although almost the same wavelength ranges are in focus (572nm-700nm; 957nm-1,010nm; 1,114nm-1,322nm; 1,496nm-1,774nm). The longer wavelengths (NIR and SWIR) achieved higher relative frequencies and wavelengths shorter than 1,322nm have a relative frequency of zero less often compared with 2013. In this context, more wavelengths have an importance for the discrimination. Both results show significant differences between the values for the relative frequency that leads to a pattern, composed of sharp decreases and increases.

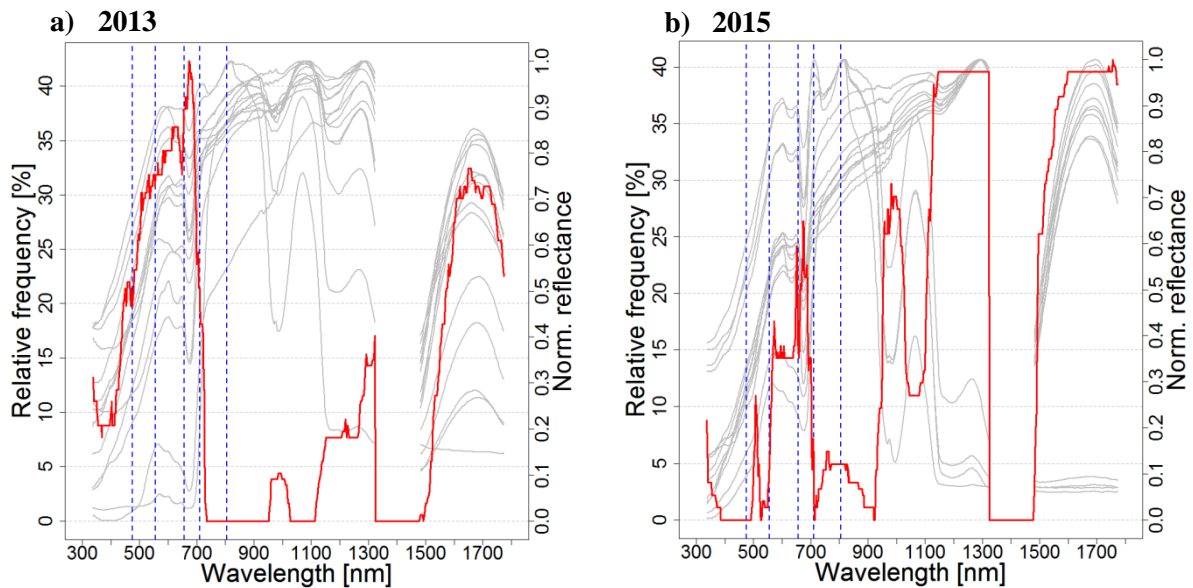


Figure 5-21: The result of the JMDFS feature selection method. The red line represents the relative frequency (i.e., importance) of the wavelengths, the grey lines are the mean spectra of the selected classes (e.g., 14 classes) and the blue dashed lines are the wavelengths of the RE bands.

Figure 5-22 shows the results of the feature extraction approach ReliefF for the years 2013 and 2015. The red line represents the importance of each wavelength expressed as unitless weight. In 2013 the most important wavelengths are shorter than 691nm or longer than 1,540nm. In between, several peaks (e.g., 940nm, 1,060nm, 1,186nm and 1,322nm) occur that increase to a certain wavelength and decrease immediately afterwards. A significant decrease in weight can be noticed after 691nm. In comparison, the result of 2015 has a significant decrease in weight after 817nm. On the other hand, high weights for the wavelengths between 718nm-829nm, 1,163nm-1,322nm and 1,540nm-1,774nm were achieved. This means that there is a significant amount of information in the red, red edge and far NIR regions that is relevant to intertidal soil characteristics. The wavelengths shorter than 718nm and between 905nm-1,129nm (peak at 976nm) have a fairly low importance. Neither result achieved a wavelength with a weight equal to zero. In this context, all wavelengths have a distinctive importance for the discrimination. Similarly to the result of the JMDFS approach, the pattern of both results are totally different, but nearly the same wavelengths are in focus. From Figure 5-21 and Figure 5-22, it can be concluded that both feature extraction approaches derived almost the same wavelength ranges as most important. The only difference occurs in 2015, where ReliefF has an additional wavelength range (718-829nm) with high values compared with the result of JMDFS. In general, it can be noted that a lot of consecutive wavelengths with almost the same weight were derived by the JMDFS and ReliefF algorithm, which is due to the fact that JMDFS and ReliefF rank wavelengths only on their discriminatory capability, without considering the correlation between them.

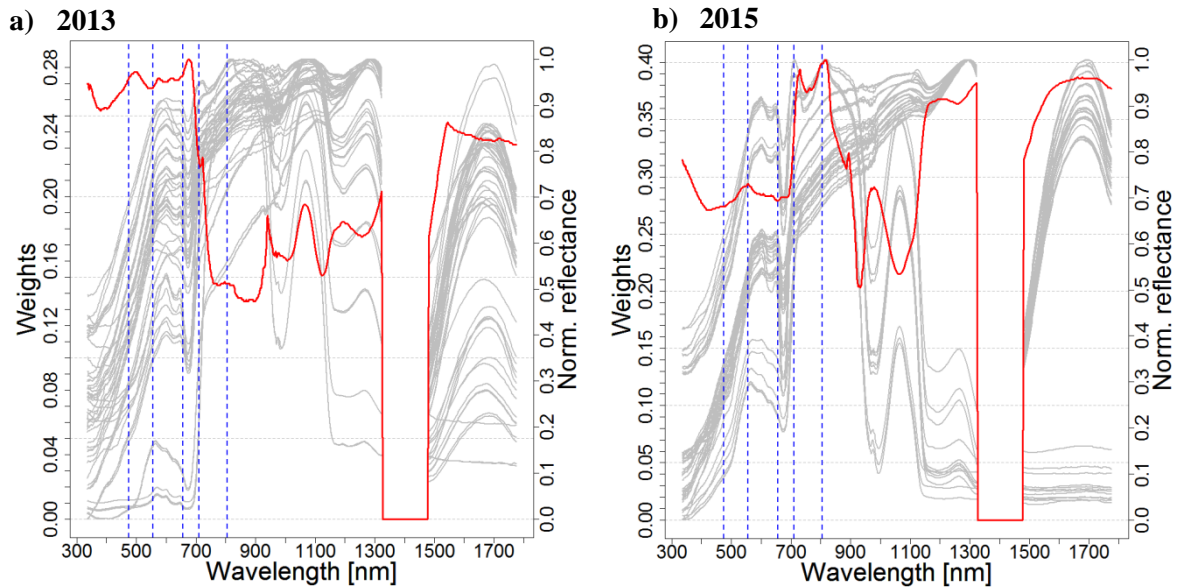


Figure 5-22: The result of the ReliefF feature selection method. The red line represents the weights (i.e., importance) for the wavelengths, the grey lines are every measured spectra (50 samples in 2013 and 45 samples in 2015) and the blue dashed lines are the wavelengths of the RE bands.

Applying the approach ‘peaks’ and ‘ranges’ from chapter 4.5.3 (to get the best feature set), the wavelengths of Table 5-22 and Figure 5-23 for both years and feature selection methods were selected. All entries in the table with a hyphen represent consecutive wavelengths. Altogether, between 14 and 321 important wavelengths were selected. Figure A-10 to A-14 visualizes the information of Table 5-22 and Figure 5-23 in detail. It can be observed that the proposed methods really retain the macro-shape of the spectral curves. In general, more wavelengths are selected by JMDFS. Furthermore, it selects more wavelengths in 2015 than in 2013, which is not consistent with ReliefF, which selects more wavelengths in 2013. Between both years and feature selection methods occur very few accordances of the most important wavelengths, especially for the approach ‘peaks’. It is more likely that they are in the same wavelength region (e.g., red band), but with difference ranging from 3nm-50nm, or even more. This is due to the unique technique by which each method selects bands. The accordance between both methods of selection can be neglected, because the approach ‘ranges’ is based on the approach ‘peaks’. The number of selected wavelengths for ReliefF with the approach ‘peaks’ is balanced over the whole data and years, whereas the JMDFS is more focused on different regions in each year. With the approach ‘ranges’ the accordance improves, which is due to the steplike results of JMDFS that widen the selection significantly. Furthermore, the plateaus built by JMDFS in 2015 leads to many wavelengths that are selected in the NIR and SWIR region. All results except for ReliefF 2015 have at least one selected wavelength in all of the abovementioned feature ranges from the literature with less than 3nm difference. Additional information of the SWIR region was also selected. This

information will be removed in the latter classification approach to analyse the impact. For the result of ReliefF, fewer bands in the visible range of the electromagnetic spectrum (compared with JMDFS) were chosen, which matches with the onsite observations, since mud, mixed sediments and sand have mostly the same colour.

Table 5-22: Selected wavelengths in [nm] from JMDFS and ReliefF applying 'peaks' and 'ranges' to the data of 2013 and 2015.

2013				2015			
JMDFS		ReliefF		JMDFS		ReliefF	
Peaks	Ranges	Peaks	Ranges	Peaks	Ranges	Peaks	Ranges
336	336-349	336	336-355	336	336-339	336	336-371
402	455-466	339	471-520	507	502-512	555	527-577
447	591-641	345	570-580	517-520	569-573	608	721-736
456-465	655-690	396	614-626	531-537	648-652	633	790-824
478	958-1014	497	661-687	572	663-687	723	890-896
505-508	1288-1322	498	720-723	582	727-880	729	950-1018
531	1606-1746	576	938-946	594	952-1022	762	1182-1235
563		619	1042-1091	605	1114-1322	815	1296-1322
580		620	1171-1224	649	1544-1774	893	1606-1749
582-584		675	1307-1322	672		968	
614-633		721	1537-1599	686		978	
660-664		940		708		1201	
671-676		950		754-762		1322	
704		967		957		1678	
959-1006		1065		969			
1220		1194		981			
1228		1197		955			
1292		1322		1144-1322			
1322		1544		1598-1767			
1649							
1653							
1656							
1660							
76	165	19	150	125	321	14	213

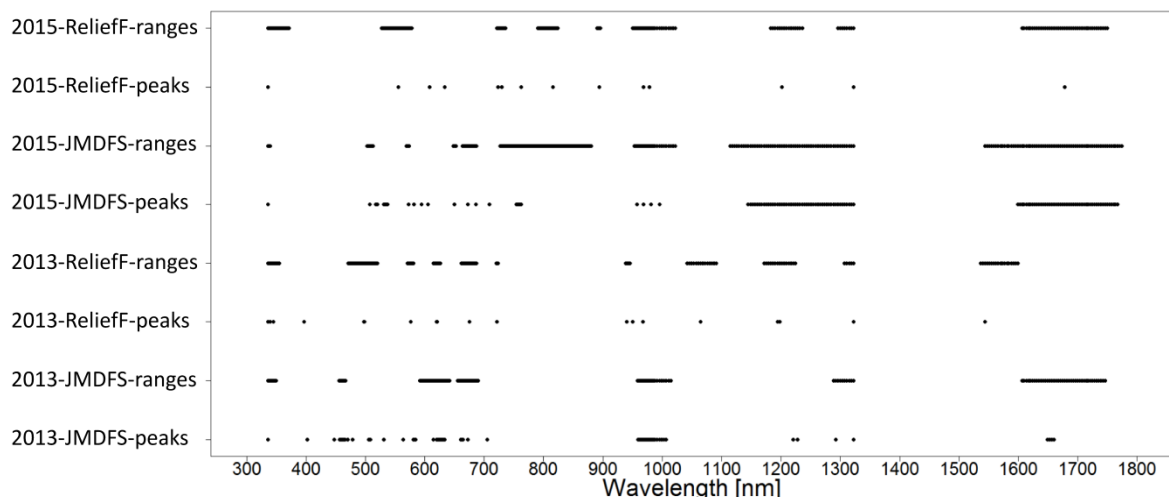


Figure 5-23: Comparison of all selected wavelengths for JMDFS and ReliefF of 2013 and 2015.

After the final wavelength combination was found, an RF classification was performed on the selected subset of wavelengths using a three-fold cross-validation to evaluate the effectiveness of the selected wavelengths. To assess the performance, the overall accuracy (OA) and Kappa coefficient were calculated. From Table 5-23 it can be observed that the approach ReliefF with the approach ‘peaks’ outperforms the other classification results for the year 2013. However, the mean OA (80%) of methods JMDFS and ReliefF with the approach ‘ranges’ is only 2% lower. Far behind are the results obtained for all wavelengths (69%) and the approach ‘ranges’ applied to the JMDFS algorithm (68%). In comparison with the result for all wavelengths, the methods JMDFS and ReliefF could improve the accuracy by 11%-13%. In 2015, both ReliefF and JMDFS (with different approaches) achieved a very high OA of 95%. It can also be noted that the result for all wavelengths is very high (91%), leading to an improvement of only 4%. A lower OA of 82% is obtained with JMDFS and the approach ‘peaks’. The values for Kappa show that the results are not a result of a random allocation process and that the classifications are very robust.

Table 5-23: Overall accuracies in percentage of the spectrometric data classifications with RF. The best results are highlighted in green colour. The value after the slash is the result of the adjusted version that explained after the table.

OA[%]	2013					2015				
	Raw	R _P	R _R	J _P	J _R	Raw	R _P	R _R	J _P	J _R
1	68	84	89	78	68	93	93	93	93	100
2	73	84	78	89	63	100	100	100	80	100
3	68	79	78	73	73	80	93	86	73	86
Mean	69	82	80	80/81	68	91	95	93	82/91	95
Kappa	Raw	R _P	R _R	J _P	J _R	Raw	R _P	R _R	J _P	J _R
1	0.61	0.81	0.88	0.75	0.63	0.92	0.92	0.92	0.92	1.0
2	0.69	0.82	0.76	0.88	0.59	1.0	1.0	1.0	0.78	1.0
3	0.64	0.76	0.78	0.70	0.70	0.78	0.92	0.85	0.71	0.85
Mean	0.64	0.79	0.80	0.77	0.64	0.90	0.94	0.92	0.80	0.95
	Raw = all wavelengths	R _P = ReliefF with ‘peaks’	R _R = ReliefF with ‘ranges’	J _P = JMDFS with ‘peaks’	J _R = JMDFS with ‘ranges’					

The results of Table 5-23 show that, on average, the approach ReliefF obtains slightly higher accuracies compared with JMDFS. Furthermore, the approach ‘peaks’ operates better with ReliefF and for JMDFS no unique and generally applicable approach can be observed. However, the approach ‘peaks’ appears to be the better method, because fewer consecutive wavelengths were selected and overall higher accuracies were achieved. In case of the JMDFS, this method has to be adjusted, because the algorithm generates plateaus, which result in many consecutive wavelengths. To prune those redundant wavelengths, the first, centre and last wavelength of a plateau are selected. The number of wavelengths was further

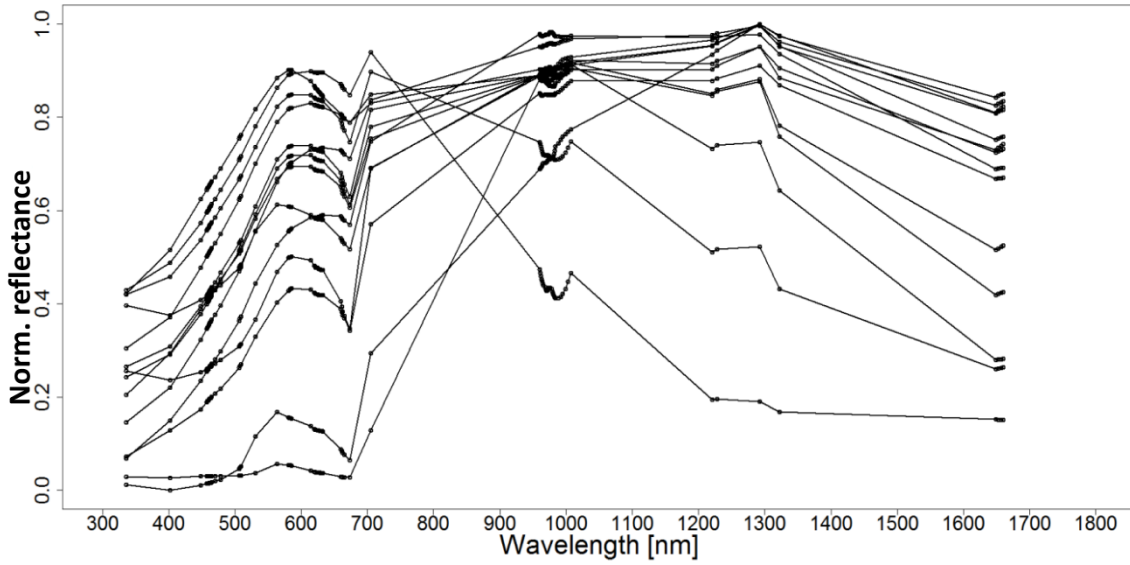
reduced from 76 to 50 and 125 to 35, respectively. The selected number of wavelengths and the adjusted (i.e., reduced) number of wavelengths can be seen in Figure 5-24 for 2013 and in Figure 5-25 for 2015 as discrete spectral band values that were linked for better comparison. Due to this adjustment, the *OA* improves to a mean of 81% (80%, 85% and 78%) for 2013 and to a mean of 91% (93%, 100% and 80%) for 2015. The Kappa coefficient improves to 0.79 (0.79, 0.84, 0.76) for 2013 and to 0.90 (0.92, 1.0, 0.78) for 2015. With the new *OAs*, the result of 2013 is almost equal to the result of ReliefF, but it is still worse in 2015. In this context, either another method of selection has to be applied or both approaches have to be applied every time the JMDFS method is used.

A second adjustment of the wavelength selection was carried out, due to the wavelength ranges represented in the literature. The information of the SWIR region was eliminated. The results showed a decrease of 2%-5% in accuracy for all results. In this context, the SWIR region is not necessarily needed to obtain high classification accuracies, which disagrees with the statements from the literature (Sørensen et al. 2006; Van der Wal & Herman 2007; Ibrahim et al. 2009; Lobell & Asner 2002).

Related to the best approach 'peaks', the most selected wavelengths are between 500nm-700nm (red and red-edge) and 950nm-1,000nm (NIR). This means that the intertidal sediments can best be discriminated by their amount of macrophytes (e.g., seagrass), microalgae (e.g, diatoms) and water content, which represents the properties of the sediments, as shown in Table 4-1. Some wavelengths were occasionally selected in the blue, green, NIR (700-950nm) and SWIR region of the electromagnetic spectrum.

Although the accuracy results of JMDFS are slightly less successful and no unique method of selection exists to choose the appropriate wavelengths every time, the processing time is significantly smaller. A personal computer configuration with an Intel® Core™ i7-860 processor, 8 GB RAM (random access memory) and Windows 7 Professional (64-bit) was used. The JMDFS needs 30min to obtain a final result, with the setting of 703 wavelengths and 14 classes. In comparison, ReliefF needs approximately 2h and 10min for one temporary result (703 wavelengths and 45-50 samples). However, the temporary result is not reproducible, due to the algorithm randomly selecting a class. This means that the algorithm has to be performed several times and these results have to be averaged to get one representative result. This extends the calculation time depending on the number of iterations. In this study, 50 iterations were executed, which resulted in approximately four days of processing time.

a) 2013, JMDFS, peaks



b) 2013, JMDFS, peaks adjusted

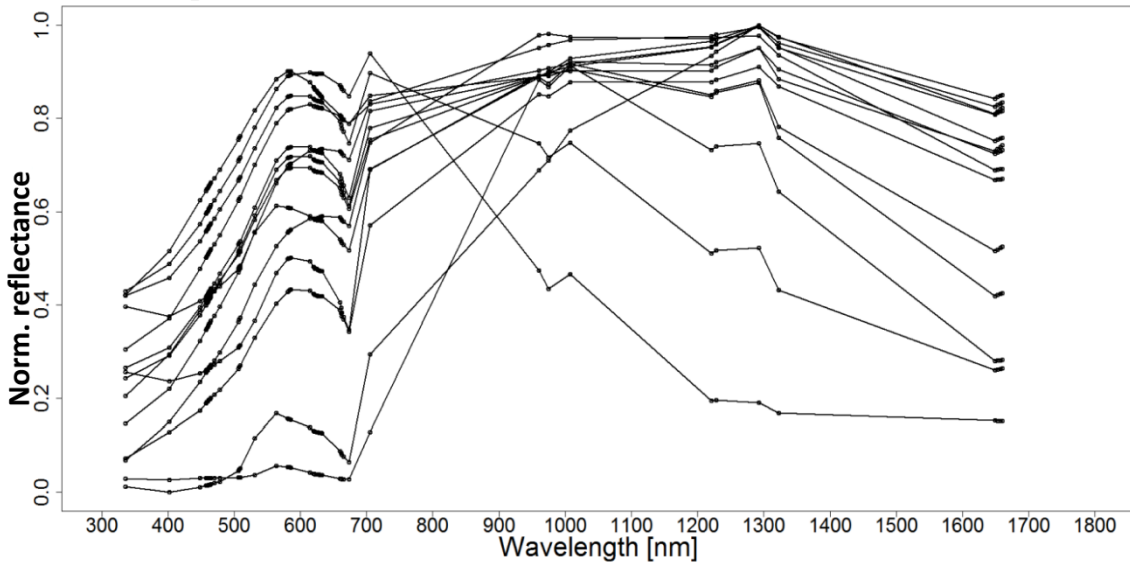
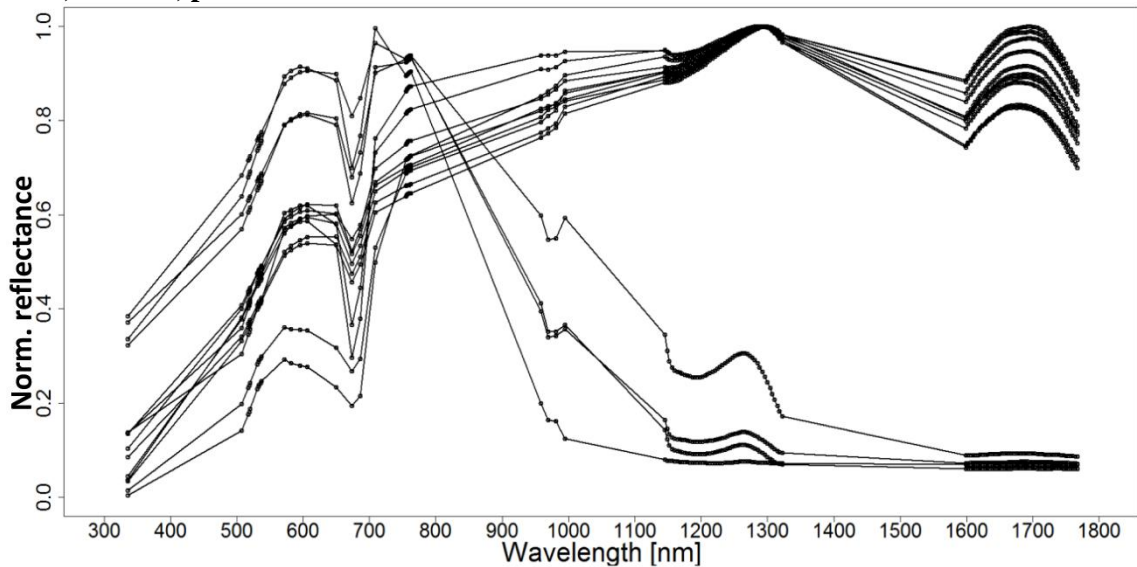


Figure 5-24: Comparison of the original selection of the wavelengths (plot a)) with the adjusted version (plot b)) of 2013.

a) 2015, JMDFS, peaks



b) 2015, JMDFS, peaks adjusted

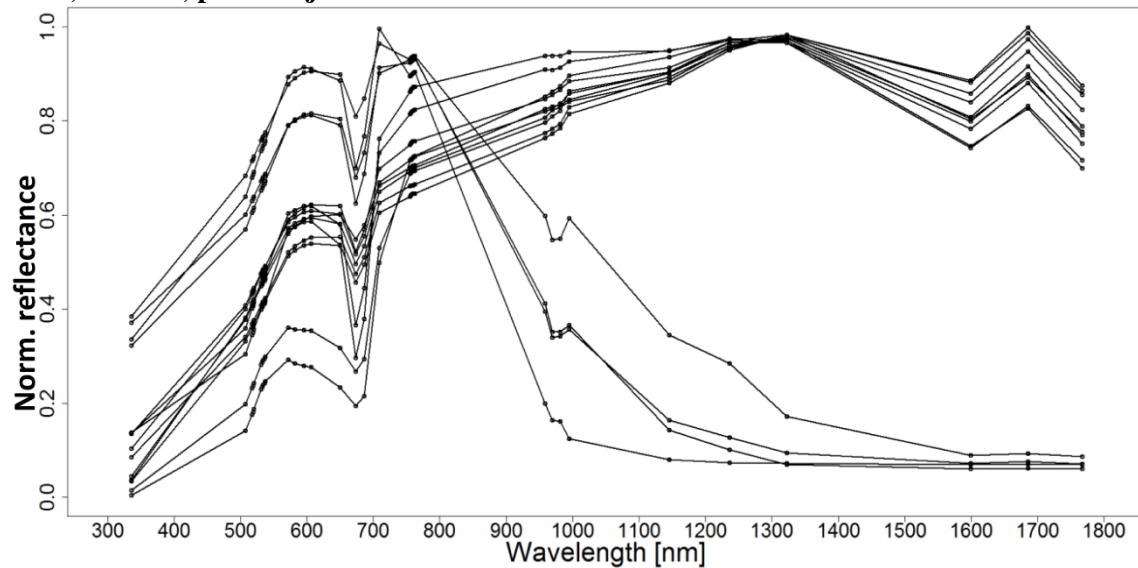


Figure 5-25: Comparison of the original selection of the wavelengths with (plot a)) with the adjusted version (plot b)) of 2015.

5.4 Summary

In this chapter, several results from pre-processing to classification and feature selection were described. It could be shown that the proposed methods achieve sufficient results and that they are comparable or even better than popular state-of-the-art methods and approaches. The semi-automatic pre-processing method for the RE was successful in eliminating periodic artefacts and improving the radiometric quality. One single filter mask in the FFT procedure could be applied to all RE images. Furthermore, an atmospheric correction was carried out for a better comparison of the electro-optical data from different acquisition dates. The pre-processing method works fully automatic until the atmospheric correction, where the user has to enter the image specific metadata. The transformation of the LiDAR point data into spatial information works very well as it was proven by the difference analysis with the RTK measurements. The differences varied from a maximum of -63cm to a minimum of 0.02cm, with an average of 6.4cm and a stdev of 7.8cm. Except for a few outliers, which are influenced by water, all differences are lower than 15cm (i.e., precision of LiDAR measures).

The evaluation methods applied to the classification results were described in chapter 5.2.1. The methods included both visual inspection and qualitative comparison with the provided or self-generated reference data. The qualitative comparison was further separated into a multi-class and a binary confusion matrix comprising several accuracy measures, such as overall accuracy, producers' accuracy, precision or true positive rate.

Applying these accuracy measures to the classification results of the hierarchical knowledge-based decision tree, the high usability for classifying salt marsh vegetation could be shown (TPR: 88%-96%; P: 80%-95%). The change detection analysis showed a stable distribution between June, July and October 2011. The increase from April 2010 to June 2011 is not an effect of an overall increase in the salt marsh areas, but rather an effect of the season (i.e., growing season) or an effect of retrieval after winter storms. It has to be noted that the vegetation classification can be easily adapted to other study areas by simply changing the MSAVI threshold and/or changing the diameter of the buffer zone.

Moderate results could be achieved for the shellfish bed detection (TPR: 48%-63%; P: 48%-54%). The classifications have a tendency to over-classify in a region of steep slope or similar rough surface and to miss the area near the border of the reference polygons. Towards the borders, the shellfish beds tend to get smaller and sparser, because they are less protected from the tide and less evolved, which makes the detection with TSX more difficult. Results from other researchers confirm the capability of multi-frequency and multi-polarimetric SAR data to detect subtle changes in surface roughness (Gade et al. 2008; Gade et al. 2014; Mattia et al. 1997; Van der Wal, Herman & Wielemaker-van den Dool 2005; Beijma, Comber & Lamb 2014). This leads to the assumption that a single polarized SAR dataset is not sufficient enough for shellfish bed detection. The change detection analysis showed many changes, which is mostly an effect of the over-classification. The shellfish bed approach could be transferred to all TSX images without adjustment.

The sediment classification achieved moderate accuracies (OA: 64-68%; PA: 4.55-86%; UA: 21-79%), whereas the sediment classes have to be considered separately. It could be shown that sand and mixed sediments could be classified satisfactorily, whereas muddy sediments very often get mixed up with sand. A separability analysis proved the assumption that the spectral reflectance of wet sand and mud is quite similar if multi-spectral data is applied. A change detection analysis revealed that the most dynamic areas are located in the southeastern part of the study area. The change comprises a temporary shift of grain sizes from sand to mixture sediment or even mud and vice versa. It mostly takes place on very flat terrain (e.g., South-East), where accumulated sediment layers, such as mud, can be washed away by higher flow velocities, revealing the underlying sediment, such as sand. The northern parts have steeper slopes and thus only sand occurs. Due to the slopes the higher flow velocities are standard, which prevents the accumulation of sediments with smaller grain sizes (e.g., mud). In general, no permanent shift of sediments takes place, but rather a moving of sediments with small grain size on top of sand.

Due to the result of the separability analysis and since the intertidal flat is mostly wet and only at exposed elevations really dry, an improvement of the sediment classification was necessary. In this context, LiDAR data were applied. First, an object-based classification of the water was carried out. An *OA* of 79% could be achieved, whereas the *OA* for intertidal channels in sandy sediment (72%) was lower compared with muddy sediments (92%). Secondly, areas with shellfish beds generated false positives, due to the simulation of an intertidal channel. The developed procedure could be transferred with minor changes of the segmentations to the other two acquisition dates (*OA*: 86-94%).

Based on the water classification, the channel network and some geometric parameters, such as number of confluences and flow direction, were extracted. It could be shown that, within a buffer zone of 1m-5m, an accuracy of 75-81% for the extracted channel network was achieved. Moreover, the geometric properties could be estimated with very high accuracy. A correlation analysis was carried out to identify the necessary input data for the later random forest classification for discriminating sand and mud. A 20-fold cross-validation revealed the possibility of LiDAR data to identify mud with high accuracy (*PA*: 85%; *UA*: 83%), but not sand (*PA*: 53%; *UA*: 58%).

The additional information of the distribution of mud was added to the existing sediment classification of RE. The *OA* was increased by only 2%, but the class mud was less mixed up with sand, resulting in an improvement of *PA* (from 4% to 42%) and *UA* (from 28% to 51%). Although the *PA* of sand (from 85.27% to 85.29%) and the *UA* of mixed sediments (from 37% to 51%) increased, the *UA* of sand slightly decreased from 79.58% to 79.57% and the *PA* of mixed sediments from 59% to 46%.

In comparison with the results of the hierarchical knowledge-based decision tree, the results of the random forest classification are worse, especially for the class 'shellfish bed'. The electro-optical data alone are not able to discriminate between vegetation and shellfish beds (*TPR*: 11%; *P*: 72%). Furthermore, the additional information of TSX does extensively increase the shellfish bed areas, leading to a very high over-classification (*P*: 23-48%).

The same is true for the salt marsh classification. The accuracies showed that mapping methods based on electro-optical data alone produce better results classifying salt marshes than with the inclusion of additional single polarized radar data. The change analysis revealed a small increase in the salt marsh distribution from April 2010 to July 2011, whereas the most significant increase takes place between July 2011 and October 2011. This means that, even at

the end of the growing season in October, the salt marsh vegetation still spreads, which is a contrary result to the hierarchical knowledge-based decision tree.

The sediment classification revealed that a combined usage of electro-optical data and SAR data can achieve better or equal results. A strong tendency to mix up ‘mud’ with ‘sand’ or ‘mixture’ and ‘sand’ with ‘mixture’ occurs. However, in the proposed decision tree, only mud gets mixed up with sand. Furthermore, the change analysis implied a very stable sediment distribution, only varying in its moisture content.

Table 5-24 summarizes all accuracy of the land cover classifications from both approaches. The green values in bold show an improvement and the red value in bold a degradation of the proposed decision tree in comparison with the random forest approach. Furthermore, the values underlined represent improvements of the proposed decision tree with LiDAR data, compared with the proposed decision tree without LiDAR data. It can be seen that the developed approach achieves better accuracies for the shellfish bed classification and partly for the others, whereas the differences are only significant worse between the *PA* of mixed sediments and the *UA* of mud.

Table 5-24: Comparison of the accuracy measurements between the random forest approach, the hierarchical knowledge-based decision tree without and with LiDAR data. Details are described in the text.

Random Forest					
OA [%]	56-66		62-78		10-24
	Sand	Mud	Mixed Sediments	Salt Marsh	Shellfish bed
PA [%]	62-75	10-23	54-72	63-94	11-52
UA [%]	77-89	17-69	30-33	82-97	23-72
Hierarchical knowledge-based decision tree without LiDAR					
OA [%]	64-68		78-88		33-41
	Sand	Mud	Mixed Sediments	Salt Marsh	Shellfish bed
PA [%]	82-86	4-23	28-51	88-96	48-63
UA [%]	76-80	20-28	37-42	80-95	48-54
Hierarchical knowledge-based decision tree with LiDAR					
OA [%]	61-71		78-88		33-41
	Sand	Mud	Mixed Sediments	Salt Marsh	Shellfish bed
PA [%]	82-86	23-42	28-46	88-96	48-63
UA [%]	76-80	20-50	37-51	80-95	48-54

Due to the moderate results in the sediment classification of both approaches, a detailed analysis of sediment spectra was carried out. It could be shown that significant spectral feature exists, which could be related to water content, vegetation (e.g., plant pigments or biomass) and organic matter content. Furthermore, the proposed feature selection method

JMDFS showed equal results compared with ReliefF and runs 216 times faster to obtain a final result. The achieved overall accuracies of 81-95% confirmed the efficiency of the feature selection methods and the capability of separating sediments, if the necessary wavelengths are given (500nm-700nm and 950nm-1,000nm).

6 Conclusion

As already stated in chapter 1, the emerging change (e.g., water quality) and the potential loss of the vulnerable ecosystem Wadden Sea has drawn much attention in recent years. As a result, the European Union implemented various directives, such as the Habitats Directive, the Water Framework Directive and the Marine Strategy Framework Directive. Every six years, the ecological status of the ecosystem has to be reported considering these directives. To accomplish this in an efficient manner, the Ministry of Environment, Energy and Climate Protection and the Ministry of Science and Culture of the Federal State of Lower Saxony need accurate and up-to-date geo-information and an ecological monitoring concept for the whole Wadden Sea area. Remote sensing sensors and applications can be very helpful for these tasks, due to their provision of a large spatial coverage and non-intrusive measurements of the Earth's surface (Foody 2002). Time-consuming fauna, flora and sediment mapping from aerial photographs or in situ measurements and visual inspections can be supported and can be focused on specific areas detected from satellite data. Moreover, with satellite data it is possible to get synoptic information of different areas simultaneously and to generate objective results. This yields a reduction in processing time and costs, because it is not necessary to examine the whole Wadden Sea by foot. “[If] remote-sensing systems are used wisely, including complementary combinations of different satellite and airborne sensors, they can provide data that enhance the research and management of coastal ecosystems. Remote sensors can monitor and assess long-term trends and short-term changes of vegetation and hydrology faster [and] more completely [...] than field or ship surveys alone” (Klemas 2013).

In this context, a hierarchical knowledge-based decision tree for a multi-sensor approach has been developed in this thesis by considering a hierarchical usage of electro-optical, radar and LiDAR data for a land cover classification of the tidal flats in the German North Sea. Starting with a semi-automatic pre-processing procedure for the electro-optical data of RapidEye, LiDAR data, spectrometric data and ground truth data, the proposed decision tree uses the advantages of each satellite sensor to reduce the drawbacks of a combined usage, which is revealed by a standard supervised classification approach called random forest. Furthermore, a discrimination analysis of the intertidal sediments with the spectrometric data was carried out.

To conclude, according to the objectives of chapter 1, this thesis has contributed to multi-sensor land cover classification of intertidal flats for spaceborne electro-optical data, radar data, airborne LiDAR data and in situ spectrometric data in the following fields:

- It could be shown that the quality of the remote sensing sensors varies and that some major pre-processing procedures need to be applied (e.g., RapidEye). The spatial, spectral and temporal resolution is partly appropriate for the intertidal flats of the Wadden Sea, especially in terms of sediments and shellfish beds.
- Using different remote sensing sensors in a hierarchical knowledge-based decision tree for land cover classification of intertidal flats showed several advantages compared with a combined classification with a standard supervised classification approach. The combined approach (e.g., RF) of electro-optical and radar data was only appropriate for the classification of sediments and salt marsh, although lower accuracies are still achieved. In general, better results were obtained if the electro-optical and radar data were applied to specific land cover classes in a hierarchical manner. The single benefits of each sensor can be optimally used in the classification procedure. Moreover, this approach also disables the disadvantages of the other sensors. An improvement of the sediment classification within the hierarchical knowledge-based decision tree could be achieved by implementing geometric information derived from LiDAR data.
- In a hierarchical knowledge-based decision tree approach, each class can be adjusted separately to a new study area, which makes the parameterization of the approach more efficient.
- It has been proven that one single satellite sensor is not efficient enough to map the land cover of intertidal flats in an efficient manner. The best results were achieved if all remote sensing sensors were used for specific classes.
- As evident from the visual and numerical validation of the obtained results, most of the classes can be correctly extracted. The reason for the false alarms or missed areas in some cases can be explained by the high similarity of different land covers in their backscatter intensity, spectral and geometric features. Additional information would be necessary, which is discussed in the next chapter.
- Using single polarized data, it has been shown that the available information of the radar backscatter is not sufficient to estimate shellfish beds with high accuracy.

- A semi-automatic monitoring concept could be developed comprising a multi-sensor approach. At several points of the procedure, the user has to define threshold values (e.g., by trial and error or expert knowledge), or has to calculate and enter metadata information (e.g., atmospheric correction), which incapacitates a fully automatic concept.
- It has been shown that the sediment classification with a combination of electro-optical and LiDAR or radar data is still a challenge, due to the constrained availability of the bands in the electromagnetic spectrum or the missing polarization information. The analysis of the spectrometric data and the subsequent feature selection approach revealed the necessary wavelength for a highly accurate sediment discrimination with electro-optical data. The results indicate that specific wavelengths between 500nm-700nm and 950nm-1,000nm are more valuable for extent mapping. Within these wavelength ranges, specific features are located that can be associated with the quantities of macrophytes, microalgae, water or organic content. These are the key features for discriminating sediments. Most of the bands of RapidEye are near those wavelengths, but still do not record the necessary information, which makes this sensor not perfectly suited for approaches in the intertidal flats.
- The results of the spectrometric data analysis led to the conclusion that there exists no unique generally applicable method for the feature selection problem. Some feature selection methods will be more suitable under certain conditions, whereas others are more appropriate under different conditions. Both JMDFS and ReliefF achieved high accuracies. It could be shown that the developed feature selection method (JMDFS) is comparable to the standard feature selection method ReliefF. A huge advantage of JMDFS is the processing time, which is 30min for a final result compared to 2h 10min for a temporarily result from ReliefF. Several temporarily results from ReliefF are necessary to obtain a final result.

A major problem that remains with the proposed decision tree is the selection of appropriate threshold values. Several manually selected threshold values are used to obtain the classes of the hierarchical knowledge-based decision tree. A higher or lower value for each class might slightly influence the number of missed or falsely detected alarms. However, the selection of a proper threshold value is not trivial and in this thesis it was set by expert knowledge; therefore it cannot be guaranteed to be the best choice. Higher accuracy might be achieved when using other threshold values, but this improvement is limited. Furthermore, the synchronicity of the high number of different remote sensing sensors, which have to be acquired at almost the same time or even tide, remain a problem for a monitoring concept.

The time gap, for instance, between RapidEye and TerraSAR-X of nearly 6h makes it impossible to acquire data at the same tide. Moreover, the constraint of ordering the airborne LiDAR data makes it cost-intensive for the whole Wadden Sea instead of cost-effective. In this context, several improvements need to be carried out in the future.

7 Outlook

A new approach for estimating land cover classes in the tidal lands of the German Bight and the suitability of electro-optical, radar and LiDAR data for this application have been demonstrated. Due to the results, the following future research topics could be of interest:

- Basic indices (e.g., MSAVI or NDWI) were derived from the satellite data. If more indicators can be extracted, such as roughness or polarimetric features, the hierarchical knowledge-based decision tree can be refined to improve the accuracy or even to extend the land cover classes. This depends strongly on the remote sensing data.
- To prove the operational suitability, further work on different study sites, larger areas, a longer time period or a detailed examination of problematic areas will be necessary. This would also include the analysis of the reproducibility of the method with other sensors and in various coastal environments (e.g., where salt marshes occur further offshore).
- Investigating the possibilities of other remote sensing data that are free of charge and have a more suitable spectral resolution, or additional polarization features, is needed. The new satellites Sentinel-1 (C-band; 5m-40m spatial resolution; 80km-400km swath width; single and dual polarization) and Sentinel-2 (13 bands from VNIR to SWIR; 10m-60m spatial resolution, 290km swath width) could be such a possibility. Sentinel-2 has a band at 665nm, which is quite near to the absorption maximum of chlorophyll at 674nm. Both satellites have a revisit time of less than 12 days, which makes them suitable for monitoring applications.
- The spatial resolution of Sentinel-1 and -2 is slightly poorer than RapidEye (5m) and TerraSAR-X (1m). Therefore, an investigation, if the higher spectral resolution outperforms the spatial resolution, would be necessary.
- Due to the results of the spectrometric data analysis a perfect remote sensor for the application in the Wadden Sea would be composed of approximately 60 bands equally distributed between the wavelength ranges 520nm-590nm, 620nm-700nm, 710nm-790nm, 940nm-1,000nm, 1,100nm-1,322nm and 1,600nm-1,800nm with specific bands at 674nm, 970nm and 1,200nm. The spatial resolution should be better than 20m and the temporal resolution should be about one day.
- The airborne LiDAR data is a cost-intensive remote sensing dataset, which needs to be exchanged with an equivalent spaceborne dataset that is free of charge. The NASA, for

instance, has a LiDAR (GEDI) at the ISS that currently provides the first global, high-resolution observations of forest vertical structure. There are also other spaceborne LiDAR systems, such as LITE, GLAS or CALIPSO, but they are investigating the atmosphere or they are already out of order.

- Another possibility is the fusion of hyperspectral sensors, such as EnMAP, with satellites of high spatial resolution, such as RapidEye, to combine the high spectral and spatial resolution.
- The first or second derivative, continuum removal or spectral unmixing as approaches for fusion results or hyperspectral data should be investigated, especially in terms of diatoms and sediments.
- A robust and automatic thresholding method using probabilities instead of hard thresholds could be helpful. In the existing procedure, several threshold values are still required. It will be difficult to establish one automatic method that can be used for all purposes.
- A further analysis of the proposed feature selection method with different data of the intertidal flats and of other land covers would be necessary to estimate the robustness and the application field. Moreover, different separability parameters, such as feature entropy, feature stability or feature redundancy (Wu et al. 2013; Datta, Ghosh & Ghosh 2014), can be applied or added to the procedure.
- There is a need to transfer the feature selection method and the results to spaceborne remote sensing data.
- The methods to select the most important wavelengths from the feature selection results need to be refined.
- In a further work, the hyperspectral data can be assumed as a time series and thus algorithms and methods belonging to this topic (e.g., efficiencies such as Nash-Sutcliff coefficient, index of agreement, RMSE, coefficient of determination, etc.) can be applied. In this context, an inverse modelling approach can be conducted where the worst agreement between two vectors will be searched.

- In this study, ground truth data of the specific land cover was used as input for the accuracy assessment of the classifications. A study of Schüchel & Kröncke (2013) shows that information of the distribution of benthic macrofauna can also be used as ground truth data. They relate different species to specific kinds of sediment and seagrass, for instance *Tubificoides benedii* to mudflats, *Bathyporeia sarsi* and *Scoloplos armiger* to sandflats, *Pygospio elegans* and *Caulleriella killariensis* to mixed sediments and *Urothoe poseidonis* to seagrass. These kinds of data can be used for the parameterization and validation of classification procedures in the future or, if available, for classifications of satellite images of the past where no ground truth data of the specific land cover exist.
- A different method of accuracy assessment approach needs to be developed for the intertidal flats, because transitional zones cannot be judged by categories ‘right’ or ‘wrong’ for each pixel. Therefore, such a method should take into account the balance between the spatial scale (e.g., study size area, pixel size, point precision) and the thematic scale (e.g., number of classes, hybrid classes, transition zones or errors in terms of spectral similarity between several features). Moreover, the most reliable comparisons can be made when ground truth data and image data are acquired at the same time. If a routine monitoring approach is being established, algorithms will therefore have to be based on coincident ground truth and image data.

Acknowledgements

First and foremost, I would like to thank my supervisor, Prof. Dr.-Ing. Manfred Ehlers, who played an invaluable role elaborating my PhD research at the Institute for Geoinformatics and Remote Sensing of the University of Osnabrueck. During my research, he always supported me in various ways and promoted me with valuable feedback. He gave me the chance to attend to international events and therefore experience the stimulating atmosphere of international conferences, workshops and special meetings in which I could develop my ideas freely. He offered the perfect balance between freedom and motivation to explore and experiment on the one hand, and support for keeping me on the right track on the other.

This research would not have been possible without the cooperative research project “Wissenschaftliche Monitoringkonzepte für die Deutsche Bucht – WIMO” (Scientific Monitoring Concepts for the German Bight) jointly funded by the Ministry for Environment, Energy and Climate Protection and the Ministry for Science and Culture of the Federal State of Lower Saxony. I thank all partners in this project and the DeMarine project for the support, especially for the provision of ground truth data. My gratitude goes to the “Deutsches Zentrum für Luft-und Raumfahrt – DLR” (German Aerospace Center) for delivering the RapidEye data in context of the RapidEye Science Archive (RESA) and for delivering the TSX images.

My sincere thanks go to my friends and colleagues in the project WIMO. Many thanks to Winny Adolph, Alena Schmidt, Ruggero Capperucci and Dr. Hubert Farke for the educational and adventurous measurement campaigns, and the professional knowledge exchange and discussions during meetings. Because of you, I was able to think outside the box.

I would like to thank my friends and colleagues at the Institute for Geoinformatics and Remote Sensing, who have read and corrected my PhD thesis, and who drew attention to logical jumps or other contradictions. Many thanks to Dr. Thomas Jarmer, Bastian Albers, Martin Kanning, Bastian Siegmann, Florian Beyer and all other that I have not mentioned by name for discussing various aspects of my work.

Finally, I would like to thank my family, especially my parents Katrin und Hartmut, who have financed my studies and therefore enabled me free, pleasant and carefree student days. I would also like to thank my wife Luisa, who supported me in difficult job-related and personal periods and was always there for me.

References

- Bachmann, M.U.R. (2007). Automatisierte Ableitung von Bodenbedeckungsgraden durch MESMA-Entmischung. PhD thesis, Julius-Maximilians-Universität Würzburg [German].
- Bajwa, S.G., Bajcsy, P. Groves, P. & Tian, L.F. (2004). Hyperspectral image data mining for band selection in agricultural applications. *American Society of Agricultural Engineers*, 47, 3, 895 – 907.
- Baltsavias, E.P. (1999). Airborne laser scanning: basic relations and formulas. *ISPRS Journal of Photogrammetry & Remote Sensing*, 54, 199 – 214.
- Baumgardner, M.F. (1985). Reflectance properties of soils. *Advances in Agronomy*, 38, 1 – 44.
- Beijma, S. Van, Comber, A. & Lamb, A. (2014). Random forest classification of salt marsh vegetation habitats using quad-polarimetric airborne SAR, elevation and optical RS data. *Remote Sensing of Environment*, 149, 118 – 129.
- Belluco, E., Camuffo, M., Ferrari, S., Modense, L., Silvestri, A. Marani, A. & Marani, M. (2006). Mapping salt-marsh vegetation by multispectral and hyperspectral remote sensing. *Remote Sensing of Environment*, 105, 54 – 67.
- Benediktsson, J. A. & Sveinsson, J. R. (1997). Feature extraction for multi-source data classification with artificial neural networks. *International Journal of Remote Sensing*, 18, 4, 727 – 740.
- Benediktsson, J. A., Sveinsson, J. R. & Arnason, K. (1995). Classification and feature extraction of AVIRIS data. *IEEE Transactions on Geoscience and Remote Sensing*, 33, 1194 – 1205.
- Beraldin, J.-A., Blais, F. & Lohr, U. (2010). Laser Scanning Technology. In: Vosselman, G. & Maas, H.-G. (Editors): *Airborne and Terrestrial Laser Scanning*. Dunbeath: Whittles Publishing, 1 – 42.
- Bhattacharyya, A. (1943). On a measure of divergence between two statistical populations defined by their probability distributions. *Bulletin of the Calcutta Mathematical Society*, 35, 99 – 109.
- BlackBridge (2013). *Satellite Imagery Product Specifications*. BlackBridge. Accessed 25th November 2013. http://blackbridge.com/rapideye/upload/RE_Product_Specifications_ENG.pdf.

- Börner, T. (2000). Kohärente Modellierung von Radarrückstreuung für die Anwendung in Polarimetrischer SAR Interferometrie. PhD thesis, Deutsches Zentrum für Luft- und Raumfahrt e.V.
- Breiman, L. (2001). Random forests. *Machine Learning*, 45, 5–32.
- Brockmann, C., & Stelzer, K. (2008). Optical Remote Sensing of Intertidal Flats. In Barale, V. & Gade, M. (Ed.), *Remote Sensing of the European Seas* (pp. 117 – 129). Heidelberg: Springer Verlag.
- Brzank, A., Heipke, C., Goepfert, J. & Soergel, U. (2008). Aspects of generating precise digital terrain models in the Wadden Sea from lidar – water classification and structure line extraction. *ISPRS Journal of Photogrammetry & Remote Sensing*, 63, 510 – 528.
- Buck, O., Klink, A., Millan, V.E.G., Pakzad, K. & Mütterthies, A. (2013). Image analysis methods to monitor Natura 2000 habitats at regional scale – the MS.MONINA state service example in Schleswig-Holstein, Germany. *Journal of Photogrammetry, Remote Sensing and Geoinformation Science*, 5, 415 – 426.
- Bund (n.d.). Pflanzen der Nordsee: Algen und See gras. <http://www.bund.net/themen_und_projekte/meeresschutz/nordsee/tiere_und_pflanzen/algen_seegras/>.
- Cartus, O. (2010). Large Area Forest Stem Volume Mapping Using Synergy of Spaceborne Interferometric Radar and Optical Remote Sensing: A Case Study of Northeast China. PhD thesis, Friedrich-Schiller University of Jena.
- CCRS (Canada Centre for Remote Sensing) (2014). Polarization in radar systems. <<http://www.nrcan.gc.ca/earth-sciences/geomatics/satellite-imagery-air-photos/satellite-imagery-products/educational-resources/9567>>.
- Chebouni, J. Q. A., A. R. Huete, Y. H. Kerr, & Sorooshian, S. (1994). A Modified Soil Adjusted Vegetation Index. *Remote Sensing of Environment*, 48, 119-126.
- Chen, J., Jönsson, P., Tamura, M., Gu, Z., Matsushita, B. & Eklundh, L. (2004). A simple method for reconstructing a high-quality NDVI time-series data set based on the Savitzky-Golay filter. *Remote Sensing of Environment*, 91, 332 – 344.
- Choe, B.-H., Kim, D., Hwang, J.-H., Oh, Y. & Moon, W.M. (2012). Detection of oyster habitat in tidal flats using multi-frequency polarimetric SAR data. *Estuarine, Coastal and Shelf Science*, 97, 28 – 37.
- Choi, J.-K., Eom, J. & Ryu, J.-H. (2011). Spatial relationship between surface sedimentary facies distribution and topography using remotely sensed data: Example from the Ganghwa tidal flat, Korea. *Marine geology*, 280, 205 – 211.

- Choi, E. & Lee, C. (2003). Feature Extraction based on the Bhattacharyya distance. *Pattern Recognition*, 36, 1703 – 1709.
- Choi, E. & Lee, C. (2001). Optimizing feature extraction for multiclass problems. *IEE Transactions on Geoscience and Remote Sensing*, 39, 3, 521 – 528.
- Clark, R. N. (1999). Chapter 1: Spectroscopy of Rocks and Minerals, and Principles of Spectroscopy, in *Manual of Remote Sensing, Volume 3, Remote Sensing for the Earth Sciences*, (Rencz, A.N. ed.), New York: John Wiley and Sons, 3 – 58. <<http://speclab.cr.usgs.gov>>.
- Cohen, J. (1960). A Coefficient of Agreement for Nominal Scales. *Educational and Psychological Measurements*, 20, 37 – 64.
- Congalton, R.G. (1991). A Review of Assessing the Accuracy of Classifications of remotely sensed data. *Remote Sensing of Environment*, 37, 35 – 46.
- Corcoran, J., Knight, J., & Gallant, A. (2013). Influence of multi-source and multi-temporal remotely sensed and ancillary data on the accuracy of random forest classification of wetlands in Northern Minnesota. *Remote Sensing*, 5, 3212–3238.
- Cutler, D.R., Edwards Jr., T.C., Beard, K.H., Cutler, A., Hess, K.T., Gibson, J. & Lawler, J.J. (2007). Random forests for classification in ecology. *Ecology*, 88, 11, 2783 – 2792.
- CWSS (Common Wadden Sea Secretariat) (2013a). The Wadden Sea, Germany and Netherlands (N1314) – Extension Denmark and Germany: Volume One. <http://www.waddensea-secretariat.org/sites/default/files/downloads/volume_i_-_the_wadden_sea_germany_and_netherlands_n1314_lq.pdf>.
- CWSS (Common Wadden Sea Secretariat) (2013b). The Wadden Sea, Germany and Netherlands (N1314) – Extension Denmark and Germany: Volume Two. <http://www.waddensea-secretariat.org/sites/default/files/downloads/volume_ii_-_annexes_the_wadden_sea_germany_and_netherlands_n1314.pdf>.
- Daniels, A.E. (2006). Incorporating domain knowledge and spatial relationships onto land cover classifications: a rule-based approach. *International Journal of Remote Sensing*, 27, 2949 – 2975.
- Datta, A., Ghosh, S. & Ghosh, A. (2014). Band elimination of hyperspectral imagery using partitioned band image correlation and capacitory discrimination. *International Journal of Remote Sensing*, 35, 2, 554 – 577.
- Decho, A.W., Kawaguchi, T., Allison, m.A., Louchard, E.M., Reid, R.P., Stephens, F.C., Voss, K.J., Wheatcroft, R.A. & Tyloe, B.B. (2003). Sediment properties influencing

- upwelling spectral reflectance signatures: The “biofilm gel effect”. *Limnology and Oceanography*, 48, 1, 431 – 443.
- Definiens (2010). Definiens eCognition 8.0.1 – Reference Book. <<http://www.ecognition.com/products/trial-software>> Part of the trial software package.
- Definiens (2007). Definiens Developer 7 – User Guide. <<http://ecognition.cc/download/userguide.pdf>>.
- Dehouck, A., Lafon, V., Baghdadi, N., Roubache, A. & Rabaute, T. (2011). Potential of TerraSAR-X imagery for mapping intertidal coastal wetlands. In: Proceedings 4th TerraSAR-X Science Team Meeting, Oberpfaffenhofen, Germany. <http://terrasar-x.dlr.de/papers_sci_meet_4/oral/LAN237_dehouck.pdf>.
- DLR (Deutsche Luft-und Raumfahrt) (2010). Terra SAR-X ground segment basic product specification document. *Cluster Applied Remote Sensing*, 1, 7, 1-109.
- Dolch, T., & Reise, K. (2010). Long-term Displacement of Intertidal Seagrass and Mussel Beds by Expanding Large Sandy Bedforms on Northern Wadden Sea. *Journal of Sea Research*, 63, 93 – 101.
- Ehlschlaeger, C. (1989). Using the AT search algorithm to develop hydrologic models from digital elevation data. In: Proceedings of International Geographic Information Systems (IGIS) Symposium '89. Baltimore, Maryland, 275 – 281.
- ENVI (2009). Atmospheric Correction Module: QUAC and FLAASH User's Guide. <https://www.exelisvis.com/portals/0/pdfs/envi/Flaash_Module.pdf>.
- Eom, J., Choi, J.-K., Ryu, J.-H., Woo, H.J., Won, J.-S. & Jang, S. (2010). Tidal channel distribution in relation to surface sedimentary facies based on remotely sensed data. *Geoscience Journal*, 16, 2, 127 – 137.
- ESRI (2010): Lidar Analysis in ArcGIS 9.3.1 for Forestry Applications. White Paper.
- Exelis VIS (Visual Information Solutions) (2015a). SAVGOL. <<http://www.exelisvis.com/docs/SAVGOL.html>>.
- Exelis VIS (Visual Information Solutions) (2015b). CONVOL. <<http://www.exelisvis.com/docs/CONVOL.html>>.
- Exelis VIS (Visual Information Solutions) (2015c). Region of Interest (ROI) Tool. <<http://www.exelisvis.com/docs/RegionOfInterestTool.html#ROIseparability>>.
- Fagherazzi, S., Bortoluzzi, A., Dietrich, W.E., Adami, A., Lanzoni, S., Marani, M. & Rinaldo, A. (1999). Tidal networks 1. Automatic network extraction and preliminary scaling features from digital terrain maps. *Water Resources Research* 35, 3891 – 3904.

- Fagherazzi, S., Hannion, M., D'Odorico, P. (2008). Geomorphic structure of tidal hydrodynamics in salt marsh creeks. *Water Resources Research* 44, W02419.
- Farke, H. (2011). Integration optischer und SAR Beobachtungsdaten für das Wattenmeermonitoring [Integration of optical and SAR satellite observation data for monitoring the Wadden Sea]. Technische Informationsbibliothek. <<https://getinfo.de/app/download?id=TIBKAT%3a722405367&cluster=tib&term=%22Nationalparkverwaltung+Nieders%3%A4chsisches+Wattenmeer%3B+Technische+Informationsbibliothek+u.+Universit%C3%A4tsbibliothek%22&tib=zbwkat&tib=roemp&tib=blcp&tib=dkf&tib=sudoc&tib=tema&tib=ceaba&tib=zbmkm&tib=ntis&tib=rdat&tib=tibkat&tib=citeseerx&tib=blse&tib=kmo3d&tib=iud&tib=zbmql&tib=kmov&tib=zmat&tib=frpu&tib=etde&tib=temaext&tib=rswb&tib=insp&tib=dkfl&tib=prob&tib=epo&page=1>>.
- Folmer, E. (2012). Tidal Basins and Mussel Beds – An analysis of distributions and developments of littoral mussel beds in the trilateral Wadden Sea. <<http://www.rijkwaddenzee.nl/assets/pdf/dossiers/natuur-en-landschap/Trilateral%20mussel%20case%20Eelke%20Folmer%20PRW.pdf>>.
- Folmer, E., Drent, J., Troost, k., Büttger, H., Dankers, N., Jansen, J., van Stralen, M., Millat, G., Herlyn, M. & Philippart, C.J.M. (2014). Large-Scale Spatial Dynamics of Intertidal Mussel (*Mytilus edulis* L.) Bed Coverage in the German and Dutch Wadden Sea. *Ecosystems*, 15, 550 – 566.
- Foody, G.M. (2002). Status of Land Cover Classification Accuracy Assessment. *Remote Sensing of Environment*, 80, 185 – 201.
- Gade, M., W. Alpers, C. Melsheimer, & Tanck, G. (2008). Classification of Sediments on Exposed Tidal Flats in the German Bight Using Multi-frequency Radar Data. *Remote Sensing of Environment*, 112, 1603 – 1613.
- Gade, M., S. Melchionna, K. Stelzer, & Kohlus, J. (2014). Multi-frequency SAR data help improving the monitoring of intertidal flats on the German North Sea coast. *Estuarine, Coastal and Shelf Science*, 140, 32 – 42.
- Gao, Z.G. & Zhang, L.Q. (2006). Multi-seasonal spectral characteristics analysis of coastal salt marsh vegetation in Shanghai, China. *Estuarine, Coastal and Shelf Science*, 69, 217 – 224.
- Gebhardt, S., Huth, J., Nguyen, L. D., Roth, A. & Kuenzer, C. (2012). A comparison of TerraSAR-X Quadpol backscattering with RapidEye multispectral vegetation indices

- over rice fields in Mekong Delta, Vietnam. *International Journal of Remote Sensing*, 33, 24, 7644 – 7661.
- Geißler, J., Stelzer, K., Kohlus, J., Farke, H. & Gade, M. (2011). Anwendung und Validierung von Fernerkundungsverfahren für ein optimiertes Wattenmeermonitoring.- In: Traub, K.P., Kohlus, J. & Lüllwitz, T. (Editor): Geoinformationen für die Küstenzone, Beiträge des 3. Hamburger Symposiums zur Küstenzone, 8. Strategie-Workshop zur Nutzung der Fernerkundung im Bereich der BfG/ WSV, HCU Hamburg, 06.-08.10.2010, Points-Verlag, Norden, pp. 213-223. ISBN: 978-3-9812883-5-3.
- Gislason, P. O., Benediktsson, J. A., & Sveinsson, J. R. (2006). RandomForests for land cover classification. *Pattern Recognition Letters*, 27, 294–300.
- Gomez-Chova, L., Calpe, J., Camps-Valls, G., Martín, J.D., Soria, E., Vila, J., Alonso-Chorda, L. & Moreno, J. (2003). Feature selection of hyperspectral data through local correlation and SFFS for crop classification. In: *Proceedings IEEE International Geoscience and Remote Sensing Symposium*, 1, 555 – 557.
- GRASS (2014). [r.stream.extract](http://grass.osgeo.org/grass71/manuals/r.stream.extract.html). <<http://grass.osgeo.org/grass71/manuals/r.stream.extract.html>>.
- GRASS (2011). [g.region](http://grass.osgeo.org/grass64/manuals/g.region.html). <<http://grass.osgeo.org/grass64/manuals/g.region.html>>.
- Green, A. A., M. Berman, P. Switzer, & Graig, M.D. (1988). A Transformation for Ordering Multispectral Data in Terms of Image Quality with Implications for Noise Removal. *IEEE Transaction on Geoscience and Remote Sensing*, 26, 1, 65-74.
- Grizzle, R.E., Adams, J.R. & Walters, L.J. (2002). Historical changes in intertidal oyster (*Crassostrea virginica*) reefs in a Florida lagoon potentially related to boating activities. *Journal of Shellfish Research* 21, 749 – 756.
- Hadjimitsis, D.G., Agapiou, A., Themistocleous, K., Toullos, G., Perdikou, S., Toullos, L. & Clyton, C. (2013). Detection of Water Pipes and Leakages in Rural Water Supply Networks Using Remote Sensing Techniques. In: Hadjimitsis, D.G. (Ed.): *Remote Sensing of Environment - Integrated Approaches*, Intech.
- Hajnsek, I. (2001). Inversion of Surface Parameters using Polarimetric SAR. PhD thesis, Friedrich-Schiller University of Jena.
- Han, L., & Rundquist, D.C. (1996). Spectral Characterization of Suspended Sediments Generated from Two Texture Classes of Clay Soil. *International Journal of Remote Sensing*, 17, 3, 643 – 649.

- Haralick, R., M., K. Shanmugan, & Dinstein, I. (1973). Textural Features for Image Classification. *IEEE Transactions on Systems, Man, and Cybernetics*, 73, 3, 6, 610 – 621.
- Heine, R.A., Lant, C.L. & Sengupta, R.R. (2004). Development and Comparison of Approaches for Automated Mapping of Stream Channel Networks. *Annals of the Association of American Geographers*, 94, 3, 477 – 490.
- Henderson, F.M., & Lewis, A. J. (Ed.) (1998). Introduction. Vol. 2 of Principles and Applications of Imaging Radar: Manual of Remote Sensing. 3rd ed. 1 – 6, New York: John Wiley and Sons.
- Hennig, B.D., Cogan, C. & Bartsch, I. (2007). Hyperspectral remote sensing and analysis of intertidal zones –A contribution to monitor coastal biodiversity. In: Car, A., Griesebner, G. & Strobl, J. (eds): Geospatial crossroads @ GI_Forum. Salzburg (= Proceedings of the first geoinformatics forum), 62-73.
- Herold, M. (2000). Ableitung hydrologischer Parameter aus multifrequenten und multipolarimetrischen E-SAR Flugzeugdaten. PhD thesis., Friedrich-Schiller University of Jena.
- Heygster, G., Dannenberg, J. & Notholt, J. (2010). Topographic mapping of the German tidal flats analyzing SAR images with the waterline method. *IEEE Transaction Geoscience and Remote Sensing* 48 (3), 1019 – 1030.
- Holmgren, P. (1994). Multiple flow direction algorithms for runoff modelling in grid based elevation models: an empirical evaluation. *Hydrological Processes*, 8, 327 – 334.
- Hudson, W.D., & Ramm, C.W. (1987). Correct Formulation of the Kappa Coefficient of Agreement. *Photogrammetric Engineering and Remote Sensing*, 53, 4, 421 – 422.
- Ibrahim, E. & Monbaliu, J. (2010). Suitability of spaceborne multispectral data for inter-tidal sediment characterization: A case study. *Estuarine, Coastal and Shelf Science*, 92, 3, 437 – 445.
- Ibrahim, E., Adam, S., van der Wal, D., De Wever, A., Sabbe, K., Forster, R. & Monbaliu, J. (2009). Assessment of unsupervised classification techniques for intertidal sediments. In: *eProceedings EARSeL*, 8, 158 – 179.
- Janke, K & Kremer, B.P. (2011). *Das Watt. Tiere und Pflanzen im Weltnaturerbe Wattenmeer*. Stuttgart: Kosmos Naturführer [German].
- Janzen, D.T., A.L. Freedon, & Wheate, R.D. (2006). Radiometric Correction Techniques and Accuracy Assessment for Landsat TM Data in Remote Forested Regions. *Canadian Journal of Remote Sensing* 32, 5, 330 – 340.

- Jasiewicz, J. & Metz, M. (2011). A new GRASS GIS toolkit for Hortonian analysis of the drainage networks. *Computers & Geosciences*, 37, 1162 – 1173.
- Jhonnerie, R., Sirgar, V.P., Nababan, B., Prasetyo, L.B. & Wouthuyzen, S. (2015). Random forest classification for mangrove land cover mapping using Landsat 5 TM and ALOS PALSAR imageries. *Procedia Environmental Science*, 24, 215 – 221.
- Jia, X. & Richards, J.A. (1999). Segmented principal components transformation for efficient hyperpsectral remote-sensing image display and classification, *IEEE Transactions on Geoscience and Remote Sensing*, 1, 37, 538 – 542.
- Jung, R., Adolph, W., Ehlers, M. & Farke, H. (2015). A multi-sensor approach for detecting the different land covers of tidal flats in the German Wadden Sea – a case study at Norderney. *Remote Sensing of Environment*, 170, 188 – 202.
- Kavzoglu, T. & Mather, P. M. (2002). The Role of Feature Selection in Artificial Neural Network Applications. *International Journal of Remote Sensing*, 23, 2787–2803.
- Kim, D.-J., Moon, W.M., kim, G., Park, S.-E. & Lee, H. (2011). Submarine groundwater discharge in tidal flats revealed by space-borne synthetic aperture radar. *Remote Sensing of Environment* 115, 793 – 800.
- King, R. L., Ruffin, C., LaMastus, F. E., & Shaw, D. R. (1999). The analysis of hyperspectral data using Savitzky–Golay filtering – Practical issues. 2. In: *Proceedings of International Geoscience and Remote Sensing Symposium*, 398–400.
- Klausing, H. & W. Holpp (2000). *Radar mit realer und synthetischer Apertur*. München: Oldenbourg Verlag.
- Klemas, V. (2013). Remote Sensing of emergent and submerged wetlands: an overview. *International Journal of Remote Sensing*, 34, 18, 6286 – 6320.
- Klonus, S., & Ehlers, M. (2012). Using TerraSAR-X and RapidEye Data for Change Detection in Wadden Sea Areas. Paper presented at the 32nd EARSeL Symposium, Mykonos Island, May 23 – 25.
- Knuth, R. (2008). Evaluation of the usability of full polarimetric ALOS PALSAR datafor a forest/non-forest discrimination of the tropical rain forest in the Democratic Republic of Congo. Diploma thesis.
- Kuo, B. C. & Landgrebe, D. A. (2004). Nonparametric Weighted Feature Extraction for Classification. *IEEE Transaction on Geoscience and Remote Sensing*, 42, 1096–1105.
- Landmap (n.d.). Object-orientated Classification course. 2.5. Multi-resolution segmentation. <<http://learningzone.rspoc.org.uk/index.php/Learning-Materials/Object-oriented-Classification/2.5.-Multi-Resolution-Segmentation>>.

- Lee, C. & Landgrebe, D. A. (2003). Feature Extraction Based on Decision Boundaries. *IEEE Transactions on Pattern Analysis and Machine Intelligence*, 15, 388–400.
- Lee, Y.-K., Parl, W., Choi, J.-K., Ryu, J.-H. & Won, J.-S. (2014). Halophyte die-off in response to anthropogenic impacts on tidal flats. *Estuarine, Coastal and Shelf Science*, 151, 347 – 354.
- Lee, Y.-K., Park, J.-W., Choi, J.-K., Oh, Y. & Won, J.-S. (2012). Potential uses of TerraSAR-X for mapping herbaceous halophytes over salt marsh and tidal flats. *Estuarine, Coastal and Shelf Science*, 115, 366 – 376.
- Li, S., Qui, J., Yang, X., Liu, H., Wan, D. & Zhu, Y. (2014). A novel approach to hyperspectral band selection based on spectral shape similarity analysis and fast branch and bound search. *Engineering Applications of Artificial Intelligence*, 27, 241 – 250.
- Li, T., Zhang, C. L. & Ogihara, M. (2004). A Comparative Study of Feature Selection and Multiclass Classification Methods for Tissue Classification Based on Gene Expression. *Bioinformatics*, 20, 2429–2437.
- Lillesand, T.M. & Kiefer, R.W. (1994³). *Remote Sensing and Image Interpretation*. New York: J. Wiles and Sons.
- Lillesand, T.M., Kiefer, R.W. & Chipman J.W. (2008⁶). *Remote Sensing and Image Interpretation*. New York: J. Wiles and Sons.
- Liu, C., Frazier, P. & Kumar, L. (2007). Comparative Assessment of the Measures of Thematic Classification Accuracy. *Remote Sensing of Environment*, 107, 606–616.
- Liu, M., Liu, X., Li, J., Ding, C. & Jiang, J. (2014). Evaluating total inorganic nitrogen in coastal waters through fusion of multi-temporal RADARSAT-2 and optical imagery using random forest algorithm. *International journal of Applied Earth Observation and Geoinformation*, 33, 192 – 202.
- Liu, H., & Zhou, Q. (2004). Accuracy analysis of remote sensing change detection by rule-based rationality evaluation with post-classification comparison. *International Journal of Remote Sensing*, 25, 5, 1037 – 1050.
- Lobell, N. & Asner, G.P. (2002). Moisture effects on soil reflectance. *Soil Science Society of America*, 66, 722 – 727.
- Lusch D.P. (1999). *Introduction to Microwave Remote Sensing*. Michigan: Center for Remote Sensing and GIS.
- Manakos I., K. Manevski, C. Kalaitzidis & Edler, D. (2011). Comparison between FLAASH and ATCOR Atmospheric Correction Modules on the Basis of WorldView-2 Imagery

- and In Situ Spectroradiometric Measurements. Paper presented at the EARSeL 7th SIG-Imaging Spectroscopy Workshop, Edinburgh, April 11 – 13.
- Marani, M., Lanzoni, S., Zandolin, D., Seminara, G. & Rinaldo, A. (2002). Tidal meanders. *Water Resources Research* 38 (11), 1225.
- Mas, J-F. (1999). Monitoring Land-Cover Changes: A Comparison of Change Detection Techniques. *International Journal of Remote Sensing*, 20, 1, 139 – 152.
- Mason, D.C. & Davenport, I.J. (1996). Accurate and efficient determination of the shoreline in ERS-1 SAR images. *IEEE Transactions on Geoscience and Remote Sensing* 34 (5), 1243 – 1253.
- Mason, D.C., Scott, T.R. & Wang, H.J. (2006). Extraction of tidal channel networks from airborne scanning laser altimetry. *ISPRS Journal of Photogrammetry and Remote Sensing* 61, 67–83.
- Mattia, F., Le Toan, T., Souyris, J.-C., De Carolis, G., Floury, N., Posa, F. & Pasquariello, G (1997). The effect of surface roughness on multifrequency polarimetric SAR data. *IEEE Transactions on Geoscience and Remote Sensing*, 35, 4, 954 – 966.
- Matthew M.W., S.M Adler-Golden, A. Berk, G. Felde, G.P. Anderson, D. Gorodetsky, S. Paswaters, & Shippert, M. (2002). Atmospheric Correction of Spectral Imagery: Evaluation of the FLAASH Algorithm with AVIRIS Data. In: *Proceedings 31st Applied Imagery Pattern Recognition Workshop from color to Hyperspectral: Advancements in Spectral Imagery Exploitation*. USA: Washington. 157 – 163.
- McFeeters, S. K. (1996). The Use of Normalized Difference Water Index (NDWI) in the Delineation of Open Water Features. *International Journal of Remote Sensing* 17, 7, 1425-1432.
- Mulder, V.L., Bruin, de S., Schaepman, M.E. & Myr, T.R. (2011). The use of remote sensing in soil and terrain mapping – A review. *Geoderma*, 162, 1 – 19.
- Myint, S.W., Gober, P., Brazel, A., Grossmann-Clarke, S. & Weng, Q. (2011). Per-pixel vs. object-based classification of urban land cover extraction using high spatial resolution imagery. *Remote Sensing of Environment*, 115, 5, 1145 – 1161.
- NPWS (National Park Wadden Sea) (2010a). Muschelwildbänke von Borkum bis Cuxhaven (GIS-Daten) [Mussel beds from Borkum to Cuxhaven (GIS-Data)]. <http://www.nationalpark-wattenmeer.de/nds/service/publikationen/1130_muschelwildb%C3%A4nke-von-borkum-bis-cuxhaven-gis-daten>.

- NPWS (National Park Wadden Sea) (2010b). Seegrasbestände im niedersächsischen Watt (GIS-Daten und Berichte) [Seagrass in the tidal flats of Lower Saxony (GIS-Data and reports)]. <http://www.nationalpark-wattenmeer.de/nds/service/publikationen/1131_seegrasbest%C3%A4nde-im-nieders%C3%A4chsischen-watt-gis-daten-und-berichte>.
- NLWKN (Niedersächsischer Landesbetrieb für Wasserwirtschaft, Küsten- und Naturschutz) (2011). Küstengewässer und Ästuar. Band 4 [Coastal waters and estuaries. Band 4]. <http://www.nlwkn.niedersachsen.de/service/veroeffentlichungen_webshop/schriften_zum_downloaden/downloads_kuestengewaesser_und_aestuare/veroeffentlichungen-aus-der-reihe-kuestengewaesser-und-aestuare-zum-downloaden-93682.html>.
- NLWKN (Niedersächsischer Landesbetrieb für Wasserwirtschaft, Küsten- und Naturschutz) (2010). Küstengewässer und Ästuar. Band 2 [Coastal waters and estuaries. Band 2]. <https://www.nationalpark-wattenmeer.de/sites/default/files/media/pdf/Seegras_2008_Adolph_2010.pdf>.
- Natura2000 (n.d.). Natura 2000. <<http://www.ffh-gebiete.de/>>.
- Naughton, D., A. Brunn, J. Czaplá-Myers, S. Douglass, M. Thiele, H. Weichelt, & Oxford, M. (2011). Absolute Radiometric Calibration of the RapidEye Multispectral Imager Using Reflectance-based Vicarious Calibration Method. *Journal of Applied Remote Sensing* 5, 1–23.
- Niedermeier, A., Romaneßen, E. & Lehner, S. (2000). Detection of coastlines in SAR images using wavelet methods. *IEEE Transactions on Geoscience and Remote Sensing* 38 (5), 2270 – 2281.
- Nieuwhof, S., Herman, P.M.J., Dankers, N., Troost, K. & Van der Wal, D. (2015). Remote Sensing of Epibenthic Shellfish Using Synthetic Aperture Radar Satellite Imagery. *Remote Sensing*, 7, 4, 3710 – 3734.
- Novakowski, K.I., Torres, R., Gardner, L.R. & Voulgaris, G. (2004). Geomorphic Analysis of Tidal Creek Networks. *Water Resources Research*, 40, 5, W05401.
- Oliver, L.R., Seed, R. & Reynolds, B. (2008). The effect of high flow events on mussels (*Mytilus edulis*) in the Conwy estuary, North Wales, UK. *Hydrobiologia*, 606, 117–127.
- O’Neil-Dunne, J.P.M., MacFaden, S.W., Royar, A.R. & Pelletier, K.C. (2013). An object-based system for LiDAR data fusion and feature extraction. *Geocarto International*, 28, 3, 227 – 242.

- Pal, M. (2006). Support Vector Machine-Based Feature Selection for Land Cover Classification: A Case Study with DAIS Hyper-Spectral Data. *International Journal of Remote Sensing*, 27, 2877–2894.
- Park, S.-E., Kim, D., Lee, H.-S., Moon, W.M. & Wagner, W. (2010). Tidal wetland monitoring using polarimetric synthetic aperture radar. In: Wagner, W. & Székely, B. (eds.): *ISPRS TC VII Symposium – 100 Years ISPRS*, Vienna, Austria, July 5 – 7 2010, *IAPRS*, Vol. XXXVIII, Part 7A.
- Pontius, R. & Millones, M. (2011). Death to Kappa: Birth of Quantity Disagreement and Allocation Disagreement for Accuracy Assessment. *International Journal of Remote Sensing*, 32, 4407–4429.
- Pudil, P., Novovicova, J. & Kittler, J. (1994). Floating Search Method in Feature Selection. *Pattern Recognition Letters*, 15, 1119–1125.
- Pudil, P. & Somo, P. (2008). Identifying the most informative variable for decision-making problems – a survey of recent approaches and accompanying problems. *Acta Oeconomica Pragensia*, 2008, 4, 37 – 55.
- Rainey, M.P., A.N. Tyler, R.G. Bryant, D.J. Gilvear, & McDonald, P. (2000). The Influence of Surface and Interstitial Moisture on the Spectral Characteristics of Intertidal Sediments: Implications for Airborne Image Acquisition and processing. *International Journal of Remote Sensing*, 21, 16, 3025 – 3038.
- Rainey, M.P., A.N. Tyler, D.J. Gilvear, R.G. Bryant, & McDonald, P. (2003). Mapping Intertidal Estuarine Sediment Grain Size Distributions through Airborne Remote Sensing. *Remote Sensing of Environment*, 86, 480 – 490.
- Raney, R.K. (1998³). Chapter 2 – Radar fundamentals: Technical perspective. In: Henderson, F. M. & A. J. Lewis (Editor) (1998³): *Principles and Applications of Imaging Radar. Manual of Remote Sensing, Volume 2*. New York: John Wiley and Sons, 9 – 124.
- Research Systems Inc. (2004). *ENVI User`s Guide*. <http://aviris.gl.fcen.uba.ar/Curso_SR/biblio_sr/ENVI_userguid.pdf>.
- Richards, J.A. (1993). *Remote sensing digital image analysis: An introduction*. 2nd ed. Berlin: Springer-Verlag.
- Richards, J.A. (2009). *Remote Sensing with Imaging Radar*. Berlin: Springer Verlag.
- Robnik-Sikonja, M. & Kononenko, I. (2003). Theoretical and empirical analysis of ReliefF and RReliefF. *Machine Learning Journal*. 53, 23 – 69.

- Rodriguez-Galiano, V.F., Ghimire, B., Rogan, J., Chica-Olmo, M. & Rigol-Sanchez, J.P. (2012). An assessment of the effectiveness of a random forest classifier for land-cover classification. *ISPRS journal of Photogrammetry and Remote Sensing*, 67, 93 – 104.
- Rutzinger, M., Höfle, B. & Kringer, K. (2012). Accuracy of automatically extracted geomorphological breaklines from airborne LiDAR curvature images. – *Geographiska Annaler: Serie A, Physical Geography* 94, 33 – 42.
- Ryu, J.-H., Eom, J.A. & Choi, J.-K. (2010). Application of Airborne Remote Sensing to the Surface Sediment Classification in a Tidal Flat. *Geoscience and Remote Sensing Symposium (IGARSS), 2010 IEEE International*, 942 – 945.
- Ryu, J.-H., Kim, C.-H., Lee, Y.-K., Won, J.-S., Chun, S.-S. & Lee, S. (2008). Detecting the intertidal morphologic change using satellite data. *Estuarine, Coastal and Shelf Science*, 78, 623 – 632.
- Ryu, J.-H., Na, Y.-H., Won, J.-S. & Doerffer, R. (2004). A critical grain size for Landsat ETM+ investigations into intertidal sediments: a case study of the Gomso tidal flats, Korea. *Estuarine, Coastal and Shelf Science*, 60, 491 – 502.
- Ryu, J.-H., Won, J.-s. & Min, K. D. (2002). Waterline extraction from Landsat TM data in a tidal flat – A case study in Gomso Bay, Korea. *Remote Sensing of Environment*, 83, 442 – 456.
- Sabins, F.F. (1997³). *Remote Sensing. Principles and Interpretation*. New York: W.H. Freeman and Company.
- Savitzky, A., & Golay, M. J. E. (1964). Smoothing and differentiation of data by simplified least squares procedures. *Analytical Chemistry*, 36, 1627– 1639.
- Scheffer, F., & Schachtschabel, P. (2010¹⁶). *Lehrbuch der Bodenkunde*. Heidelberg: Spektrum, Akademischer Verlag.
- Schill, S.R., Porter, D., Coen, L.D., Bushek, D. & Vincent, J. (2006). Development of an automated mapping technique for monitoring and managing shellfish distributions. <<http://ciceet.unh.edu/news/releases/springReports/pdf/schill.pdf>>.
- Schmidt, A., Niemeyer, J., Rottensteiner, F. & Soergel, U. (2014). Contextual classification of full waveform lidar data in the Wadden Sea. *IEEE Geoscience and Remote Sensing Letters*, 11, 9, 1614 – 1618.
- Schmidt, K.S. & Skidmore, A.K. (2003). Spectral discrimination of vegetation types in coastal wetland. *Remote Sensing of Environment*, 85, 92 – 108.
- Schott, J.R. (1997). *Remote sensing: the image chain approach*. Oxford: Oxford University Press.

- Schückel, U. & Kröncke, I. (2013). Temporal changes in intertidal macrofauna communities over eight decades: A result of eutrophication and climate change. *Estuarine, Coastal and Shelf Science*, 117, 210 – 218.
- Schückel, U., Beck, M. & Kröncke, I. (2013). Spatial variability in structural and functional aspects of macrofauna communities and their environmental parameters in the Jade Bay (Wadden Sea Lower Saxony, southern North Sea). *Helgoland Marine Research*, 87, 121 – 136.
- Serpico, S. B. & Bruzzone, L. (2001). A New Search Algorithm for Feature Selection in Hyperspectral Remote Sensing Images. *IEEE Transaction on Geoscience and Remote Sensing*, 39, 1360–1367.
- Singh, A. (1989). Digital change detection techniques using remotely-sensed data. *International Journal of Remote Sensing*, 10, 6, 989 – 1003.
- Small, C., Steckler, M., Seeber, L., Akhter, S. H., Goodbred, S., Mia, B. & Imam, B. (2009). Spectroscopy of sediments in the Ganges-Brahmaputra: Spectral effects of moisture, grain size and lithology. *Remote Sensing of Environment*, 113, 342-361.
- Smith, G.F., Bruce, D.G. & Roach, E.B. (2001). Remote acoustic habitat assessment techniques used to characterize the quality and extent of oyster bottom in the Chesapeake Bay. *Marine Geodesy* 24, 171 – 189.
- Sørensen, T.H., K. Bartholdy, C. Christiansen, & Pedersen, J.B.T. (2006). Intertidal Surface Type Mapping in the Danish Wadden Sea. *Marine Geology*, 235, 87 – 99.
- Sokolova, M. & Lapalme, G. (2009). A Systematic Analysis of Performance measures for classification tasks. *Information Processing and Management*, 45, 427 – 437.
- Spectravista (2015). Field Portable Spectroradiometers: SVC HR-1024i. <<http://www.spectravista.com/HR1024i.html>>.
- SphereOptics (2015). Zenith Polymer® / Spectralon® – Diffuse Reflection Targets. <<http://sphereoptics.de/en/product/zenith-polymer-spectralon-fullmaterial-targets/>>.
- Stelzer, K., Brockmann, C. & Geißler, J. (2009). Remote sensing of the Wadden Sea – a tool supporting TMAP and WFD monitoring. *Proceedings of the 12th international Scientific Wadden Sea Symposium, Germany*, 87 – 92.
- Stelzer, K., J. Geißler, M. Gade, K. Eskildsen, J. Kohlus, H. Farke, & Reimers, H.-C. (2010). *DeMarine Umwelt: Operationalisierung mariner GMES-Dienste in Deutschland – 4 Integration optischer und SAR Erdbeobachtungsdaten für das Wattenmeermonitoring. Jahresbericht 2009 – 2010.*

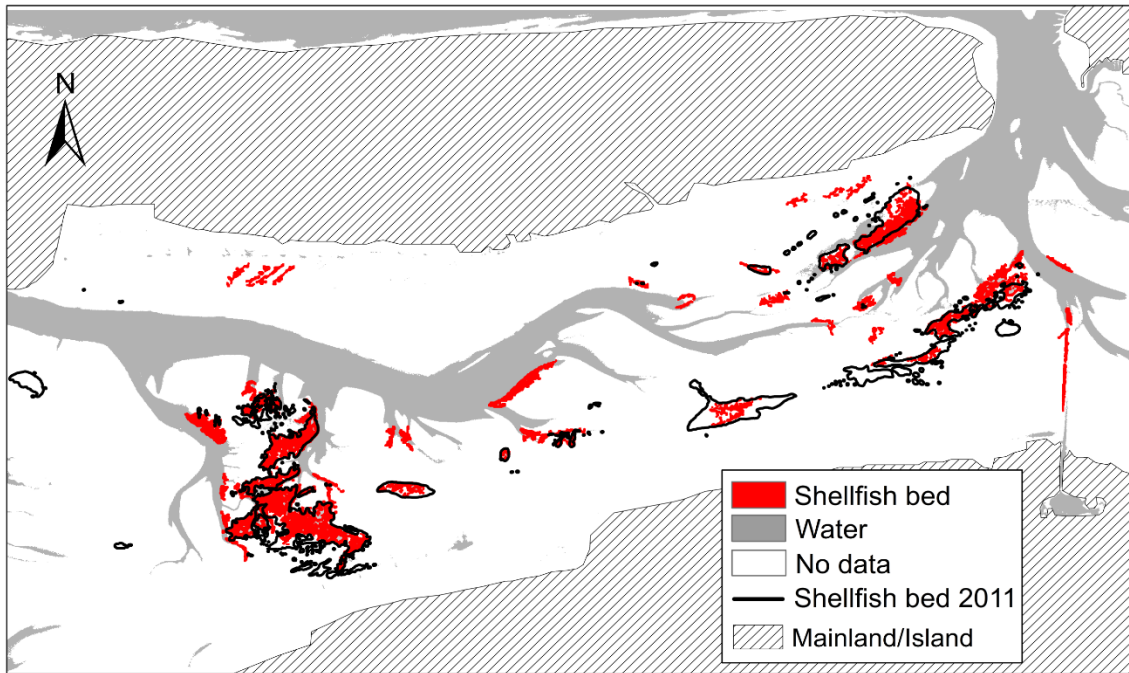
- Stoehr, F. (2007). DER_SNR: A simple & general spectroscopic signal-to-noise ratio measurement algorithm. *ST-ECF Newsletter*, 42, 4 – 5.
- Stoehr, F., White, R., Smith, M., Kamp, I., Thompson, R., Durand, D., Freudling, W., Fraquelli, D., Haase, J., Hook, R., Kimball, T., Kümmel, M., Levay, K., Lombardi, M., Micol, A. & Rogers, T. (2008). DER_SNR: A simple & general spectroscopic signal-to-noise measurement algorithm. *Astronomical Data Analysis Software and Systems XVII ASP Conference Series*, Vol XXX.
- Swain, P. H., & Davis, S.M. (1978). *Remote sensing: The quantitative approach*. New York: McGraw-Hill.
- Temmerman, S., Bouma, T.J., Van de Koppel, J., Van der Wal, D.D., De Vries, M.B., Herman, P.M.J., (2007). Vegetation causes channel erosion in a tidal landscape. *Geology* 35, 631 – 634.
- Thiel C. (2004). Extrahierung hydrologisch relevanter Parameter aus hochaufgelösten polarimetrischen L-Band sowie interferometrischen X-Band SAR-Daten. PhD thesis, Friedrich-Schiller University of Jena [German].
- Thomson, A.G., R.M. Fuller, T.H. Sparks, M.G. Yates, & Eastwood, J.A. (1998). Ground and Airborne Radiometry over Intertidal Surfaces: Waveband Selection for Cover Classification. *International Journal of Remote Sensing*, 19, 6, 1189 – 1205.
- Tian, J. (2013). 3D change detection from high and very high resolution satellite stereo imagery. PhD thesis, University Osnabrueck.
- Timm, B.C. & McGarigal, K. (2012). Fine-scale remotely-sensed cover mapping of coastal dune and salt marsh ecosystems at Cape Cod National Seashore using Random Forests. *Remote Sensing of Environment*, 127, 106 – 117.
- Troost, K. (2010). Causes and effects of a highly successful marine invasion: Case-study of the introduced Pacific oyster *Crassostrea gigas* in continental NW European estuaries. *Journal of Sea Research*, 64, 145–165.
- Van der Sanden, J.J. (1997). *Radar remote sensing to support tropical forest management*. Wageningen: Ponsen & Looijen bv.
- Van der Wal, D., & Herman, P.M.J. (2007). Regression-based Synergy of Optical, Shortwave Infrared and Microwave Remote Sensing for Monitoring the Grain-size of Intertidal Sediments. *Remote Sensing of Environment*, 111, 89 – 106.
- Van der Wal, D., P.M.J. Herman, & Wielemaker-van den Dool, A. (2005). Characterisation of Surface Roughness and Sediment Texture of Intertidal Flats Using ERS SAR Imagery. *Remote Sensing of Environment*, 98, 96 – 109.

- Vaudour, E., J. Moeys, J.M. Gilliot, & Coquet, Y. (2008). Spatial Retrieval of Soil Reflectance from SPOT Multispectral Data Using the Empirical Line Method. *International Journal of Remote Sensing*, 29, 19, 5571 – 5584.
- Venkataraman, S., Bjerke, H., Copenhaver, K. & Glaser, J. (2006). Optimal band selection of hyperspectral data for transgenic corn identification. Presented at MAPPS/ASPRS 200 Fall Conference, San Antonio, Texas, November 06 - 10.
- Verblya, D.L., & Hammond, T.O. (1995). Conservative Bias in Classification Accuracy Assessment due to pixel-by-Pixel Comparison of Classified Images with Reference Grids. *International Journal of Remote Sensing*, 16, 3, 581 – 587.
- Verpoorter C., Carrère V. & Combe, J.P. (2014). Visible, near-infrared spectrometry for simultaneous assessment of geophysical sediment properties (water and grain size) using the Spectral Derivative-Modified Gaussian Model. *Journal of Geophysical Research: Earth Surface*, 119, 10, 2098 – 2122.
- Wang, C., Liu, H.-Y., Zhang, Y. & Li, Y.-F. (2013). Classification of land-cover types in muddy tidal flat wetlands using remote sensing data. *Journal of Applied Remote Sensing*, 7.
- Waske, B., van der Linden, S., Oldenburg, C., Jakimow, B., Rabe, A. & Hostert, P. (2012). imageRF – A user-oriented implementation for remote sensing image analysis with random forests. *Environmental Modelling and Software*, 35, 192 – 193.
- Watmough, G.R., Atkinson, P.M. & Hutton, C.W. (2011). A Combined Spectral and Object-based Approach to Transparent Cloud Removal in an Operational Setting for Landsat ETM+. *International Journal of Applied Earth Observation and Geoinformation*, 13, 220 – 227.
- Won, J.-S. (2009). Investigation of intertidal zone using TerraSAR-X. In: Proceedings 3rd TerraSAR-X Science Team Meeting, Oberpfaffenhofen, Germany. <http://sss.terrasar-x.dlr.de/cgi-bin/wcm.pl?page!4sci_meet_3_abstract;id!495>.
- Wu, B., Chen, C., Kechadie, T.M. & Sun, L. (2013). A comparative evaluation of filter-based feature selection methods for hyper-spectral band selection. *International journal of Remote Sensing*, 34, 22, 7974 – 7990.
- Wu, J., Wang, D. & Bauer, M.E. (2005). Image-based Atmospheric Correction of Quickbird Imagery of Minnesota Cropland. *Remote Sensing of Environment*, 99, 315 – 325.
- Xu, J.-F., & Huang, J.-F. (2008). Empirical Line Method Using Spectrally Stable Targets to Calibrate IKONOS Imagery. *Pedosphere* 18 ,1, 124 – 130.

- Yand, X. & Morris, J. (2008). Extracting Tidal Stream Networks from High-Resolution Remote Sensor Imager: A Preliminary Study. The international Archives of the Photogrammetry, Remote Sensing and Spatial Information Sciences, Vol. XXXVII, Part B8.
- Yates, M.G., Jones, A.R., McGrorty, S. & Goss-Custard, J.D. (1993). The Use of Satellite Imagery to Determine the Distribution of Intertidal Surface Sediments of the Wash, England. *Estuarine, Coastal and Shelf Science*, 36, 333 – 344.
- Young, D., Clinton, P. & Specht, D. (2010). Mapping intertidal eelgrass (*Zostera marina L.*) in three coastal estuaries of the Pacific Northwest USA using false colour near-infrared aerial photography. *International Journal of Remote Sensing*, 31, 7 – 8, 1699 – 1715.
- Yuan, J., & Niu, Z. (2008). Evaluation of Atmospheric Correction Using FLAASH. In *International Workshop on Earth Observation and Remote Sensing Applications*, 1 – 6. China: Beijing.

Appendix

a)

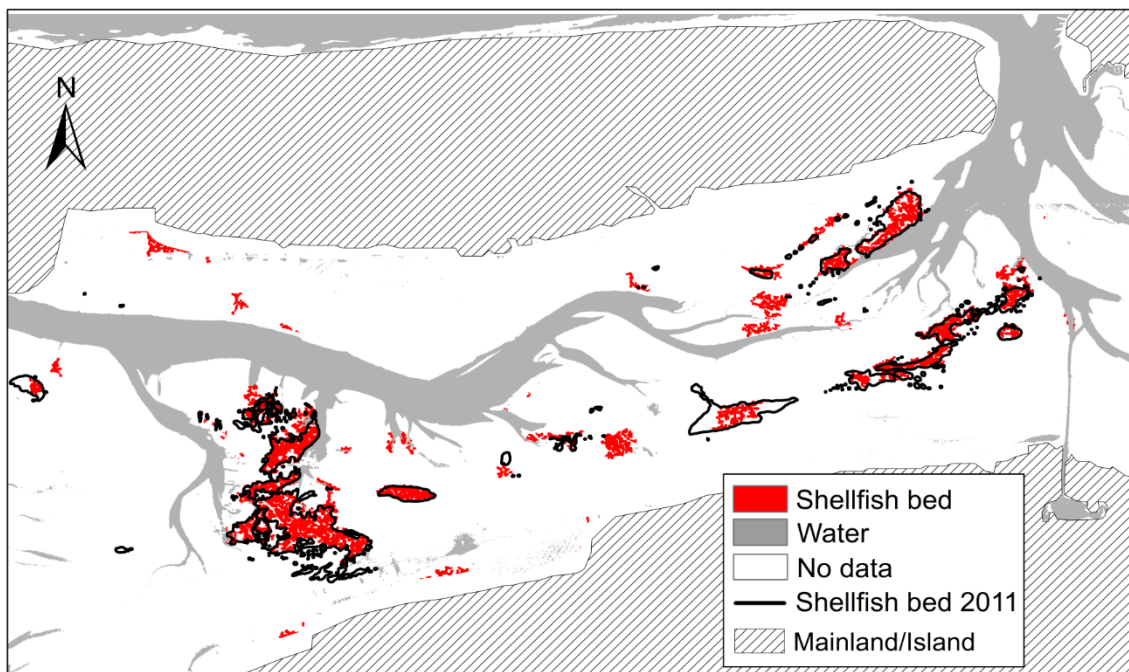


Shellfish bed classification of Terra SAR-X from June 2, 2011

Data source: National park Wadden Sea, WiMo
Projection: UTM-32, WGS-84

0 0.5 1 2 3 4 5 Km

b)



Shellfish bed classification of Terra SAR-X from July 16, 2011

Data source: National park Wadden Sea, WiMo
Projection: UTM-32, WGS-84

0 0.5 1 2 3 4 5 Km

c)

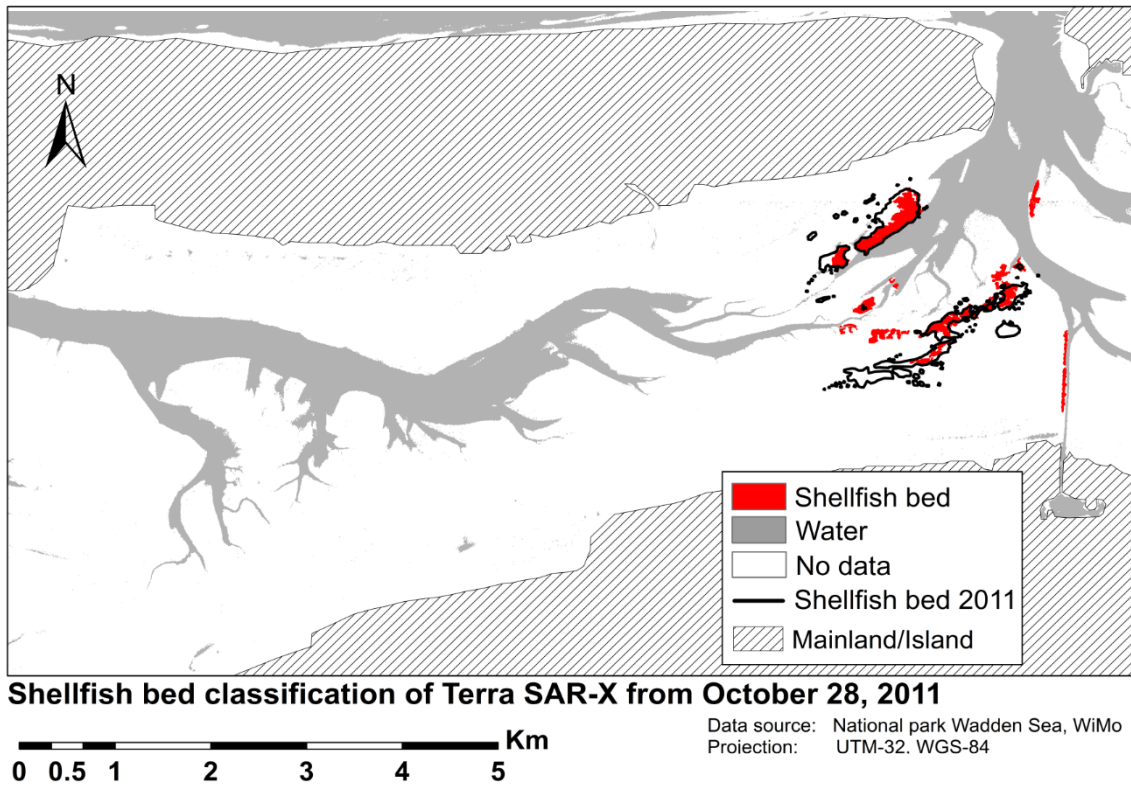
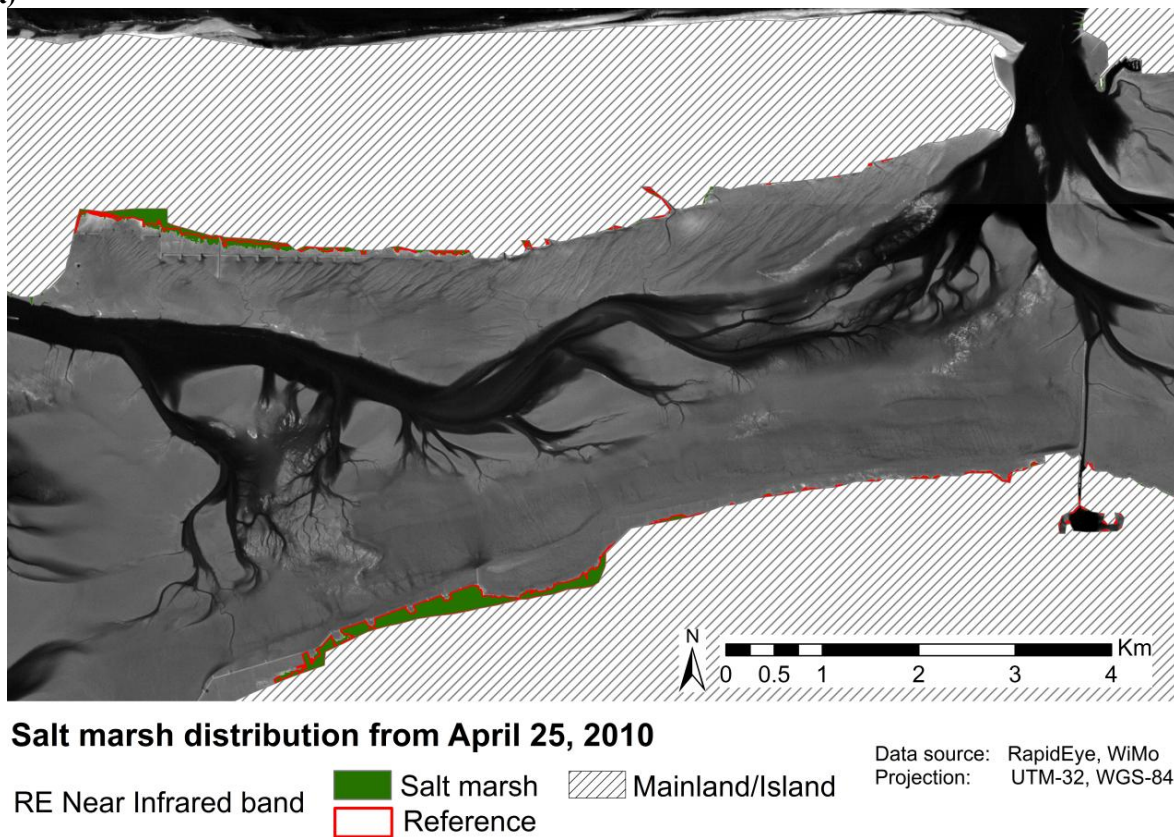
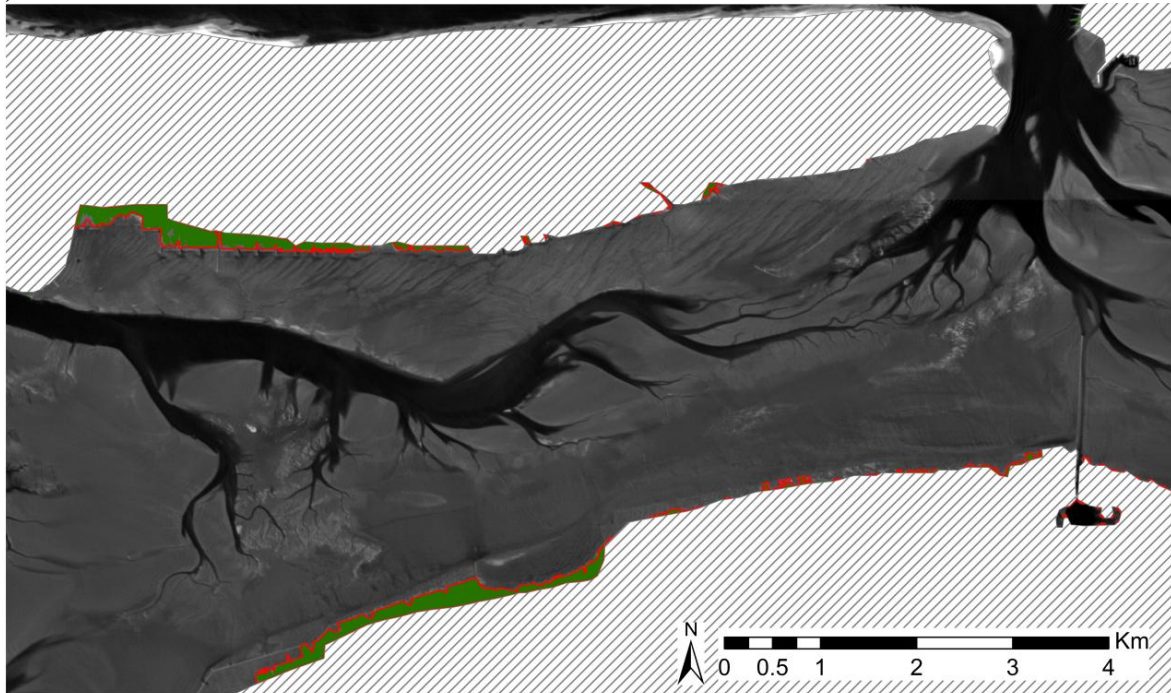


Figure A-1: Shellfish bed classification results from TSX obtained with the hierarchical knowledge-based decision tree.

a)



b)

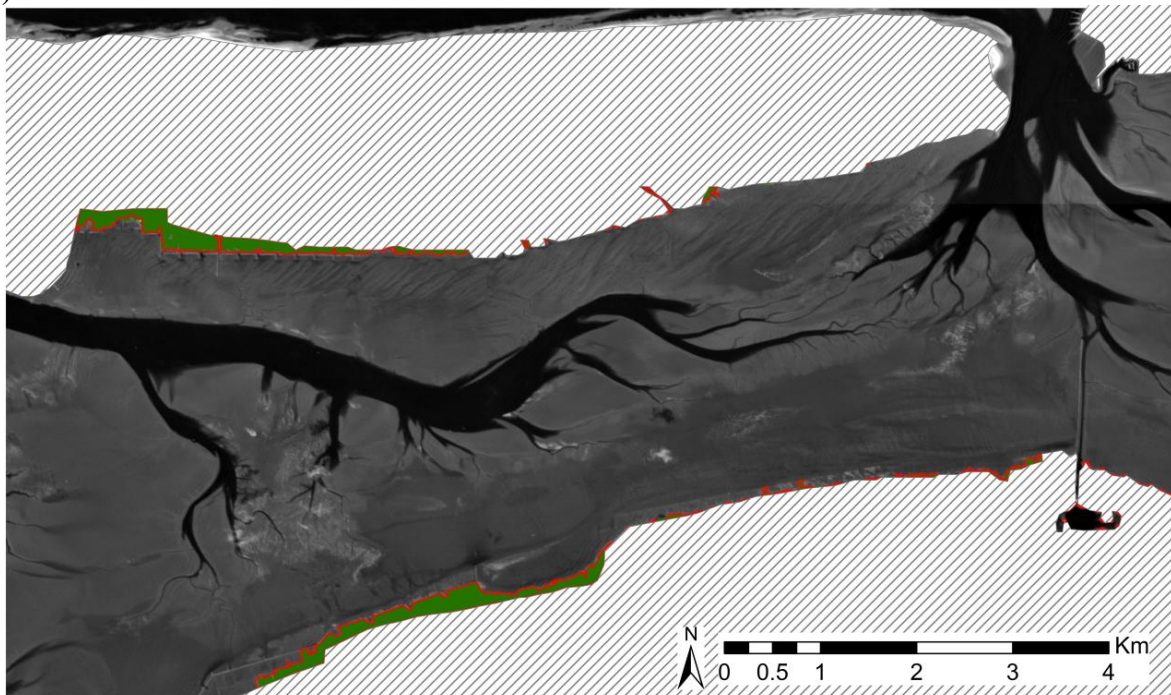


Salt marsh distribution from June 27, 2011

RE Near Infrared band  Salt marsh  Mainland/Island
 Reference

Data source: RapidEye, WiMo
Projection: UTM-32, WGS-84

c)

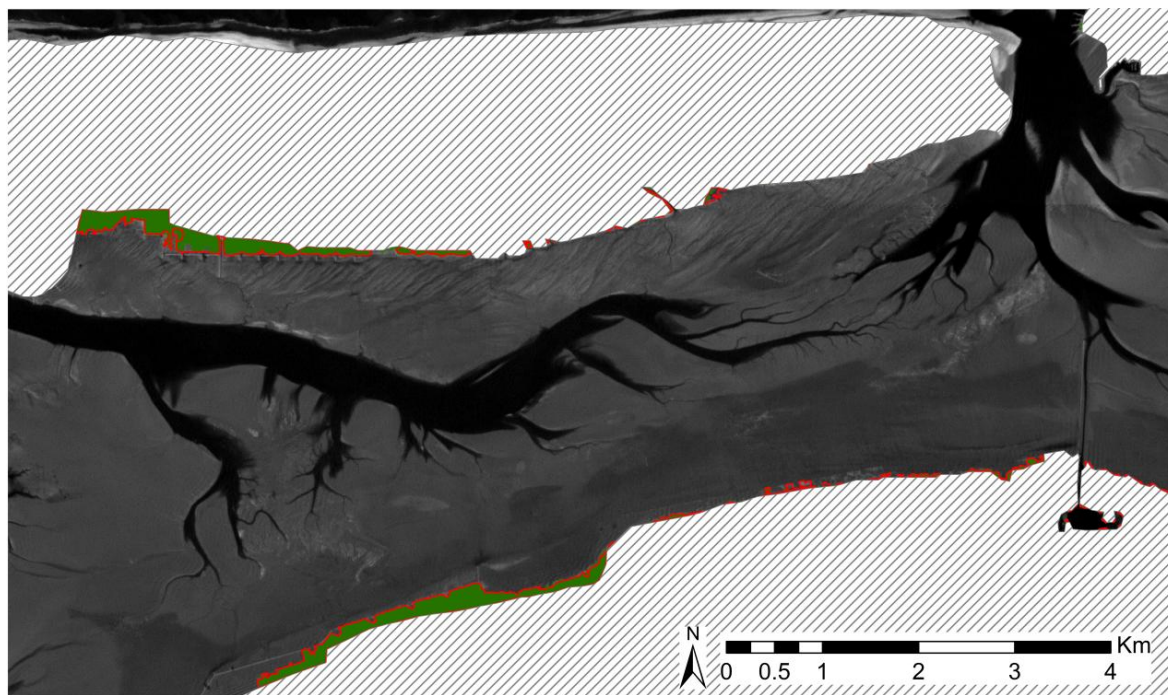


Salt marsh distribution from July 11, 2011

RE Near Infrared band  Salt marsh  Mainland/Island
 Reference

Data source: RapidEye, WiMo
Projection: UTM-32, WGS-84

d)

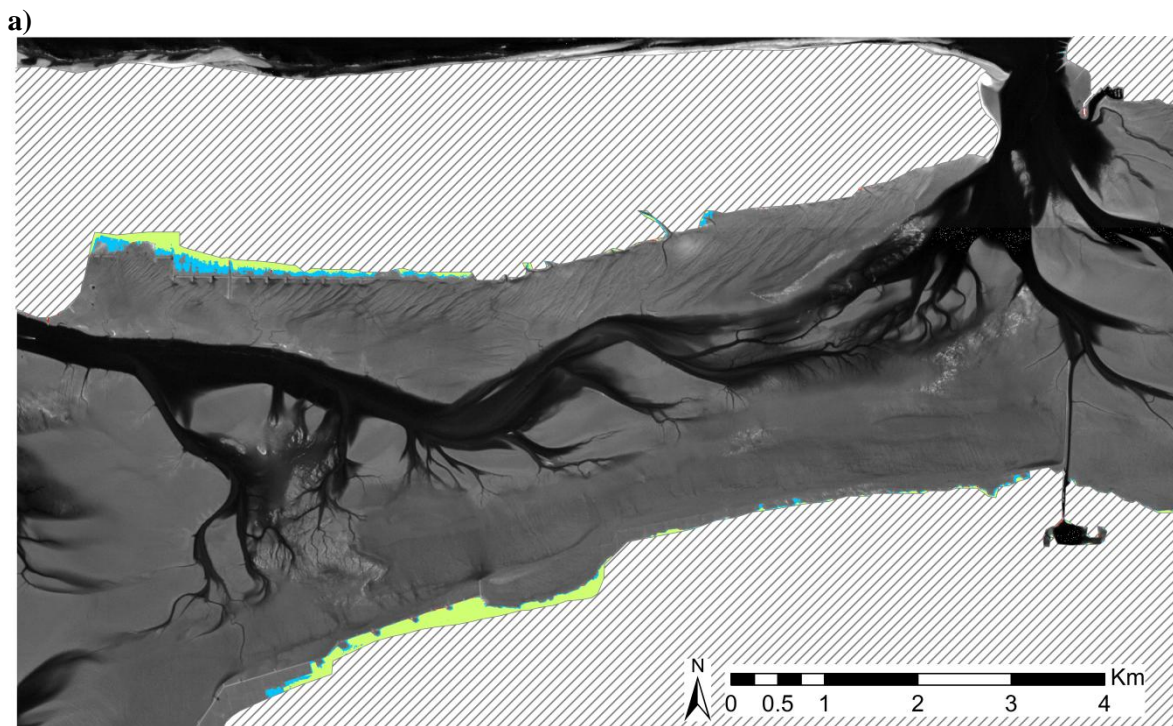


Salt marsh distribution from October 22, 2011

RE Near Infrared band ■ Salt marsh Mainland/Island
 Reference

Data source: RapidEye, WiMo
 Projection: UTM-32, WGS-84

Figure A-2: Salt marsh classifications obtained with the hierarchical knowledge-based decision tree.

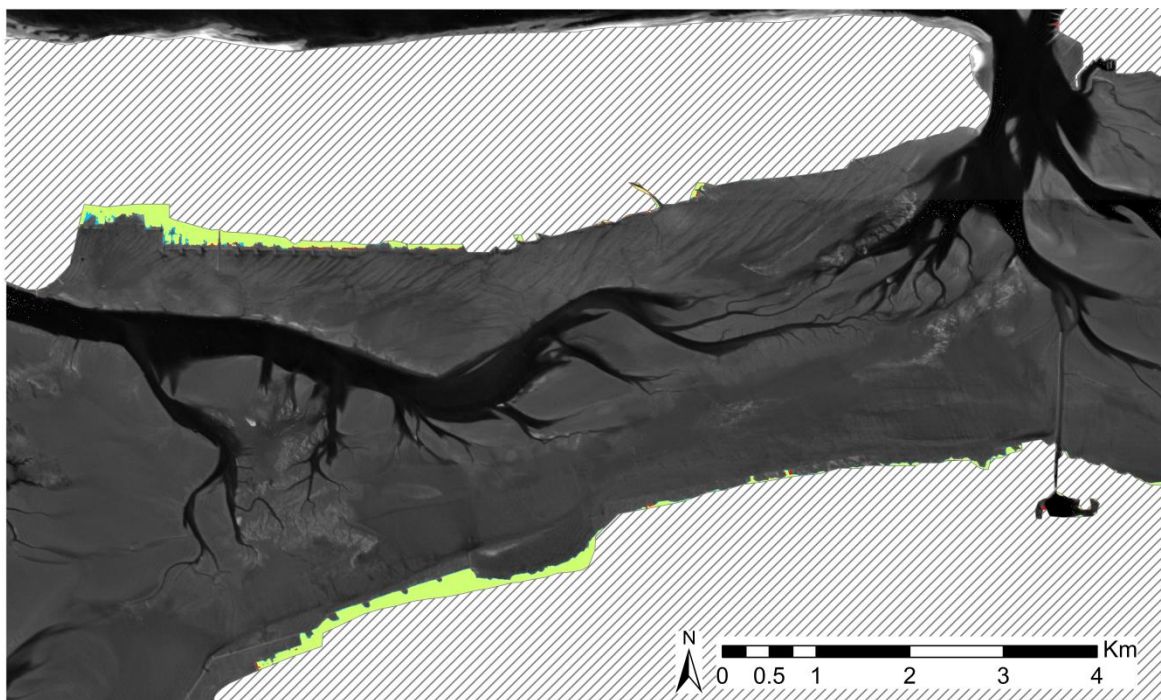


Change of salt marsh distribution from April 25, 2010 to June 27, 2011

RE Near Infrared band ■ Decrease ■ Increase
■ No change Mainland/Island

Data source: RapidEye, WiMo
 Projection: UTM-32, WGS-84

b)

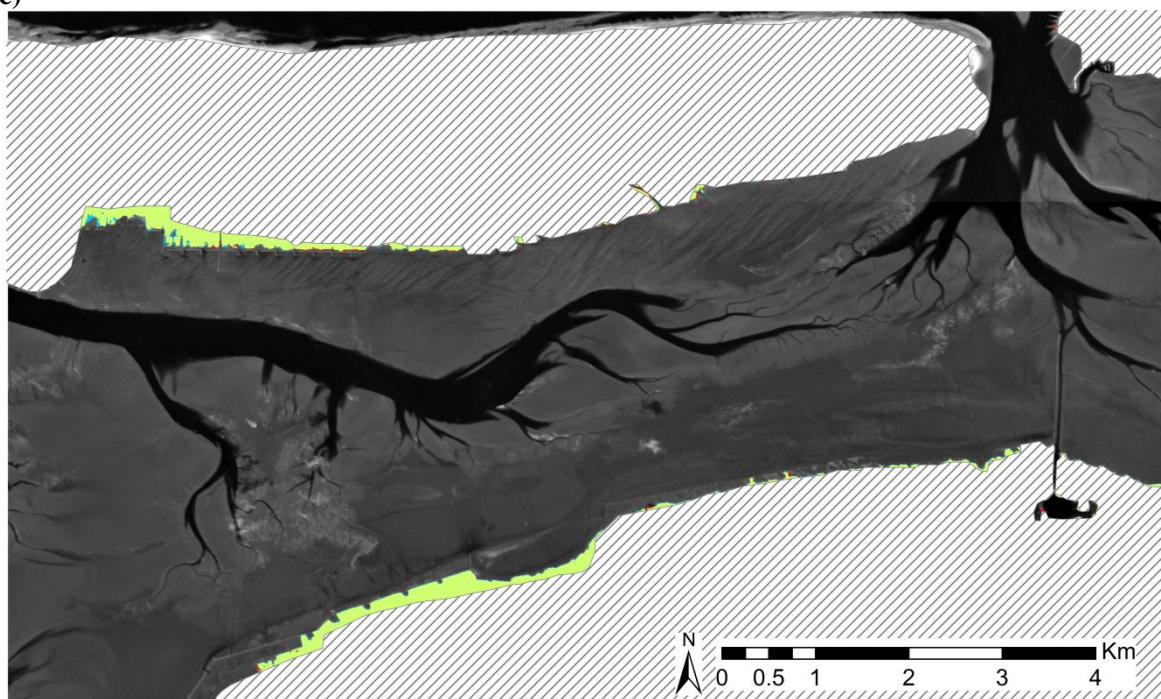


Change of salt marsh distribution from June 27 ,2011 to July 11, 2011

RE Near Infrared band ■ Decrease ■ Increase
■ No change Mainland/Island

Data source: RapidEye, WiMo
 Projection: UTM-32, WGS-84

c)



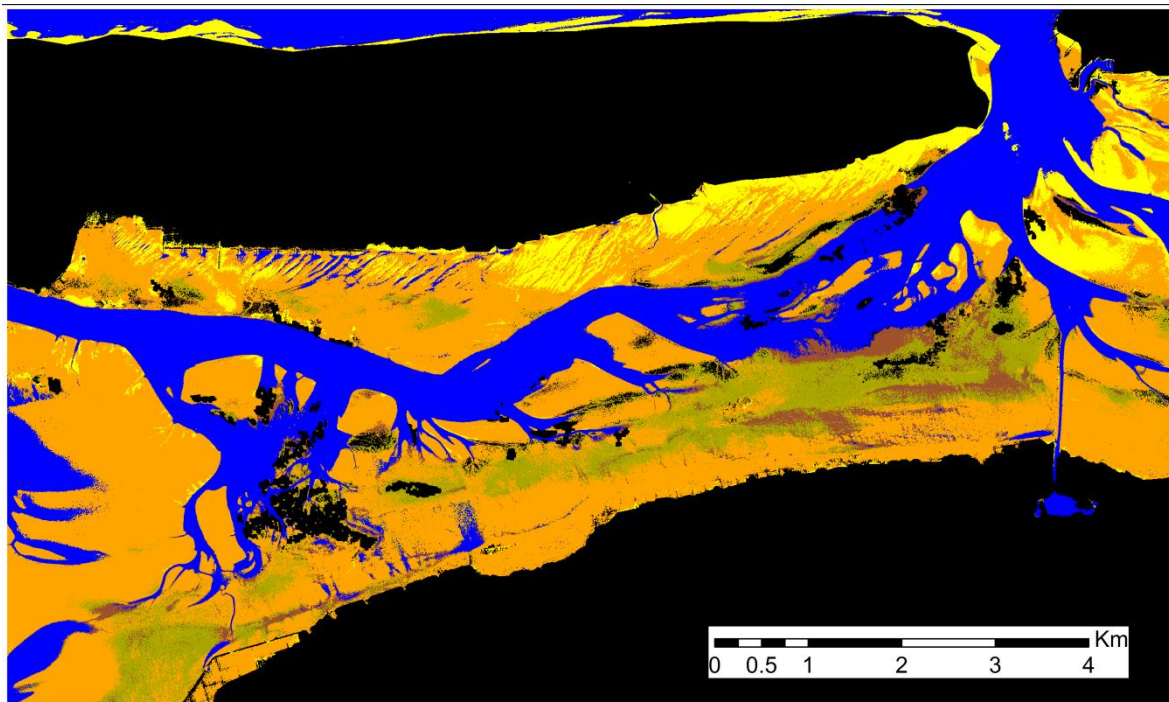
Change of salt marsh distribution from to July 11, 2011 to October 22, 2011

RE Near Infrared band ■ Decrease ■ Increase
■ No change Mainland/Island

Data source: RapidEye, WiMo
 Projection: UTM-32, WGS-84

Figure A-3: Change maps of the salt marsh distribution obtained with the hierarchical knowledge-based decision tree.

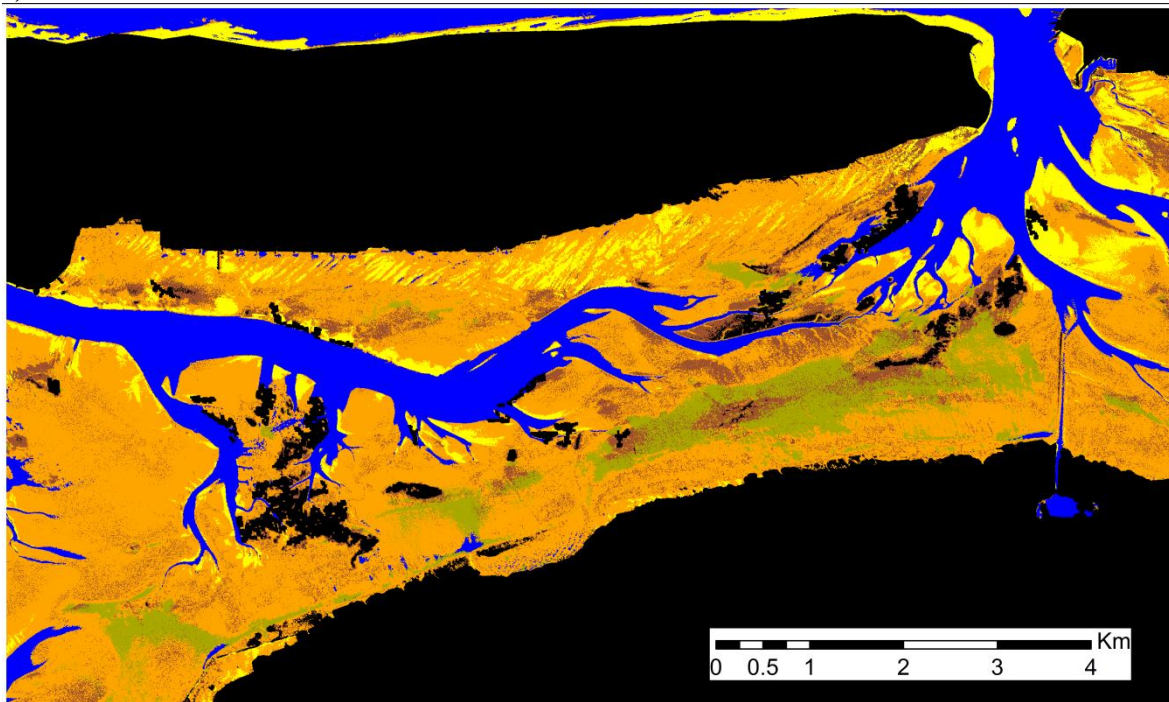
a)



Classification result of April 25, 2010
Data source: WiMo
Projection: UTM-32, WGS-84

N	Water	Mixture
	Dry sand	Mud
	Wet sand	Unclassified

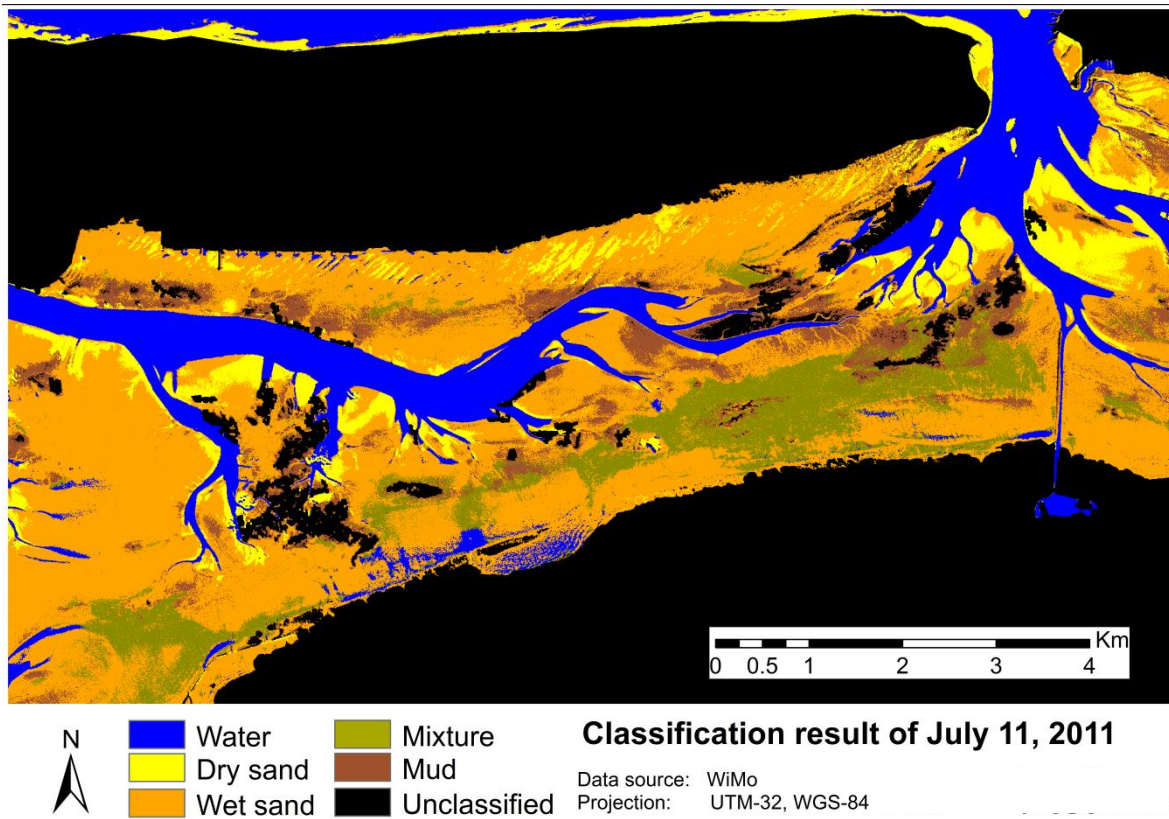
b)



Classification result of June 27, 2011
Data source: WiMo
Projection: UTM-32, WGS-84

N	Water	Mixture
	Dry sand	Mud
	Wet sand	Unclassified

c)



d)

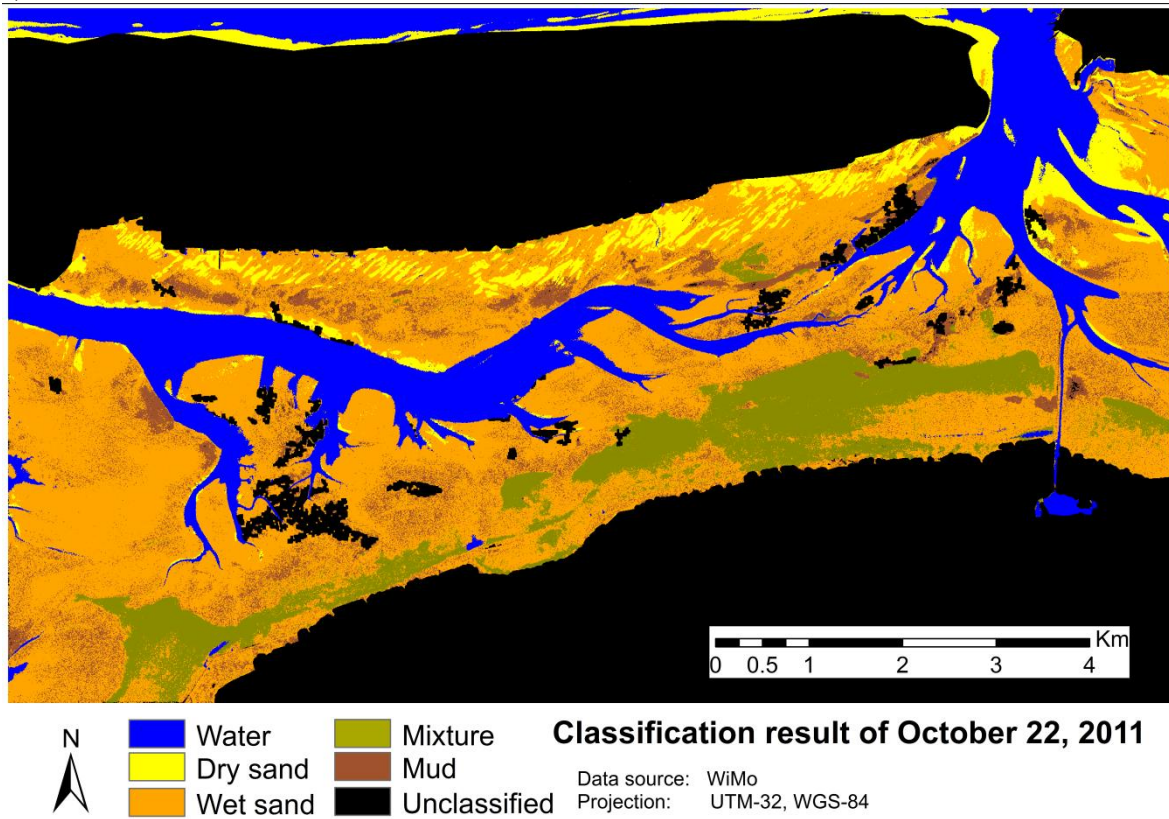
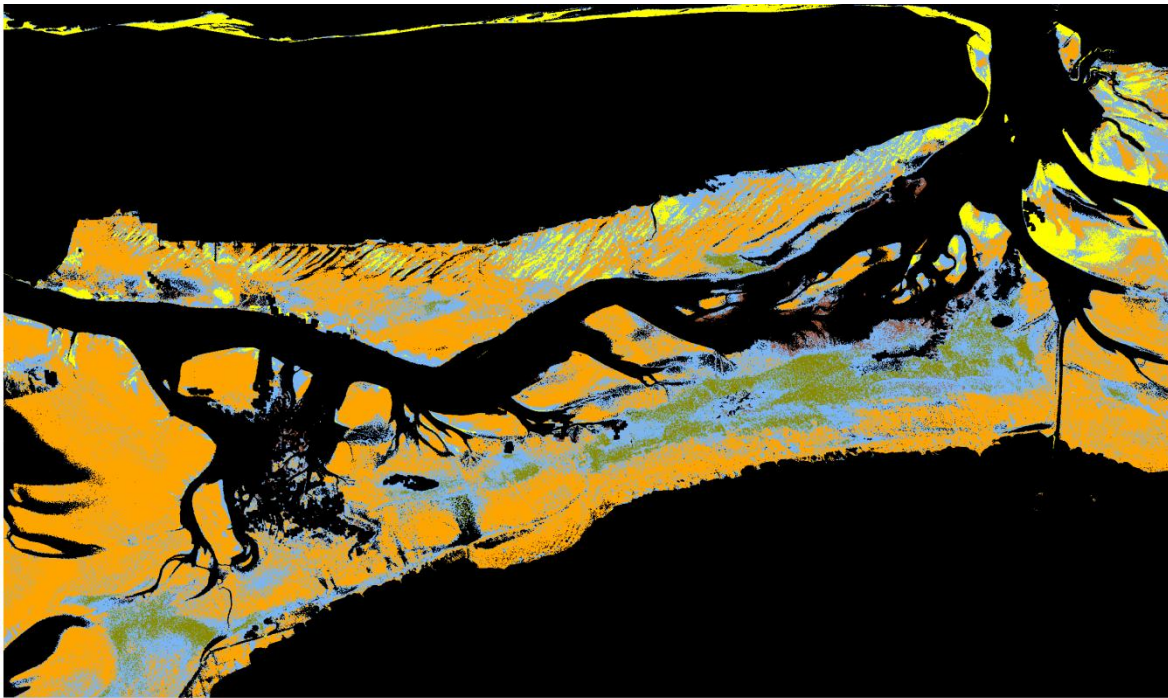


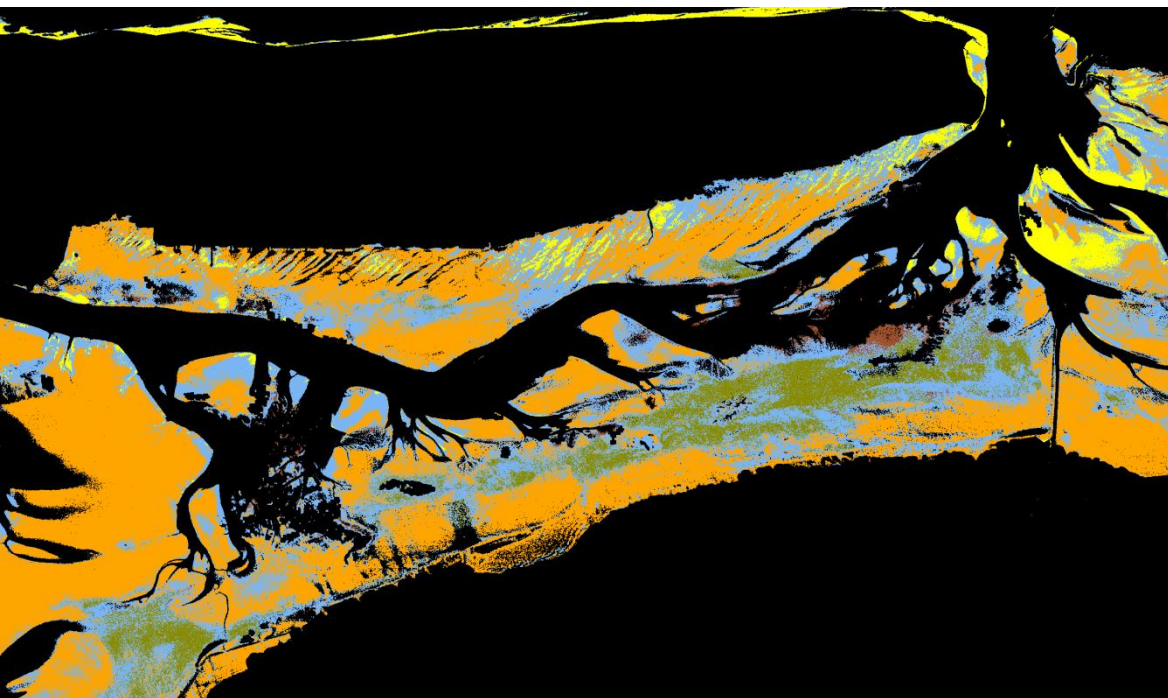
Figure A-4: Sediment maps obtained with the hierarchical knowledge-based decision tree.



- Change
- Dry sand
- Wet sand
- Mixture
- Mud
- Unclassified

**Change between the sediment classifications
between April 25, 2010 and June 27, 2011**

0 0.5 1 2 Km

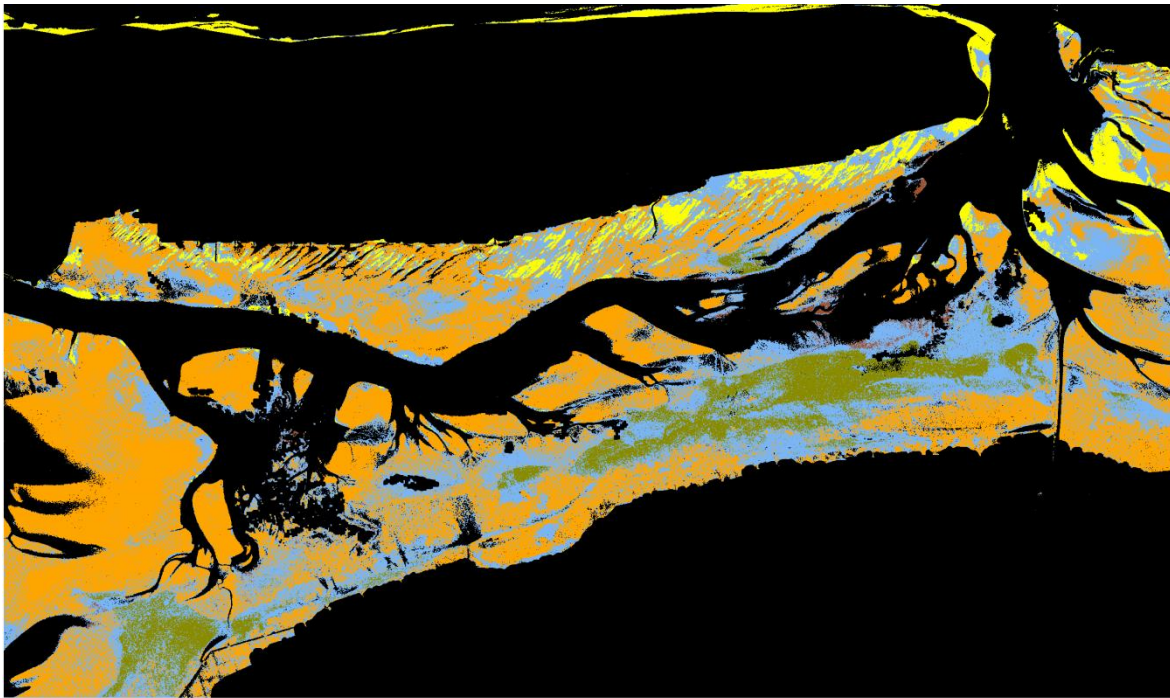


- Change
- Dry sand
- Wet sand
- Mixture
- Mud
- Unclassified

**Change between the sediment classifications
between April 25, 2010 and July 11, 2011**

0 0.5 1 2 Km

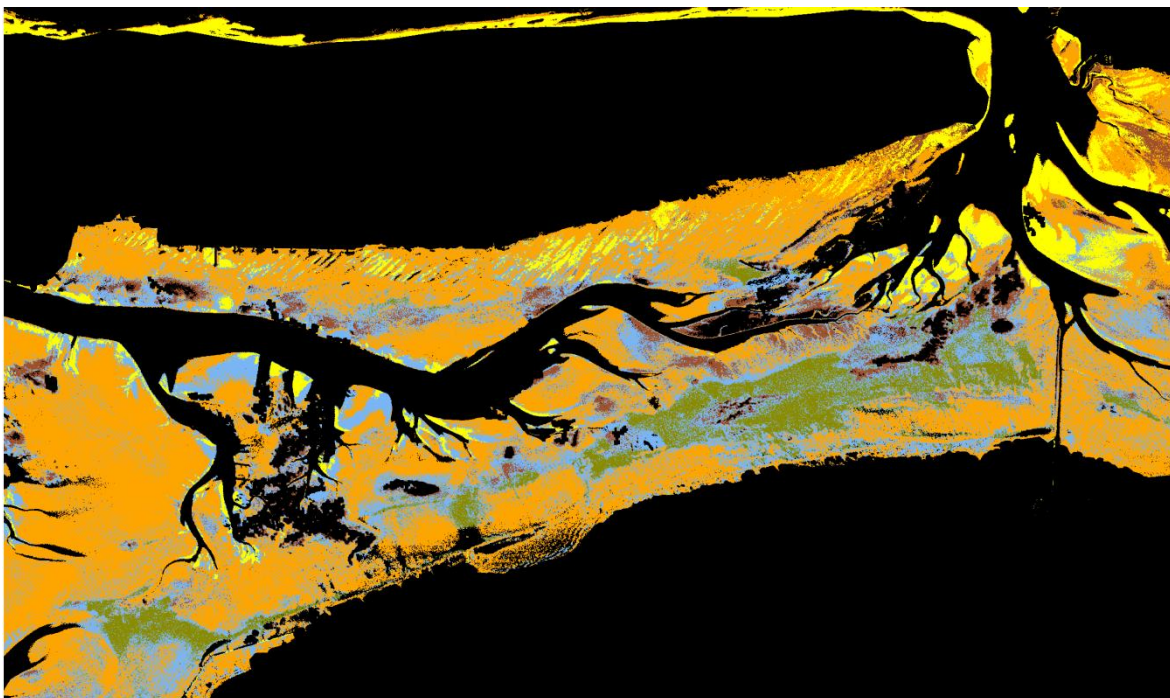




- Change
- Dry sand
- Wet sand
- Mixture
- Mud
- Unclassified

Change between the sediment classifications between April 25, 2010 and October 22, 2011

0 0.5 1 2 Km



- Change
- Dry sand
- Wet sand
- Mixture
- Mud
- Unclassified

Change between the sediment classifications between June 27, 2011 and July 11, 2011

0 0.5 1 2 Km



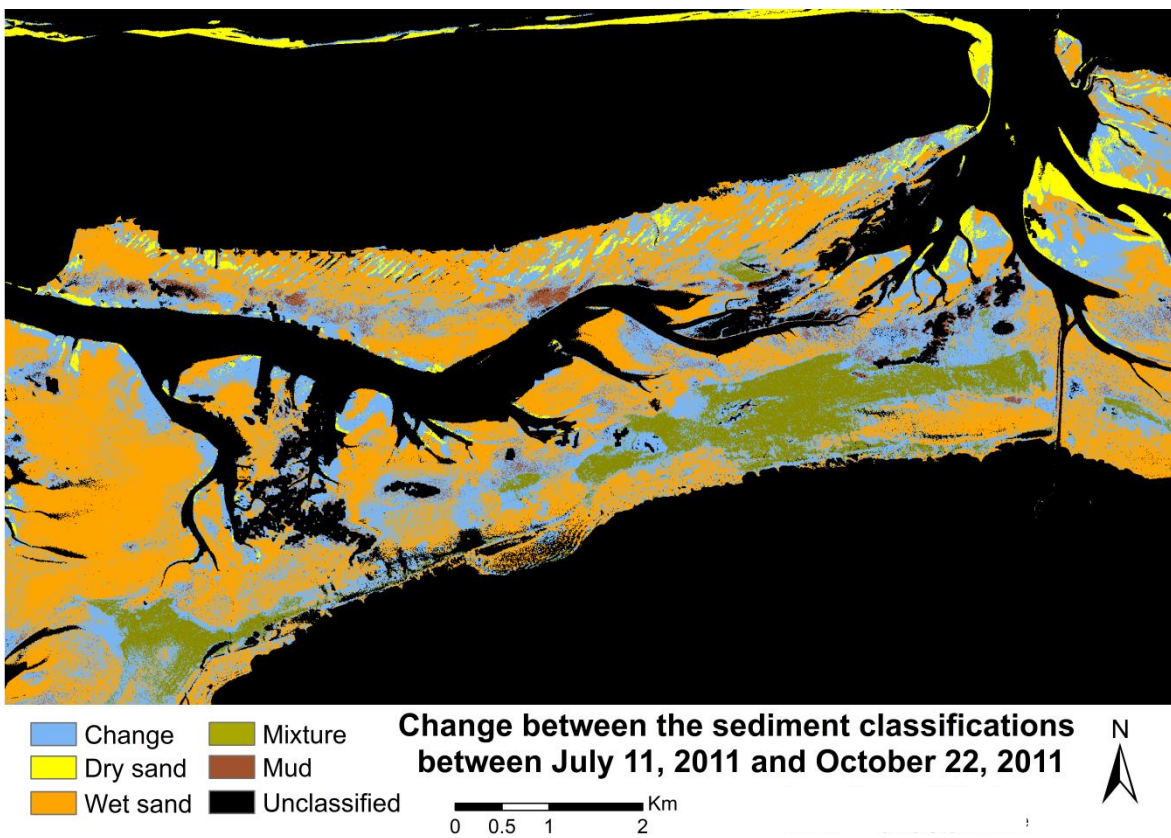
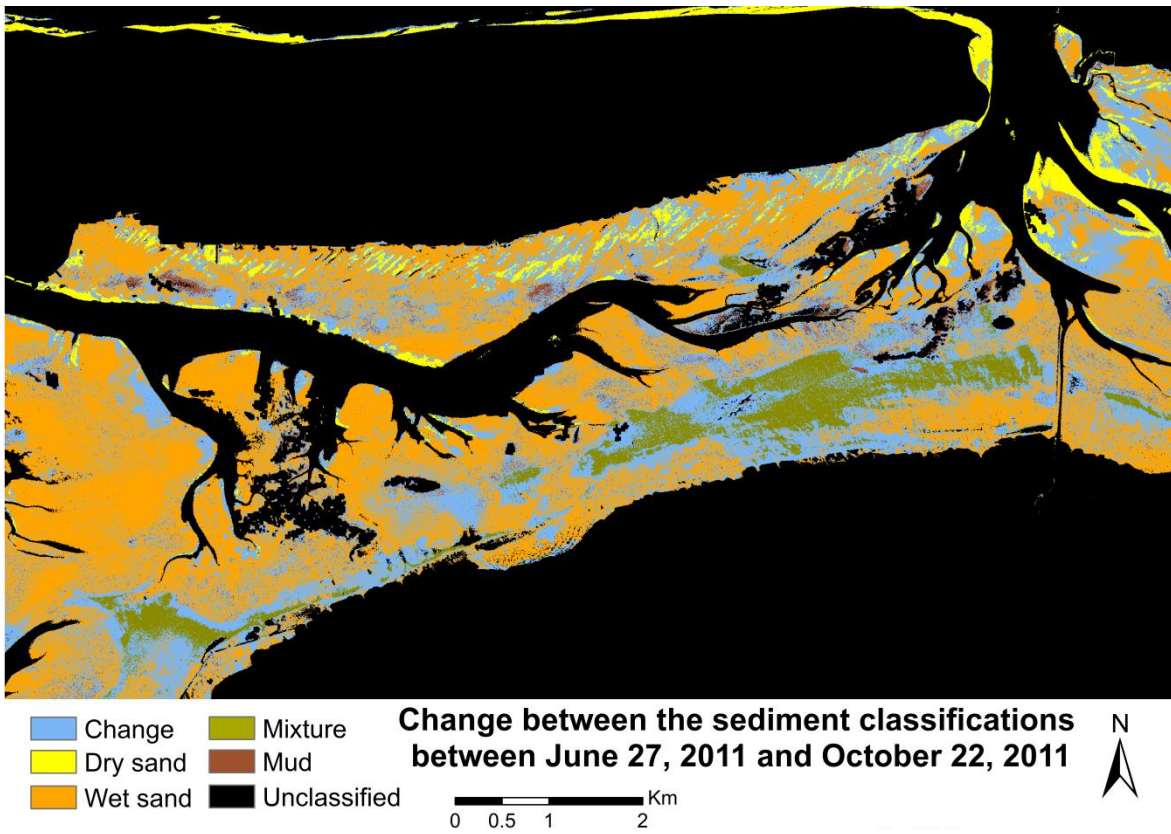
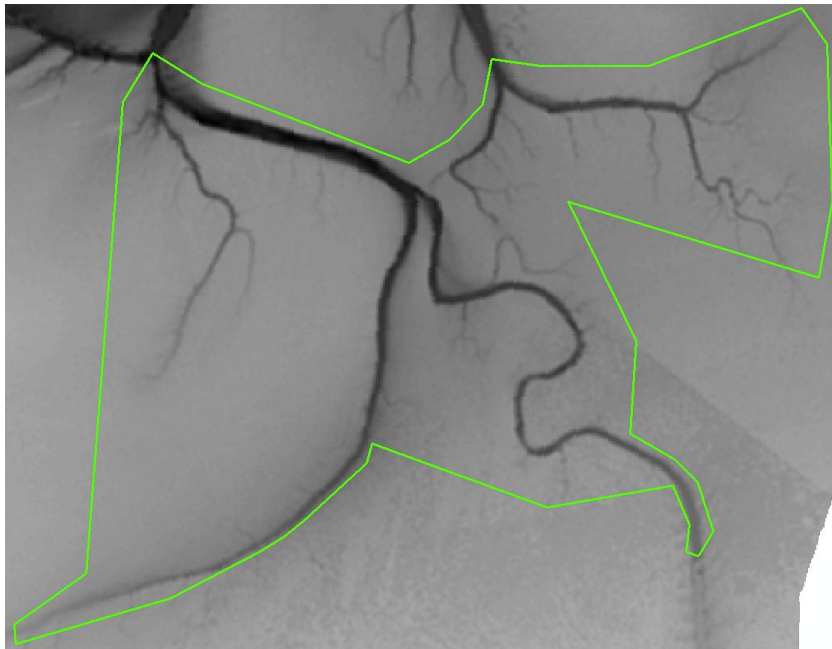
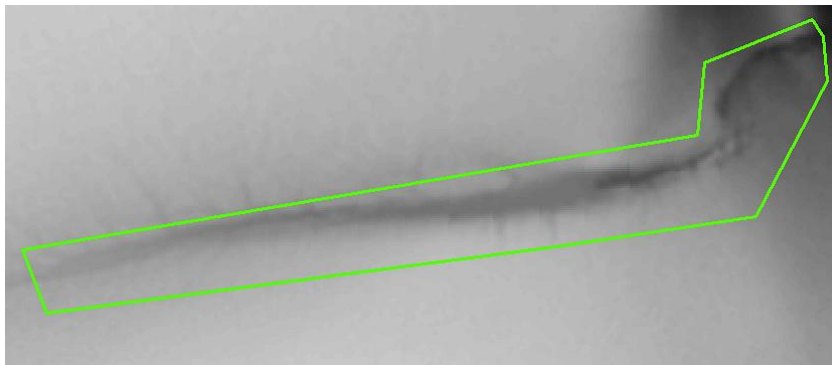
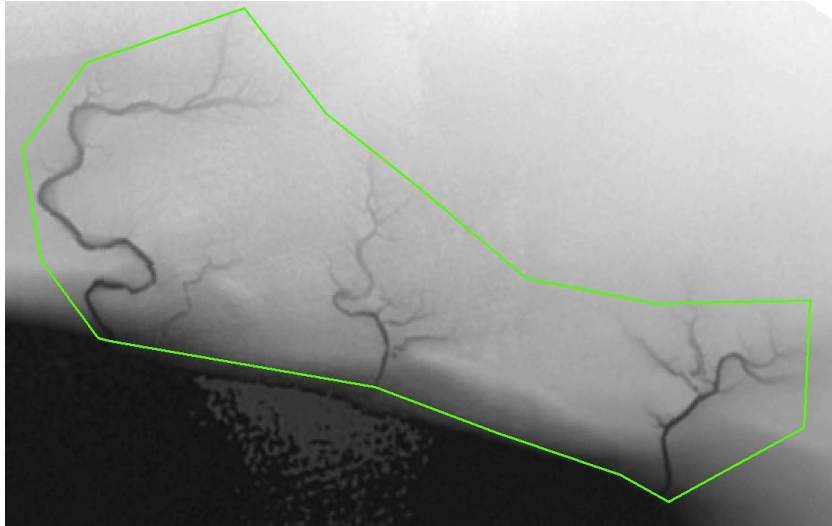


Figure A-5: Change maps of the four sediment classifications obtained with the hierarchical knowledge-based decision tree.



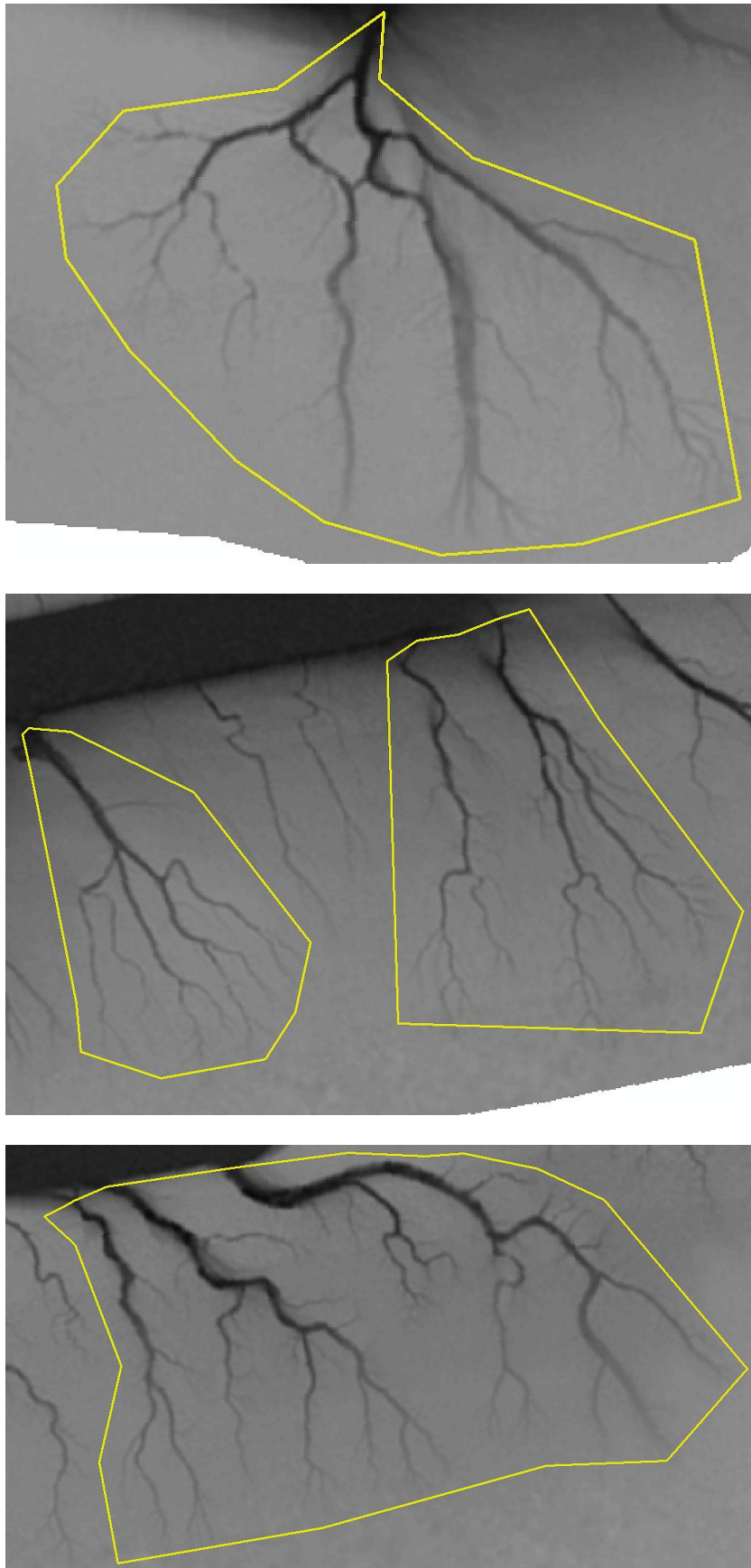
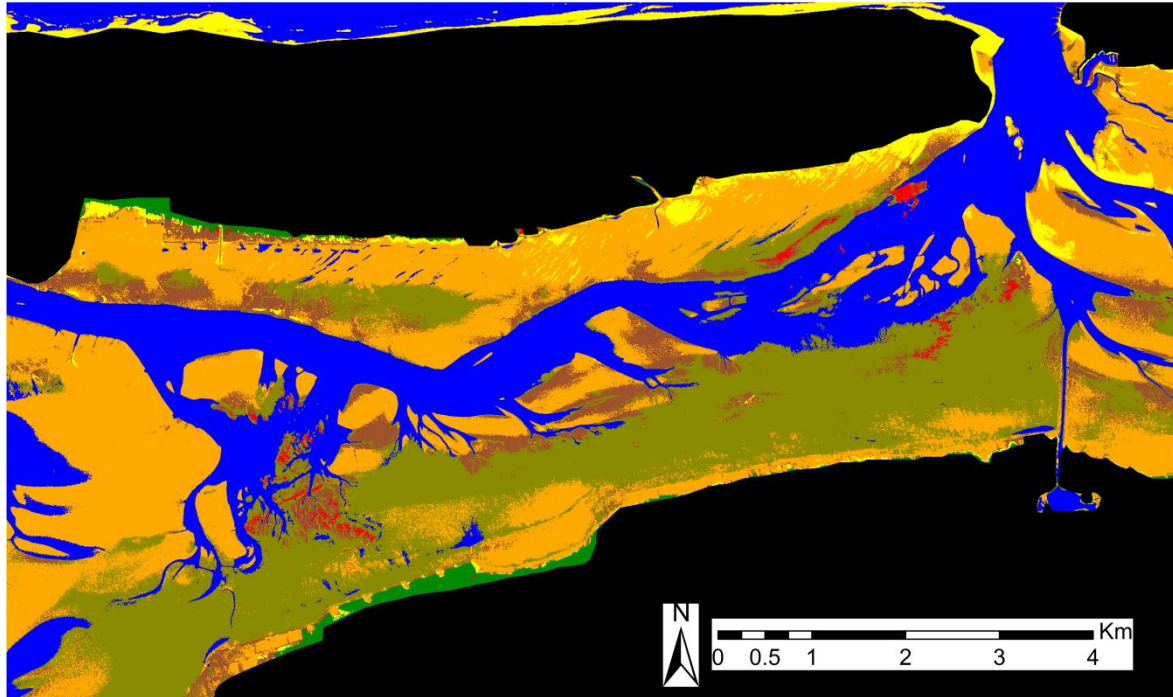


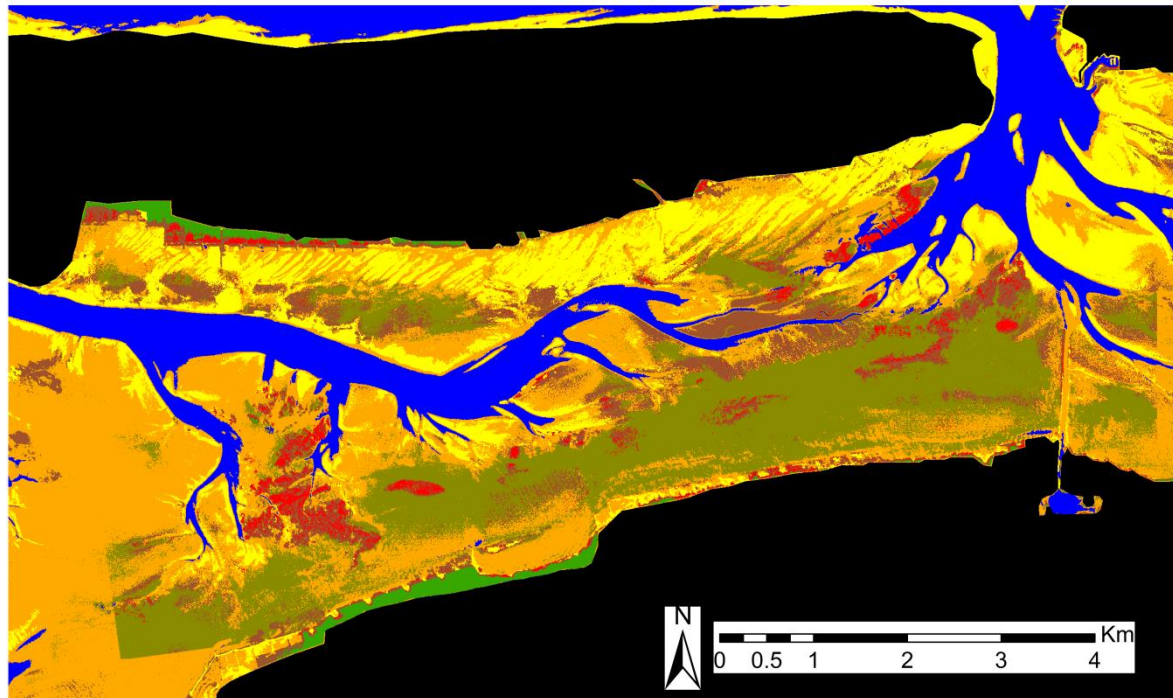
Figure A-6: Representative areas for the channel extraction evaluation. The green polygons represent sand flat areas and the yellow polygons mudflat areas.

a)



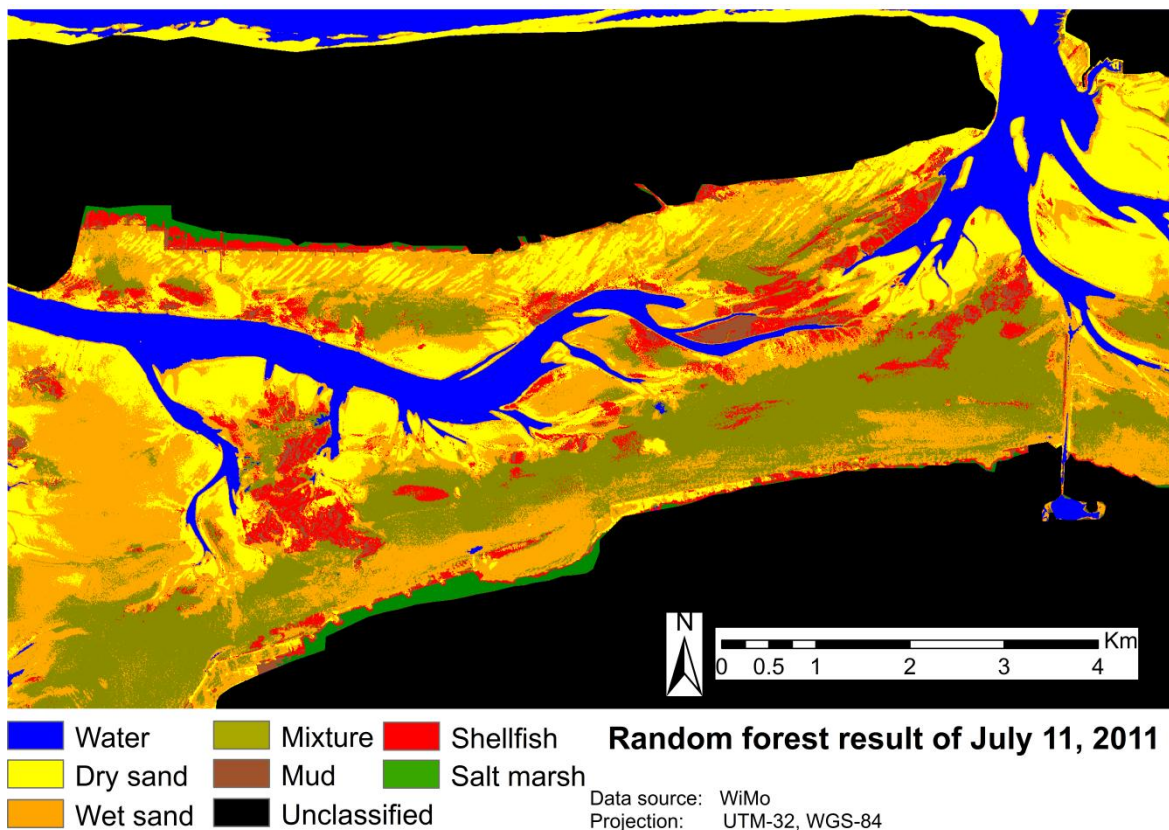
Water
 Mixture
 Shellfish
 Random forest result of April 25, 2010
 Dry sand
 Mud
 Salt marsh
 Wet sand
 Unclassified
 Data source: WiMo
 Projection: UTM-32, WGS-84

b)



Water
 Mixture
 Shellfish
 Random forest result of June 27, 2011
 Dry sand
 Mud
 Salt marsh
 Wet sand
 Unclassified
 Data source: WiMo
 Projection: UTM-32, WGS-84

c)



d)

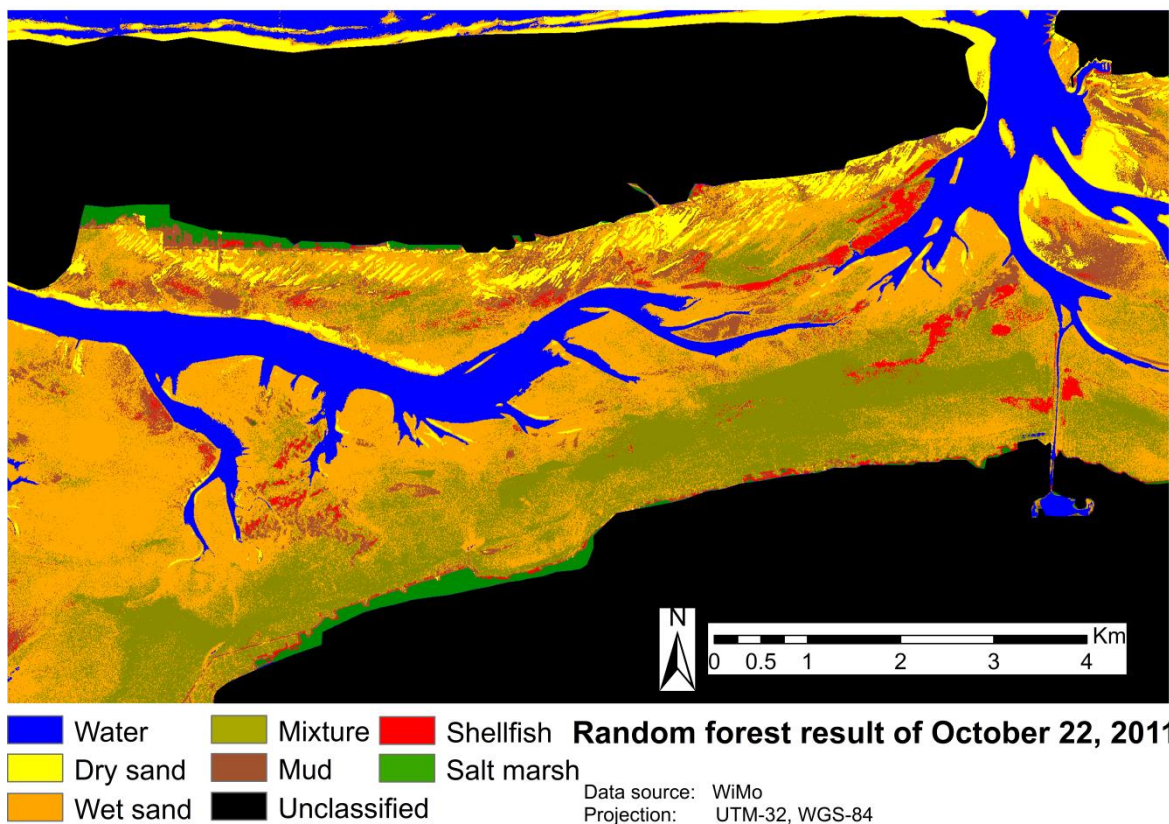
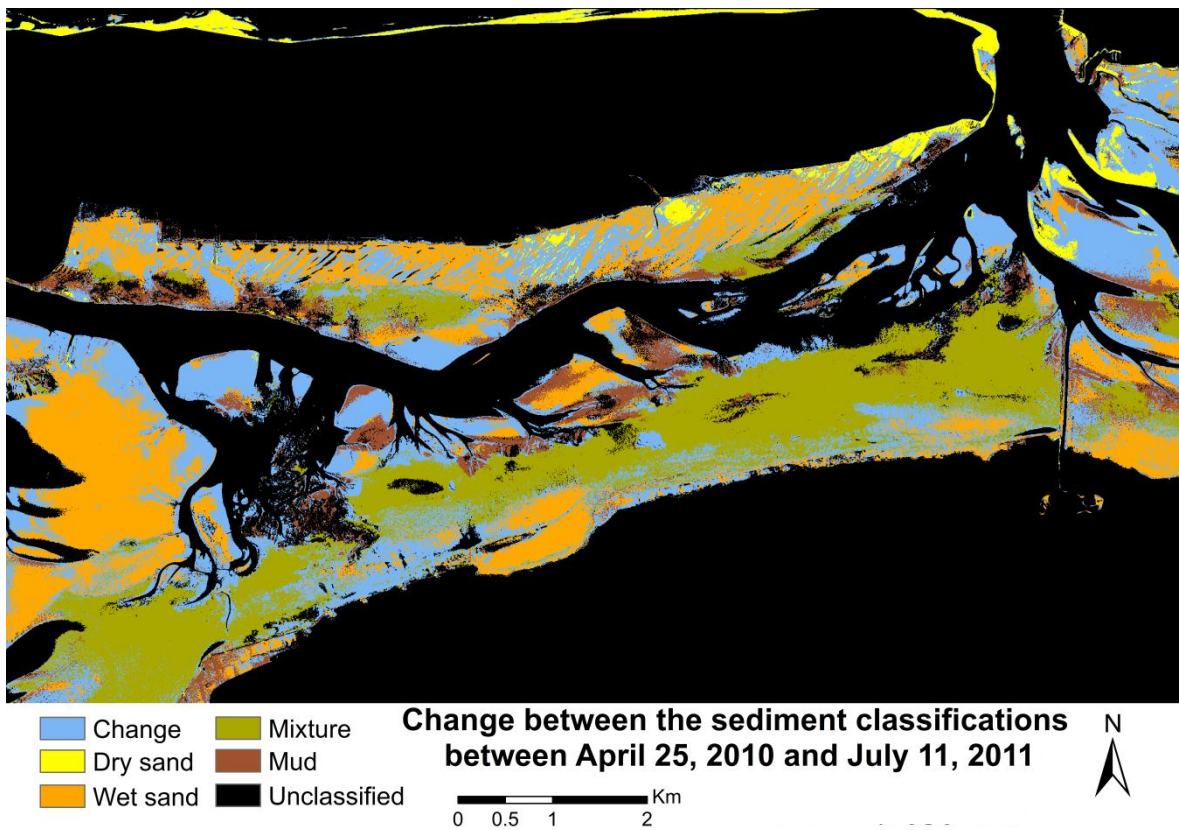
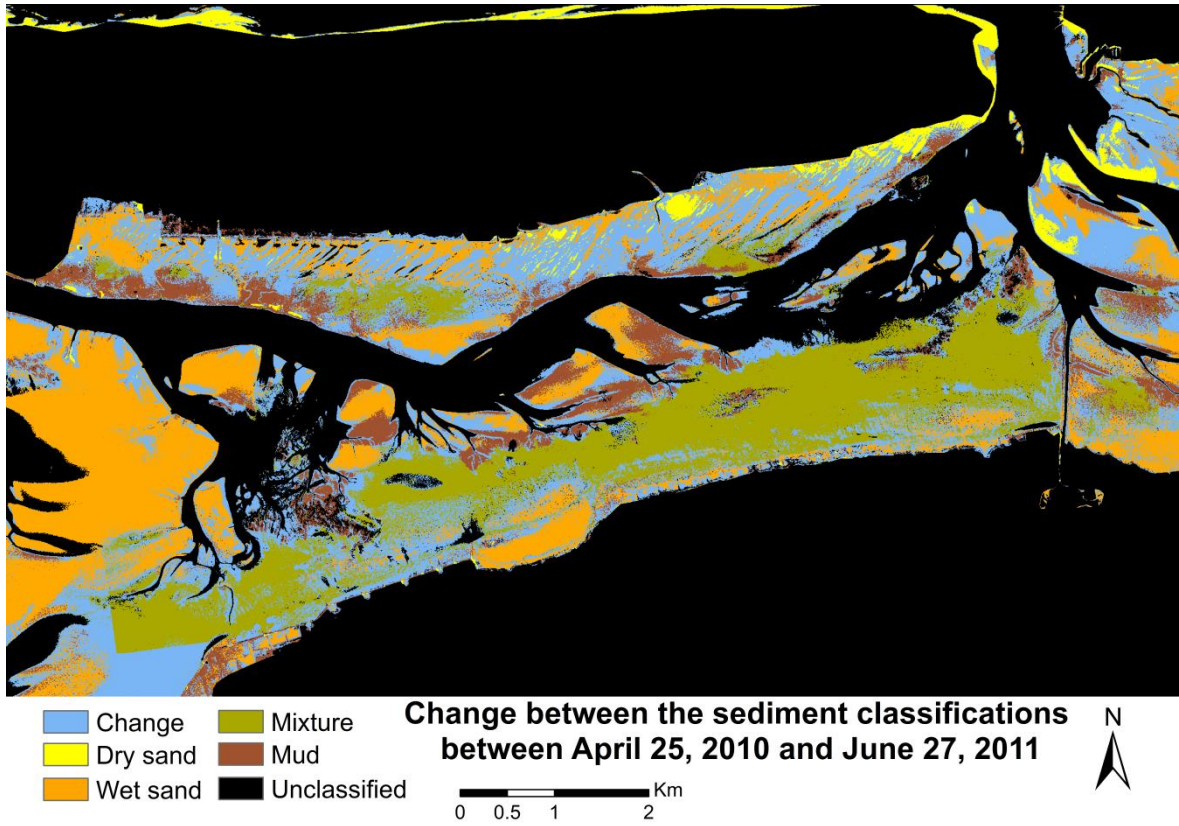
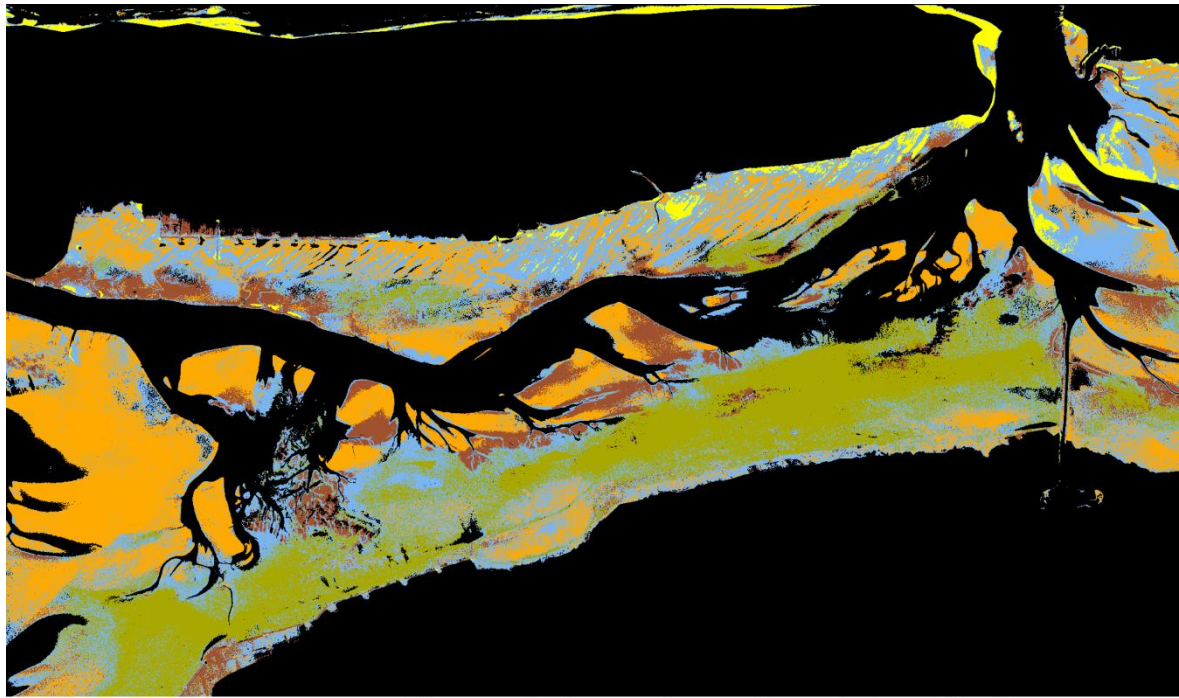


Figure A-7: Results of the random forest land cover classifications. Plot a) has only a single dataset as input (RE), whereas plots b) to d) have two datasets as input (RE and TSX).



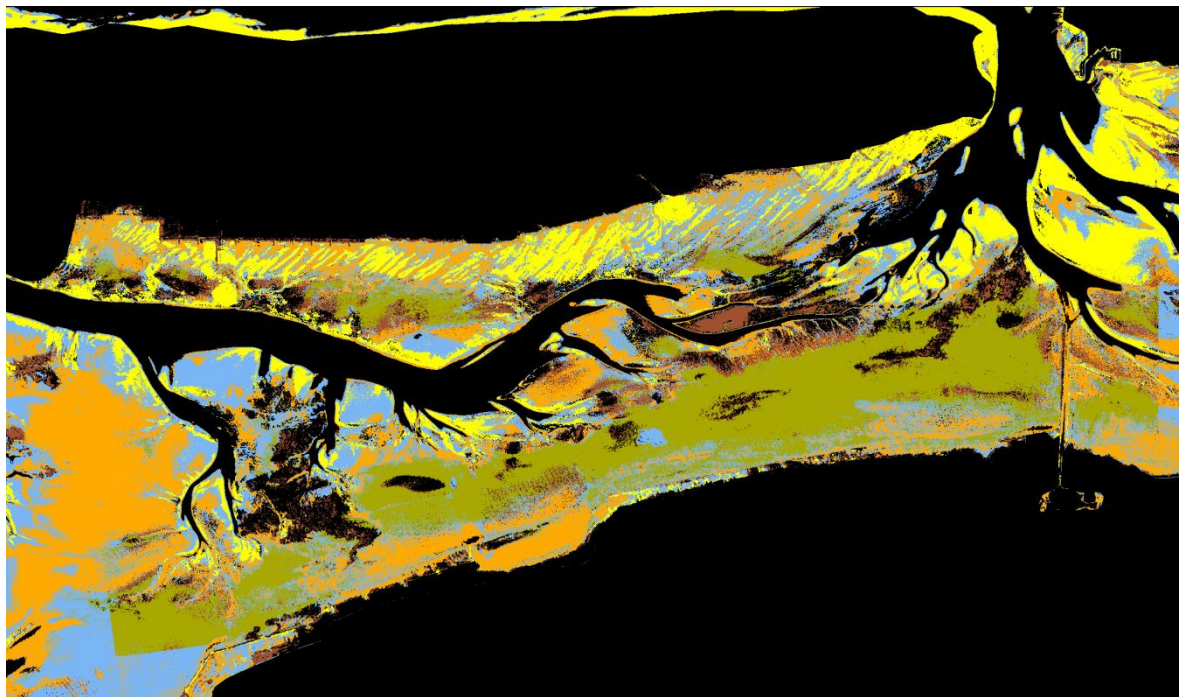


**Change between the sediment classifications
between April 25, 2010 and October 22, 2011**

Change	Mixture
Dry sand	Mud
Wet sand	Unclassified

0 0.5 1 2 Km

N



**Change between the sediment classifications
between June 27, 2011 and July 11, 2011**

Change	Mixture
Dry sand	Mud
Wet sand	Unclassified

0 0.5 1 2 Km

N

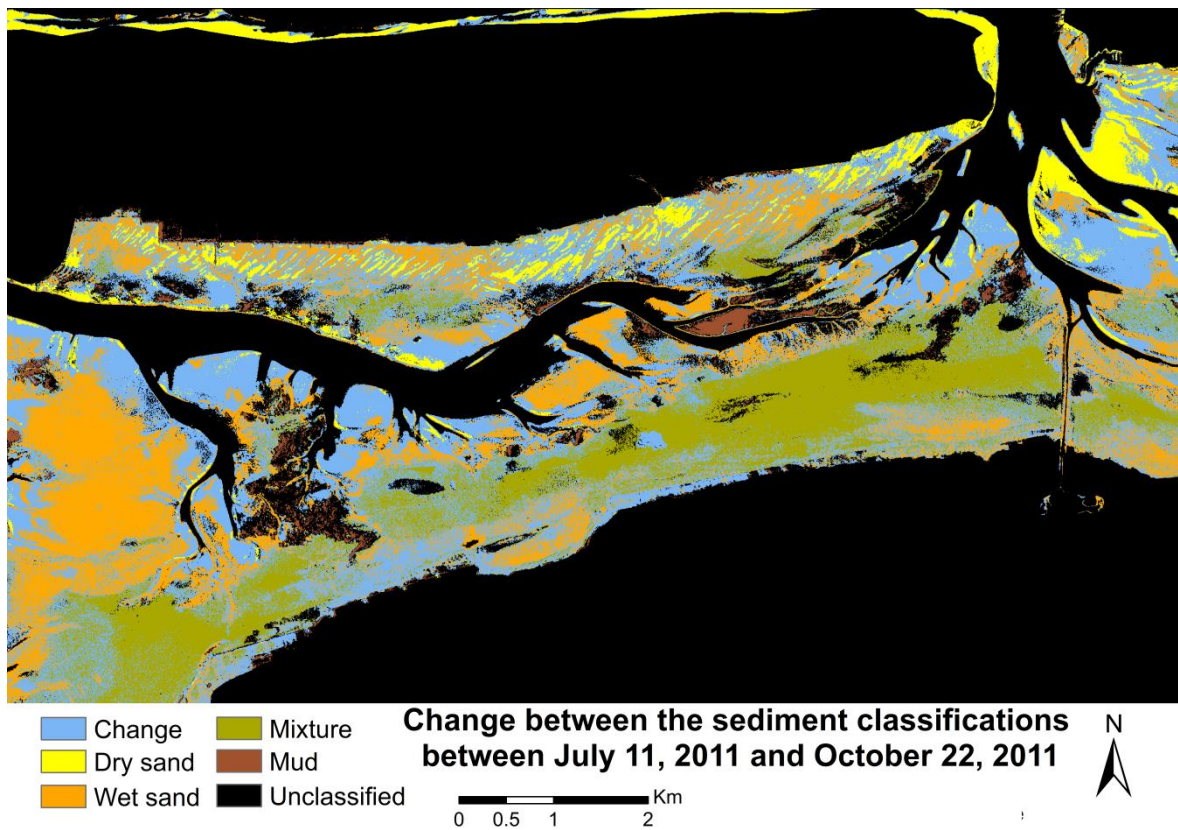
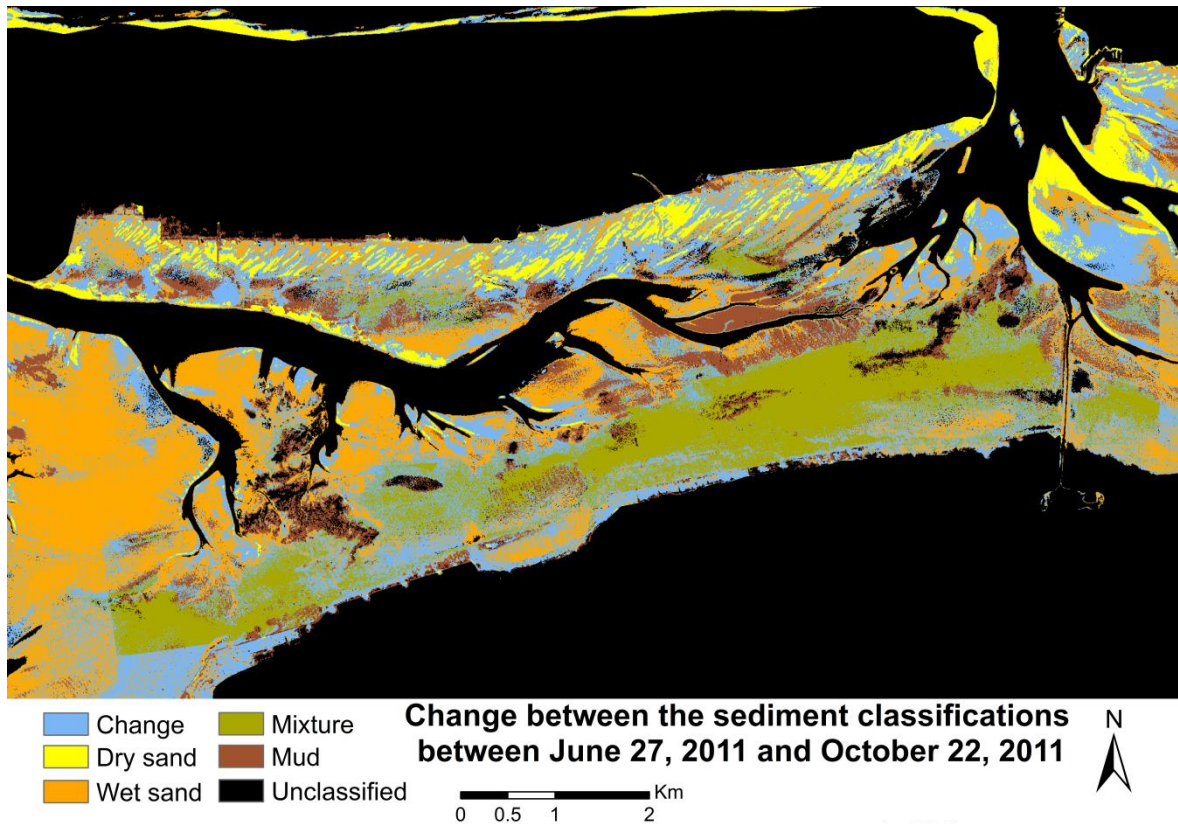
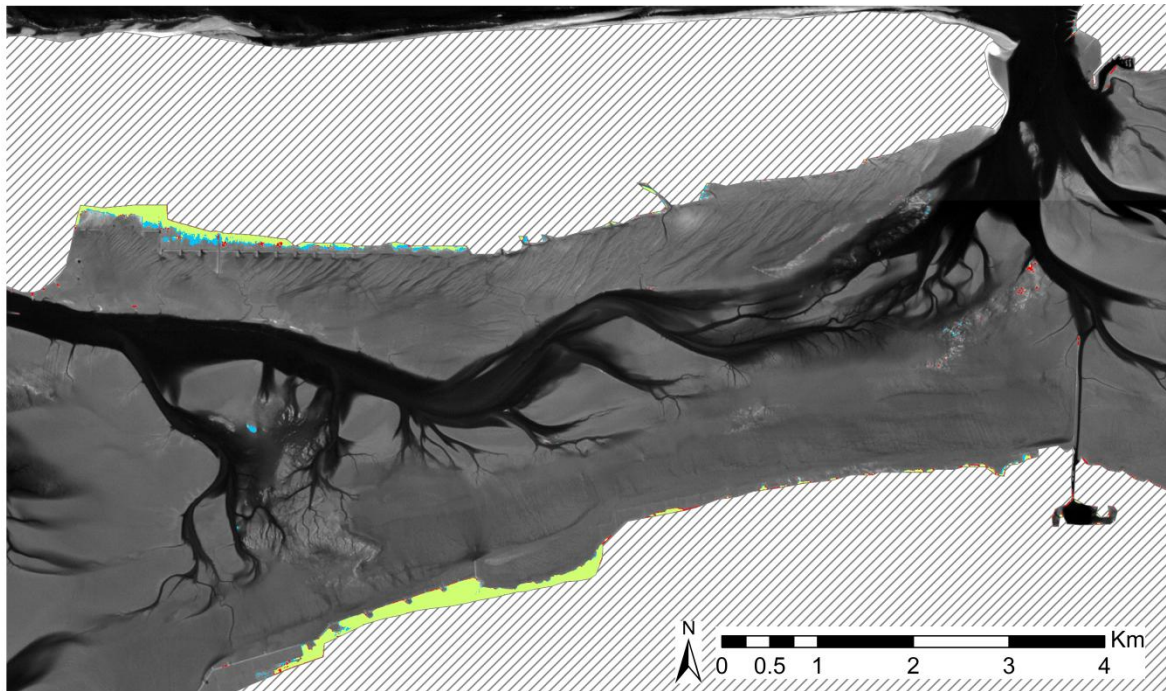


Figure A-8: Change maps of the four sediment classification derived with the random forest classification approach.

a)

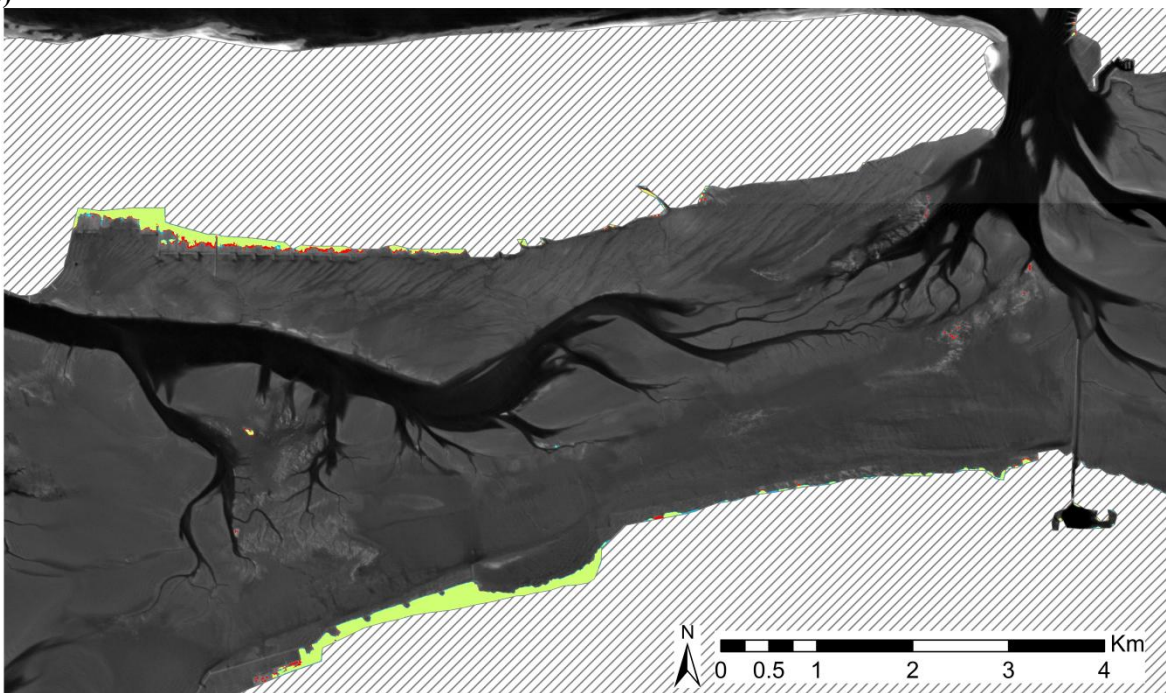


Change of salt marsh distribution from to April 25, 2010 to July 11, 2011

RE Near Infrared band ■ Decrease ■ Increase
■ No change Mainland/Island

Data source: RapidEye, WiMo
 Projection: UTM-32, WGS-84

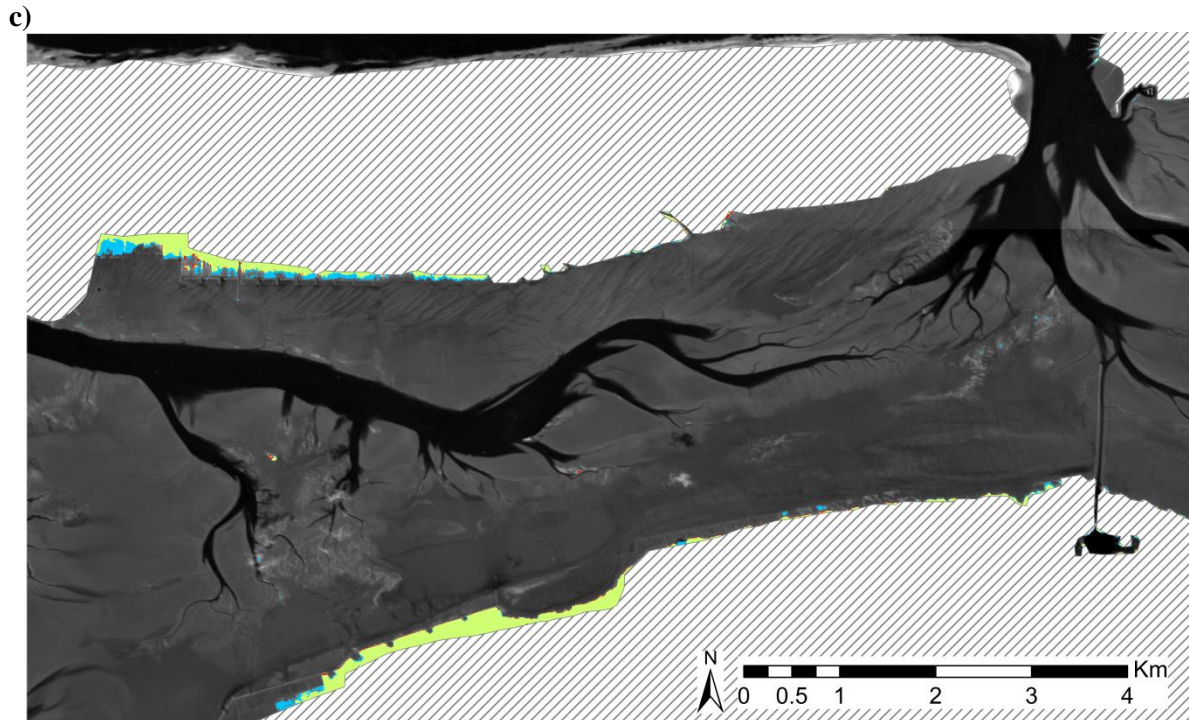
b)



Change of salt marsh distribution from to June 27, 2011 to July 11, 2011

RE Near Infrared band ■ Decrease ■ Increase
■ No change Mainland/Island

Data source: RapidEye, WiMo
 Projection: UTM-32, WGS-84

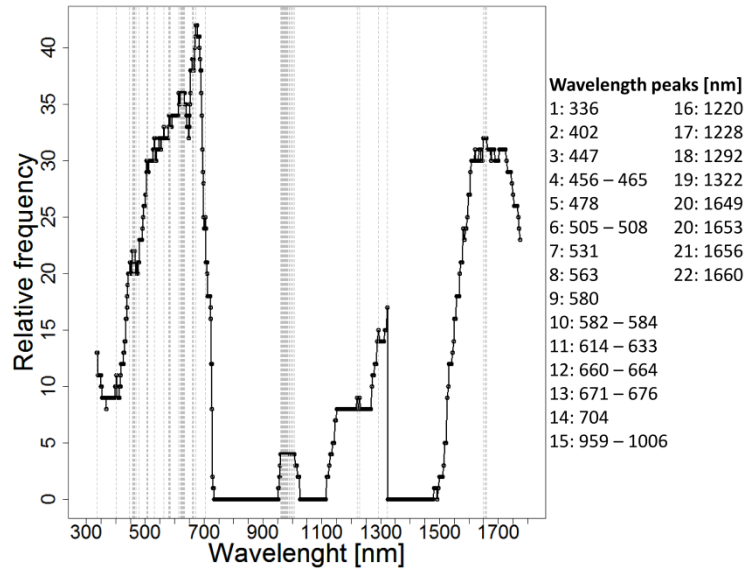


Change of salt marsh distribution from to July 11, 2011 to October 22, 2011

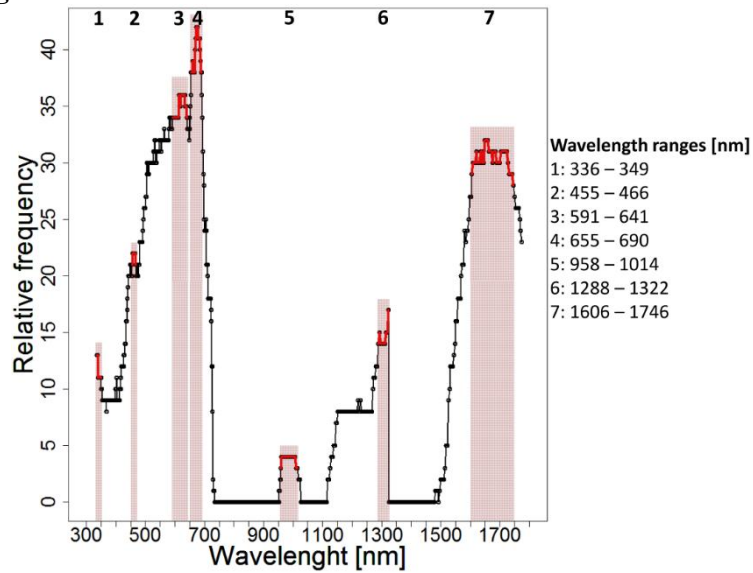
RE Near Infrared band	■ Decrease	■ Increase	Data source: RapidEye, WiMo
	■ No change	Mainland/Island	Projection: UTM-32. WGS-84

Figure A-9: Changes of the salt marsh distribution between 25 April 2010 and 27 June 2011 (a)), 27 June 2011 and 11 July 2011 (b)) and 11 July 2011 and 22 October 2011 (c)). The results are obtained with the random forest classification algorithm.

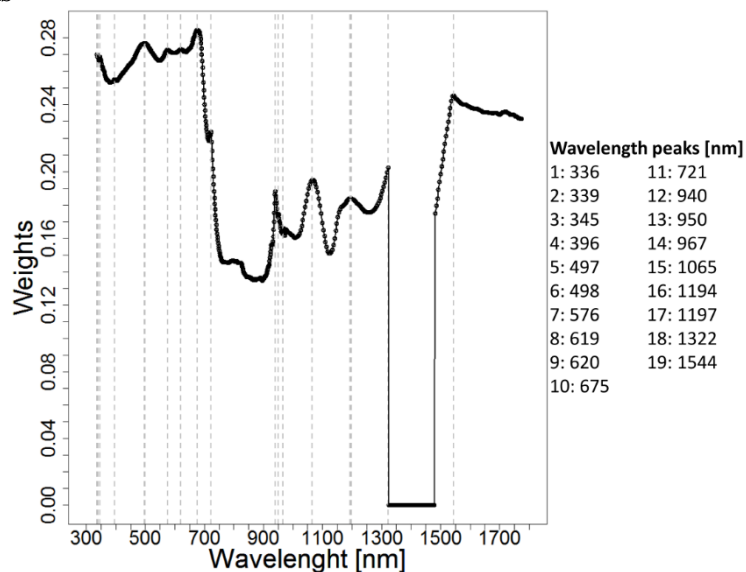
2013 JMDFS peaks



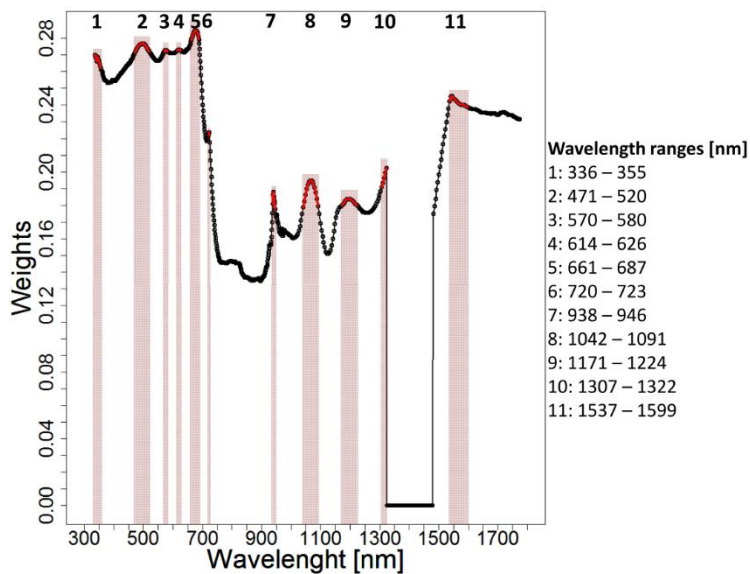
2013 JMDFS ranges



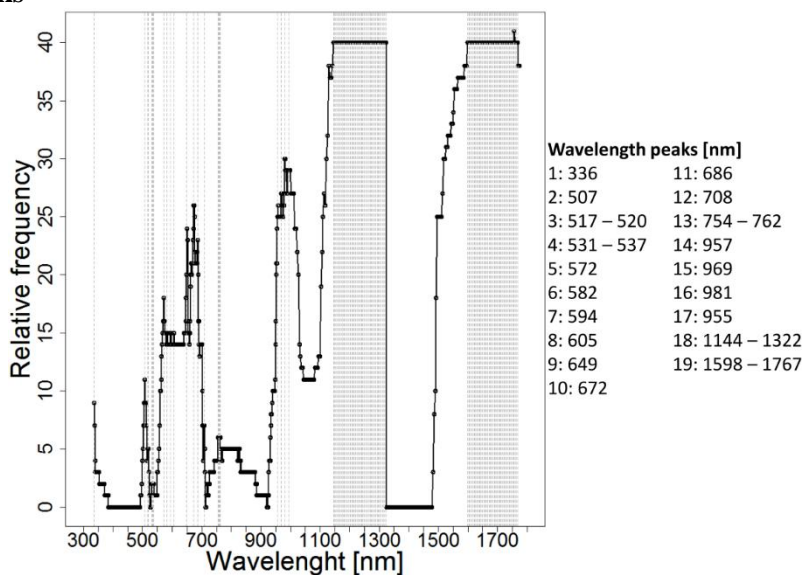
2013 ReliefF peaks



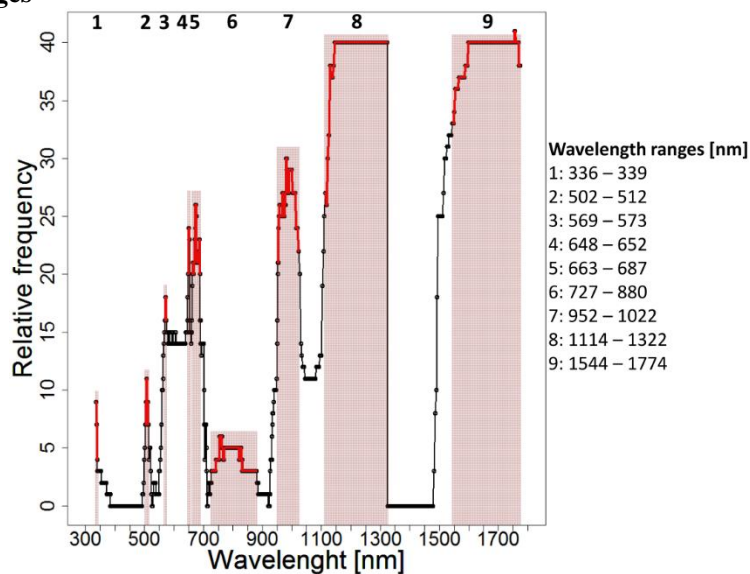
2013 ReliefF ranges



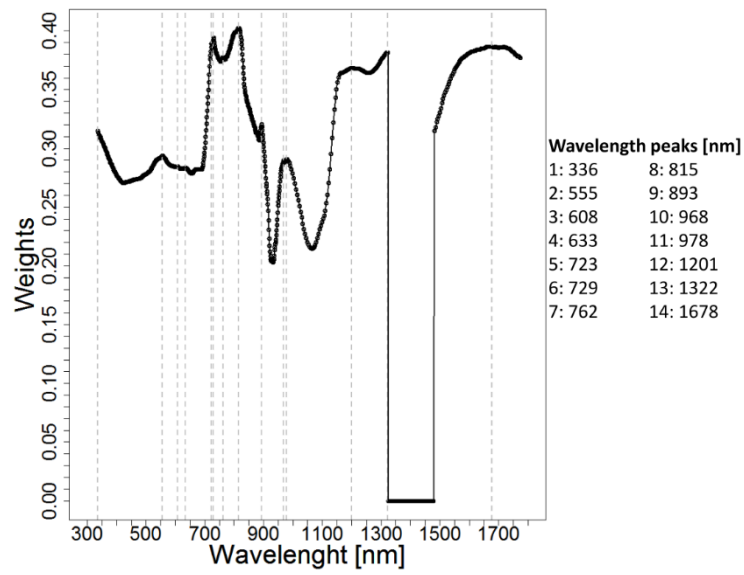
2015 JMDFS peaks



2015 JMDFS ranges



2015 ReliefF peaks



2015 ReliefF ranges

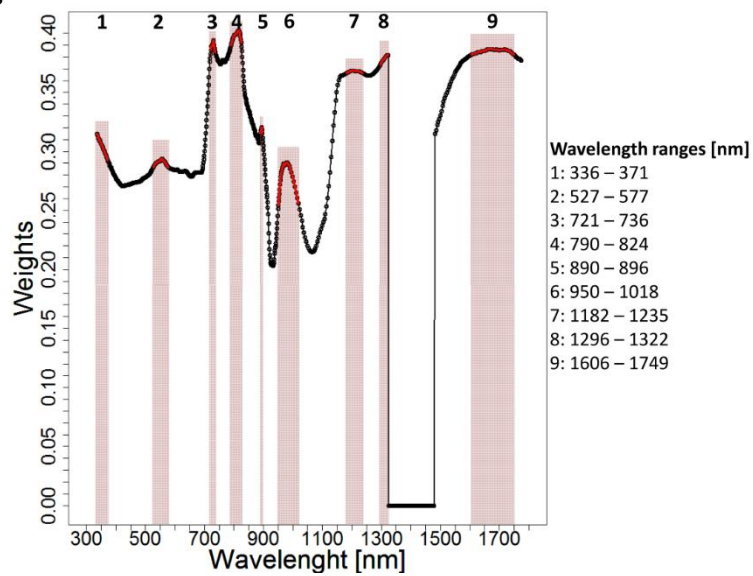
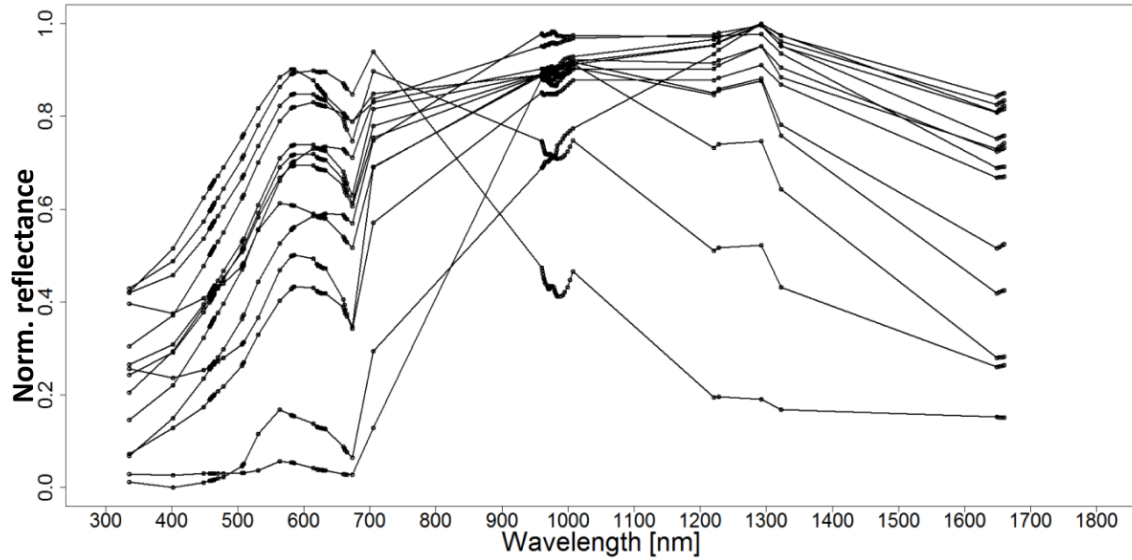
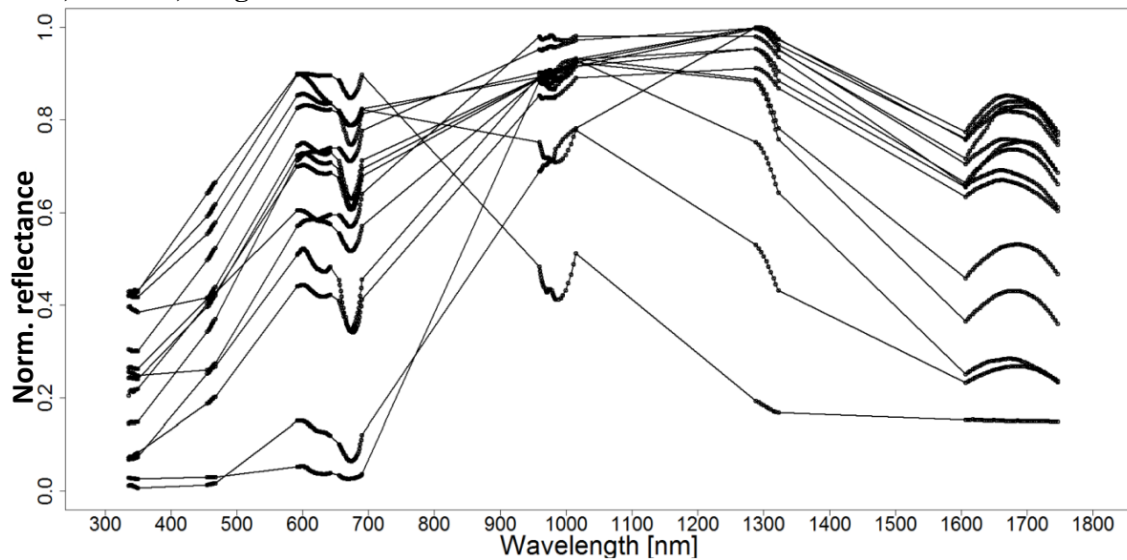


Figure A-10: Chosen wavelengths applying the method ‘peaks’ and ‘ranges’ to the spectrometric data of 2013 and 2015.

a) 2013, JMDFS, peaks



b) 2013, JMDFS, ranges



c) 2013, JMDFS, all wavelengths

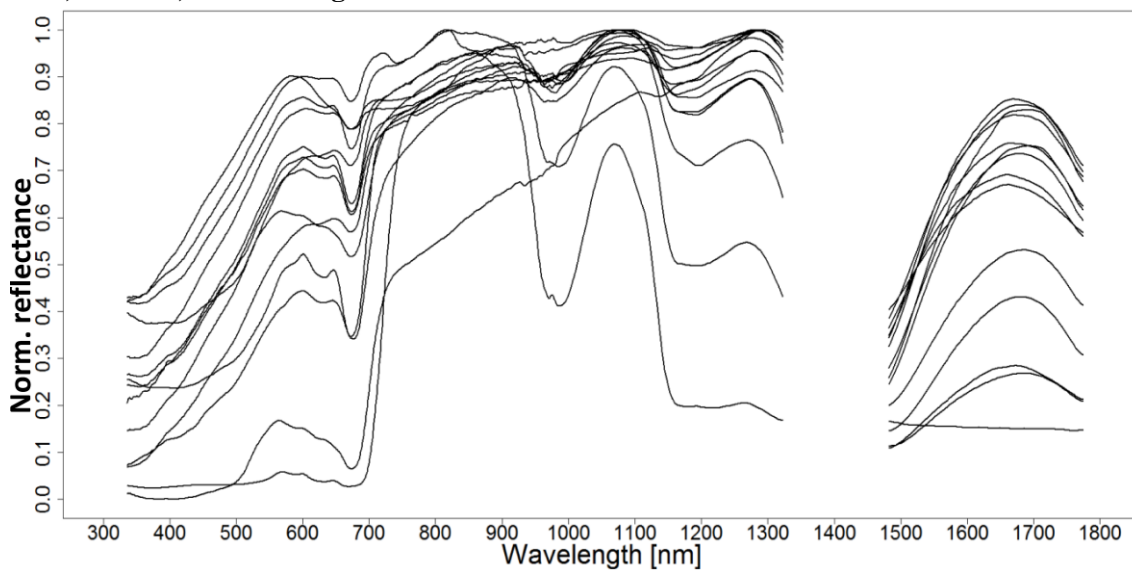
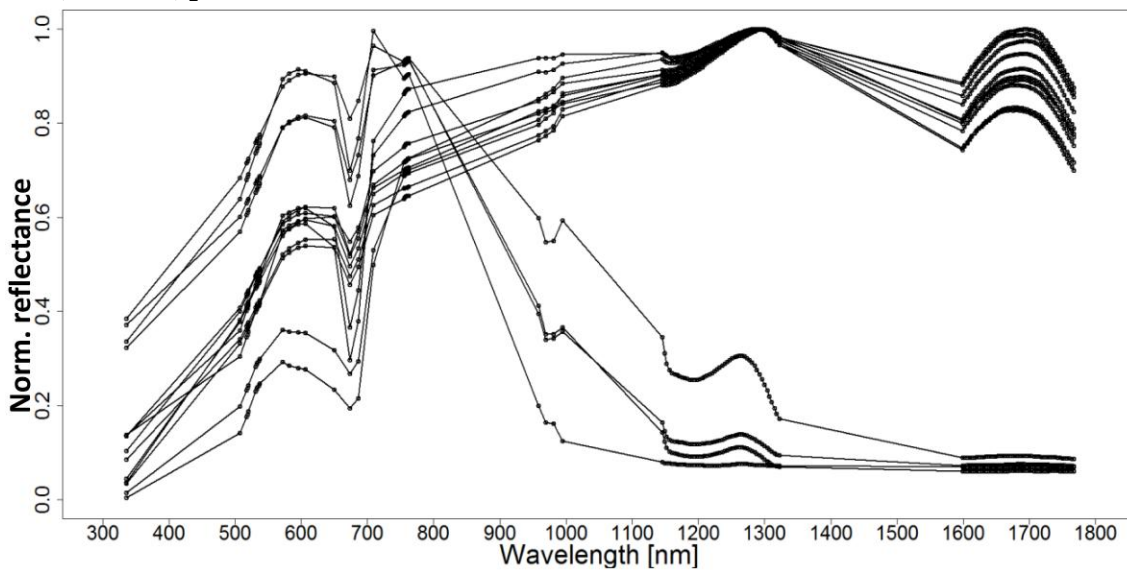
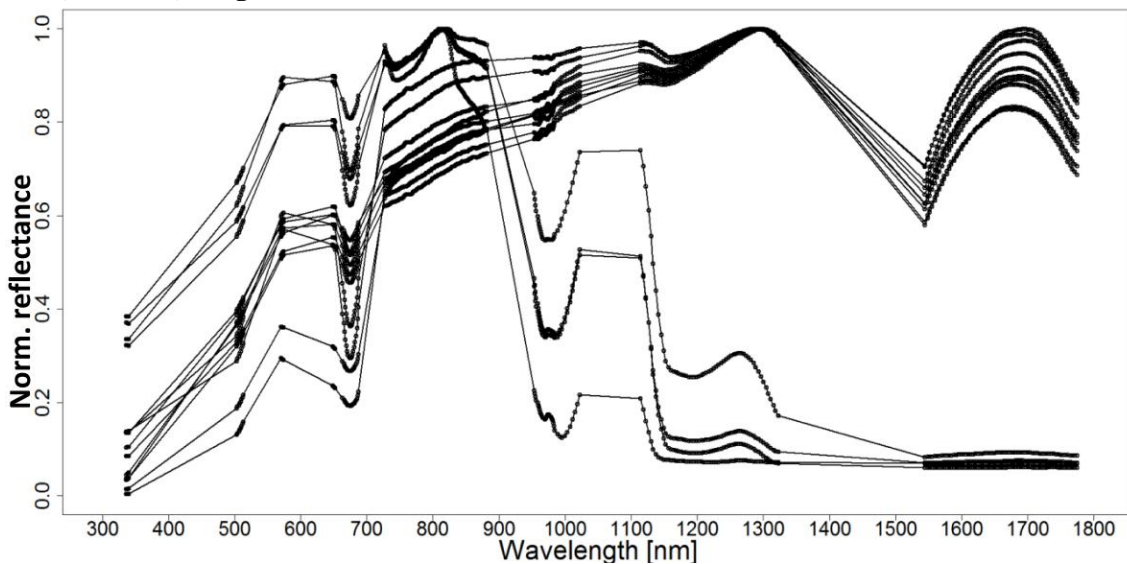


Figure A-11: Plots a) and b) represents the selected wavelengths from JMDFS with method ‘peaks’ and ‘ranges’ of the mean spectra of 2013 compared with all wavelengths in plot c). The discrete spectral band values of plots a) and b) were linked for better comparison.

a) 2015, JMDFS, peaks



b) 2015, JMDFS, ranges



c) 2015, JMDFS, all wavelengths

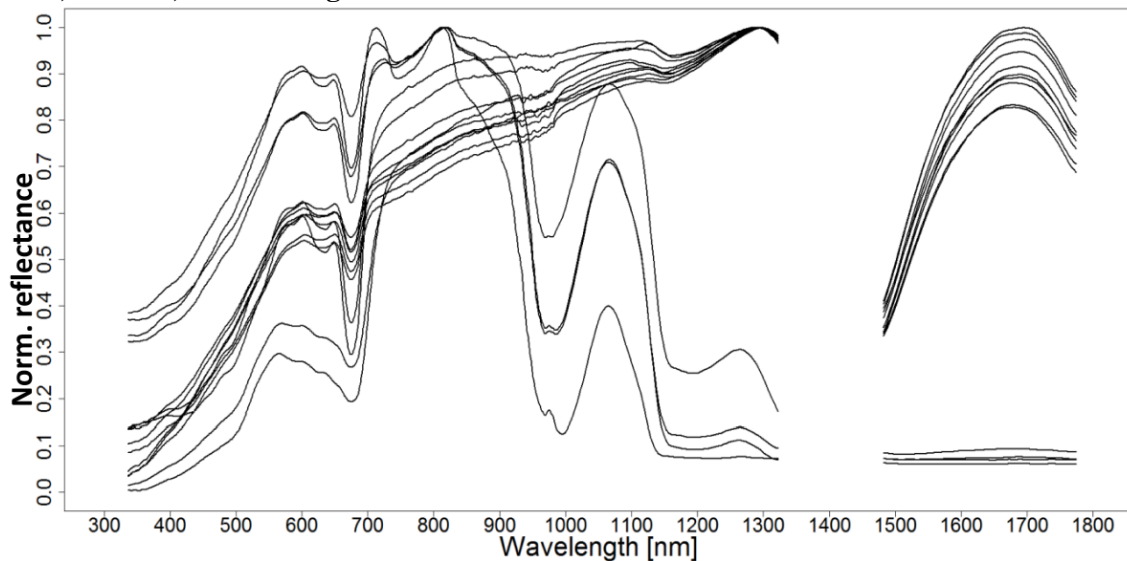
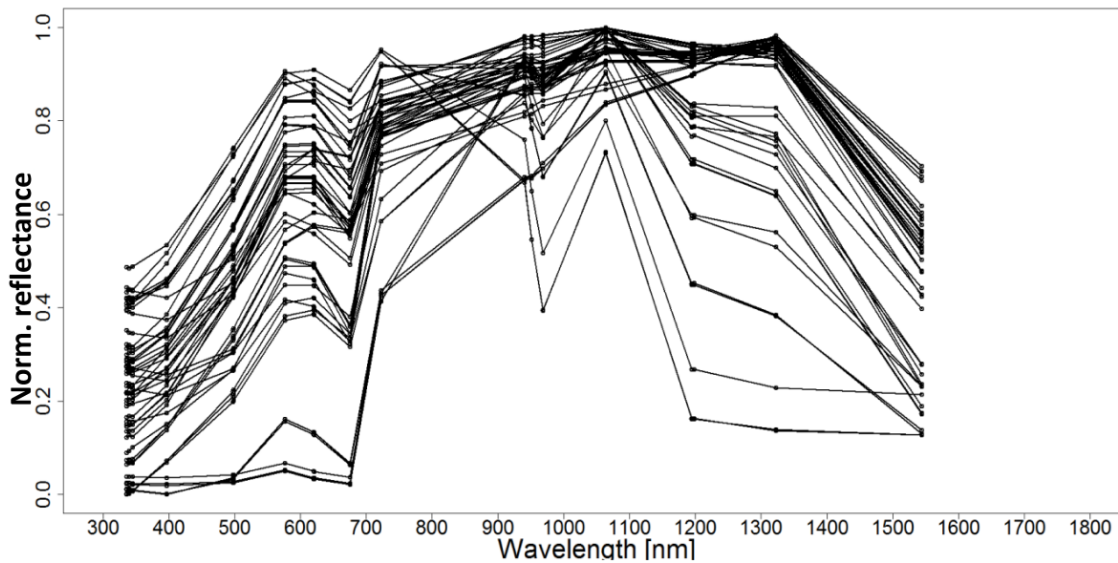
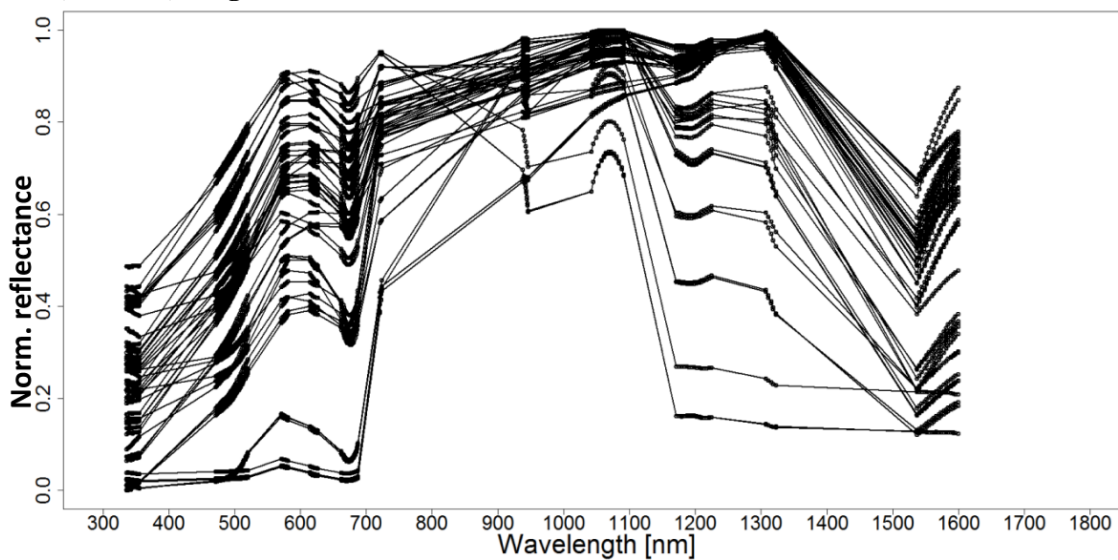


Figure A-12: Plot a) and b) represents the selected wavelengths from JMDFS with methods ‘peaks’ and ‘ranges’ of the mean spectra of 2015 compared with all wavelengths in plot c). The discrete spectral band values of plots a) and b) were linked for better comparison.

a) 2013, ReliefF, peaks



b) 2013, ReliefF, ranges



c) 2013, ReliefF, all wavelengths

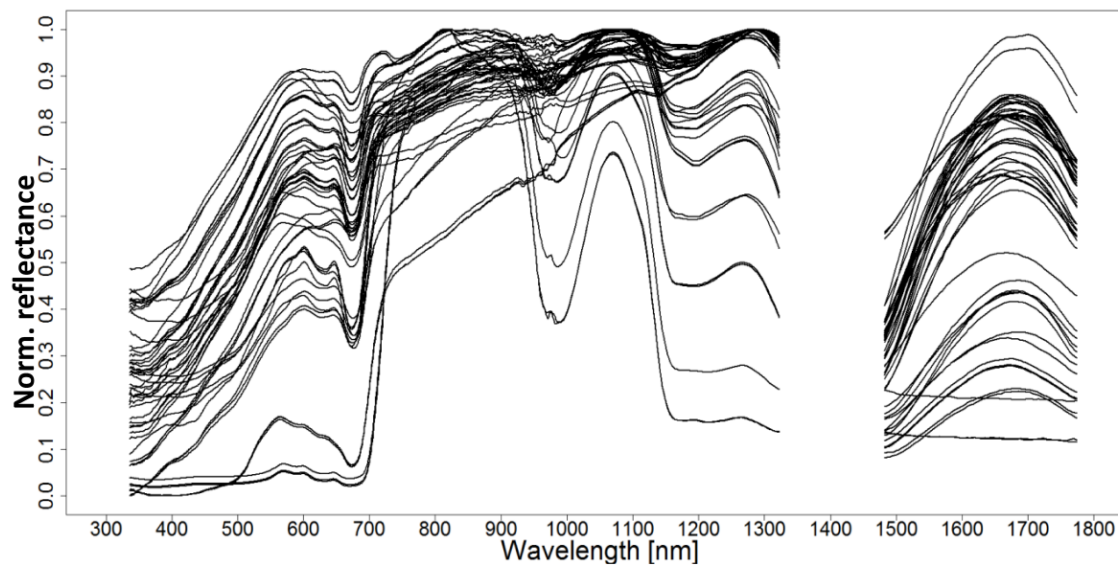
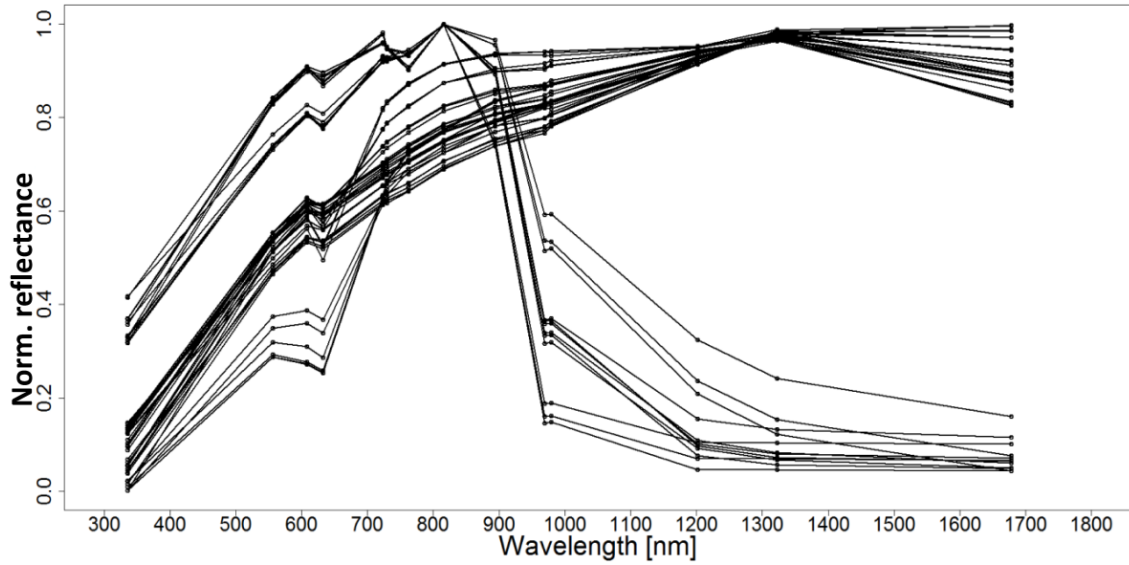
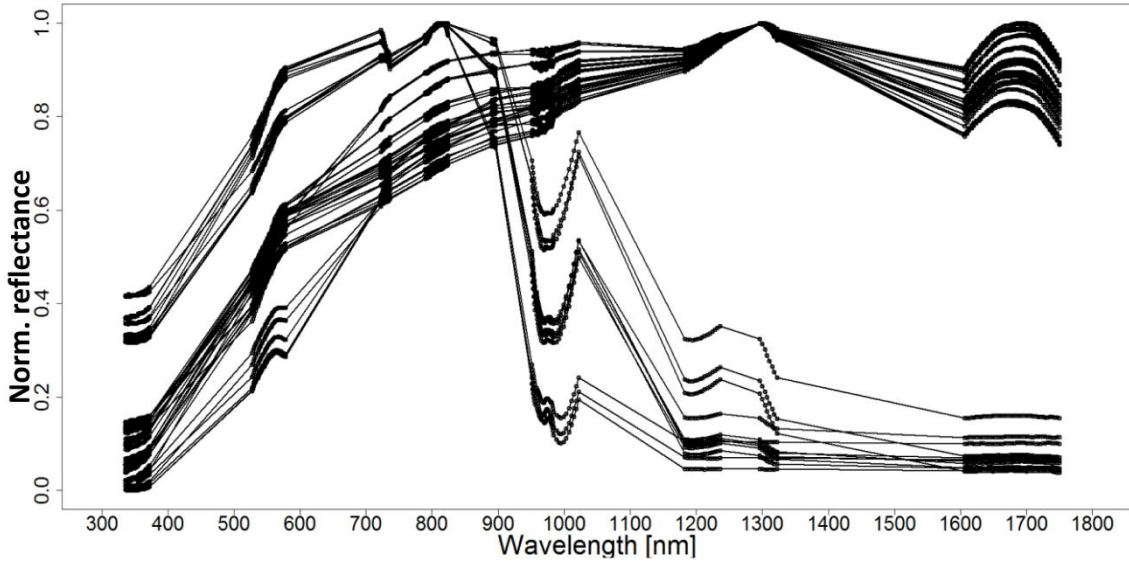


Figure A-13: Plot a) and b) represents the selected wavelengths from ReliefF with method 'peaks' and 'ranges' of the spectra of 2013 compared with all wavelengths in plot b). The discrete spectral band values of plots a) and b) were linked for better comparison.

a) 2015, ReliefF, peaks



b) 2015, ReliefF, ranges



c) 2015, all wavelengths

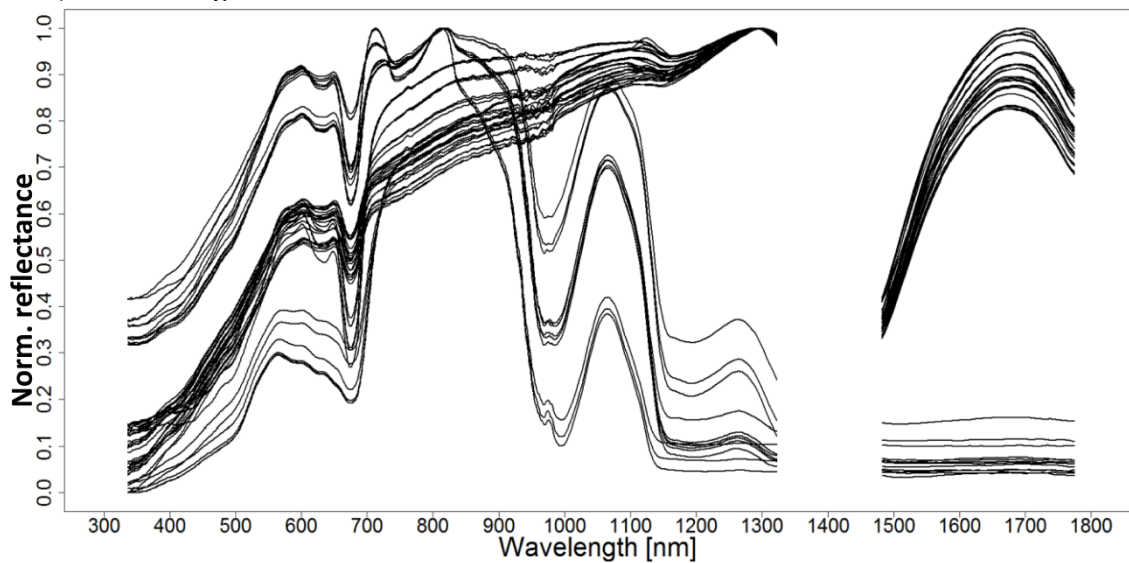


Figure A-14: Plot a) and b) represents the selected wavelengths from ReliefF with method ‘peaks’ and ‘ranges’ of the spectra of 2015 compared with all wavelengths in plot c). The discrete spectral band values of plots a) and b) were linked for better comparison.

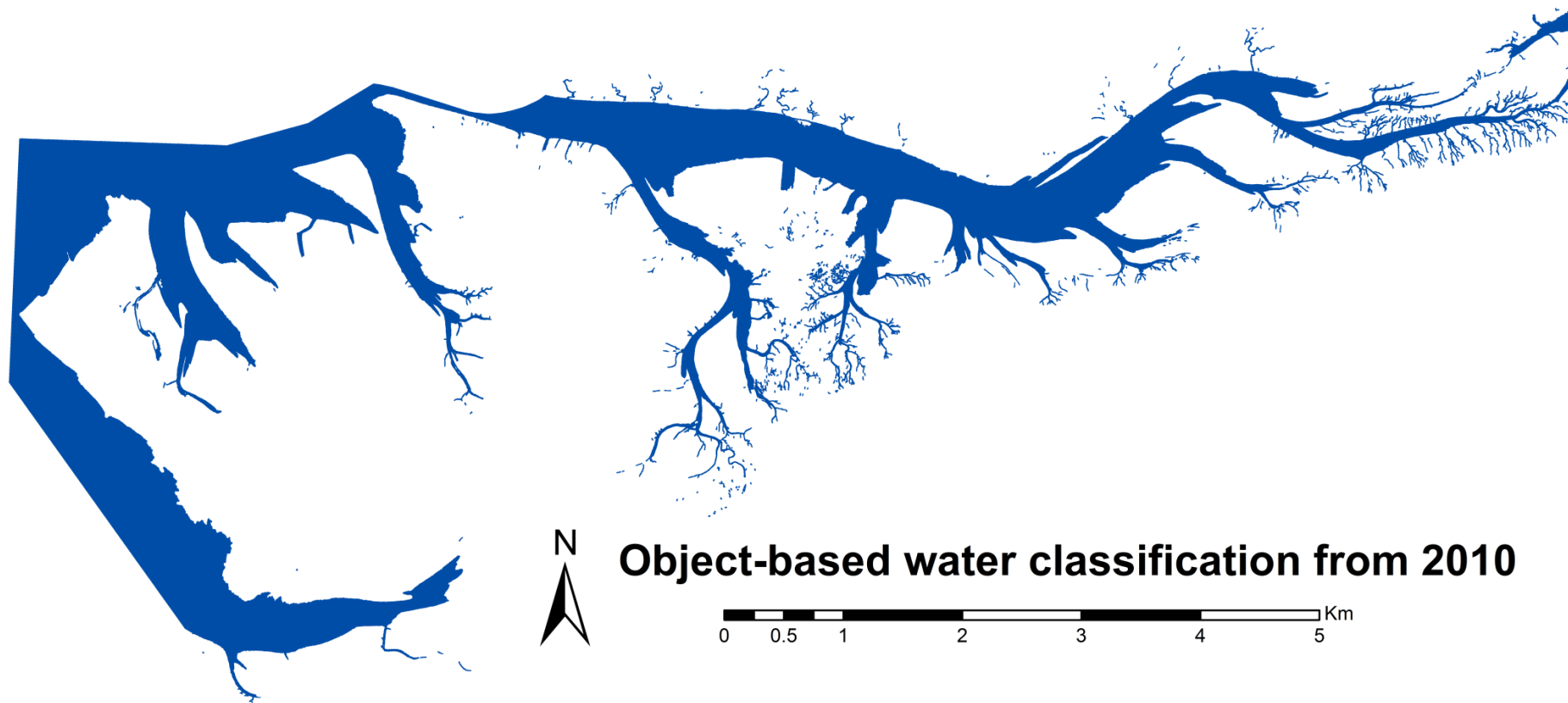


Figure A-15: Objected-based water classification of the LiDAR DEM from 2010.

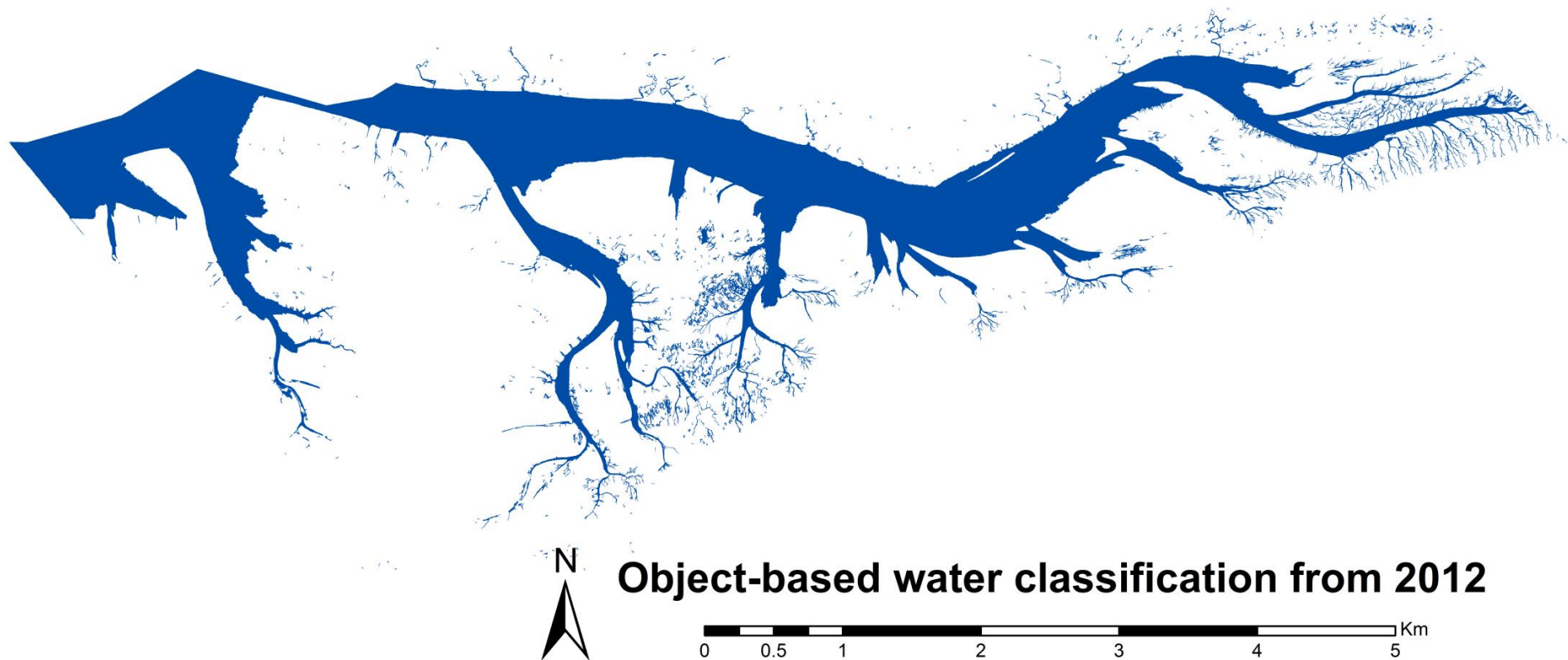


Figure A-16: Objected-based water classification of the LiDAR DEM from 2012.

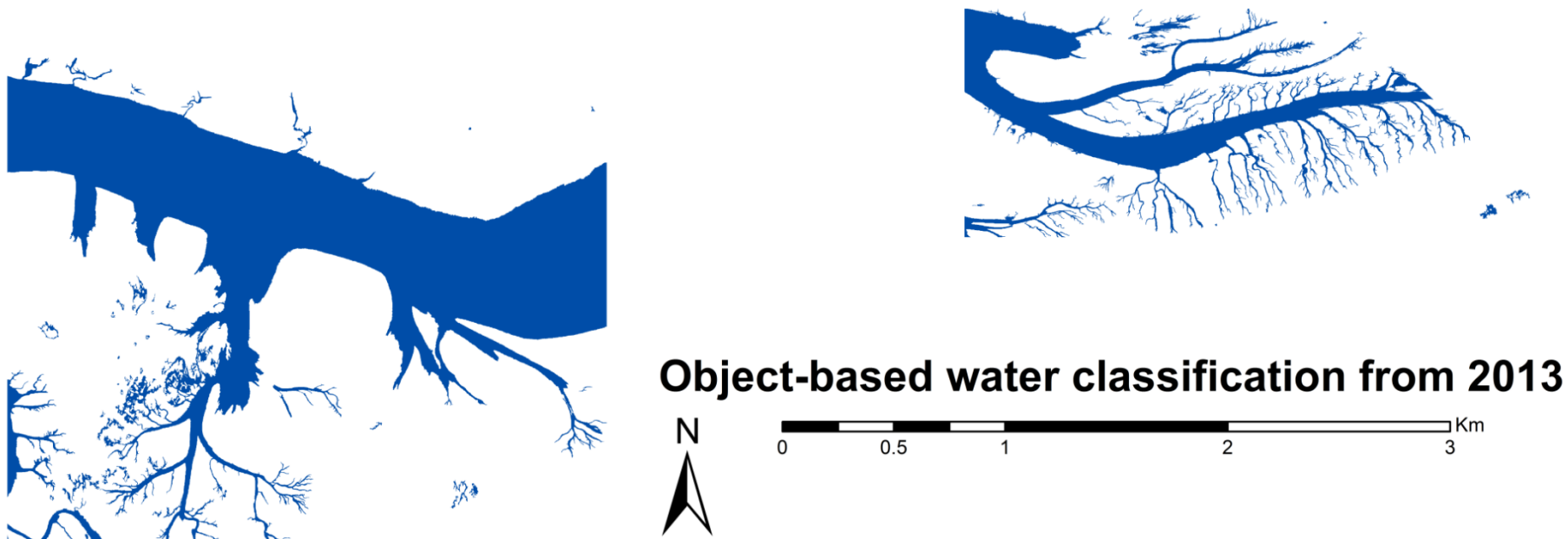


Figure A-17: Objected-based water classification of the LiDAR DEM tiles from 2013.